

ISSN:1305-130X

e-ISSN:1305-1385

CELAL BAYAR UNIVERSITY JOURNAL OF SCIENCE



Manisa Celal Bayar Üniversitesi
Fen Bilimleri Dergisi

2025

VOLUME:21

ISSUE:1



Journal of Science

Volume: 21, Issue: 1, Year: 2025

Contact

Manisa Celal Bayar University

The Graduate School

Campus of Şehit Prof Dr İlhan Varank 45140 Yunussemre – MANİSA, TÜRKİYE

Tel: (00 90) 236 201 27 05

Fax: (00 90) 236 241 21 49

E-mail: lee.fendergi@cbu.edu.tr

Web: <https://dergipark.org.tr/tr/pub/cbayarfbe>

“CBU Journal of Science is indexed by ULAKBIM-TUBITAK TR-DIZIN”



ISSN 1305-130X

E-ISSN 1305-1385

CBUJOS is published quarterly at The Graduate School of Manisa Celal Bayar University

“CBU Journal of Science is a refereed scientific journal”



Celal Bayar University Journal of Science

Owner: Manisa Celal Bayar University, The Graduate School

Coordinator of Scientific Publishing: Prof. Dr. Kamil ŞİRİN

Editor in Chief: Prof. Dr. Kamil ŞİRİN

Editor: Assoc. Prof. Dr. İlker Çetin KESKİN

Layout Editor

Res. Assist. Musa OVALI

Res. Assist. Gencay TEPE

Subject Editors

Prof. Dr. Ali KONURALP, Manisa Celal Bayar University, Mathematics

Prof. Dr. Fatih KALYONCU, Manisa Celal Bayar University, Biology

Prof. Dr. Hülya DURMUŞ, Manisa Celal Bayar University, Mechanical Engineering

Prof. Dr. Kamuran AKTAŞ, Manisa Celal Bayar University, Biology

Prof. Dr. Tuğba ÖZACAR ÖZTÜRK, Manisa Celal Bayar University, Computer Engineering

Assoc. Prof. Dr. Bora CANBULA, Manisa Celal Bayar University, Computer Engineering

Assoc. Prof. Dr. Emriye AY, Manisa Celal Bayar University, Chemical

Assoc. Prof. Dr. Mehmet Ali ILGIN, Manisa Celal Bayar University, Industrial Engineering

International Scientific Advisory Board

Prof. Dr. Arianit REKA; State University of Tetova, Macedonia

Prof. Dr. Tomasz NIEMIEC; Warsaw University of Life Sciences, Poland

Prof. Dr. Alyani ISMAIL; Universiti Putra, Malaysia

Prof. Dr. Iuliana APRODU; Dunarea de Jos University, Romania

Assoc. Prof. Can BAYRAM; University of Illinois, USA

Assoc. Prof. Dr. Johanan Christian PRASANN; Madras Christian College, South India

Assoc. Prof. Dr. Noureddine ISSAOUI; Université de Monastir, Tunisie.

Assoc. Dr. Edward Albert UECKERMANN; North-West University, South Africa

Assoc. Dr. Zhi-Qiang ZHANG; The University of Auckland, Holland

Assist. Prof. Dr. Young Ki KIM; Pohang University of Science and Technology, South Korea

Assist. Prof. Dr. Mona MIRHEYDARI; Rutgers University, USA

Assist. Prof. Dr. Donatella ALBANESE; Università Degli Studi Di Salerno, Italy

Assist. Prof. Dr. Jinghua JIANG; The University of Memphis, USA

Assist. Prof. Dr. Jens OLDELAND; University of Hamburg, Germany

Dr. Cheng CHENG; Apple Inc., USA

Dr. Sajedeh AFGHAH; Microsoft Corporation, USA

Dr. Jinghua JIANG; The University of Memphis

National Scientific Advisory Board

Prof. Dr. Mustafa Ersöz; Selçuk University

Prof. Dr. Oğuz Gürsoy; Mehmet Akif University

Prof. Dr. Mehmet Çevik; İzmir Katip Çelebi University

Prof. Dr. Sezgin Çelik; Yıldız Teknik University

Prof. Dr. Osman Dayan; Çanakkale Onsekiz Mart University

Prof. Dr. Serdar İplikçi; Pamukkale University

Prof. Dr. Yasin Üst; Yıldız Teknik University

Prof. Dr. Mahmut Kuş; Konya Teknik University

Prof. Dr. Ertunç Gündüz; Hacettepe University

Prof. Dr. Tülin Aydemir; Manisa Celal Bayar University

Prof. Dr. Sezai Taşkın; Manisa Celal Bayar University

Prof. Dr. Fatma Şaşmaz Ören; Manisa Celal Bayar University

Prof. Dr. Fatih Selimefendigil; Manisa Celal Bayar University

Prof. Dr. Osman Çulha; Manisa Celal Bayar University

Prof. Dr. Ali Konuralp; Manisa Celal Bayar University

Prof. Dr. Erol Akpınar; Abant İzzet Baysal University

Prof. Dr. Ali Demir; Manisa Celal Bayar University

Prof. Dr. Serap Derman; Yıldız Teknik University

Prof. Dr. Özlem Çağındı; Manisa Celal Bayar University

Assoc. Prof. Dr. Fatih Doğan; Çanakkale Onsekiz Mart University

Assoc. Prof. Dr. Yeliz Yıldırım; Ege University

Assoc. Prof. Dr. Hayati Mamur; Manisa Celal Bayar University

Assoc. Prof. Dr. Mehmet Söylemez; Adıyaman University

Assoc. Prof. Dr. Nil Mansuroğlu; Ahi Evran University

Assist. Prof. Dr. Zeynep Çipiloğlu Yıldız; Manisa Celal Bayar University



CBU Journal of Science

Celal Bayar University Journal of Science (CBUJOS) covers scientific studies in the fields of Engineering and Science and publishes accounts of original research articles concerned with all aspects of experimental and theoretical studies. CBU Journal of Science is a refereed scientific journal published four times annually (March, June, September and December) by The Graduate School of Manisa Celal Bayar University. CBU Journal of Science considers the original research articles written in English for evaluation.

CBU Journal of Science is indexed by TUBİTAK ULAKBİM TR-DİZİN, and also is included in DOAJ, Cite Factor, Journal TOCS, Advanced Science Index and OAJI databases. Digital Object Identifier (DOI) number will be assigned for all the articles being published in CBU Journal of Science.

Instructions for Authors and Article Template can be found on the page of Celal Bayar University Journal of Science DergiPark (<https://dergipark.org.tr/tr/pub/cbayarfb>)





Vol: 21, Issue: 1, Year: 2025



Contents

Research Article

Pages

- 1. Comparative Anatomy of Some Verbascum Taxa (Scrophulariaceae) in Southeastern Anatolia and Distinguishing Characteristics of These Taxa** 1-19
DOI: 10.18466/cbayarfbe.1480614
Murat Kılıç*, Fatma Mungan Kılıç
- 2. Determination of Carbon Footprint: Düzce University Konuralp Campus** 20-26
DOI:10.18466/cbayarfbe.1456641
İrem Duzdar*, Rabia Yıldız
- 3. Propeller Modification with Groove Structure on Thrust Performance** 27-34
DOI:10.18466/cbayarfbe.1531094
Duygu Özyurt, Hürrem Akbıyık*
- 4. Spectroscopic (FT-Raman, FT-IR, UV-Vis, and NMR) and Theoretical Analysis of 1-Methylindole: Structural Characterization, Non-Covalent Interactions, and Electronic Properties** 35-49
DOI: 10.18466/cbayarfbe.1554031
Çağlar Karaca*
- 5. Transforming University Life with Virtual Reality: Campus 2.0 – MetaCBU** 40-59
DOI:10.18466/cbayarfbe.1538384
Barış Çukurbaşı, Ali Geriş*, Orkun Teke, Murat Kılınç
- 6. Improvement of Mechanical and Viscoelastic Properties of Polypropylene with Wood and Wollastonite Fillers** 60-65
DOI: 10.18466/cbayarfbe.1565156
Mustafa Öncül*, Kutlay Sever
- 7. Naringenin-Based Oximes and Hydrazones: Synthesis, Molecular Docking with Bovine Serum Albumin and Drug-Likeness, Admet Profiling Studies** 66-74
DOI: 10.18466/cbayarfbe.1552978
Ferhat Melihcan Abay, Hafize Özcan*, Ayşen Şuekinci Yılmaz, Ömer Zaim
- 8. Integrating GIS and Fuzzy BWM for Solar PV Power Plant Site Selection: A Case Study of Konya, Turkey** 75-89
DOI: 10.18466/cbayarfbe.1589809
Ömer Öztaş, Bilal Ervural*
- 9. Analysis of Level-Off Flight Segments of Descending Aircraft for Busy Terminal Maneuvering Areas** 90-94
DOI: 10.18466/cbayarfbe.1478719
Ramazan Kürşat Çeçen*
- 10. Antireflection Coating for MWIR on Calcium Fluoride Using Ion-Assisted E-Beam Deposition** 95-102
DOI: 10.18466/cbayarfbe.1523797
Yusuf Doğan, İlhan Erdoğan*
- 11. A Contribution To Solve A Linear Equation With One Variable And Reverse A Matrix In 3-Cyclic Refined Neutrosophic Ring** 103-108
DOI: 10.18466/cbayarfbe.1488451
Hamiyet Merkepçi*
- 12. Investigation of Salinity Tolerance Related Gene Expression in Rice (Oryza sativa L.)** 109-120
DOI: 10.18466/cbayarfbe.1529138
Atilla Salman, Sinan Meriç, Tamer Gümüş, Çimen Atak, Alp Ayan*
- 13. DeepFake Detection Using Fine-Tuned CNN Architectures** 121-128
DOI: 10.18466/cbayarfbe.1530209
Dilber Çetintaş, Zehra Yücel*
- 14. Updated Distribution and Future Concerns of Crocus balansae** 129-132
DOI: 10.18466/cbayarfbe.1562245
Almıla Çiftçi*

Comparative Anatomy of Some *Verbascum* Taxa (Scrophulariaceae) in Southeastern Anatolia and Distinguishing Characteristics of These Taxa

Murat KILIÇ^{1*} , Fatma MUNGAN KILIÇ¹ 

¹ Department of Crops and Animal Production, Mardin Artuklu University, 47200 Mardin, Artuklu, Türkiye
[*muratkiloc04@gmail.com](mailto:muratkiloc04@gmail.com)

* Orcid No: 0000-0002-6408-9660

Received: 8 May 2024

Accepted: 23 September 2024

DOI: 10.18466/cbayarfbe.1480614

Abstract

The *Verbascum* L. genus (Scrophulariaceae) is global in distribution. Türkiye is the genus's hub of genetic diversity, and it contains the greatest number of species within it worldwide. The genus *Verbascum* has significant morphological diversity, making species classification difficult. The anatomy of the roots, stems and leaves of seven *Verbascum* taxa (*Verbascum agrimoniifolium* subsp. *agrimoniifolium*, *V. orientale* subsp. *orientale* (group A), *V. laetum* (group C), *V. geminiflorum* (group D), *V. andrusii*, *V. kotschyi* (group K), *V. lasianthum* (group L)) found in the Southeastern Anatolia Region (Diyarbakır, Mardin, and Şanlıurfa Province) of Türkiye formed the basis of this study. Cross-section of root, stem and leaf samples from seven different *Verbascum* taxa were cut by hand and then examined under a light microscope. The xylem components play an important role in taxonomic root parts. The distribution and size of xylem elements vary according to taxa. The pith region is a large region in stem sections, and the upper part of the epidermis cells is surrounded by a separate indented cuticle layer. The main vein of the leaves is represented by lateral bundles. The presence of idioblasts (*V. laetum* and *V. geminiflorum*) has observed in the leaf. In this study, the importance of various characteristics in *Verbascum* taxa limitation was investigated. In order to support morphological features in taxonomic classification and assist in genus systematics, some characters typically associated with anatomical patterns (such as the presence of idioblasts in the leaf) can be applied.

Keywords: anatomy, light microscopy, Southeastern Anatolia, taxonomy, Türkiye, *Verbascum*

1. Introduction

The genus *Verbascum* L., belonging to the family Scrophulariaceae includes approximately 360 species in the world and a total of 257 species in Türkiye under 13 groups, 132 of which are hybrids. The number of endemic species is approximately 202 and the endemism rate is 80%. The breed is the gene and endemism center for our country and is generally distributed in Eastern, Southern and Central Anatolia. Iran-Turan phytogeographic region is the general distribution area of the species [1-3]. *Verbascum* genus has a wide distribution area and a large number of species. Therefore, there are taxonomic difficulties with the genus *Verbascum*, and its infrageneric classification is a little haphazard and informal. Moreover, taxonomic identification may be difficult due of the difficulties in creating a useful key. To this end, the morphology and systematics of *Verbascum* taxa are being studied by a

large number of scientists in Türkiye and around the globe [4]. 13 different artificial groups have been composed for the *Verbascum* genus. Studies on the *Verbascum* genus, which is widespread in Türkiye, were carried out by Huber-Morath [5] and Karavelioğulları [6], and more than 10 species and six hybrid species were described.

Being one of the largest genera in terms of total species, *Verbascum* is known to present challenges in taxonomy and diagnosis due to its high level of general hybridization. Studies on the genus's anatomical traits are few [7]. There are not many anatomical studies on the genus [8-19], there are still lacks and unstudied taxa in Türkiye.

It has been recorded that the genus, which has had medicinal use since ancient times, has been used by the

Egyptians and Romans throughout history and is effective against cough, toothache, cramps, bronchitis, diarrhea and hoarseness. Today, it is known that it is grown for the production of tea, tincture and natural medicine. It has been recorded that it is used externally as a tissue softener and mild analgesic, to relieve menstrual pain, rheumatism, ear aches and hemorrhoids, lung, diabetes, arteriosclerosis and to heal animal wounds, and internally as an expectorant and chest softener [20]. Furthermore, it has antiviral, anti-inflammatory, anticancer, antispasmodic, antiseptic, antimalarial, antiulcerogenic, cytotoxic, sedative, and bactericidal properties in its flowers, leaves, and roots [21-22].

Determining the anatomical links between seven *Verbascum* taxa (*V. agrimoniifolium* subsp. *agrimoniifolium*, *V. orientale* subsp. *orientale* (group A), *V. laetum* (group C), *V. geminiflorum* (group I), *V. andrusii*, *V. kotschyi* (group K), *V. lasianthum* (group L)) that are distributed throughout the Southeastern Anatolia Region is the goal of this study. The relationships between the *Verbascum* taxa were also investigated in order to provide pertinent comparative data, support the morphological features, and provide anatomical information that will aid in their classification. The data gathered ought to be employed

for the purpose of classifying or offering solid backing for the assessment of the group and genus in later studies.

2. Materials and Methods

Samples of seven taxa belonging to the genus *Verbascum*, collected for use in anatomy, were collected from different localities of Diyarbakır, Mardin and Şanlıurfa (Figure 1). The voucher samples were stored in the Department of Plants and Animal Production's herbarium at Mardin Artuklu University, Türkiye's Kızıltepe Vocational School (MARIUM). The places of collection, the collector's number, and the habitat of the samples that were analyzed for micromorphological traits are listed in Table 1. The taxonomic description of the plant was determined using the guidelines provided by Davis et al. [1] and Karavelioğulları [2].

Collected specimens were kept in falcon tubes with 70% ethyl alcohol for use in anatomical study. Sections of the plant were taken from the root, stem, and leaf sections using a razor. After staining them with safranin-fast green, they were examined under a light microscope (LM) and photographed [23]. Terms used in the anatomy align with those used by Metcalfe and Chalk [24].

Table 1. *Verbascum* taxa used for anatomy studies and collected localities.

Taxa	Collection areas and habitat	Collector number
<i>V. agrimoniifolium</i> subsp. <i>agrimoniifolium</i>	Mardin, Artuklu, Hamzabey Neighborhood, road side, damp wet places, 37°22'22"N 40°42'11"E, 971 m.	M.Kılıç 272 M.Kılıç 364
	Şanlıurfa, Karaköprü, Akbayır Neighborhood, road side, damp wet places, 37°11'22"N 38°48'49"E, 554 m.	M.Kılıç 288 M.Kılıç 383
	Diyarbakır, Siverek-Diyarbakır road, road side, rocky slope, 1014 m.	M.Kılıç 359
<i>V. orientale</i> subsp. <i>orientale</i>	Mardin, Artuklu, 13 Mart Neighborhood, rocky slope, 37°20'44"N 40°43'44"E, 835 m.	M.Kılıç 269 M.Kılıç 365 M.Kılıç 412
	Mardin, Artuklu, Cevizpınar Neighborhood, road side, stone area, 37°20'12"N 40°46'26"E, 848 m.	M.Kılıç 247 M.Kılıç 258
<i>V. laetum</i>	Mardin, Artuklu, Sultanköy Neighborhood, road side, stone area, fallow fields, 37°22'49"N 40°39'14"E, 1147 m.	M.Kılıç 273
	Mardin, Mazıdağı, Ömürlü Neighborhood, road side, 37°30'14"N 40°31'19"E, 939 m.	M.Kılıç 281
	Mardin, Mazıdağı, Kebapçı Neighborhood, road side, rocky slope, 37°32'19"N 40°31'51"E, 917 m.	M.Kılıç 282
	Şanlıurfa, Viranşehir-Urfa road, road side, rocky slope.	M.Kılıç 282
	Mardin, Midyat, road side, rocky slope, 37°27'54"N 41°04'59"E, 1030 m.	M.Kılıç 312
	Mardin, Midyat, road side, rocky slope, 37°26'15"N 41°18'07"E, 928 m.	M.Kılıç 314-4
	Mardin, Midyat-Dargeçit road, road side, rocky	M.Kılıç 315-4

	slope, stone area, 37°26'15"N 41°18'07"E, 928 m.	
	Mardin, Savur, Savur-Kayatepe road, road side, rocky slope, 37°31'31"N 40°53'37"E, 933 m.	M.Kılıç 340-2
	Mardin, Savur, Savur-Kayatepe road, road side, stone and rocky place, 37°31'18"N 40°54'26"E, 1070 m.	M.Kılıç 341-1
<i>V. geminiflorum</i>	Mardin, Artuklu, Ofis Neighborhood, 37°16'22"N 40°40'49"E, 591 m.	M.Kılıç 284
	Şanlıurfa, Siverek, Siverek-Karacadağ road, road side, cultivated area, 37°43'30"N 39°25'05"E, 867 m.	M.Kılıç 358
<i>V. andrusii</i>	Mardin, Artuklu, Yenişehir Neighborhood, Türkmenler road, road side, serpentine, 37°17'46"N 40°42'47"E, 695 m.	M.Kılıç 252
	Mardin, Artuklu, Çiftlikköy Neighborhood, road side, stony areas, 37°17'09"N 40°43'33"E, 652 m.	M.Kılıç 259
	Mardin, Artuklu, Eskikale Neighborhood, Eskikale road, road side, serpentine, 37°18'09"N 40°46'03"E, 935 m.	M.Kılıç 263
	Mardin, Artuklu, Kötek Neighborhood, Ortaköy-Mardin road, road side, rocky slope, 37°16'34"N 40°46'12"E, 686 m.	M.Kılıç 265
	Mardin, Nusaybin, Akarsu road, streamside, stony area, 37°08'11"N 41°04'44"E, 536 m.	M.Kılıç 300-2
	Mardin, Artuklu, Eskikale Neighborhood, Deyrulzafaran road, road side, 37°17'48"N 40°47'31"E, 876 m.	M.Kılıç 303
	Mardin, Ömerli, Ömerli-Midyat road, road side, rocky slopes.	M.Kılıç 303
	Mardin, Midyat, Düzgeçit Neighborhood, road side, rocky slope, 37°28'15"N 41°07'18"E, 1001 m.	M.Kılıç 313
	Mardin, Midyat, road side, stony area, rocky slope, 37°26'15"N 41°18'07"E, 928 m.	M.Kılıç 314-2
	Mardin, Midyat-Dargeçit road, road side, stony area, rocky slope, 37°26'15"N 41°18'07"E, 928 m.	M.Kılıç 315-3
	Mardin, Dargeçit, road side, 37°33'08"N 41°40'16"E, 933 m.	M.Kılıç 316
	Mardin, Midyat, Yemişli Neighborhood, road side, rocky slope, 37°19'38"N 41°20'57"E, 960 m.	M.Kılıç 318
	Mardin, Kızıltepe, Soğanlı Neighborhood, stony area, rocky slope.	M.Kılıç 322
	Mardin, Kızıltepe, Başdeğirmen road, road side, rocky slope, 37°16'31"N 40°32'41"E, 655 m.	M.Kılıç 323-1
	Mardin, Yeşilli, Bülbül Neighborhood, road side, rocky slope, 37°18'31"N 40°49'54"E, 733 m.	M.Kılıç 328-1
	Mardin, Yeşilli, Bülbül-Uzunköy road, road side, stony and rocky area, 37°17'32"N 40°50'41"E, 698 m.	M.Kılıç 330-1
	Mardin, Savur, Pınardere-Savur road, road side, serpentine, 37°29'33"N 40°49'35"E, 887 m.	M.Kılıç 335
	Mardin, Mardin-Diyarbakır road, road side, calcareous slopes, 1039 m.	M.Kılıç 344-1
	Mardin, Mazıdağı, Mardin-Diyarbakır road, 24 km before Çınar, road side, calcareous slopes, 929 m.	M.Kılıç 345-1
	Diyarbakır, Çınar, 6 km before Çınar, road side, 37°40'47"N 40°27'28"E, 725 m.	M.Kılıç 346-1
	Mardin, Artuklu, Yardere Neighborhood, road side,	

	stony area, 37°13'22"N 40°58'23"E, 701 m.	M.Kılıç 363-2
	Mardin, Artuklu, Sultanköy Neighborhood, Leylak street road, water source location, 37°22'55"N 40°39'07"E, 1132 m.	M.Kılıç 396-2
	Mardin, Artuklu, Nur Neighborhood, location around Çağatay Cemetery, road side, streamside, 37°21'37"N 40°40'26"E, 930 m.	M.Kılıç 400-1
<i>V. kotschy</i>	Mardin, Artuklu, Eskikale Neighborhood, Bakırkırı-Yeşilli road, road side, stony area, 37°19'38"N 40°47'48"E, 828 m.	M.Kılıç 252
	Mardin, Artuklu, Eryeri Neighborhood, Eryeri-Cezaevi road, road side, vineyards, 37°17'50"N 40°45'11"E, 770 m.	M.Kılıç 262
	Mardin, Artuklu, Kötek Neighborhood, Mardin-Ortaköy road, road side, 37°17'07"N 40°46'32"E, 742 m.	M.Kılıç 264
	Mardin, Artuklu, 13 Mart Neighborhood, 13 Mart-Hamzabey road, road side, stony area, 37°20'44"N 40°43'44"E, 834 m.	M.Kılıç 268
	Şanlıurfa, Karaköprü, Borsa İstanbul Middle School, road side, rocky slope, 37°12'40"N 38°47'22"E, 621 m.	M.Kılıç 298
	Mardin, Nusaybin, Akarsu road, road side, stony area, 37°08'06"N 41°04'41"E, 546 m.	M.Kılıç 299
	Mardin, Ömerli, Ömerli-Midyat road, road side, rocky slopes.	M.Kılıç 308-1
	Mardin, Dargeçit-Midyat road, 29 km before Midyat, road side.	M.Kılıç 317-2
	Mardin, Yeşilli, Şirinevler Neighborhood, road side, stony area, rocky slopes, 37°20'40"N 40°49'53"E, 904 m.	M.Kılıç 327-2
	Mardin, Yeşilli, Bülbül-Uzunköy road, road side, stony area, 37°16'53"N 40°50'46"E, 676 m.	M.Kılıç 331-4
	Mardin, Savur, Dereyanı-Köprülü road, road side, 37°27'12"N 40°51'38"E, 940 m.	M.Kılıç 333-1
	Mardin, Artuklu, Dara-Yardere road, road side, rocky and stony area, 37°12'02"N 40°57'37"E, 619 m.	M.Kılıç 361-1
	Mardin, Artuklu, 13 Mart Neighborhood, 13 Mart-Hamzabey road, road side, stony area, 37°20'44"N 40°43'44"E, 834 m.	M.Kılıç 371-2
<i>V. lasianthum</i>	Şanlıurfa, Karaköprü, Borsa İstanbul Middle School, road side, 37°12'26"N 38°47'30"E, 606 m.	M.Kılıç 293-2
	Şanlıurfa, Karaköprü, Güllübağ Neighborhood, Necip Fazıl Kısakürek School, 37°13'46"N 38°49'06"E, 665 m.	M.Kılıç 294
	Mardin, Yeşilli, Bülbül-Uzunköy road, road side, stony area, 37°16'53"N 40°50'46"E, 676 m.	M.Kılıç 331-3
	Mardin, Savur, 1 km after Pınardere, road side, 37°29'05"N 40°49'40"E, 903 m.	M.Kılıç 334
	Diyarbakır, Çınar, 6 km from Çınar, road side, 37°40'47"N 40°27'28"E, 725 m.	M.Kılıç 346-2
	Diyarbakır, Yenişehir, 28 km from Ergani, road side, cultivated area, 766 m.	M.Kılıç 349
	Diyarbakır, Ergani, 9 km from Ergani, road side, stony and rocky area, 38°11'53"N 39°49'57"E, 809 m.	M.Kılıç 350

Şanlıurfa, Hilvan, road side, 592 m.	M.Kılıç 390
Diyarbakır, Siverek-Diyarbakır road, 48 km from Diyarbakır, road side, stony area, 37°49'55"N 39°40'06"E, 1077 m.	M.Kılıç 393
Mardin, Artuklu, Sultanköy Neighborhood, Leylak Street road, water supply location, 37°22'55"N 40°39'07"E, 1132 m.	M.Kılıç 396-1
Mardin, Ömerli, 6 km after Ömerli, road side.	M.Kılıç 402-2



Figure 1. General appearance of the genus *Verbascum*. (a) *V. agrimoniifolium* subsp. *agrimoniifolium*, (b) *V. orientale* subsp. *orientale*, (c) *V. laetum*, (d) *V. geminiflorum*, (e) *V. andrusii*, (f) *V. kotschyi*, (g) *V. lasianthum*.

3. Results and Discussion

3.1. Anatomy

3.1.1. Root Anatomy

V. agrimoniifolium subsp. *agrimoniifolium*: Peridermis, cortex, phloem, and xylem are oriented from outside to inside in root cross-sections. The peridermis typically has 3-5 cell layers. Beneath the periderm is a stratified parenchyma. Beneath the parenchyma are 3-5 layers of phloem cells. There is unclear cambium. The center of the root is filled with xylem, which covers a wider region. Trachea cells are longer than they are wide, and their locations are asymmetrical. The phloem has a smaller area than the xylem. There are 1-2 rows of

rectangular and quadrangular cells in its pith rays. The round or polygonal parenchymatous cells make up the pith (Table 2, Figure 2).

V. orientale subsp. *orientale*: Peridermis, cortex, phloem, and xylem are oriented from outside to inside in root cross-sections. The peridermis typically has 5-7 cell layers. Beneath the periderm is a stratified parenchyma. Beneath the parenchyma are 3-5 layers of phloem cells. There is unclear cambium. The center of the root is filled with xylem, which covers a wider region. Trachea cells are longer than they are wide, and their locations are asymmetrical. The phloem has a smaller area than the xylem. There are 1-2 rows of rectangular and quadrangular cells in its pith rays. The

round or polygonal parenchymatous cells make up the pith (Table 2, Figure 2).

V. laetum: Peridermis, cortex, phloem, and xylem are oriented from outside to inside in root cross-sections. The peridermis typically has 5-7 cell layers. Beneath the periderm is a stratified parenchyma. Beneath the parenchyma are 3-5 layers of phloem cells. There is unclear cambium. The center of the root is filled with xylem, which covers a wider region. Trachea cells are longer than they are wide, and their locations are asymmetrical. The phloem has a smaller area than the xylem. There are 2-4 rows of rectangular and quadrangular cells in its pith rays. The round or polygonal parenchymatous cells make up the pith (Table 2, Figure 2).

V. geminiflorum: In root cross-sections, peridermis, cortex, phloem and xylem are oriented from outside to inside. Peridermis cells are crushed and typically have 5-7 cell layers. There is a multilayered parenchyma under the periderm. There are 3-5 rows of phloem cells under the parenchyma. There is indistinct cambium. The middle of the root is filled with xylem, which covers a larger area. Tracheal cells are longer than wide and their position is asymmetrical. Phloem has a smaller area than xylem. There are 1-3 rows of rectangular and quadrangular cells in its core rays. The round or polygonal parenchymatous cells form the pith (Table 2, Figure 2).

V. andrusii: Peridermis, cortex, phloem, and xylem are oriented from outside to inside in root cross-sections. The peridermis typically has 7-15 cell layers. Beneath the periderm is a stratified parenchyma. Beneath the parenchyma are 5-7 layers of phloem cells. There is

unclear cambium. The center of the root is filled with xylem, which covers a wider region. Trachea cells are longer than they are wide, and their locations are asymmetrical. The phloem has a smaller area than the xylem. There are 1-3 rows of rectangular and quadrangular cells in its pith rays. The round or polygonal parenchymatous cells make up the pith (Table 2, Figure 2).

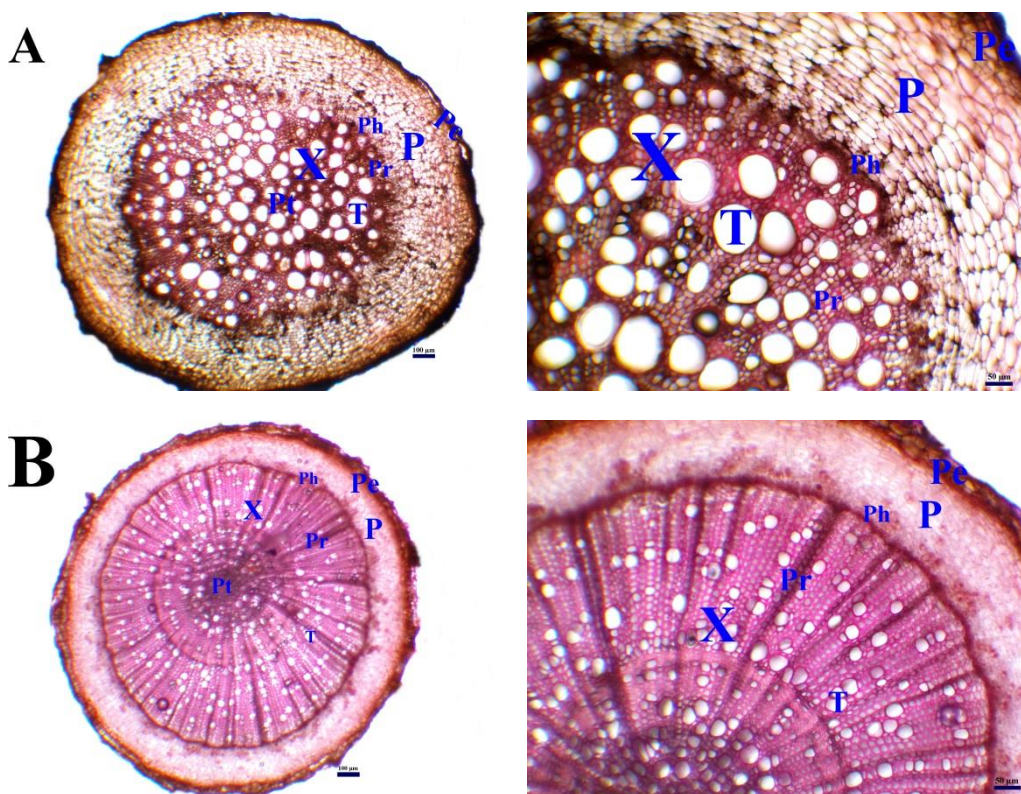
V. kotschyi: Peridermis, cortex, phloem, and xylem are oriented from outside to inside in root cross-sections. The peridermis typically has 7-9 cell layers. Beneath the periderm is a stratified parenchyma. Beneath the parenchyma are 3-5 layers of phloem cells. There is unclear cambium. The center of the root is filled with xylem, which covers a wider region. Trachea cells are longer in width than in length and their positions are asymmetrical. The phloem has a smaller area than the xylem. There are 2-4 rows of rectangular and quadrangular cells in its pith rays. The round or polygonal parenchymatous cells make up the pith (Table 2, Figure 2).

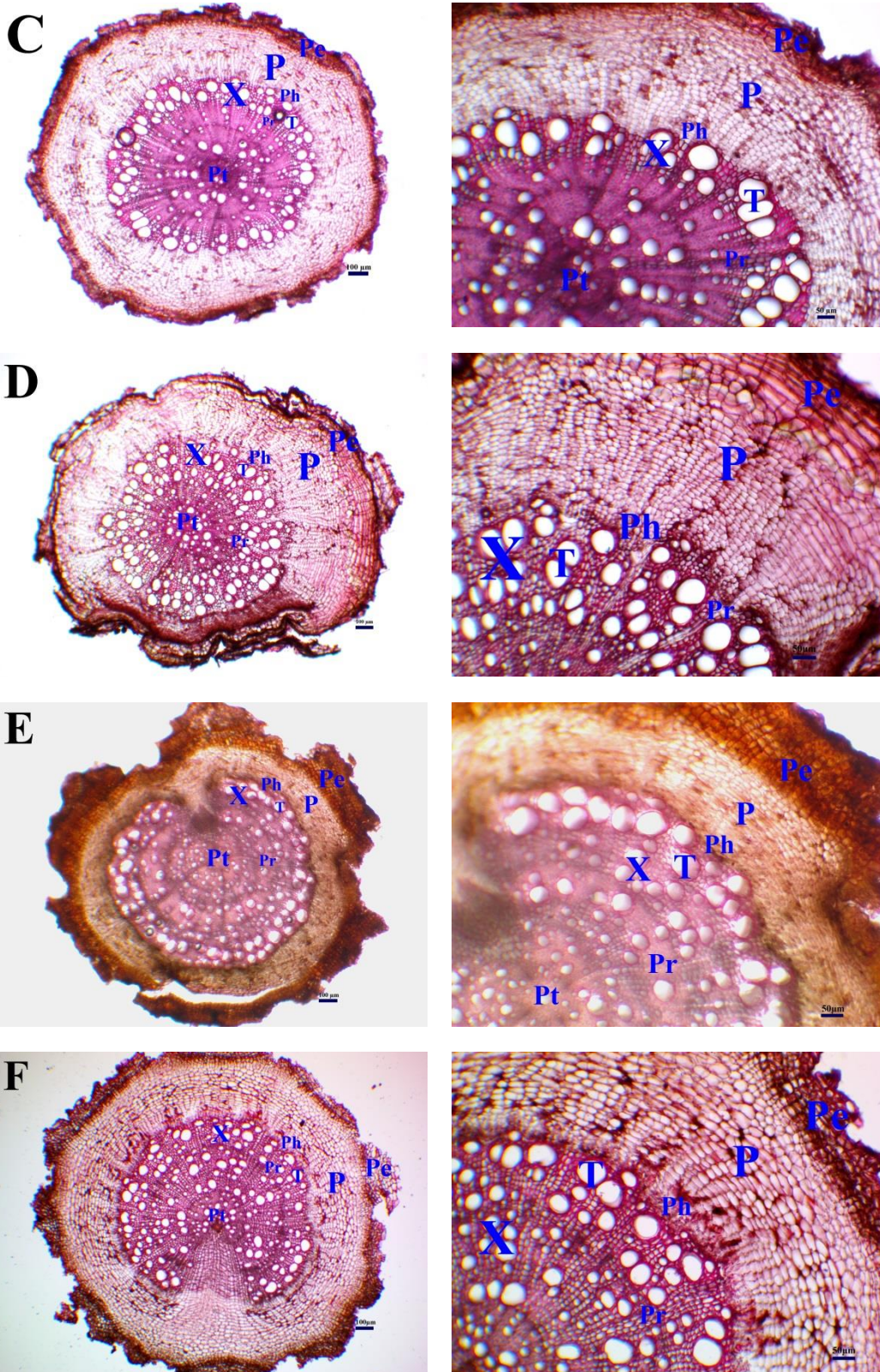
V. lasianthum: Peridermis, cortex, phloem, and xylem are oriented from outside to inside in root cross-sections. The peridermis typically has 7-9 cell layers. Beneath the periderm is a stratified parenchyma. Beneath the parenchyma are 3-5 layers of phloem cells. There is unclear cambium. The center of the root is filled with xylem, which covers a wider region. Trachea cells are longer in width than in length and their positions are asymmetrical. The phloem has a smaller area than the xylem. There are 1-3 rows of rectangular and quadrangular cells in its pith rays. The round or polygonal parenchymatous cells make up the pith (Table 2, Figure 2).

Table 2. The root anatomical measurements of taxa belonging to the genus *Verbascum* (µm).

Taxa	Tissues	Width			Length		
		Min.	Max.	Mean±S.	Min.	Max.	Mean±S.
<i>V. agrimoniifolium</i> subsp. <i>agrimoniifolium</i>	Peridermis	18.42	61.44	32.09±11.76	10.01	29.59	17.36±5.99
	Parenchyma	19.39	75.70	46.33±14.42	12.07	36.52	22.74±6.04
	Phloem	11.21	23.32	16.17±3.25	6.20	16.74	11.50±2.94
	Trachea	47.02	129.90	89.86±23.55	45.70	113.10	87.38±18.57
<i>V. orientale</i> subsp. <i>orientale</i>	Peridermis	11.05	53.92	27.37±11.36	9.01	28.49	17.73±6.97
	Parenchyma	12.37	41.01	24.61±8.74	8.34	16.97	11.98±2.20
	Phloem	5.73	12.73	8.81±1.96	4.76	9.89	6.75±1.23
	Trachea	16.97	39.80	26.88±6.31	19.20	42.26	32.25±6.69
<i>V. laetum</i>	Peridermis	8.58	39.33	21.51±9.22	8.18	24.51	15.45±4.33
	Parenchyma	14.98	49.86	28.71±9.98	9.99	24.97	18.37±4.15

	Phloem	7.49	23.43	13.57±4.68	5.48	11.84	8.44±1.67
	Trachea	28.91	74.87	45.05±12.02	31.28	90.38	54.45±15.91
<i>V. geminiflorum</i>	Peridermis	14.55	60.45	31.87±10.23	7.19	30.53	18.10±6.94
	Parenchyma	17.03	43.58	28.01±6.23	8.24	23.10	14.44±3.64
	Phloem	5.91	27.70	14.83±5.20	4.02	14.98	8.62±2.69
	Trachea	19.78	63.69	39.12±12.48	20.29	76.91	47.28±18.35
<i>V. andrusii</i>	Peridermis	14.38	45.87	25.14±7.97	14.56	39.19	22.73±5.87
	Parenchyma	10.88	43.71	27.53±8.58	8.68	17.04	13.19±2.14
	Phloem	5.63	16.19	10.15±3.15	5.41	16.44	9.01±2.58
	Trachea	32.42	85.67	55.37±15.13	35.36	91.28	60.29±16.19
<i>V. kotschyi</i>	Peridermis	22.79	49.44	35.76±8.16	13.39	33.97	24.24±5.50
	Parenchyma	19.00	65.38	37.27±12.15	10.89	26.12	19.97±4.56
	Phloem	7.54	17.44	11.70±2.54	6.81	13.92	9.88±2.36
	Trachea	29.64	72.92	48.83±13.59	26.79	75.43	48.01±14.04
<i>V. lasianthum</i>	Peridermis	10.00	23.45	16.54±4.14	6.09	21.31	11.54±3.41
	Parenchyma	11.38	38.90	19.52±6.77	10.54	19.77	13.06±2.27
	Phloem	8.17	19.48	12.36±2.71	6.32	15.37	11.05±2.40
	Trachea	35.66	99.45	59.84±21.18	39.50	83.17	55.14±12.94





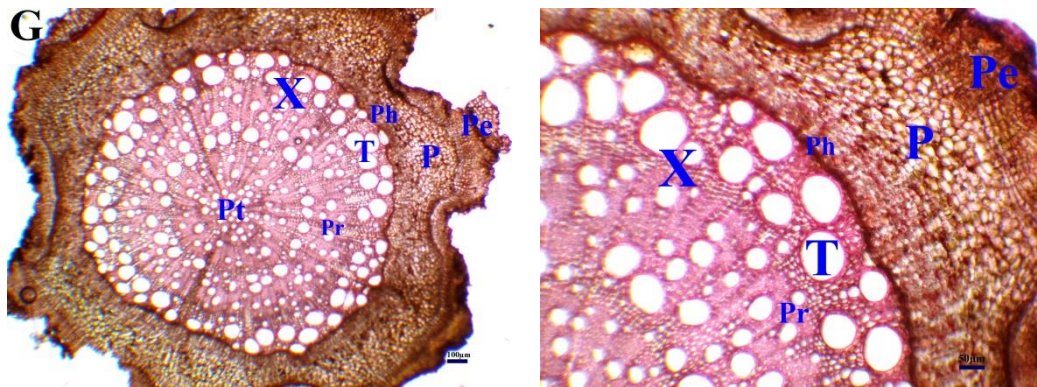


Figure 2. Cross-section of the root of *Verbascum* (A) *V. agrimoniifolium* subsp. *agrimoniifolium*, (B) *V. orientale* subsp. *orientale*, (C) *V. laetum*, (D) *V. geminiflorum*, (E) *V. andrusii*, (F) *V. kotschyi*, (G) *V. lasianthum*. Pe: Periderm, P: Parenchyma, Ph: Phloem, X: Xylem, Pr: Pith ray, T: Trachea, Pt: Pith region. Bars: 100 and 50 μ m.

3.1.2. Stem Anatomy

V. agrimoniifolium subsp. *agrimoniifolium*: Cross-sections from the plant's stem showed a single-layered epidermis with a wavy cuticle. Cells that are round or rectangular make up the epidermis. Under the epidermis are 2-3 rows of collenchyma cells. Oval and round parenchyma cells are arranged in 4-6 rows to form parenchyma tissue. Underneath the parenchyma lies a layer of sclerenchyma arranged in 2-4 rows. There is no difference in the cambium. The phloem is found in a smaller area than xylem. Six or octagonal circular parenchymatous cells with intercellular gaps make up the pith (Table 3, Figure 3).

V. orientale subsp. *orientale*: Cross-sections from the plant's stem showed a single-layered epidermis with a wavy cuticle. Cells that are round or rectangular make up the epidermis. The epidermis is covered with glandular and eglandular hairs. Under the epidermis are 3-4 rows of collenchyma cells. Oval and round parenchyma cells are arranged in 2-3 rows to form parenchyma tissue. Underneath the parenchyma lies a layer of sclerenchyma arranged in 2-4 rows. There is no difference in the cambium. The phloem is found in a smaller area than xylem. Six or octagonal circular parenchymatous cells with intercellular gaps make up the pith (Table 3, Figure 3).

V. laetum: Cross-sections from the plant's stem showed a single-layered epidermis with a wavy cuticle. Cells that are round or rectangular make up the epidermis. The epidermis is covered with eglandular hairs. Under the epidermis are 3-4 rows of collenchyma cells. Oval and round parenchyma cells are arranged in 5-7 rows to form parenchyma tissue. Underneath the parenchyma lies a layer of sclerenchyma arranged in 3-6 rows. There is no difference in the cambium. The phloem is found in a smaller area than xylem. Polygonal circular

parenchymatous cells with intercellular spaces form the pith (Table 3, Figure 3).

V. geminiflorum: Cross-sections from the plant's stem showed a single-layered epidermis with a wavy cuticle. Cells that are round or rectangular make up the epidermis. The epidermis is covered with glandular and compound hairs. Under the epidermis are 2-3 rows of collenchyma cells. Oval and round parenchyma cells are arranged in 7-9 rows to form parenchyma tissue. Underneath the parenchyma lies a layer of sclerenchyma arranged in 2-4 rows. There is no difference in the cambium. The phloem is found in a smaller area than xylem. Polygonal circular parenchymatous cells with intercellular spaces form the pith (Table 3, Figure 3).

V. andrusii: Cross-sections from the plant's stem showed a single-layered epidermis with a wavy cuticle. Cells that are round or rectangular make up the epidermis. The epidermis is covered with glandular, eglandular and compound hairs. Under the epidermis are 2-3 rows of collenchyma cells. Oval and round parenchyma cells are arranged in 5-9 rows to form parenchyma tissue. Underneath the parenchyma lies a layer of sclerenchyma arranged in 2-7 rows. There is no difference in the cambium. The phloem is found in a smaller area than xylem. Polygonal circular parenchymatous cells with intercellular spaces form the pith (Table 3, Figure 3).

V. kotschyi: Cross-sections from the plant's stem showed a single-layered epidermis with a wavy cuticle. Cells that are round or rectangular make up the epidermis. The epidermis is covered with glandular and eglandular hairs. Under the epidermis are 2-4 rows of collenchyma cells. Oval and round parenchyma cells are arranged in 9-11 rows to form parenchyma tissue. Underneath the parenchyma lies a layer of sclerenchyma arranged in 4-7 rows. There is no

difference in the cambium. The phloem is found in a smaller area than xylem. Polygonal circular parenchymatous cells with intercellular spaces form the pith (Table 3, Figure 3).

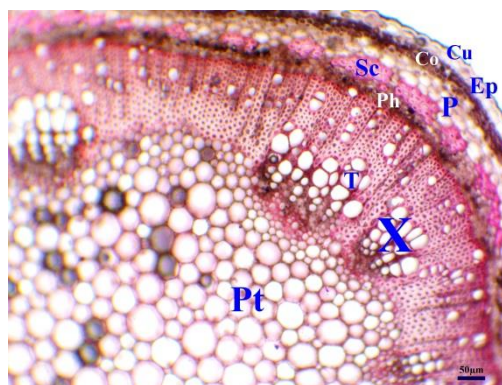
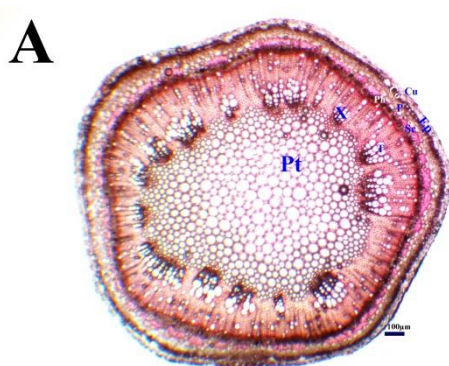
V. lasianthum: Cross-sections from the plant's stem showed a single-layered epidermis with a wavy cuticle. Cells that are round or rectangular make up the epidermis. The epidermis is covered with glandular, eglandular and compound hairs. Under the epidermis are 2-3 rows of collenchyma cells. Oval and round parenchyma cells are arranged in 5-7 rows to form

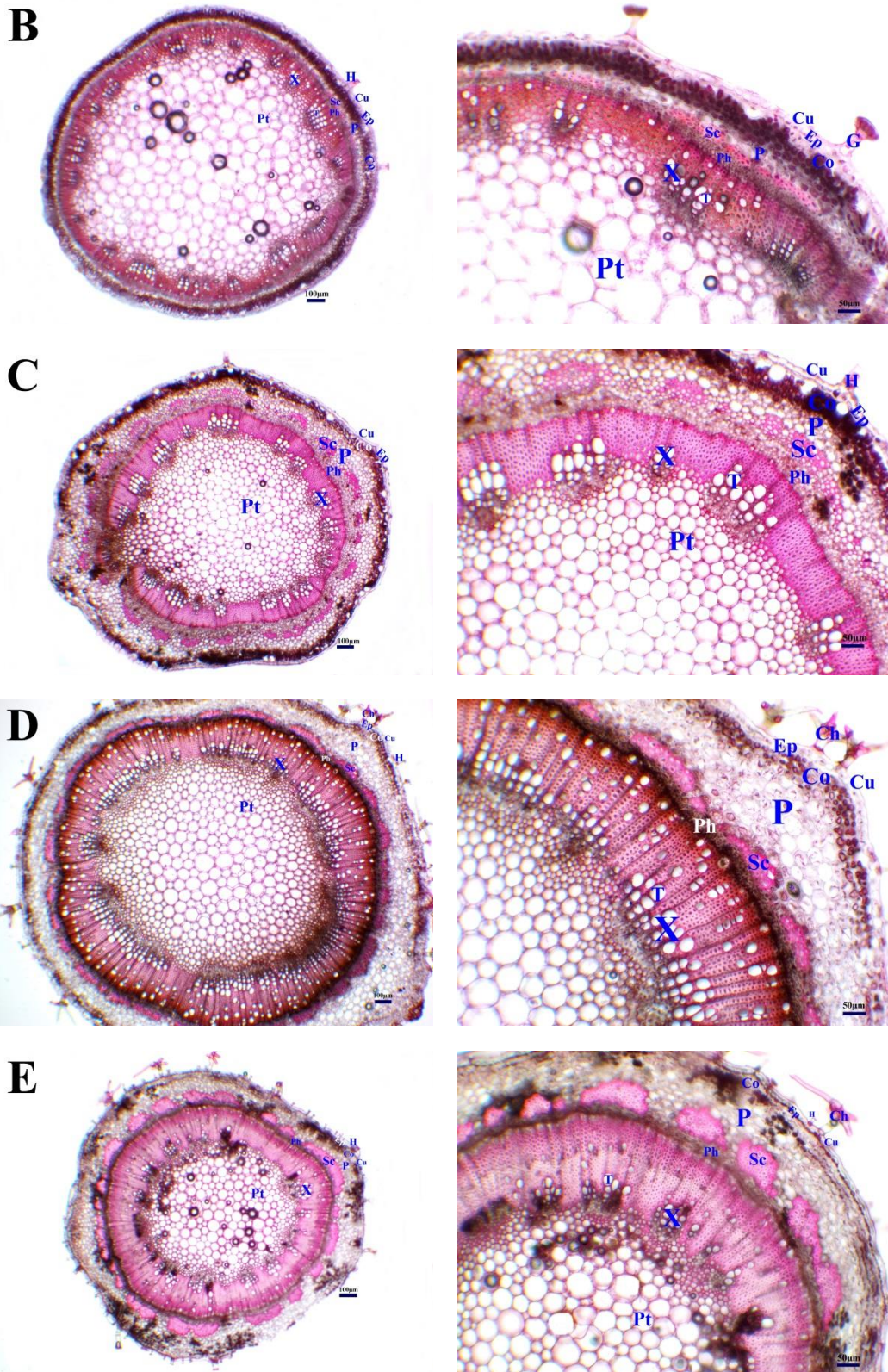
parenchyma tissue. Underneath the parenchyma lies a layer of sclerenchyma arranged in 3-5 rows. There is no difference in the cambium. The phloem is found in a smaller area than xylem. The pith region of the stem consists of large and small parenchymatic polygonal and round-shaped cells (Table 3, Figure 3).

Table 3. The stem anatomical measurements of taxa belonging to the genus *Verbascum* (μm).

Taxa	Tissues	Width			Length		
		Min.	Max.	Mean \pm S.	Min.	Max.	Mean \pm S.
<i>V. agrimoniifolium</i> subsp. <i>agrimoniifolium</i>	Cuticle	-	-	-	6.45	13.09	8.69 \pm 1.79
	Epidermis	19.13	44.54	30.28 \pm 7.46	10.40	27.48	19.22 \pm 4.76
	Collenchyma	6.47	18.48	11.67 \pm 3.44	6.12	16.96	9.48 \pm 2.87
	Parenchyma	12.24	53.52	27.21 \pm 11.51	7.93	31.72	15.75 \pm 6.47
	Phloem	6.11	13.46	9.02 \pm 2.04	4.90	10.51	7.00 \pm 1.45
	Trachea	17.07	36.65	26.50 \pm 5.62	16.63	51.84	31.39 \pm 9.35
	Pith	27.97	87.96	51.06 \pm 14.42	29.08	85.60	50.76 \pm 13.50
<i>V. orientale</i> subsp. <i>orientale</i>	Cuticle	-	-	-	3.27	7.44	5.85 \pm 1.21
	Epidermis	13.09	33.82	23.78 \pm 6.00	13.20	22.00	16.77 \pm 2.52
	Collenchyma	10.13	20.23	14.79 \pm 2.84	12.00	32.76	19.85 \pm 4.93
	Parenchyma	16.13	55.76	33.53 \pm 12.08	10.77	27.11	17.94 \pm 4.67
	Phloem	6.15	14.69	8.78 \pm 2.44	4.28	8.82	5.94 \pm 1.25
	Trachea	15.09	35.78	21.80 \pm 5.12	15.91	32.96	22.61 \pm 4.57
	Pith	55.96	185.96	128.01 \pm 44.49	57.06	174.81	119.66 \pm 42.45
<i>V. laetum</i>	Cuticle	-	-	-	3.79	7.51	6.42 \pm 0.90
	Epidermis	13.76	33.61	23.29 \pm 5.24	14.80	24.88	19.03 \pm 2.41
	Collenchyma	9.01	16.08	13.04 \pm 2.00	9.34	15.92	12.75 \pm 1.89
	Parenchyma	14.75	38.10	24.34 \pm 6.49	16.06	39.14	24.84 \pm 5.81
	Phloem	4.14	10.54	8.20 \pm 1.70	3.76	11.24	6.85 \pm 2.14
	Trachea	12.13	38.90	21.30 \pm 6.62	12.16	43.45	24.08 \pm 8.14
	Pith	34.01	92.32	57.46 \pm 16.49	33.68	94.06	61.78 \pm 16.62
<i>V. geminiflorum</i>	Cuticle	-	-	-	5.71	10.85	8.63 \pm 1.33
	Epidermis	11.28	37.41	19.45 \pm 6.14	11.36	24.33	16.25 \pm 3.46
	Collenchyma	9.45	25.15	16.87 \pm 3.80	8.57	21.68	15.68 \pm 3.49
	Parenchyma	24.90	54.80	39.88 \pm 6.91	14.64	42.80	27.02 \pm 7.05

	Phloem	5.57	14.49	9.26±2.45	4.83	9.26	7.06±1.71
	Trachea	15.78	41.58	26.51±6.76	20.75	51.20	35.35±9.70
	Pith	33.69	108.44	66.89±21.40	31.20	101.45	72.51±21.36
<i>V. andrusii</i>	Cuticle	-	-	-	3.67	7.93	5.73±1.14
	Epidermis	2.92	16.87	11.09±4.42	6.70	16.69	10.80±2.58
	Collenchyma	6.11	23.66	14.14±4.37	7.65	20.12	13.78±3.69
	Parenchyma	33.99	68.23	47.26±9.66	15.12	33.46	25.60±4.49
	Phloem	3.91	15.26	9.82±3.22	3.01	14.06	6.81±2.35
	Trachea	23.30	53.47	38.13±8.10	24.75	69.99	48.76±13.09
	Pith	11.36	28.40	19.57±5.28	11.40	31.50	20.21±5.93
<i>V. kotschyi</i>	Cuticle	-	-	-	5.73	11.38	9.06±1.38
	Epidermis	13.46	23.38	17.48±2.80	16.96	24.10	20.25±1.94
	Collenchyma	11.49	26.99	16.39±4.60	11.26	27.32	16.72±4.31
	Parenchyma	21.11	67.50	45.21±15.47	15.90	37.21	27.14±7.15
	Phloem	4.66	15.11	9.11±2.71	5.14	12.78	7.78±2.13
	Trachea	16.45	40.98	28.34±7.08	18.06	50.18	32.22±7.93
	Pith	25.05	81.45	51.79±17.71	25.85	88.67	55.33±20.53
<i>V. lasianthum</i>	Cuticle	-	-	-	3.91	11.44	8.84±1.69
	Epidermis	7.00	18.48	11.44±3.52	7.81	18.02	12.28±2.92
	Collenchyma	10.32	22.54	16.77±2.98	10.38	20.30	14.59±2.71
	Parenchyma	19.43	43.63	32.50±7.39	20.60	44.82	33.69±7.41
	Phloem	4.98	14.03	10.35±2.62	7.54	12.58	9.51±1.44
	Trachea	10.26	25.95	18.37±4.52	15.01	40.07	24.99±5.70
	Pith	19.09	63.31	43.72±11.64	14.72	41.94	28.72±7.59





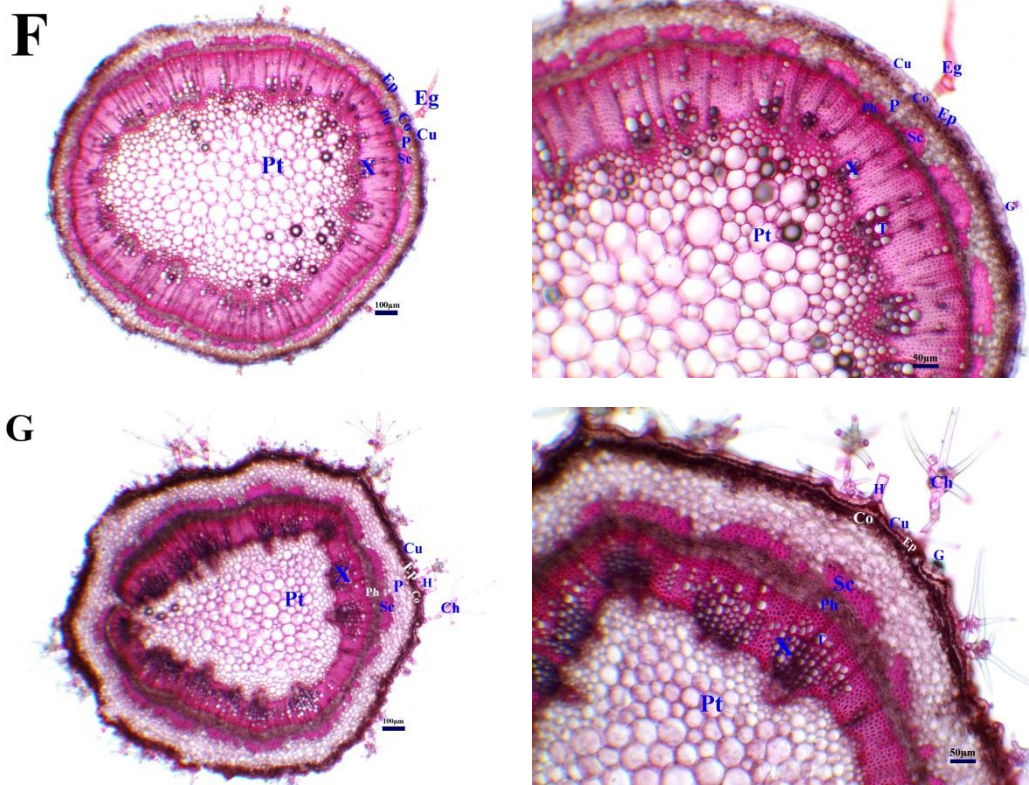


Figure 3. Cross-section of the stem of *Verbascum* (A) *V. agrimoniifolium* subsp. *agrimoniifolium*, (B) *V. orientale* subsp. *orientale*, (C) *V. laetum*, (D) *V. geminiflorum*, (E) *V. andrusii*, (F) *V. kotschyi*, (G) *V. lasianthum*. Eg: Eglandular, G: Glandular hair, Ch: Compound hair, H: Hair, Cu: Cuticle, Ep: Epidermis, Co: Collenchyma, P: Parenchyma, Sc: Sclerenchyma, Ph: Phloem, X: Xylem, T: Trachea, Pt: Pith region.

3.1.3. Leaf Anatomy

V. agrimoniifolium subsp. *agrimoniifolium*: The epidermis consists of a single row of round, rectangular or oval cells. The epidermis is covered with a thin layer (5.43-12.23 μm) of cuticle. Covering and glandular hairs were observed in both epidermis. Mesophyll tissue is divided into palisade and sponge parenchyma. While there are 2-3 layers of palisade parenchyma under the upper epidermis and 1-2 layers of palisade parenchyma above the lower epidermis, there are 2-3 layers of sponge parenchyma in between (Table 4, Figure 4).

V. orientale subsp. *orientale*: The epidermis consists of a single row of round, rectangular or oval cells. The epidermis is covered with a thin layer (4.72-10.79 μm) of cuticle. Glandular hairs were observed in both epidermis. Mesophyll tissue is divided into palisade and sponge parenchyma. While there are 2-3 rows of palisade parenchyma under the upper epidermis, 1-2 rows of palisade parenchyma above the lower epidermis, there are 2-3 rows of sponge parenchyma in between (Table 4, Figure 4).

V. laetum: The epidermis consists of a single row of round, rectangular or oval cells. The epidermis is covered with a thin layer (7.63-16.66 μm) of cuticle.

The glandular, eglandular and compound hairs were observed in both epidermis. Mesophyll tissue is divided into palisade and sponge parenchyma. While there are 3-4 rows of palisade parenchyma under the upper epidermis, 2-3 rows of palisade parenchyma above the lower epidermis, there are 3-4 rows of sponge parenchyma in between. The idioblasts have also been found in the mesophyll tissue of leaves (Table 4, Figure 4).

V. geminiflorum: The epidermis consists of a single row of round, rectangular or oval cells. The epidermis is covered with a thin layer (5.53-13.42 μm) of cuticle. The glandular and compound hairs were observed in both epidermis. Mesophyll tissue is divided into palisade and sponge parenchyma. While there are 3-4 rows of palisade parenchyma under the upper epidermis, 2-3 rows of palisade parenchyma above the lower epidermis, there are 3-4 rows of sponge parenchyma in between. The idioblasts have been found in the mesophyll tissue of leaves. Intercellular spaces are noticeable in the mesophyll. Additionally, there is an amaryllis type stoma in the mesophyll (Table 4, Figure 4).

V. andrusii: The epidermis consists of a single row of round, rectangular or oval cells. The epidermis is covered with a thin layer (5.42-9.45 μm) of cuticle. The

glandular, eglandular and compound hairs were observed in both epidermis. Mesophyll tissue is divided into palisade and sponge parenchyma. While there are 2-3 rows of palisade parenchyma under the upper epidermis, 1-2 rows of palisade parenchyma above the lower epidermis, there are 3-5 rows of sponge parenchyma in between. Intercellular spaces are noticeable in the mesophyll. Additionally, there is an amaryllis type stoma in the mesophyll (Table 4, Figure 4).

V. kotschyi: The epidermis consists of a single row of round, rectangular or oval cells. The epidermis is covered with a thick layer (10.48-14.83 μm) of cuticle. The glandular, eglandular and compound hairs were observed in both epidermis. Mesophyll tissue is divided into palisade and sponge parenchyma. While there are 1-2 rows of palisade parenchyma under the upper epidermis, 1-2 rows of palisade parenchyma above the lower epidermis, there are 2-3 rows of sponge

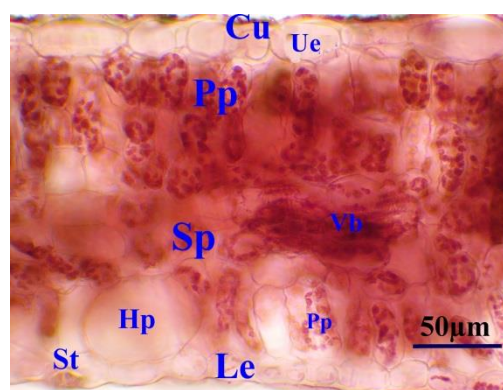
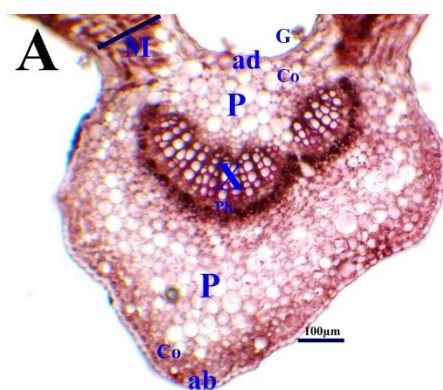
parenchyma in between. Additionally, there is an amaryllis type stoma in the mesophyll (Table 4, Figure 4).

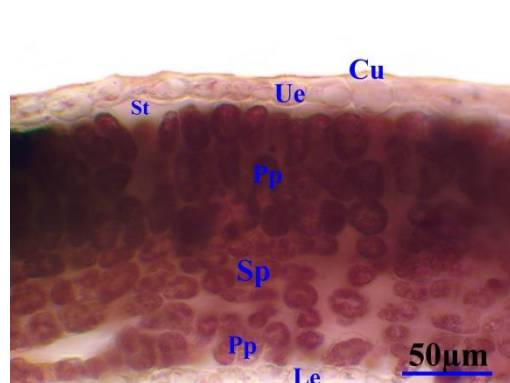
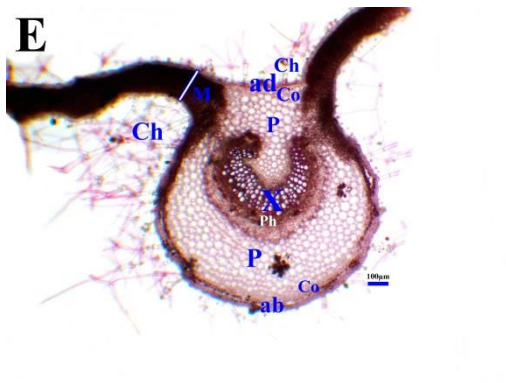
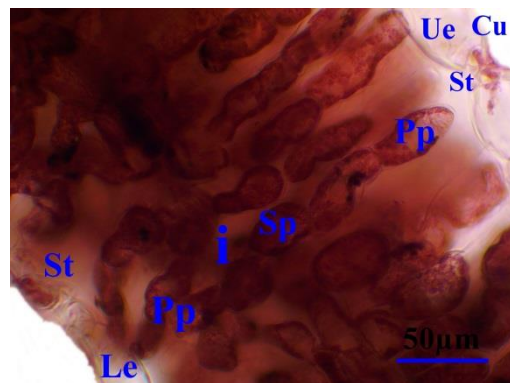
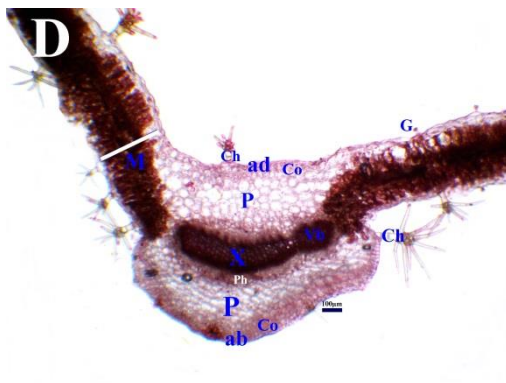
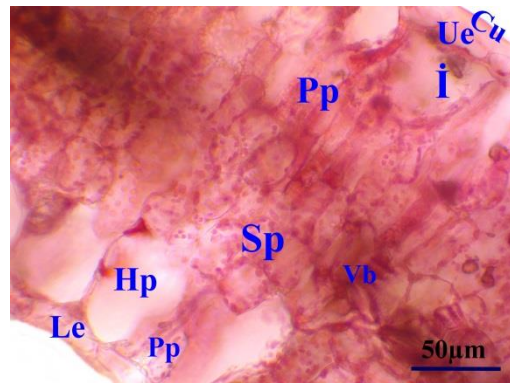
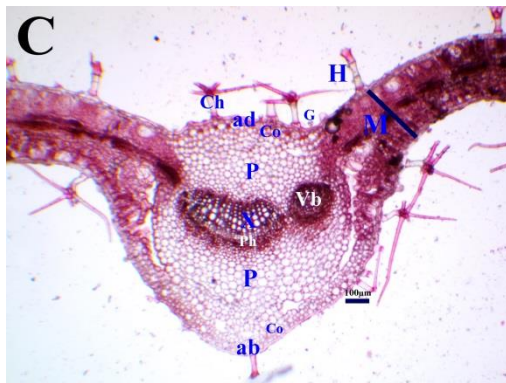
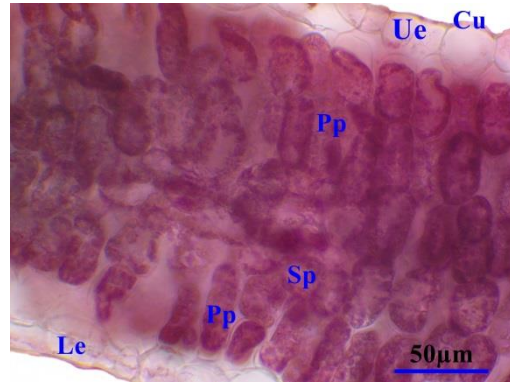
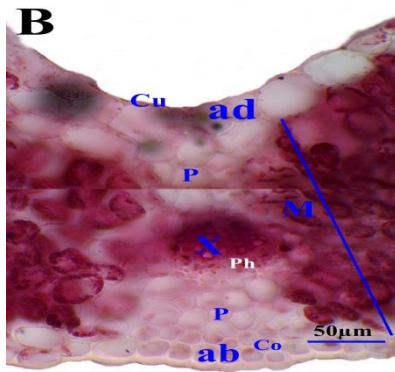
V. lasianthum: The epidermis consists of a single row of round, rectangular or oval cells. The epidermis is covered with a thin layer (6.21-10.99 μm) of cuticle. The glandular, eglandular and compound hairs were observed in both epidermis. Mesophyll tissue is divided into palisade and sponge parenchyma. While there are 2-3 rows of palisade parenchyma under the upper epidermis, 1-2 rows of palisade parenchyma above the lower epidermis, there are 3-5 rows of sponge parenchyma in between. Additionally, there is an amaryllis type stoma in the mesophyll (Table 4, Figure 4).

Table 4. The leaf anatomical measurements of taxa belonging to the genus *Verbascum* (μm).

Taxa	Tissues	Width			Length		
		Min.	Max.	Mean \pm S.	Min.	Max.	Mean \pm S.
<i>V. agrimoniifolium</i> subsp. <i>agrimoniifolium</i>	Cuticle	-	-	-	5.43	12.23	8.15 \pm 2.30
	Upper epidermis	13.32	41.70	25.26 \pm 6.39	17.79	30.90	25.92 \pm 3.35
	Palisade parenchyma	10.23	18.61	15.42 \pm 2.27	27.60	44.85	35.37 \pm 3.81
	Spongy parenchyma	14.00	31.02	20.87 \pm 4.66	15.00	27.79	20.52 \pm 3.64
	Mesophyll layer	-	-	-	222.55	277.65	251.59 \pm 15.89
<i>V. orientale</i> subsp. <i>orientale</i>	Lower epidermis	5.44	21.27	14.59 \pm 3.90	6.09	20.96	13.08 \pm 3.56
	Cuticle	-	-	-	4.72	10.79	7.38 \pm 1.70
	Upper epidermis	12.36	37.81	21.60 \pm 6.87	12.69	30.28	20.69 \pm 5.45
	Palisade parenchyma	14.01	29.19	22.41 \pm 3.51	30.58	52.67	38.34 \pm 5.77
	Spongy parenchyma	13.38	31.82	22.00 \pm 4.44	15.67	32.06	22.29 \pm 4.30
<i>V. laetum</i>	Mesophyll layer	-	-	-	189.05	267.44	234.43 \pm 20.03
	Lower epidermis	20.48	57.42	32.55 \pm 11.05	22.08	44.05	31.50 \pm 6.73
	Cuticle	-	-	-	7.63	16.66	11.10 \pm 2.53
	Upper epidermis	12.41	46.71	24.71 \pm 8.41	12.04	26.27	20.57 \pm 3.93
	Palisade parenchyma	7.37	21.46	15.70 \pm 3.26	23.96	65.33	44.45 \pm 9.96
<i>V. geminiflorum</i>	Spongy parenchyma	13.91	25.26	20.13 \pm 2.73	14.99	33.48	22.93 \pm 5.45
	Mesophyll layer	-	-	-	265.96	372.48	314.04 \pm 29.23
	Lower epidermis	13.52	29.27	20.66 \pm 4.37	12.70	25.83	18.88 \pm 3.51
	Cuticle	-	-	-	5.53	13.42	9.23 \pm 1.80
	Upper epidermis	26.62	62.16	39.84 \pm 8.75	27.76	51.75	36.22 \pm 6.57

	Palisade parenchyma	15.28	32.07	22.90±4.67	30.76	62.91	49.62±9.46
	Spongy parenchyma	14.22	26.86	21.16±3.18	12.97	33.19	22.19±5.00
	Mesophyll layer	-	-	-	383.00	196.26	297.50±50.65
	Lower epidermis	9.32	23.11	17.99±3.67	9.23	24.32	16.74±3.68
<i>V. andrusii</i>	Cuticle	-	-	-	5.42	9.45	6.73±0.96
	Upper epidermis	11.85	23.06	16.28±3.22	11.06	18.35	14.50±2.23
	Palisade parenchyma	12.18	24.28	17.35±2.94	19.21	36.90	26.72±4.72
	Spongy parenchyma	12.29	19.97	16.04±2.23	9.74	18.08	13.38±2.25
	Mesophyll layer	-	-	-	190.12	256.82	182.41±38.09
	Lower epidermis	9.17	20.03	14.93±3.59	8.05	16.03	11.93±2.22
<i>V. kotschyi</i>	Cuticle	-	-	-	10.48	14.83	12.05±1.11
	Upper epidermis	15.82	40.32	26.91±6.83	9.92	19.90	13.78±2.47
	Palisade parenchyma	8.56	17.72	12.12±2.43	21.55	38.41	28.71±4.61
	Spongy parenchyma	11.76	20.59	16.02±2.51	13.81	25.43	19.47±3.75
	Mesophyll layer	-	-	-	167.48	325.89	212.52±46.54
	Lower epidermis	10.50	24.03	17.93±4.62	9.83	21.35	13.48±2.92
<i>V. lasianthum</i>	Cuticle	-	-	-	6.21	10.99	8.04±1.19
	Upper epidermis	9.18	23.41	15.40±3.76	7.30	17.77	12.72±2.96
	Palisade parenchyma	4.69	9.18	6.61±0.93	7.59	15.94	12.71±1.98
	Spongy parenchyma	6.44	11.80	8.94±1.56	7.12	13.03	10.57±1.79
	Mesophyll layer	-	-	-	88.97	191.27	128.24±26.39
	Lower epidermis	11.15	22.12	15.57±3.78	7.97	13.52	11.13±2.65





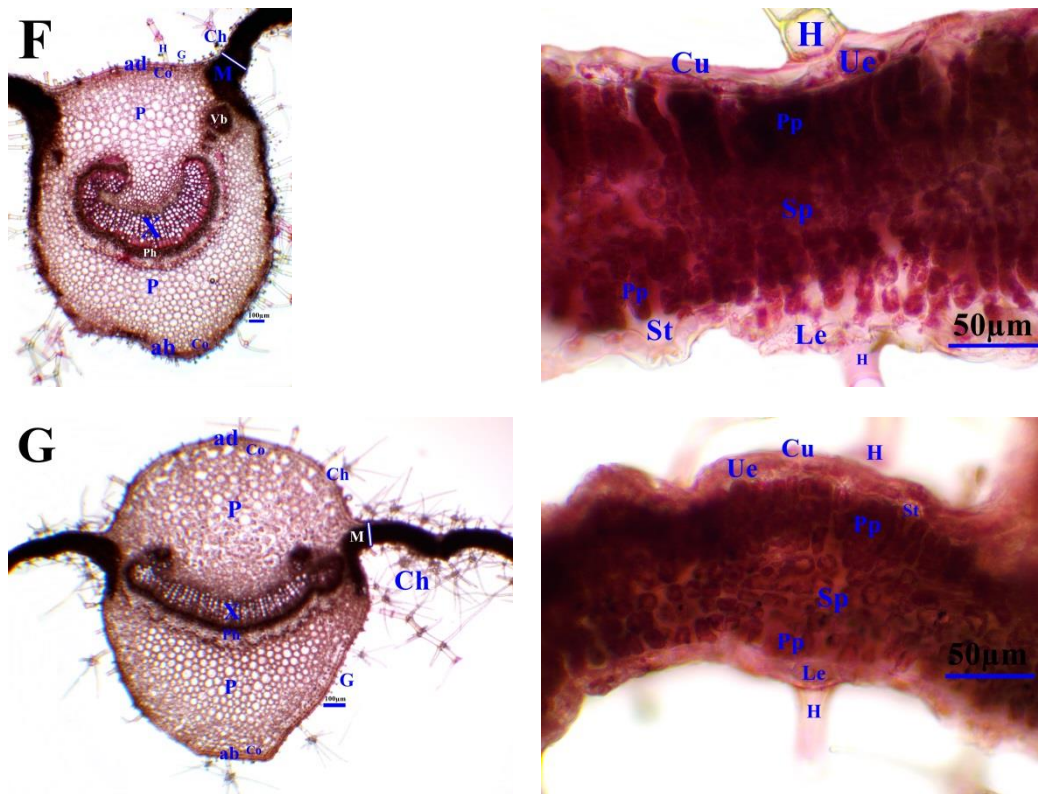


Figure 4. Cross-section of the stem of *Verbascum* (A) *V. agrimoniifolium* subsp. *agrimoniifolium*, (B) *V. orientale* subsp. *orientale*, (C) *V. laetum*, (D) *V. geminiflorum*, (E) *V. andrusii*, (F) *V. kotschyi*, (G) *V. lasianthum*. G: Glandular hair, Ch: Compound hair, M: Mesophyll layer, ad: Adaxial surface, Co: Collenchyma, P: Parenchyma, X: Xylem, Ph: Phloem, ab: Abaxial surface, Ue: Upper epidermis, Le: Lower epidermis, Pp: Palisade parenchyma, Sp: Spongy parenchyma, Hp: Hypodermis, i: idioblast, Vb: Vascular bundle.

4. Conclusion

In this study, the anatomical analyzes of seven taxa belonging to the *Verbascum* genus, distributed in the Southeastern Anatolia Region, were examined to ensure comparability with other *Verbascum* members examined.

The tracheae located in the root of the taxa show differences in size and magnitude. *V. agrimoniifolium* subsp. *agrimoniifolium* has the largest tracheae, while *V. orientale* subsp. *orientale* has the smallest. In *V. laetum*, *V. geminiflorum*, *V. andrusii* and *V. lasianthum* species, the tracheae are arranged close to the phloem, while in other taxa the tracheae are distributed throughout the vascular bundle. However, all taxa show differences in size and magnitude. A substantial xylem region was seen in the root of every taxon, and the stem had a thick coating of cuticle. Additionally, comparable traits were discovered in earlier research [8,13-19]. Various studies have reported that the cambium in the vascular bundle of the root is unclear [15, 18-19, 25], and this study has shown that the roots of taxa show similar characteristics. With the exception of *V. orientale* subsp. *orientale*, cross-sectional studies of the leaf's epidermal cells revealed densely glandular, non-glandular, and compound multicellular hairs. Similar

outcomes have been reported for other *Verbascum* species under investigation [15]. Identification within the *Verbascum* genus may be aided by the presence of idioblasts in the leaf's mesophyll tissue [26]. This work and others have reported the presence of idoblasts (*V. laetum* and *V. geminiflorum*) in the leaf mesophyll [13]. Leaf epidermal characteristics of the common taxa (*V. agrimoniifolium* subsp. *agrimoniifolium*, *V. andrusii*, *V. geminiflorum*, *V. laetum*) used in this study with the study by El-Haadety et al. [27] are similar.

Because the stem of vascular plants is less susceptible to external factors, it is the primary subject of anatomical studies [28]. The distinct physical makeup of this taxa lends credence to this information.

In this study, the importance of several features in the classification of *Verbascum* taxa was investigated (presence of idioblasts in the leaves, stem shape-structure and measurements, etc.). The anatomical investigations revealed that while the taxa's root, stem, and leaf structures were similar, their shapes and sizes, and tissue layer counts varied. Anatomical characteristics such the existence or lack of cambium in the root, the number of collenchyma layers in the stem, the mesophyll forms in the leaves, the presence of idioblasts, and the shape of the midrib provide crucial

taxonomic information as a result of all the data that have been mentioned. In Addition to this, systematic distinction or interpretation of taxa of the genus may benefit from the use of specific features typically associated with their anatomical patterns.

As a result the availability of anatomical data indicates that species distinction can be established with greater accuracy in addition to morphological characteristics. Furthermore, it is obvious that carrying out and supporting such research will contribute both the taxonomic classification of species and genera and modern plant science.

Acknowledgement

We wish to thank Scientific Investigation Project to Coordinate of Mardin Artuklu University (Project No. MAÜ.BAP.22.KMY.011) for financial support.

Author's Contributions

Murat KILIÇ: He did field work. Prepared and wrote the manuscript, performed the anatomical experiments and result analysis.

Fatma Mungan KILIÇ: Assisted in analytical analysis on the structure, supervised the experiment's progress, result interpretation and helped in manuscript preparation.

Ethics

There are no ethical issues after the publication of this manuscript.

References

- [1]. Davis, PH, Mill, RR, Tan, K. 1988. Flora of Turkey and the East Aegean Islands (Suppl. 1). Edinburgh University Press, Edinburgh, England, Vol. 10, pp. 191-193.
- [2]. Karavelioğulları, FA. 2012. *Verbascum* L. In: Güner, A. et al. (eds), Türkiye Bitkileri Listesi (Damarlı Bitkiler). Nezahat Gökyiğit Botanik Bahçesi ve Flora Araştırmaları Derneği Yayını, İstanbul, pp. 850-870.
- [3]. Fırat, M. 2022. *Verbascum zerdust* (Scrophulariaceae), a new species from Bitlis province (Turkey) belonging to section *Bothrosperma*. *Nordic Journal of Botany*. doi: 10.1111/njb.03649
- [4]. Öztürk, A, Güney, KB, Bani, B, Güney, K, Karaveliogullari, FA, Pinar, NM, Çeter, T. 2018. Pollen morphology of some *Verbascum* (Scrophulariaceae) taxa in Turkey. *Phytotaxa*; 333(2): 209-218. <https://doi.org/10.11646/phytotaxa.333.2.4>
- [5]. Huber-Morath, A. 1978. *Verbascum* L. In: Davis, P. H. (ed.), Flora of Turkey and the East Aegean Islands. Edinburgh University Press, Edinburgh, England, Vol. 6, pp. 461-603.
- [6]. Karaveliogullari, FA, Yüce, E, Başer, B. 2014. *Verbascum duzgunbabadagensis* (Scrophulariaceae), a new species from eastern Anatolia, Turkey. *Phytotaxa*; 181: 47-53.
- [7]. Çakir, T, Bağci, E. 2006. A taxonomical study on the *Verbascum euphraticum* Benth and *Verbascum melitenense* Boiss (Scrophulariaceae). *Sci Eng J Firat Univ.*; 18 (4): 445-58.
- [8]. Özdemir, C, Altan, Y. 2007. Some morphological and anatomical properties of endemic *Verbascum oreophilum* C. Koch var. *oreophilum* (Scrophulariaceae). *Afyon Kocatepe Univ J Sci.*; 7: 429-437.
- [9]. Kheiri, S, Khayami, M, Mahmoudzadeh, A. 2009. Micromorphological and anatomical studies of certain species of *Verbascum* (Scrophulariaceae) in West Azerbaijan, Iran. *Iran Journal of Botany*; 15: 105-13.
- [10]. Yılmaz, G, Dane, F. 2011. Studies on *Verbascum ovalifolium* and *V. purpureum* (Scrophulariaceae) from the vicinity of Edirne (European Turkey). *Phytologia Balcanica*; 17 (2): 205-212.
- [11]. Alan, S, Gökman, AB. 2015. Investigation of morphological, morphometric and anatomical characteristics of endemic *Verbascum orgyale* Boiss. & Heldr. *Biodicon*; 8 (1): 94-103.
- [12]. Küçük, NR. 2017. Anatomical characteristics of endemic *Verbascum bellum* Hub. and Mor. (Scrophulariaceae). *Anadolu Univ. J Sci. Technol. C- Life Sci. Biotechnol*; 6: 22-30.
- [13]. Tekin, M, Yılmaz, G. 2018. Anatomical and Palynological Studies on Endemic *Verbascum weideman-nianum* Fisch. & Mey. (Scrophulariaceae) In Turkey. *Inter. J. Agricult, For. Life Sci.*; 2 (2): 6-15.
- [14]. Aktas, K. 2019. Morphology, Anatomy, Palynology and Seed Micromorphology of Turkish Endemic *Verbascum splendidum* Boiss. (Scrophulariaceae). *Fresenius Environmental Bulletin*; 28 (12): 10004-10010.
- [15]. Aktas, K, Özdemir, C, Özdemir, B. 2020. Morphology, Anatomy, Palynology and Seed Micro-morphology of Turkish Endemic *Verbascum exuberans* Hub.-Mor. (Scrophulariaceae). *Planta Daninha*. v38:e020191125
- [16]. Küçük, S, Elmaskaya, A, Göktürk, RS. 2021. Endemic *Verbascum detersile* Boiss. & Heldr.'s (Scrophulariaceae) Anatomical Features. *Bio. Div. Con.*; 14 (3): 390-395.
- [17]. Kılıç, M. 2023. Anatomy, Pollen and Seed Morphology of Endemic Species *Verbascum globiferum* Hub.-Mor. and *V. lysiosepalum* Hub.-Mor. (Scrophulariaceae) In Diyarbakır, Turkey and Their Taxonomic Importance. *Bangladesh Journal of Plant Taxonomy*; 30 (2): 201-212. <https://doi.org/10.3329/bjpt.v30i2.70497>
- [18]. Mungankılıç, F, Kılıç, M. 2023. Anatomical studies on endemic *Verbascum stepporum* Murb., and *Verbascum tenue* Hub.-Mor., (Scrophulariaceae) species distributed in Şanlıurfa. *Biological Diversity and Conservation*; 165 (2): 132-139.
- [19]. Mungankılıç, F, Kılıç, M. 2024. Anatomy, palynology and seed micromorphology of Turkish rare *Verbascum racemiferum* Boiss. & Hausskn Ex Boiss. (Scrophulariaceae). *Biological Diversity and Conservation*; 17 (1): 63-71. <https://doi.org/10.46309/biodicon.2023.1367629>
- [20]. Baytop, T. 1999. Therapy with Medicinal Plants in Turkey (Past and Present). 2nd ed., Nobel Tıp Kitabevleri Ltd. İstanbul, pp. 334-335.
- [21]. Kahraman, C, Akdemir, ZS, Tatlı, İ. 2012. Promising cytotoxic activity profile, biological activities and phytochemical screening of *Verbascum* L. species. *Medicinal and Aromatic Plant Science and Biotechnology*; 6 (2): 63-75.



- [22]. Tatli, II, Akdemir, Z F. 2006. Traditional uses and biological activities of *Verbascum* species. *FABAD Journal of Pharmaceutical Sciences*; 31 (2): 85.
- [23]. Bozdağ, B, Kocabaş, O, Akyol, Y, Özdemir, C. 2016. A New Staining Method for Hand-Cut in Plant Anatomy Studies. *Marmara Pharm. J.*; 20: 184-190.
- [24]. Metcalfe, C R., Chalk, L. 1950. *Anatomy of Dicotyledons*. Clarendon Press, Oxford, 1st edition, Vol. 2.
- [25]. Kılıç, M, Mungan Kılıç, F. 2024. Comparative Anatomy, Pollen and Seed Morphology of Two *Verbascum* Varieties (Scrophulariaceae) and Their Taxonomic Significance. *Celal Bayar University Journal of Science*; 20(1): 49-60. <https://doi.org/10.18466/cbayarfbe.1433245>
- [26]. Lersten, N. R., Curtis, J. D. 2001. Idioblasts and other unusual internal foliar secretory structures in Scrophulariaceae. *Plant Syst. Evol.* , 227, 63-73.
- [27]. Al-Hadeethy, M, Al-Mashhadan, A, Al-Khesraji, T, Barusrux, S, Al-Jewari, H, Theerakulpisut, P, Pornpongrungrueng, P. 2014. Pollen morphology of *Verbascum* L. (Scrophulariaceae) in Northern and Central Iraq. *Bangladesh J. Plant Taxon.*; 21: 159-165.
- [28]. Lopes, LKC, Góes-Neto, LAA, Feio, AC. 2020. Stem anatomy and its relevance for the Taxonomic survey of *Selaginella* subg. *Gymnogynum* (Selaginellaceae). *Plant Systematics and Evolution*; 306: 13. doi:10.1007/s00606-020-01655-x

Determination of Carbon Footprint: Düzce University Konuralp Campus

İrem Düzdar^{1*} , Rabia Yıldız¹ 

¹ Düzce University, Faculty of Engineering, Department of Industrial Engineering, Düzce, Türkiye

* iremduzdar@gmail.com

* Orcid No: 0000-0002-7642-8121

Received: 13 May 2024

Accepted: 23 December 2024

DOI: 10.18466/cbayarfb.1456641

Abstract

Climate change, one of the most important problems of our age, is a problem that needs an urgent solution as soon as possible. Mathematical models of climate support this idea. With the results of mathematical models related to climate change, it is aimed to predict effects such as increase in the average surface temperature of the planet, rise in sea level, more frequent and intense natural disasters, decrease in water resources, and imbalances in ecosystems. This study was carried out with the aim to emphasize the possible effects of climate change with mathematical models and encouraging people to take action on this issue and to take appropriate measures to minimize the negative consequences. For this reason, this study was presented to calculate the carbon footprint of Düzce University Konuralp Campus with the IPCC methodology Tier1 approach. The amount of carbon footprint was found to be 4.781.841 tons of CO₂. As a result of this analysis, the investment cost of solar energy usage has been calculated since the solar energy availability in the region is appropriate. This study was conducted to draw attention to sustainable campuses and to lead the transition from sustainable campuses to sustainable cities.

Keywords: Carbon footprint, Climate change, IPCC, Sustainability

1. Introduction

Climate change has a general definition as long-term and slow-moving changes in climatic conditions that have universal and important local effects, regardless of the cause [1]. The concentrations of anthropogenic greenhouse gas emissions such as Carbon dioxide (CO₂), Methane (CH₄), Nitrous oxide (N₂O) in the atmosphere are greatly increasing due to the use of fossil fuels since the pre-industrial period, industrialization, increasing population, unplanned urbanization, improper use of lands, deforestation, wastes harmful to nature. Despite the climate change from the first moment of the Earth's existence until today, is occurring faster than it should be due to anthropogenic reasons today. The 5th Assessment report of the Intergovernmental Panel on Climate Change (IPCC) also proves that the increase in global temperature is anthropogenic [2].

As a result of various mathematical climate models, it is concluded that the changes that started in the climate will continue in the future. As a result of this; Floods, drought and drought-related desertification, catastrophic storms, biological outbreaks are some of these problems.

These and potential problems will continue to spread to wider regions and will be seen more frequently [3]. Due to these effects, the United Nations Framework Convention on Climate Change was first discussed at the Earth Summit in 1992 in order to prevent the greenhouse gas concentration in the atmosphere from reaching levels that would endanger the atmosphere. In the third conference held, the Kyoto Protocol was signed, in which the countries were envisaged to reduce their absorption rates by at least 5 percent of the 1990 absorption rate [4]. With the Kyoto Protocol, an emission quota was introduced to the responsible countries in order to calculate the carbon emission amounts, and the greenhouse gas emissions should not exceed the quota. It was stated that the carbon footprint of the emission causing the greenhouse gas should be made and a greenhouse gas inventory should be created. As a result of these studies, awareness on reducing emissions has been created for organizations and investors and carbon footprint calculation studies are carried out in different sectors [5]. In 2019, the European Union announced the European Green Deal, in which it stated that EU aims to become a climate neutral continent in 2050, which the industry will have a new growth strategy and will be

reshaped according to climate change. Following this agreement, countries such as South Korea, China and Japan, which have an important place in international trade, began to announce their goals regarding green transformation. Thailand, Sweden, Canada, Norway and Chile are among other countries that have declared net zero emissions [6].

The green agreement action plan was announced in our country in 2021. It is planned that greenhouse gas emissions will decrease by 41% in 2023 by 2030 and the net zero target in greenhouse gas emissions will be achieved by 2053. Studies are being carried out in our country for this purpose [7].

Figure 1 shows the amount of emissions per capita in countries for 2022.

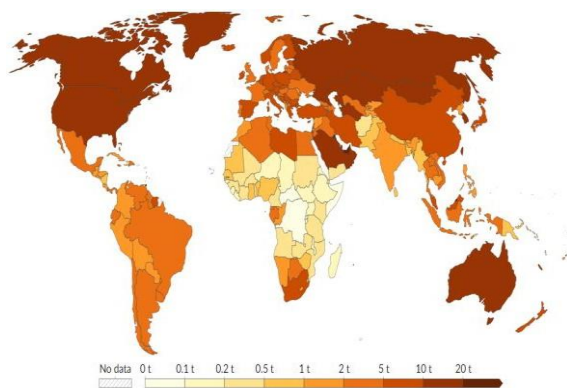


Figure 1. Per capita CO₂ emissions, 2022 [8]

In addition, the most up-to-date method to determine the amount of greenhouse gases caused by human activities is the calculation of carbon footprint.

Carbon footprint is a measure of the total carbon dioxide emissions that result directly or indirectly from a process of individuals, communities, governments, industry sectors, etc. and that a product produces over its entire life cycle [9]. Examining the carbon footprint is also important for monitoring climate change by measuring greenhouse gas emissions of individuals, households, sectors, organizations and cities. In this way, it creates a road map that governments can follow and supports international accountability [10]. While calculating carbon footprint, examinations are made with two main headings as primary and secondary carbon footprint. The primary carbon footprint is a measure of CO₂ emissions directly from the combustion of fossil fuels, including household energy and transportation. The secondary carbon footprint is a measure of indirect CO₂ emissions throughout the entire life cycle of the products used [11]. Carbon emission amount calculations were made using different approaches and criteria in the literature review.

Since cattle farming in Colombia accounts for approximately 15% of greenhouse gas emissions, González-Quinter et al. in their study measured the

carbon footprint (CF) of 82 dairy farms with the survival analysis evaluation technique using IPCC data and determined that *Acacia Decurrens*, *Baccharis Latifolia* and *Sambucus Peruviana*. They investigated its contribution to milk production increase and greenhouse gas reduction potential and examined gas emissions [12]. This study revealed that emissions from municipal solid waste have a significant share in China's efforts to reduce carbon emissions. They examined the production and emissions of municipal solid waste in Yunnan Province under four different waste classification scenarios. In the research, municipal solid waste production was predicted with the STIRPAT model and carbon emissions from municipal solid waste were calculated with the methodologies recommended by IPCC [13]. In this research, He et al. used the IPCC methodology to evaluate the carbon emissions produced by China's Electrical and Electronic Equipment (EEE) emissions between 2012 and 2020 and included the grey model to estimate emissions for that year [14]. In this research, Ezhilkumar et al. estimated the amount and distribution of greenhouse gas emissions at Nile University in Abuja, Nigeria. They calculated the main emission sources at the site, such as energy production, transport, horticulture and cooking fuels, using IPCC guidelines [15].

Binboğa and Ünal conducted a study on calculating the carbon footprint of Manisa Celal Bayar University from a sustainability perspective. Using the IPCC Tier 1 methodology, they determined that the university's primary carbon footprint was 8,953.906 tons of CO₂ emissions for the year 2016 [16]. Kumaş, Akyüz, and Güngör Annex 2014 conducted a study on the carbon footprint detection of higher education units at Burdur Mehmet Akif Ersoy University Bucak Campus. They calculated the total carbon footprint of three different colleges as 959,585 CO₂ per year [5]. Seyhan and Çerçi investigated the determination of the carbon footprint using IPCC Tier 1 and DEFRA methods, focusing on the fuel and electricity consumption of Erzincan Binali Yıldırım University. Using both methods, they calculated the amount of emissions for the pandemic years 2020 and 2021. They found that the emission amount in 2020 was 21% less than in 2021 [17]. Gökçek, Bozdağ, and Demirbağ conducted a study on the determination of carbon footprint using Niğde Ömer Halisdemir University as an example. They used SPSS statistics application to find the consumption habits statistics of the students and analyzed the spatial distribution of the data using ArcGIS 10.2 software [18]. Yaka, Koçer, and Güngör conducted a study on the detection of carbon footprint at Akdeniz University Vocational School of Health Services. They calculated the carbon footprint of the college using the Annex 2014 method [19]. Atabey conducted a study as part of his master's thesis, focusing on calculating the carbon footprint for Diyarbakır. He used both Tier 1 and Tier 2 approaches in his calculations [11].

Carbon footprint studies are carried out by various institutions and organizations in different countries. It was decided to contribute to our country's 2053 zero emission targets and to make this contribution at the university, which is the pioneer of scientific developments. Calculating the carbon footprint on campus provides many important benefits such as environmental sustainability, combating climate change, energy efficiency, awareness and education, corporate image and competitive advantage. In this study, Konuralp campus of Düzce University, which has specialized in the field of environment and health, was chosen as the study area. The aim of this study is to lead the transition from sustainable campuses to sustainable cities. Due to the increasing use of solar energy systems on roofs and fields, especially in Düzce, a cost analysis of solar energy installation was also made. The Green Deal action plan also aims to increase the costs of carbon regulations in sectors covered by border carbon regulations and consider aid such as EU ETS state aid as an alternative [6]. In this study, this was calculated for Düzce University and it was aimed to contribute to other studies.

In terms of originality, it is aimed to provide an original contribution locally and regionally, as it is one of the limited number of studies conducted on the carbon footprint of university campuses in Turkey.

In addition, this study does not only analyze the current situation, but also offers concrete suggestions that can be implemented in order to achieve sustainability goals. It is aimed to be a scientific resource by evaluating the environmental impacts of university campuses in a similar way to other higher education institutions in order to develop sustainability strategies with the data obtained.

2. Materials and Methods

2.1. Sources of information and study area

In this study, the carbon footprint was calculated for Düzce University Konuralp campus. As it can be seen Figure 2, there are faculties, central classrooms, Rectorate, training and research hospital, experimental laboratory research center, indoor sports hall in the campus. Monthly electricity and natural gas usage data of these centers for 2022 were calculated by Düzce University Construction and Technical Department. Table 5 gives the monthly electricity consumption of the campus and the hospital within the campus, and Table 6 gives the monthly natural gas consumption of different buildings on the campus.

Transportation data was obtained by calculating the average monthly numbers of trips and the average distance traveled by the lines to the university.



Figure 2. General view of Düzce University [20]

First of all, the natural gas and electricity consumptions of these buildings were obtained from the official records registered by the university. The transportation data is calculated by using the daily average of trips and average of trip distances.

2.2. Methods

Calculations were made using the emission factors given for the Tier 1 approach in the IPCC 2006 guideline. The steps of this method are as follows:

- Equation 1 is used to find the consumption values of fuels. The energy consumption values are obtained by multiplying the conversion values in the IPCC guideline given in Table 1 with the fuel consumption values [16].

Table 1. The Net Calorific Values of Fuels [16]

Fuel Types	Net Calorific Value (TJ/Gg)
Natural Gas	48.0
Diesel	43.0
Gasoline	44.3

$$\text{Energy Consumption (TJ)}$$

$$= \text{Fuel Consumption (t)} \times \text{Net Calorific Values} \left(\frac{\text{TJ}}{\text{Gg}} \right) \quad (1)$$

- Equation 2 is used to find the total carbon content in the fuel. The average values of the carbon emission factors in the IPCC guide in Table 2 are selected and calculated. The energy consumption and carbon emission factor are multiplied to find the amount of carbon content [16].

Table 2. The Emission Factors of Fuels [21]

Fuel Types	Emission Factors
Diesel	20.20
Gasoline	18.90
Natural Gas	5.30

$$\text{Carbon Content (t C)} = \frac{\text{Emission Factor (t C/TJ)} \times \text{Energy Consumption (TJ)}}{C} \quad (2)$$

3) Equation 3 is used to calculate the carbon emission. The oxidation percentages (combustion efficiency) values in Table 3 given by the IPCC are multiplied by the carbon content and the amount of carbon that is completely involved in combustion is found [16].

Table 3. Oxidation Ratio of Fuels [21]

Fuel Types	Oxidation Ratio
Diesel	0.990
Gasoline	0.990
Natural Gas	0.995

$$\text{Carbon Emission (Gg C)} = \text{Carbon Content (Gg C)} \times \text{Carbon Oxidation Ratio} \quad (3)$$

4) As a final step, Equation 4 is used to find the net carbon value of CO₂. The molecular weight of carbon is 44/12. When the carbon emission is multiplied by the molecular weight of the carbon, the CO₂ emission is obtained [16].

$$\text{CO}_2 \text{ Emission (Gg CO}_2\text{)} = \text{Carbon Emission (Gg C)} \times (44/12) \quad (4)$$

3. Findings

The total amount of electricity consumed in the campus is given in Table 5. When the consumption data is examined, the amount of electricity consumption in the campus is less in June, July, August and September compared to other months. As seen in Figure 3, the total amount of electricity consumed in the hospital is approximately twice the amount of electricity consumed on campus.

Table 5. Electrical Energy Consumption Values (kWh)

MONTHS	CAMPUS	HOSPITAL
JANUARY	438.253,500	619.523,40
FEBRUARY	378.278,700	549.854,10
MARCH	453.033,300	606.137,40
APRIL	342.495,300	537.213,30
MAY	286.833,000	548.060,10
JUNE	271.314,900	639.084,90
JULY	252.740,100	635.062,20
AUGUST	288.392,400	737.858,40
SEPTEMBER	264.414,900	585.451,20
OCTOBER	364.182,000	533.977,20
NOVEMBER	388.173,300	555.339,60
DECEMBER	448.168,800	601.141,80
TOTAL (kWh)	4.176.280,20	7.148.703,60
OVERALL TOTAL (kWh)	11.324.983,80	

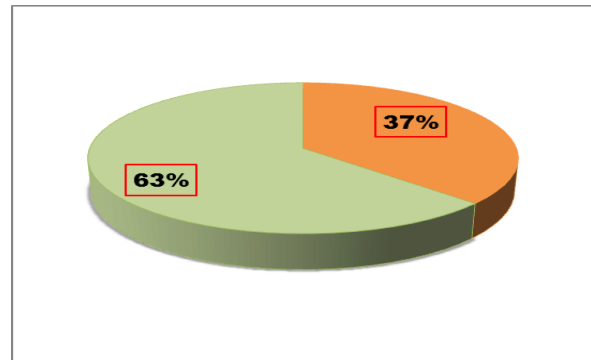


Figure 3. Electrical Energy Consumption Distribution

The natural gas consumption data is on Table 6. Since natural gas is mostly used for heating purposes, natural gas consumption is zero in many buildings in June, July, August and September. When calculations were made using the data, the data in Table 7 of the CO₂ emission were obtained.

Table 6. Natural Gas Consumption Data (m³)

Months	Heating Center	Hospital	Rectorate	Faculty of Science & Literature (A-B)	Foreign Languages School	Transportation	New Central Amphitheatre	Central Laboratory	Experimental Research Laboratory	Faculty of Medicine E Block
January	115.620	104.432	27.715	25.319	9.948,52	1.298,70	15.966,56	0,0	0,0	10.860,35
February	92.328	93.667	19.243	12.553	4.982,72	837,38	8.358,49	4.073,30	0,0	6.706,64
March	115.455	109.332	22.058	13.404	5.970	764,0	12.339	4.276,38	2.158	7.859,83
April	55.925	32.757	7.854	5.210	1.668,54	259,72	3.980,82	688,79	1.394	3.356,40
May	129	50.258	121	0,0	0,0	34,76	0,0	0,0	773,35	0,0
June	0,0	15.178	0,0	0,0	0,0	49,97	0,0	0,0	0,0	0,0
July	0,0	17.131	0,0	0,0	0,0	77,46	0,0	0,0	0,0	0,0
August	0,0	15.688	0,0	0,0	0,0	82,44	37,08	0,0	0,0	0,0
September	0,0	16.190	0,0	0,0	0,0	95,0	0,0	0,0	0,0	0,0
October	32.196	53.301	6.290	3.230	1.509	426,0	2.720	0,0	845	1.895
November	72.295	68.185	10.045	7.283	2.604	459,0	4.059	0,0	1.480	2.860
December	89.761	84.028	7.309	7.741	1.808	298,0	5.455	1053	1.003	2.285
Total (m³)	573.709	660.147	100.635	74.740	28.490,77	4.682,43	52.915,9	10.091,47	7.653,35	35.823,22
Overall Total (m³)	1.548.888,19									

Table 7. CO₂ Emission Values

	Tons CO ₂	%
Electrical Energy	5.447,32	0.12
Natural Gas	3.319.700,00	69.42
Transportation (Diesel)	1.456.694,32	30.46
Total	4.781.841,64	100

When Table 7 and Figure 4 are examined, it is concluded that the CO₂ emission amount is caused by natural gas consumption with a rate of approximately 70 percent. Transportation comes next with 30 percent. The amount of emissions from electricity is much lower than the others.

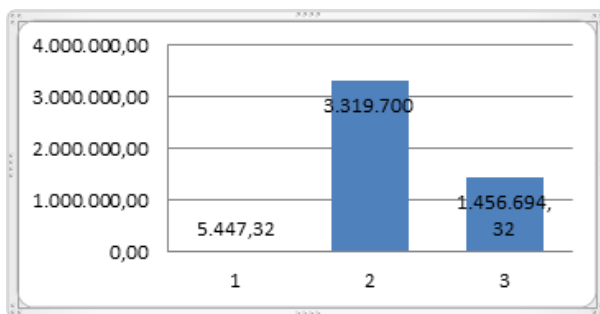


Figure 4. CO₂ Emission Values

In our country, there is no legal obligation to reduce emissions, since the emission values are not yet at a dangerous level. Therefore, our country cannot do carbon trade. Figure 5 shows how the carbon trading certificate works. However, although there is no obligation, projects are actively carried out in voluntary markets [22]. In these projects, if 35 million tons of CO₂ is processed, certified and converted into carbon trade, the value is 200 million dollars.

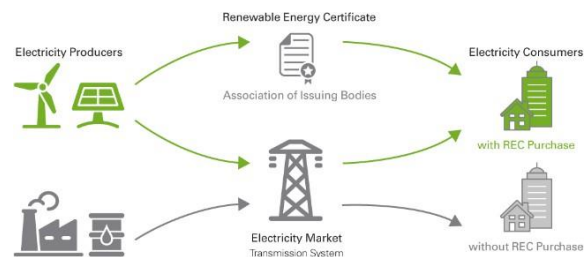


Figure 5. Renewable energy certificate system[23]

In case of carbon trading, the certificate value calculation was made for the amount of carbon originating from electricity consumption for Düzce University. For this, the electrical energy must be completely met by the energy obtained from solar energy. The following steps were followed for the calculation [24].

- 1) Initially, it is calculated how many solar panels will meet the electrical energy demand. For this reason, in Equation 5, the total amount of electricity consumed annually is divided by the

total amount of hours in 1 year, and the amount of kWh used is found as a result of this process. Solar panel preference is panels with 250 watts of power. For this reason, the amount in kW in Equation 6 is converted into watts.

- 2) The number of solar panels needed is obtained when the converted value is divided by 250 watts in Equation 7. In order to meet the electrical energy consumed at the university, 5,172 solar panels with a power of 250 watts are needed.

$$\frac{11.324.983,800 \frac{kWh}{Year}}{8760 \frac{Hours}{Year}} = 1.292,80 kW \quad (5)$$

$$1.292,80 kW = 1.292.806,37 w \quad (6)$$

$$\frac{1.292.806,37 watt}{250 watt} = 5.172 Panels \quad (7)$$

- 3) Solar panel installation cost is calculated. Solar energy cost per watt varies between \$0.40 and \$0.80 [13]. The cost was assumed as an average value and taken in the calculations \$ 0.60. When the cost per watt is calculated in Equation 8, the cost is \$775.683,822.

$$1.292.806,37 \times 0.60 \$ = 775.683,822 \$ \quad (8)$$

- 4) It is €10 per ton in carbon emission trade. In Table 7, the emission amount due to electricity consumption is 5,447.3168 tons CO₂. In Equation 9, the amount to be obtained from carbon sales is calculated by multiplying the amount of emissions per ton in carbon trade. If the amount of electricity could be certified and sold, € 54,473 would have been obtained.

$$5) 447,3168 \times 10 € = 54.473 € \quad (9)$$

- 5) The expense arising from the annual electricity consumption in the case where the solar energy panel is not installed is calculated in Equation 10. The unit price of 1 kW of electricity is \$45 . When we convert it into dollars with the June'23 dollar rate of 20.68, we have a cost of 509.624.271 dollars

$$11.324.983,80 \times 45 = 509.624.27\$ \quad (10)$$

According to the analysis, when we take into account the annual electricity cost and the carbon we would sell if we could participate in the carbon emission trade, the system pays for itself in a short period of about 1 year.

4. Results And Discussion

A campus carbon footprint calculation is an important tool for a university or educational institution to determine its greenhouse gas emissions and guide its reduction efforts. Finding the carbon footprint allows determining what the organization's greenhouse gas emissions are from and how much it is. This information helps the organization to understand its environmental impact and set future goals. Carbon footprint calculation is an important step in the struggle against climate change. Institutions can make contribution for minimizing the effects of climate change by reducing greenhouse gas emissions. Carbon footprint calculation provides a starting point for determining emissions and developing reduction strategies. By analyzing energy consumption data, organizations can identify opportunities for energy savings and develop energy management strategies. This helps to both create a more environmentally sustainable campus and lower energy costs. Sustainability-focused institutions gain reputation and competitive advantage among students, staff and potential students. The carbon footprint calculation provides an opportunity to declare the sustainability goals of the organization and support them with concrete actions.

For this purpose, carbon footprint analysis was carried out in Konuralp Campus of Düzce University. As a result of this analysis, the investment cost has been calculated since solar energy availability in the region is sufficient. In Düzce, the annual sunshine duration and the intensity of the sun's rays are at levels suitable for the use of solar energy systems.

As a result of the study, the amount of carbon footprint was found to be 4.781.841 tons of CO₂. Some effort can be organized to reduce this expense.

- Since most of the carbon footprint comes from natural gas, thermal insulation can be controlled.
- Information and studies on global climate change and sustainable campus can be increased.
- The use of environmentally friendly and fully recyclable items can be increased.
- Employing electric buses widespread. Encouraging the use of micro-mobility vehicles such as bicycles and electric scooters in individual transportation.
- The use of renewable energy should be increased. The university should be made to meet its own needs.
- The number of trees and ornamental plants suitable for Düzce vegetation can be increased.

- Newly designed buildings can produce in accordance with green building concept.

Turkey is the country with the highest potential to produce thermal energy in Europe - excluding the countries with a coast on the Mediterranean. Electricity generation with solar energy is one of the most important energy policies. After the conversion of solar energy to thermal energy, it has recently started to be popularized with small steps such as traffic lights, park and garden lighting [25].

Acknowledgment

We would like to thank all the staff of Düzce University for their help in obtaining the necessary data to carry out the study.

Author's Contributions

İrem Düzdar: analytical analysis on the structure, supervised the experiment's progress, result interpretation and manuscript preparation.

Rabia Yıldız: Drafted and wrote the manuscript, performed the experiment and result analysis.

Ethics

There are no ethical issues after the publication of this manuscript.

References

- [1]. M. Türkeş, M. Sümer, and U. M. Çetiner, "Küresel İklim Değişikliği Ve Olası Etkileri," *Istanbul Sanayi Odası*, pp. 7–24, 2000.
- [2]. R. Aydın and M. Demirbaş, "21. Yüzyılın En Büyük Tehdidi: Küresel İklim Değişikliği," *NWSA Acad. Journals*, vol. 15, no. 4, 2020.
- [3]. K. Öztürk, "Küresel İklim Değişikliği Ve Türkiyeye Olası Etkileri," *Gazi Üniversitesi Gazi Eğitim Fakültesi Dergisi*, c. 22, sy. 1, 2002..
- [4]. İ. Demir, "Kyoto Protokolü Amaçlarına Ulaşabilme Yolunda Dünya Enerji Kullanımında Meydana Gelebilecek Değişiklikler," *Gazi Üniversitesi İktisadi ve İdari Bilimler Fakültesi Dergisi*, c. 8, sy. 2, ss. 241–251, 2006.
- [5]. K. Kumaş, A. Akyüz, A. Güngör, "Burdur mehmet akif ersoy üniversitesi bucak yerleşkesi yükseköğretim birimlerinin karbon ayak izi tespiti," *Niğde Ömer Halisdemir Üniversitesi Mühendislik Bilim. Dergisi*, 2019.
- [6]. Türkiye Cumhuriyeti Ticaret Bakanlığı, "Yeşil Mutabakat Eylem Planı," *Yeşil Mutabakat Eylem Planı*, p. 60, 2021.
- [7]. Türkiye Cumhuriyeti Çevre, Şehircilik ve İklim Değişikliği Bakanlığı, "İklim Değişikliği Azaltım Stratejisi ve Eylem Planı (2024-2030)," p. 198, 2024.
- [8]. "Per capita CO₂ emissions, 2022." <https://ourworldindata.org/grapher/co-emissions-per-capita>
- [9]. Wiedmann T., Minx J.C., "A Definition of 'Carbon Footprint'", *Ecological Economics Research Trends*, (Pertsova C.C., Ed.), Chapter 1, Nova Science Publishers, Hauppauge NY, USA, 2008, ss.1-11.
- [10]. S. Surachotivet, J. Keawboonchu, T. Sangsawang, J. Posin, and T.

Orachun, "Comprehensive Analysis of City Carbon Footprint from Energy Consumption in a District of the Central Region of Thailand," *EnvironmentAsia*, vol. 17, no. 2, pp. 28–37, 2024, doi: 10.14456/ea.2024.18.

- [11]. T. Atabey, "Karbon Ayak İzinin Hesaplanması: Diyarbakır Örneği," Yüksek Lisans Tezi, Fırat Üniversitesi, 2013.
- [12]. R. González-Quintero, A. M. Sierra-Alarcón, J. C. Benavides-Cruz, and O. L. Mayorga-Mogollón, "The contribution of local shrubs to the carbon footprint reduction of traditional dairy systems in Cundinamarca, Colombia," *Agrofor. Syst.*, vol. 98, no. 4, pp. 873–890, 2024, <https://doi.org/10.1007/s10457-024-00958-z>.
- [13]. Li, Baokun, et al. "Carbon emission of municipal solid waste under different classification methods in the context of carbon neutrality: A case study of Yunnan Province, China." *Fuel* 372 (2024): 132167.
- [14]. Wang, J., He, Y. Q., & Feng, Y., "Analysis and prediction on carbon emissions from electrical and electronic equipment industry in China," *Environmental Impact Assessment Review*, 106, 107539, 2024.
- [15]. M. R. Ezhilkumar, et al. "Estimation of Carbon Footprint Pattern at Nile University of Nigeria: A Technical Campus in Nigeria." *E3S Web of Conferences*. Vol. 455. EDP Sciences, 2023.
- [16]. G. Binboğa And A. Ünal, "Sürdürülebilirlik Ekseninde Manisa Celal Bayar Üniversitesi'nin Karbon Ayak İzinin Hesaplanmasına Yönelik Bir Araştırma," *Uluslararası İktisadi Ve İdari İncelemeler Derg.*, No. 21, Pp. 187–202, Apr. 2018, <https://doi.org/10.18092/ulikidince.323532>.
- [17]. A. K. Seyhan, & M. Çerçi, "IPCC Tier 1 ve DEFRA Metotları ile Karbon Ayak İzinin Belirlenmesi: Erzincan Binalı Yıldırım Üniversitesi'nin Yakıt ve Elektrik Tüketimi Örneği," *Süleyman Demirel Üniversitesi Fen Bilimleri Enstitüsü Dergisi*, 26(3), 386-397, 2022.
- [18]. B. Gökçek, A. Bozdağ, & H. Demirbaş, "Niğde Ömer Halisdemir Üniversitesi örneğinde karbon ayak izinin belirlenmesi," *Niğde Ömer Halisdemir Üniversitesi Mühendislik Bilimleri Dergisi*, 8(2), 721-730, 2019.
- [19]. İ. F. Yaka, A. Koçer, & A. Güngör, "Akdeniz üniversitesi sağlık hizmetleri meslek yüksekokulu karbon ayak izinin tespiti," *Makine Teknolojileri Elektronik Dergisi*, 12(3), 37-45, 2015.
- [20]. "Düzce Üniversitesi | Anasayfa." Accessed: Nov. 04, 2024. [Online]. Available: <https://www.duzce.edu.tr/>
- [21]. "Publications - IPCC-TFI." Accessed: Nov. 04, 2024. [Online]. Available: <https://www.ipcc-nggip.iges.or.jp/public/2006gl/vol1.html>
- [22]. C. Gürbüz, Ö. N. K. Aracı, & İ Bekci, "Dünya'da Ve Türkiye'de Karbon Ticareti Ve Karbon Muhasebesi Uygulamaları Üzerine Bir Araştırma-A Research On Carbon Trade And Carbon Accounting Applications In The World And Turkey," *Mehmet Akif Ersoy Üniversitesi Sosyal Bilimler Enstitüsü Dergisi*, 11(28), 424-438, 2019.
- [23]. "ASIA CARBONX CHANGE – A Greener Tomorrow.Today." Accessed: Nov. 04, 2024. [Online]. Available: <https://asiacarbonxchange.org/>
- [24]. Sreng R., "Otomotiv endüstrisinde karbon ayak izi", Yüksek Lisans Tezi, Sakarya Üniversitesi (Türkiye), 2016.
- [25]. O. O. Yolcan, R. Köse, "Türkiye' Nin Güneş Enerjisi Durumu Ve Güneş Enerjisi Santrali Kurulumunda Önemli Parametreler," *Kırklareli Üniversitesi Mühendislik ve Fen Bilim. Derg.*, vol. 6, no. 2, pp. 196–215, Dec. 2020 <https://doi.org/10.34186/klujes.793471> .

Propeller Modification with Groove Structure on Thrust Performance

Duygu Özyurt¹ , Hürrem Akbiyik^{2*} 

^{1,2} Adana Alparslan Türkeş Science and Technology University, Aerospace and Aeronautical Engineering
Department, 01250, Türkiye

* hakbiyik@atu.edu.tr

* Orcid No: 0000-0002-1880-052X

Received: 9 August 2024

Accepted: 25 November 2024

DOI: 10.18466/cbayarfbe.1531094

Abstract

This study includes an investigation into the application of grooves in drone propellers that inspired from the structure of a bird's wing. The designed propeller involves the application of grooves at angles of 30, 45 and 60 degrees. Main purpose of using biomimetic design is to determine whether it is effective in improving thrust performance by directing the flow to the propeller blade through the grooves. Experimental investigation of the effects of these grooves on the propeller-engine thrust and the underlying causes of these effects were tried to be presented experimentally with TiO₂ based surface oil visualization technique. From the experimental results, the highest thrust value was obtained for the modified prop-60° model compared to the base propeller. Thrust measurements were measured at various RPM/V values. The maximum increase in thrust improvement is reached when the engine driven by 25% nominal power.

Keywords: Biomimetics, Propeller modification, Thrust measurement, TiO₂ surface oil visualization

1. Introduction

The expectation of continuous development based on human needs plays a leading role in prioritizing inspiration from nature. For this reason, the field of biomimetics aroused interest from researchers and development in areas such as aerospace, robotics, transport, military and art. So far, many innovations and technological developments have been achieved in the

field of aviation by using biomimetic. The steps taken in the past just to fly have evolved into today's technology, and designs that prioritize efficiency in aircraft systems continue to be developed. In Table 1, the inspired livings in nature and the distribution of the examples of these livings that have found application in the field of aviation according to years are presented. Moreover, findings affecting aerodynamic efficiency obtained in the field of aviation due to these applications are presented.

Table 1. Biomimetic studies in the field of aerospace.

Date	Ref.	Animal	Anatomical Structures	Engineering Application	Aerodynamic Efficiency
2000-2005	[1]	Dragonfly	Flapping wings and legs	Entomopter	<ul style="list-style-type: none">Controlled vortex separation points
	[2]	Birds	Hyper-Elliptic Cambered Span	UAV	<ul style="list-style-type: none">Higher lift with less drag,Higher maneuverability.
	[3]	Aphids	Thin and flexible wing	Flying Insect Robot	<ul style="list-style-type: none">The ability to determine the wing area and flapping frequency.
	[4]	Insects	Flapping flight mechanisms	MAV	<ul style="list-style-type: none">Improving maneuverabilityIncreasing thrust force
2006-2010	[5]	Insects	Flapping wings	FW-MAV	<ul style="list-style-type: none">Improving flapping behavior,Increase in thrust force
	[6]	Dragonfly	Wing	UAV	<ul style="list-style-type: none">Increase in lift force



2011-2016	[7]	Beetles	Wing	UAV	<ul style="list-style-type: none"> • An efficient design of flapping wing mechanism
	[8]	Owl	Fully structure	MAVs	<ul style="list-style-type: none"> • Increase in aerodynamic performance • Improvement perching capability
	[9]	Locust	Wing	MAV	<ul style="list-style-type: none"> • Providing improvement in lift for large range of angles of attack
	[10]	Humpback whale	Tubercles	Airplane	<ul style="list-style-type: none"> • Delaying stall • Enhancement in energy efficiency
	[11]	Birds	Flexible wing	UAV	<ul style="list-style-type: none"> • Decrease the power requirement at maximum speed
2017-2022	[12]	Bees	Fully structure	MAV	<ul style="list-style-type: none"> • Reduction in power consumption
	[13]	Dove	Wing	UAV	<ul style="list-style-type: none"> • Lateral stability improvement • Rolling maneuver improvement • Wing-tip vortex strength reduction
	[14]	Owl	Wing	FUAV	<ul style="list-style-type: none"> • Better control facing gust
	[15]	Birds	Wing	sUAV	<ul style="list-style-type: none"> • Minimizing energy consumption • Energy recovery
	[16]	Flying squirrels	Wing	UAV	<ul style="list-style-type: none"> • Improve maneuverability
	[17]	Organic molecules (CH4)	Bond structure	BioTetra	<ul style="list-style-type: none"> • Improve flight efficiency • Improve stability.
	[18]	Humpback whale	Tubercles	UAV	<ul style="list-style-type: none"> • Increasing lift • Delaying stall • Extended flight time • Carry heavier payloads
	[19]	Birds	Wing	Propeller	<ul style="list-style-type: none"> • Reduced acoustic power level
2023-Present	[20]	Owls	Feathers	Propeller	<ul style="list-style-type: none"> • Reduction in noise
	[21]	Birds	Wing	Propeller	<ul style="list-style-type: none"> • Generate more torque • Reduction of noise-inducing tip speed ratio
	[22]	Birds	Wing	Propeller	<ul style="list-style-type: none"> • Reduction in noise level
	[23]	Birds	Fold ability the wing	Monocopter	<ul style="list-style-type: none"> • Stable flight • Position control
	[24]	Butterfly	Wing	UST Butterfly	<ul style="list-style-type: none"> • Improving control in all lateral, longitudinal, and vertical directions
	[25]	Humming birds	Wing	MAV	<ul style="list-style-type: none"> • Increase in lift • Increase in drag.
	[26]	Eagle	Claw	Quadrotor	<ul style="list-style-type: none"> • Dynamically grasp various unknown objects • Enhanced perching ability.
	[27]	Birds	Primary feathers	UAV	<ul style="list-style-type: none"> • Improvement in aerodynamic forces • Increase in rolling coefficient

Biomimetic inspirations not only bring innovation to the literature, but they also provide many different perspectives to the engineering field as a result of using nature efficiently. In the design development phase, studies are carried out for the determined purpose. These objectives include issues such as making the design more durable, making it lighter, increasing energy efficiency, reducing sound or noise, increasing aerodynamic efficiency. In addition to many advantages, biomimetic also has some disadvantages. If it is considered briefly, we can first say the limitations of existing production

technologies, especially for nanomaterials in surface structures, and then the lack of techniques for researching and determining the functioning and biomimetic concepts within the biological system [28]. Some studies in the aviation sector have been inspired by the profiles of bird wings in UAVs to increase aerodynamic performance [29]. Studies on dragonfly models to reduce drag force [30], utilization of the alula of peregrine falcon in the field of flow separation control [31], observation of owls in the reduction of sound noise [32] are among the important topics studied in this field.

Biomimetic is also a field that contributes to increasing thrust generation in aircraft. In a study, Xue et al. (2024) focused on improving the design of ornithopter aircraft in order to increase the cruising speed of the vehicle by considering the flapping performance of birds. In the experimental phase of their design, it was observed that increasing the lift force and increasing the flapping frequency significantly enhanced the thrust force, as it is the main determining factor in the speed increase of the aircraft [33]. Considering the studies carried out in this field, various configurations inspired by nature are aimed to increase the thrust by transferring them to the propeller blades. Propellers are one of the parts that are open to development with biomimetic designs. The shape, number, width, size and material of the propeller blades may vary according to the vehicle used. These can be listed as aircraft, unmanned aerial vehicles, marine vehicles and wind turbines. Further improvements in the performance of the blades have led to the general use of customized blade types for each vehicle, in addition to the traditional propeller blade. In particular, to obtain maximum thrust, the wing's chord length, bending angle and shape are among the important parameters. Consideration of these parameters provides many alternative, non-traditional designs [34]. Seeni et al. (2018) investigated a biomimetic method to improve the aerodynamic performance of a propeller. The progress of the study was about adding tubercles to the propeller blades. It has been previously tested on blades and wind turbines has provided the researchers with the prediction that it will provide improvements in performance when applied to the propeller blade. In the experiments, the increase in thrust force was calculated as 1.5% and supported the previous studies [35]. Butt and Talha (2019), observed that although the new design created by the addition of tubercles increased the propeller efficiency [36]. The study of Bui et al. (2023) is an alternative example of a developed biomimetic propeller blade. In this design, which is considered suitable for drone propellers, the flexible structure of the dragonfly wing is taken into account. It is generally aimed to adapt to collisions and complete the flight with minimal damage in these situations [37]. In terms of reducing risk and ensuring safety when using the Tombo propeller, it was found that the drone suffered two-thirds less damage during collision with an obstacle than with conventional propellers. The Tombo propeller was found to be particularly suitable for use in gliders and flapping wings. Ksiazek et al. (2023) investigated the noise reduction methods of UAV propellers inspired by the feathers on owl wings. In the experiments, the propellers varied with creating grooves engraved in 3 different positions with the base propeller. These positions were determined as inlet surface, outlet surface or both sides of the blade. The results were evaluated only on the outputs obtained with a rotational speed of 700 RPM. It is reported that using this technique provides noise reduction. As a result of the biomimetic approach, the propeller with grooves at both inlet and outlet showed a 6.2 dB reduction compared to

the reference propeller [20]. Noda et al. (2022) proposed a new biomimetic design to reduce propeller noise by various methods. By adding a Gurney design to the airfoil shape, the blade area was enlarged. As a result of their application, the lift force of the propeller was increased, and the noise generated was significantly reduced as the propeller rotation speed decreased [38]. In another study on noise reduction, Rao et al. (2017) tried a new design, and this design was successful in noise reduction and the measured efficiency was close to the reference propeller [39]. Since the efficiency was low in previous studies, a new design was tried. This innovation was realized by adding a plate to the trailing edge of the propeller. The optimum position of the plate was found empirically. One of the most important studies on noise reduction was carried out by Wei et al. (2020). In this study, different designs were compared, and the best performance was determined. In the rotational tests, it was found that the sawtooth propeller showed the best result in terms of thrust increase (3.53%) and noise reduction (max. 4.18 dB). It was observed that the previous design, which was created by cutting grooves in the propeller blade, was more successful in noise reduction. The saw-toothed propeller is extra good in that aerodynamic performance is also improved [40].

Kudo et. al. (2001) have been studied groove modification under supercavity condition on the propeller blade for obtain higher thrust values maximum efficiency [41]. Another study of the groove modification in the literature has done by Shengwang et. al. (2022). In their experimental research on four blades propeller the achieved noise reduction was %35 [42]. Additionally, a design on pump jet propeller duct surface done by Zhang et. al. (2024), for suppressing of the tip vortex cavitation and to prevented from radiative noise [43]. On the propeller's optimization in the field of UAV's endurance and operational range provides improvement in thrust force and reduced torque. According to this subject, Seeni (2020) studied a passive flow control technique which is groove design on the propeller surface. Findings show that, at low Reynolds Number (Re) when angle of attack increased, the wake structures progressed from trailing edge to leading edge [44]. It is concluded, biomimetic design has made a great contribution to the development of more effective designs today.

In this present study, the surface geometry of the propeller modified with an inspired geometry which is including groove structures as in the bird feather surface. In this context, thrust experiments of the base model and modified models with 3 different groove placement angles were carried out. In addition, TiO₂ based surface oil flow visualization technique, which is an important method to reveal the effects of these geometries on thrust changes and to explain the flow structures on the models containing groove structures, is used. It is aimed to reveal both the changes in thrust values of the relevant models and to explain the flow structures on the surface.

2. Materials and Methods

KingKong 6040R model propeller was chosen for modification and tests. The reason for this is that the modification process is easier on this propeller, which has two blades in design. Another reason is that it is a widely used propeller for drones. It is a self-tightening propeller and is made of ABS plastic [45]. Another part to be used in the test system is the motor to be connected to the propeller. One of the first parameters to be considered when choosing the motor is whether it is compatible with the propeller and the other is whether it is compatible with the battery. Brushless motors are generally preferred in experiments with drone propellers. For this reason, EMAX XA2212 brushless motor was used in the experimental setup due to its compatibility with the selected propeller and being cost-effective [46]. Some of the propulsion test equipments were designed specifically for the experiments. The designed parts were produced by using a 3D printer. The system includes motor holder, load cell, carbon rib and support elements. The motor holder part holds the motor and stabilizes it. It also helps to provide connection control of the motor and propeller system. As shown in Figure 1, the motor-propeller pair is integrated on a single axis Honeywell brand loadcell by the help of a connection rod. The loadcell amplifies the signals with the help of a Smowo brand amplifier. Each thrust measurement is repeated 3 times and averaged.



Figure 1. Experimental setup and devices.

This system is connected to the NI-DAQ card and provides the data acquisition process with the use of computer. This DAQ card shown in Figure 2 is a National Instruments brand and is NI-USB-6009 model. Also shown in Figure 2, two power supplies were used for driving the motor-propeller pair and for the use of the amplifier which is connected to loadcell. These power supplies are AA-Tech brand and ADC-3050DD model. A servo tester was used to adjust the speed of the motor and an ESC with a value of 30A was used in the motor version.

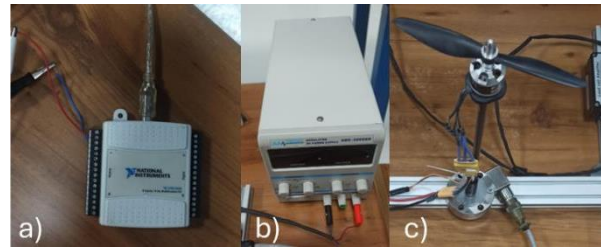


Figure 2. a) DAQ card (left), b) power supply (mid) and c) motor-propeller-ESC (right) equipments.

Figure 3 represents the base model and modified test models. In order to increase the flow control and thrust performance, modifications were made with grooves in the chordwise direction. In this context, these grooves are designed to be 30°, 45° e 60° in the flow direction of the rotary wing. In this study, groove structures inspired by bird wings are in the direction of flow, as in the feathers on bird wings in nature, and are known to contribute to the control of flow [47]. For this purpose, it is desired to contribute to the study of thrust change in rotary wing systems by controlling the flow with these modifications. Figure 3 shows the direction of rotation of the propellers and the modifications of the grooves in the direction of rotation. The number of these flow control surfaces is proportional to the placement angle.

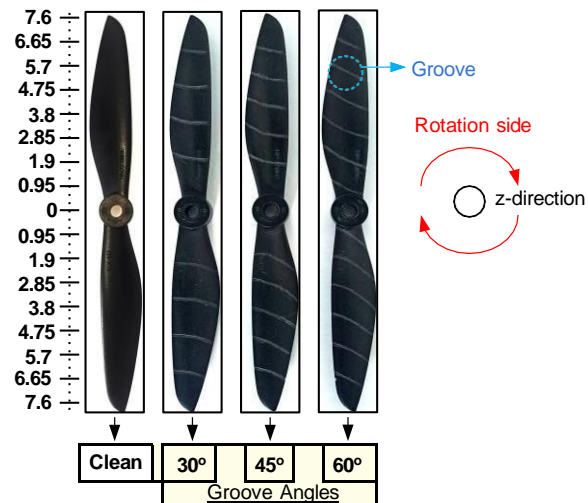


Figure 3. Base propeller and modified propellers.

Although it is aimed to increase the thrust performance with the modified propeller, TiO₂ based surface oil flow visualization experiments shown in Figure 4 were carried out to understand the reasons for this thrust change. These flow visualization experiments are an effective technique used to reveal the flow structures on the model surface. In this study, titanium powder, oleic acid and SAE30 gas oil were mixed in a 1:5:7 ratio. Seyhan and Akbıyık (2024) successfully revealed the flow topologies on the surface using this mixture ratio in their study [48].

In this study, the number of revolutions, which is one of the parameters affecting the thrust level in examining

these flow structures and observing the thrust change, was set as 25%, 50%, 75% and 100%.



Figure 4. Test setup used for surface flow visualization.

3. Result and Discussion

In this section, the thrust test results and TiO_2 based surface oil visualization test results for the base model and the modified test models are presented. Previously, KK6040 propeller's thrust have been measured in gram unit by Abhishek et. al. (2017). Present study's base propeller average thrust data and data from in literature measured thrust values are coincided [49]. Figure 5

shows the thrust-KV values for different models. At the minimum value of 280 RPM/V, the thrust value of the base propeller-motor is 72 g, while the thrust values of all modified propeller-engine pairs are higher than this value. Compared to the base model, the highest thrust increase value is obtained for the Modified-Prop-60° model at around 26.5% for 280 RPM/V. It is revealed that the modified-prop-60° model has the highest thrust value according to the direction of rotation at all speeds. The main reason for this is thought to be that the modified micro grooves effectively control the flow in the rotational direction of the propeller. However, it is revealed that the improvement in thrust value decreases as the number of revolutions increases. As a result of the numerical study by Oktay and Erarslan (2020), for the effect of rotational speed and airspeed on thrust coefficient based on UAV propeller, it is concluded that as the rotational speed increases, higher turbulent flow is effective at blade tip region. Moreover, it is found that the turbulence intensity is effective in transform the laminar flow structure on the propeller blade to turbulent, leading to a decrease in thrust coefficient [50]. It is observed from the results of the study that the effectiveness of this modification will be higher in flights at low RPM/V. At 1120 RPM/V, the improvement in thrust value was again obtained as 3.2% in the Modified-Prop-60° model.

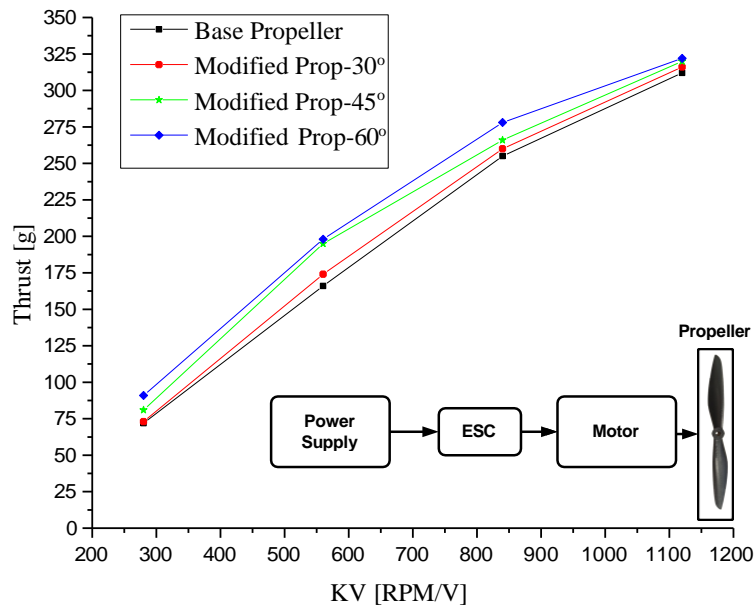


Figure 5. Thrust values of base and modified models for various RPM/V values.





As seen in Table 2, TiO_2 based surface oil flow visualization results were made for all models. It is clearly seen that the flow structures on all experimental models were revealed. In the base model, the rotational direction of the propeller drives the TiO_2 based flow visualization mixture. It is clearly seen that the flow separation line and reattachment line are formed on the surface of all experimental models. Montagner (2024) demonstrated the flow separation line and reattachment line on the propeller surface with surface oil flow

visualization experiments. In addition to, it is reported that LSB occurred between the flow separation line and the reattachment line [51]. Considering the region near the center where the base propeller is connected to the motor (propeller root), transition zones and regions where the flow is at low speeds are obvious. Svorcan (2023) reported that the velocity values are high towards the ends of the propeller and there is a low velocity profile around the propeller root [52]. When propellers are modified with groove geometry, these transition

zones become narrower towards to central region. In this case, it can be said that more fluid plays an active role on

the propeller surface and as a result of this situation, the thrust value increases.

Table 2. TiO₂ surface oil flow visualization result at 280 RPM/V value

Model Name	TiO ₂ Surface Oil Flow Visualization Results
Base Model	
Modified Prop-30°	
Modified Prop-45°	
Modified Prop-60°	

4. Conclusion

In this study, a modification method is proposed to improve the thrust produced by the propeller-motor pair used in drones. This modification method includes inspiration of the structure of bird feathers in the biomimetic field. Also, this groove structure was applied on the propeller at various angles in the direction of rotation of the propeller.

In the data obtained, thrust increase was observed in each of the propellers to which modifications were applied, and the best thrust increase was observed in the Modified Prop-60° propeller. When the propeller-motor pair was operating at 280 RPM/V, 26.5% improvement in thrust was observed when comparing the base propeller with Modified Prop-60°. When the propeller-motor pair was operating at 1120 RPM/V, the improvement in thrust was 3.2%. As a result of the experimental process, it is seen that the modifications provide more improvement in thrust production at low speeds. TiO₂ based flow visualization experiments revealed the flow structures on the propeller surface. Moreover, TiO₂ based flow visualization experiment results showed that the laminar separation line and reattachment line formed on the propeller blades. Furthermore, the region of very low velocity flow at the propeller root was clearly defined and it was demonstrated that this region was narrowed towards the propeller root by means of flow control grooves.

Author's Contributions

Duygu Özyurt: Writing-review and editing, Writing-original draft, Visualization, Validation, Methodology, Investigation, Conceptualization

Hürrem Akbıyık: Writing-review and editing, Writing-original draft, Visualization, Validation, Methodology, Investigation, Conceptualization

Ethics

There are no ethical issues after the publication of this manuscript.

References

- [1]. Colozza, A. 2000. Planetary Exploration Using Biomimetics, GN:07600-051.
- [2]. Davidson, J., Chwalowski, P., Lazos, B. 2003. Flight dynamic simulation assessment of a morphable hyper-elliptic cambered span winged configuration, AIAA Atmospheric Flight Mechanics Conference and Exhibit, Austin, Texas, AIAA 2003-5301.
- [3]. Chan, H. Y., Lam, J. H., Li, W. J. 2004. A biomimetic flying silicon microchip: Feasibility study, IEEE International Conference on Robotics and Biomimetics, Shenyang, China, 447- 451.



- [4]. Jones, K. D., Bradshaw, C. J., Papadopoulos, J., Platzer, M. F. 2005. Bio-inspired design of flapping-wing micro air vehicles. *The Aeronautical Journal*; 109(1098): 385-393.
- [5]. Nguyen, Q. V., Truong, Q. T., Park, H. C., Goo, N. S., Byun, D. 2010. Measurement of force produced by an insect-mimicking flapping-wing system. *Journal of Bionic Engineering*; 7, S94-S102.
- [6]. Kim, S. H., Chang, J. W., Sohn, M. H. 2008. Flow visualization and aerodynamic-force measurement of a dragonfly-type model. *Journal of visualization*; 11, 37-44.
- [7]. Nguyen, T. T., Byun, D. 2008. Two-dimensional aerodynamic models of insect flight for robotic flapping wing mechanisms of maximum efficiency. *Journal of Bionic Engineering*; 5(1), 1-11.
- [8]. Nelson, D., Keating, F., Leonard, J., Jacob, J. 2013. Design of a Biomimetic Unmanned Aircraft System, 51th AIAA Aerospace Sciences Meeting including the New Horizons Forum and Aerospace Exposition, Grapevine (Dallas/Ft. Worth Region), Texas, AIAA 2013-0761.
- [9]. Laliberté, J. F., Kraemer, K. L., Dawson, J. W., Miyata, D. 2013. Design and manufacturing of biologically inspired micro aerial vehicle wings using rapid prototyping. *International journal of micro air vehicles*; 5(1), 15-38.
- [10]. Fish, F. E., Weber, P. W., Murray, M. M., Howle, L. E. 2011. The tubercles on humpback whales' flippers: application of bio-inspired technology. *Integrative and Comparative Biology*; 51(1), 203-213.
- [11]. Galantai, V. P., Sofla, A. Y. N., Meguid, S. A., Tan, K. T., Yeo, W. K. 2011. Bio-inspired wing morphing for unmanned aerial vehicles using intelligent materials. *International Journal of Mechanics and Materials in Design*; 8, 71-79.
- [12]. Bluman, J. E., Pohly, J. A., Sridhar, M. K., Kang, C. K., Landrum, D. B., Fahimi, F., Aono, H. 2018. Achieving bioinspired flapping wing hovering flight solutions on Mars via wing scaling. *Bioinspiration & Biomimetics*; 13(4), 046010.
- [13]. Hui, Z., Zhang, Y., Chen, G. 2019. Aerodynamic performance investigation on a morphing unmanned aerial vehicle with bio-inspired discrete wing structures. *Aerospace Science and Technology*; 95, 105419.
- [14]. Abbasi, S. H., Mahmood, A. 2019. Modeling, simulation and control of a bio-inspired electromechanical feather for gust mitigation in flapping wing UAV, 2nd International Conference on Communication, Computing and Digital systems (C-CODE), Islamabad, Pakistan, 195-200.
- [15]. Gudmundsson, S., Golubev, V. V., Drakunov, S., Reinholtz, C. A. 2017. Biomimetic Energy-Conserving/Harvesting Trajectory Planning for a sUAV, AIAA Atmospheric Flight Mechanics Conference, Denver, Colorado, 3889.
- [16]. Pons, A., Cirak, F. 2022. Pitch-axis supermanoeuvrability in a biomimetic morphing-wing aircraft. *arXiv preprint arXiv:2205.09431*.
- [17]. Li, B., Wang, D., Ma, L. 2019. BioTetra: a bioinspired multi-rotor aerial vehicle, IEEE International Conference on Robotics and Biomimetics (ROBIO), Dali, China, 114-119.
- [18]. ElGhazali, A. F., Dol, S. S. 2020. Aerodynamic optimization of unmanned aerial vehicle through propeller improvements. *Journal of Applied Fluid Mechanics*, 13(3), 793-803.
- [19]. 손창호, 김상현, 송지훈, 이동렬. 2023. A Study on Aerodynamic and Acoustic Characteristics of Blades by Biomimetic Design for UAM. *Journal of the Korean Society for Precision Engineering*, 40(7), 571-580.
- [20]. Książek, P., Lalik, K., Pasławski, P., Pietrzak, M., Przejczowski, P., Przepióra, J. 2023. A preliminary measurement verification of sound power level emitted by biomimetic drone propellers inspired by an owl's feather, *International Carpathian Control Conference (ICCC)*, Miskolc-Szilvásvárad, Hungary, 225-229.
- [21]. Rajendran, P., Jayaprakash, A. 2023. Numerical performance analysis of a twin blade drone rotor propeller. *Materials Today: Proceedings*; 80(2), 492-498.
- [22]. Hasegawa, M., Sakaue, H. 2024. Propeller-noise reduction by microfiber coating on a blade surface. *Sensors and Actuators A: Physical*; 371, 115273.
- [23]. Bhardwaj, H., Cai, X., Win, L. S. T., Foong, S. 2023. Nature-inspired in-flight foldable rotorcraft. *Bioinspiration & Biomimetics*; 18(4), 046012.
- [24]. Huang, H., He, W., Zou, Y., Fu, Q. 2024. USTButterfly: a servo-driven biomimetic robotic butterfly. *IEEE Transactions on Industrial Electronics*; 71(2), 1758-1767.
- [25]. Min, Y., Zhao, G., Pan, D., Shao, X. 2023. Aspect ratio effects on the aerodynamic performance of a biomimetic hummingbird wing in flapping. *Biomimetics*, 8(2), 216.
- [26]. Xu, M., De, Q., Yu, D., Hu, A., Liu, Z., Wang, H. 2024. Biomimetic Morphing Quadrotor Inspired by Eagle Claw for Dynamic Grasping. *IEEE Transactions on Robotics*; 40, 2513-2528.
- [27]. Bardera, R., Rodríguez-Sevillano, Á. A., Barroso, E., Matías, J. C. 2023. Numerical analysis of a biomimetic UAV with variable length grids wingtips. *Results in Engineering*; 18, 101087.
- [28]. Banken, E., Oeffner, J. 2023. Biomimetics for innovative and future-oriented space applications-A review. *Frontiers in Space Technologies*; 3, 1000788.
- [29]. Rao, C., Liu, H. 2020. Effects of Reynolds number and distribution on passive flow control in owl-inspired leading-edge serrations. *Integrative and Comparative Biology*; 60(5), 1135-1146.
- [30]. Mulligan, R. 2020. Bio-inspired aerofoils for small wind turbines, International Conference on Renewable Energies and Power Quality (ICREPQ'20), Granada, Spain, 753-758.
- [31]. Ito, M. R., Duan, C., Wissa, A. A. 2019. The function of the alula on engineered wings: a detailed experimental investigation of a bioinspired leading-edge device. *Bioinspiration & biomimetics*; 14(5), 056015.
- [32]. Gu, Y., Song, F., Bai, H., Wu, J., Liu, K., Nie, B., Lu, Z. 2024. Numerical and experimental studies on the owl-inspired propellers with various serrated trailing edges. *Applied Acoustics*, 220, 109948.
- [33]. Xue, D., Li, R., Liu, J. 2024. Research on Improvement Methods for Driven System of Bio-Inspired Aircraft to Increase Flight Speed. *Drones*; 8(4), 133.
- [34]. Kutty, H. A., Rajendran, P. 2017. Review on numerical and experimental research on conventional and unconventional propeller blade design. *Int. Rev. Aerosp. Eng*; 10(2), 61-73.
- [35]. Seeni, A., Rajendran, P., Kutty, H. A. 2018. A critical review on tubercles design for propellers. In *IOP Conference Series: Materials Science and Engineering*, 370(1), 012015.
- [36]. Butt, F. R., Talha, T. 2019. Numerical investigation of the effect of leading-edge tubercles on propeller performance. *Journal of Aircraft*, 56(3), 1014-1028.
- [37]. Bui, S. T., Luu, Q. K., Nguyen, D. Q., Le, N. D. M., Loianno, G. 2023. Tombo propeller: bioinspired deformable structure toward

collision-accommodated control for drones. *IEEE Transactions on Robotics*, 39(1), 521-538.

[38]. Noda, R., Ikeda, T., Nakata, T., Liu, H. 2022. Characterization of the low-noise drone propeller with serrated Gurney flap. *Frontiers in Aerospace Engineering*, 1, 1004828.

[39]. Rao, C., Ikeda, T., Nakata, T., Liu, H. 2017. Owl-inspired leading-edge serrations play a crucial role in aerodynamic force production and sound suppression. *Bioinspiration & Biomimetics*, 12(4), 046008.

[40]. Wei, Y., Xu, F., Bian, S., Kong, D. 2020. Noise reduction of UAV using biomimetic propellers with varied morphologies leading-edge serration. *Journal of Bionic Engineering*; 17, 767-779.

[41]. Kudo, T., Ukon, Y., Sumino, Y. 2001. Proposal of a Groove Cavitator on a Supercavitation Propeller, <http://resolver.caltech.edu/cav2001:sessionB9.003>.

[42]. Shengwang, Z. H. U., Guijian, X. I. A. O., Yi, H. E., Gang, L. I. U., Shayu, S. O. N. G., JIAHUA, S. 2022. Tip vortex cavitation of propeller bionic noise reduction surface based on precision abrasive belt grinding. *Journal of Advanced Manufacturing Science and Technology* 2(1), 2022003.

[43]. Zhang, K., Ye, J., Zhong, H., Fu, B., Zhang, Y. 2024. Study on the tip flow control effect of pump jet propeller with groove structure. In Fourth International Conference on Mechanical, Electronics, and Electrical and Automation Control, Xi'an, China, 13163, 1771-1777.

[44]. Seeni, A. S. 2020. Effect of grooves on aerodynamic performance of a low Reynolds number propeller, (Doctoral dissertation).

[45]. de Oliveira, T. L., de Carvalho, J. 2021. Design and numerical evaluation of quadrotor drone frame suitable for fabrication using fused filament fabrication with consumer-grade ABS. *Journal of the Brazilian Society of Mechanical Sciences and Engineering*, 43(9), 436 (1-19).

[46]. Nikhil, N., Shreyas, S. M., Vyshnavi, G., Yadav, S. 2020. Unmanned aerial vehicles (UAV) in disaster management applications, In 2020 Third International Conference on Smart Systems and Inventive Technology (ICSSIT), Tirunelveli, India, 140-148.

[47]. Feng, B., Chen, D., Wang, J., Yang, X. 2015. Bionic research on bird feather for drag reduction. *Advances in Mechanical Engineering*; 7(2), 849294.

[48]. Seyhan, M., Akbıyık, H. 2024. An experimental investigation on the flow control of the partially stepped NACA0012 airfoil at low Reynolds numbers. *Ocean Engineering*; 306, 118068.

[49]. Abhishek, A., Krishna, M., Sinha, S., Bhowmik, J., Das, D. 2017. Design, development and flight testing of a novel quadrotor convertiplane unmanned air vehicle. In 73rd Annual Forum of the American Helicopter Society. Fairfax, VA: *AHS International, Inc.*

[50]. Tuğrul Oktay, Yüksel Eraslan, 2020. Numerical investigation of effects of airspeed and rotational speed on quadrotor UAV propeller thrust coefficient. *Journal of Aviation*, 5(1), 9-15.

[51]. Montagner, S. 2024. On the effects of freestream turbulence on a small drone propeller aerodynamics and aeroacoustics, (Doctoral dissertation, Politecnico di Torino).

[52]. Svorcan, J. 2023. WMLES of flows around small-scale propellers-estimating aerodynamic performance and wake visualization. *Theoretical and Applied Mechanics*, 50(2), 133-144.

Spectroscopic (FT-Raman, FT-IR, UV-Vis, and NMR) and Theoretical Analysis of 1-Methylindole: Structural Characterization, Non-Covalent Interactions, and Electronic Properties

Çağlar Karaca^{1*} 

¹Manisa Technical Sciences Vocational School, Manisa Celal Bayar University, Manisa, Türkiye

* caglar.karaca@cbu.edu.tr

* Orcid No: 0000-0002-2835-7269

Received: September 21, 2024

Accepted: December 3, 2024

DOI: 10.18466/cbayarfbe.1554031

Abstract

The structural and spectroscopic characterization of 1-Methylindole (1MI) by favors of FT-Raman (4000–200 cm^{-1}), FT- IR (4000–400 cm^{-1}), UV-Vis, and ^1H and ^{13}C NMR techniques is presented. The experimental observations were enlightened by density functional theory (DFT) calculations at the B3LYP/6-311G(d,p) level of theory. Geometrical structure of the molecule was obtained, and bond order analysis was performed based on the optimized structure. Non-Covalent Interactions (NCIs) were analyzed by using the Reduced Density Gradient (RDG) with energy density descriptors to visualize the limiting regions of these interactions. Furthermore, molecular charge distribution and isosurface mappings with local extrema were obtained and the critical regions on the molecular surface were visualized. The vibrational spectra were calculated, and the normal modes were assigned based on total energy distribution (TED) calculations. The electronic properties of 1MI were explored experimentally through UV-Vis spectroscopy and analyzed in detail via Atoms in Molecules (AIMs) methodology. Total and partial density of state (TDOS and PDOS) and overlap population density of state (OPDOS) diagrams were calculated and fractional contributions of nonpolar methyl group and aromatic indole to frontier molecular orbitals were obtained through this methodology. Theoretical NMR chemical shifts were assigned based on DFT calculations that use the gauge-invariant atomic orbital (GIAO) method. Inclusion of solvents effect in NMR calculations produces twice less dispersive data and better fitting results to experimental observations. Non-linear optical properties: polarizability, anisotropy of polarizability, and first hyperpolarizability of the molecule were also computed to explore the potential of 1MI as nonlinear spectroscopy agent.

Keywords: 1-methylindole, DFT, UV, IR and Raman, NMR, Non-Covalent Interactions, Orbital Fragmentation.

1. Introduction

Indole is a heterocyclic aromatic organic compound which occur in nature [1–4] as a five-membered ring with the formula of $\text{C}_9\text{H}_7\text{N}$. The indole family has significant distribution in the central nervous system and thus has shown an extensive range of biological effects [5,6] such as antibacterial, antifungal, anticonvulsant, antiviral, and antiproliferative activities [7–10]. An important indole derivative tryptophan for example is an extremely important biomolecule because it carries a vital amino acid essential in human nutrition found in a vast number of proteins across the biosphere [11,12]. Anticancer activity of indole derivatives is another critical perspective; some indole based compounds exhibit significant antiproliferative/cytotoxic activity

against human cancer cells [13]. Methyl-indole inhibits pancreatic cancer cell viability by down-regulating ZFX expression and targeting the P13K/AKT pathway, suggesting potential as a therapeutic agent for pancreatic cancer [14]. Besides, electro synthetical production of polyindoles with low electrical conductivity is another important characteristic of indole containing compounds [15–18].

Based on studies showing great potential of indole-based compounds, structural properties of indole molecule have been studied extensively in experiments and theoretical works. Roychowdhury [19] performed X-ray diffraction studies of indole in the orthorhombic space group, and Catalan [20] carried out the molecular geometry of indole theoretically.

IMI consists of a six-membered benzene ring fused to five-membered pyrrole ring in which a methyl group substituted on to the nitrogen. The methyl group can donate electrons through the C–N σ bond, and its hydrogen atoms can interact with the nearby π electrons in the aromatic ring through hyper conjugation. Thus, N-methyl substitution can lead to a change in the electron density of the molecular species, the electronic transition energy, and the frequency of some vibrations [21]. 1-methylindole shows improved stability in hydrogen storage reactions compared to indole [22]. Mourik et. al. have performed high-level ab initio calculations on indole and 1-methylindole-water system because of the importance of water in the solvation processes of the biologically active indole derivatives [23]. Muñoz et. al. [24] reported to FT-IR and fluorescence studies on the ground and excited state hydrogen-bonding interactions between 1-methylindole and water in water–triethylamine mixtures, and hydrogen-bonding interactions between 1-methylindole and alcohols [25]. Semi-empirical analysis was brought by Mons et al. [26] on modelled indole–water and 1-methylindole–water complexes. Absorption and emission energies in seven step methodology followed in our previous work [27] for both formalisms have been obtained using TD-DFT calculations with B3LYP/6-311G(d,p) model chemistry based the ground and first excited state optimized geometries obtained.

To the best of our knowledge, no literature has been yet available on description of the structural and spectroscopic behaviors of the IMI compound by utilization of broad range of spectral techniques and tools of quantum chemical calculations. Therefore, we have focused on both experimental and theoretical exploration of IMI by using FT-IR, Raman, UV-Vis, and NMR spectral techniques along with DFT and TD-DFT calculations. The geometrical structure investigations were enriched by bond order analysis and non-covalent interaction visualizations. Besides, further informative properties such as the dipole moment, nonlinear optical (NLO) properties, chemical hardness, electronegativity, chemical potential, and electrophilicity index were determined, and their relations with the structure of the molecule were discussed.

2. Materials and Methods

2.1. Experimental Details

The FT-IR spectrum of the IMI was recorded between 4000 and 400 cm^{-1} on an Agilent Cary 660 FT-IR spectrometer with ATR objectives. The spectrum was recorded at room temperature, with a scanning speed of 8 $\text{cm}^{-1} \text{min}^{-1}$ and the spectral resolution of 4.0 cm^{-1} . FT-Raman spectrum of the sample was recorded at 4000-200 cm^{-1} region on a Bruker RFS 100/S FT-Raman instrument, which uses a liquid nitrogen-cooled Ge detector, using 1064 nm excitation from an Nd: YAG

laser. Five hundred scans were accumulated at 4 cm^{-1} resolution using a laser power of 100 mW. The ultraviolet absorption spectra of the IMI in water and ethanol were examined in the range 200–400 nm by using Shimadzu UV–2101PC spectrometer. ^1H and ^{13}C Nuclear magnetic resonance spectra were recorded on a Bruker-Spectroscopy Advance DPX 400 MHz Ultra-Shield in dimethyl sulfoxide (DMSO- d_6) with TMS as internal reference.

2.2. Quantum Calculations

The DFT and TD-DFT ab initio calculations were carried out using Gaussian 16 program [28]. Molecular geometries of the singlet ground state of the IMI was fully optimized in the gas phase at the B3LYP/6-311G(d,p) level of theory [29–31]. All spectroscopic properties were calculated on the basis of optimized structure. The harmonic vibrational wavenumbers were computed and scaled with 0.983 and 0.958 for up to 1700 cm^{-1} and greater than 1700 cm^{-1} , respectively, to correct overestimations [32]. The TED calculation, which showed the relative contributions of the redundant internal coordinates to each normal vibrational mode of the molecule, thus enable us numerically to describe the character of each mode, was carried out by the scaled quantum mechanical (SQM) method [33] by using Parallel Quantum Solutions (PQS) program and visualized using GaussView 6 [34]. In this method, the output files created at the end of the frequency calculations are used to compute vibrational energies of each mode.

The contributions of each fragment to total molecular orbital was calculated using Mulliken population analysis. GaussSum 3.0 [35] was used to calculate group contributions to the molecular orbitals to determine the partial density of states and overlap population density of states (OPDOS) diagrams. The OPDOS diagram was created by convoluting the molecular orbital information with gaussian curves of unit height and FWHM of 0.3 eV.

The quantum theory of Atoms in Molecules proposed by Bader [36] allows one to partition a molecular space into atomic basins. It provides a route for consistent description of atoms (e.g. atomic volume and electron population, dipole moment) and interactions between atoms (i.e. covalent, ionic, and hydrogen bonds, van der Waals interactions) in terms of the topological properties of the electron density $\rho(r)$. Reduced Density Gradient (RDG) and Mayer Bond Order (MBO) [37,38] was calculated with use of Multiwfn program [39,40].

3. Results and Discussion

3.1. Geometrical Structure and Bond Order

The geometrical structure obtained by DFT calculations and atom labelling of IMI are shown in Figure 1, and the

optimized parameters are gathered in Table 1 in comparison with the experimental values from literature along with the MBO values. Because the crystallographic data on 1MI has not been recorded in literature, we compared geometric parameters obtained in calculations to that of methylindole available from experiments of indole [19]. This comparison also allows exploration of variations in bond lengths and angles differs due to substitution of methyl group to MI.

The calculated bond lengths of C–C in benzene group in range from 1.388 to 1.42 Å for B3LYP with 6-311G(d,p) basis set which are in good agreement with experimental values reported between 1.372 and 1.411 Å for indole [19,20].

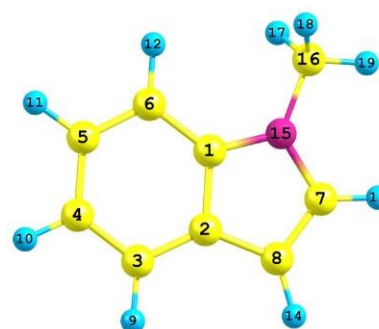


Figure 1. The optimized geometrical structure of 1MI. Blue: Hydrogen, Yellow: Carbon, and Pink: Nitrogen.

Table 1. The geometric parameters (bond lengths (Å), angles (°)) and MBO of 1MI obtained by DFT/B3LYP/6-311G(d,p) comparison of experimental indole parameters.

Parameters		Bond Lengths (Å)		Bond Angles (°)		
	Calculated	X-Ray ^[19]	MBO	Calculated	X-Ray ^[19]	
C ₁ -C ₂	1.423	1.411	1.2589	C ₂ -C ₁ -C ₆	122.141	116.4
C ₁ -C ₆	1.398	1.395	1.3282	C ₂ -C ₁ -N ₁₅	107.767	
C ₁ -N ₁₅	1.381	1.374	1.0878	C ₆ -C ₁ -N ₁₅	130.092	
C ₂ -C ₃	1.403	1.398	1.3404	C ₁ -C ₂ -C ₃	118.839	
C ₂ -C ₈	1.434	1.436	1.2990	C ₁ -C ₂ -C ₈	106.722	
C ₃ -C ₄	1.387	1.381	1.4921	C ₃ -C ₂ -C ₈	134.439	
C ₃ -H ₉	1.085	1.087	0.9729	C ₂ -C ₃ -C ₄	119.130	
C ₄ -C ₅	1.408	1.396	1.3727	C ₃ -C ₄ -C ₅	121.112	
C ₄ -H ₁₀	1.084	1.087	0.9690	C ₄ -C ₅ -C ₆	121.220	124.8
C ₅ -C ₆	1.388	1.372	1.4896	C ₁ -C ₆ -C ₅	117.559	119.7
C ₅ -H ₁₁	1.084	1.087	0.9690	C ₈ -C ₇ -H ₁₃	129.858	
C ₆ -H ₁₂	1.084	1.088	0.9596	C ₈ -C ₇ -N ₁₅	110.262	111.5
C ₇ -C ₈	1.368	1.358	1.5879	H ₁₃ -C ₇ -N ₁₅	119.880	
C ₇ -H ₁₃	1.079	1.082	0.9627	C ₂ -C ₈ -C ₇	106.875	105.5
C ₇ -N ₁₅	1.383	1.381	1.1566	C ₂ -C ₈ -H ₁₄	127.219	
C ₈ -H ₁₄	1.079	1.082	0.9783	C ₇ -C ₈ -H ₁₄	125.906	
N ₁₅ -C ₁₆	1.449	-	0.9589	C ₁ -N ₁₅ -C ₇	108.373	
C ₁₆ -H ₁₇	1.094	-	0.9604	C ₁ -N ₁₅ -C ₁₆	125.528	
C ₁₆ -H ₁₈	1.094	-	0.9604	C ₇ -N ₁₅ -C ₁₆	126.100	
C ₁₆ -H ₁₉	1.090	-	0.9707	N ₁₅ -C ₁₆ -H ₁₇	111.063	

The variation, due to substitution of methyl group to indole, in the bond length of C₁-N₁₅ bond is only 0.007 Å while we expect much higher deviations. Average deviation of bond lengths from experimental values is nearly 0.006 Å already. This is a preliminary indication that the methyl group is not dominant in determination of characteristics of the ring systems. Bond angle calculations also well correlated with experimental results with only average of 2.8° deviations. The maximum drift, 5.7°, is observed in C₂-C₁-C₆ bond angle indicating that the substitution plays a significant role in

distortion of the benzene ring despite creating no effect on bond lengths. The C–H bond lengths are in a good agreement with indole [19]. For example, the calculated average of C–H bond lengths, 1.084 Å and 1.079 Å, are in good agreement with experimental reports of 1.087 Å and 1.082 Å for in the rings, respectively.

The linearity between the experimental and calculated bond lengths of 1MI can be estimated from plotting the calculated versus experimental values. The relation

between experiment and calculation for bond lengths for IMI can be described by the following equation.

$$\delta_{\text{cal}} = 0.9692\delta_{\text{exp}} + 0.0362, R^2 = 0.9992 \quad (3.1)$$

Bond order is an important concept for understanding the nature of a chemical bond. The MBO square with empirical bond order that is close to 1.0, 2.0, and 3.0 for single, double, and triple bond, respectively. In our study, the MBO calculated between C₁-C₂, C₁-C₆, C₂-C₃, C₂-C₈, C₃-C₄, C₄-C₅, and C₅-C₆ are 1.258, 1.328, 1.340, 1.299, 1.492, 1.372, and 1.489, respectively. These values fall into the region where the aromatic C-C bonds calculated from 1.229 to 1.455 [41]. The only MBO for C₇-C₈ was calculated to be 1.5879 that is slightly stronger than the other aromatic carbons. In order to find the reason behind this anomaly, orbital occupancy-perturbed Mayer bond orders (OOP-MBO) analysis [42] is performed using Multiwfn program to determine contributions of individual occupied molecular orbitals. If two electrons are replaced from HOMO, then Mayer bond order between C₇ and C₈ decrease from 1.5879 to 1.1538, and the contribution from HOMO-1 orbital is 0.20008. Therefore, we can state that HOMO orbital must be greatly beneficial for bonding and this orbital shows strong character of π -bonding between C₇ and C₈, which give higher bond order values than expected.

3.2. Electrostatic Potential and Weak Interaction Profile

Electrostatic potential (ESP) analysis is one of the most effective ways of proposing physicochemical properties, reactivity, and intermolecular interactions of molecules under study because the size and shape of molecular electrostatic potential and extremum positively/negatively charged regions can be visualized clearly by color-coding [39]. ESP is calculated directly from atomic coordinates obtained in geometrical optimization without any further second order mathematical derivations.

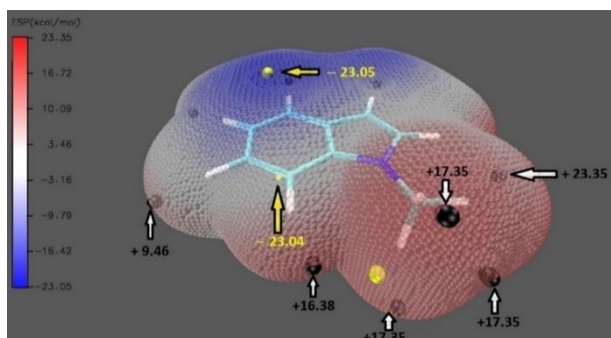


Figure 2. Electrostatic potential surface of IMI with indications of extrema.

Here, we investigated quantitative electrostatic potential (ESP) analysis of molecular van der Waals (vdW) surface of IMI. ESP obtained for IMI is given in Figure 2 where it shows the most positive regions with red and the most

negative regions with blue in nearly 46 kcal/mol region. Extremum charged points are shown with dots and the values are given as well. The minimum -23.05 kcal/mol is the global minimum of the vdW surface. So the below and above of IMI has abundant π electrons on the global minimum regions. We also calculated the ESP in the positive values ranging from $+9.46$ to $+23.35$ kcal/mol. Maximum value, $+23.35$ kcal/mol, is the global maximum rises from the positively charged H13 atom. Another important positive value is $+17.35$ kcal/mol due to presence of methyl group. We ultimately examine the molecular surface area in each ESP range due to its quantitatively fall out with ESP distribution on the whole molecular surface. From the Figure S1, it can be seen that there is a large portion of molecular surface having small ESP value, namely from -25 to $+25$ kcal/mol. Among these areas, the negative areas mainly correspond to the surface above and below the pyrrole region, and shows effect of the abundant π electron cloud while the positive part results from the positive charged the C-H hydrogens. This can be due to effect of van der Waals interactions between methyl groups and pyrrole hydrogen (H12), which keeps ESP value ($+17.35$ kcal/mol) smaller than global maximum region.

To understand and quantitatively describe the intramolecular weak interactions rather than estimate from their outcomes, Johnson and co-workers [43] developed an approach to investigate the weak interactions in real space based on the electron density and its derivatives. The reduced density gradient (RDG) is a fundamental dimensionless quantity formulated from the electron density and its first derivative, and described as follows.

$$RDG(r) = \frac{1}{2(3\pi^2)^{1/3}} \frac{|\nabla\rho(r)|}{\rho(r)^{4/3}} \quad (3.2)$$

The weak interactions can be specified in regions in terms of low electron density and low RDG value. The density values of the low-gradient spikes (in the plot of RDG versus ρ) appear to be an indicator of the interaction strength. The sign of λ_2 , which is the second largest eigenvalue of electron density Hessian matrix at position r , is utilized to distinguish the bonded ($\lambda_2 < 0$) from non-bonding ($\lambda_2 > 0$) interactions. The plot of the RDG versus the electron density ρ multiplied by the sign of λ_2 can allow analysis and visualization of a wide range of interaction types such as hydrogen bonding, van der Waals interactions, and steric effects. Large negative values of sign (λ_2) ρ are indicative of strong attractive interactions whereas the positive values correspond to repulsive interactions. Furthermore, these interactions can be visualized on the molecule using color-coding depending on the strength of interaction where the blue indicates the attraction and red is associated with repulsive effects. RDG calculations are obtained via

Multiwfn wavefunctions analyzer and visualization are plotted in VMD program [44,45]. The results of our analysis on 1MI are given in Figure 3.

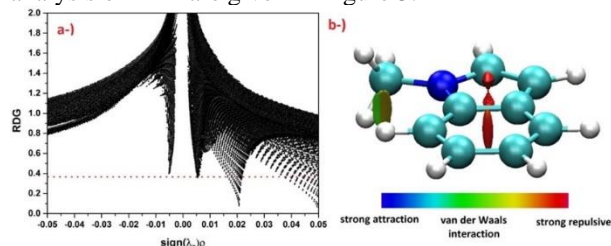


Figure 3. Schematic view of a) RDG profile and b) visualization of weak interaction of 1MI.

Weak interactions in 1MI are only two kinds, either vdW or steric effects. The region marked by green-brown in Figure 3 b) can be identified as vdW interaction region which corresponds to the two central spikes below $\text{sign}(\lambda_2)\rho=0.01$ and above $\text{sign}(\lambda_2)\rho=-0.01$ with nearly $\text{RDG}=0.4$ in Figure 3 a). We can also understand this effect from the extremum ESP points in Figure 2. The region between methyl group and the nearest hydrogen of the benzene ring is at under a positive ESP with the magnitude of +16.38 kcal/mol. Therefore, it is natural to have some attractive interaction in this region. Steric effects are observed in two levels. The first sharp spike is observed around $\text{sign}(\lambda_2)\rho = 0.02$ and characterized to be due to a weaker repulsion at the center of phenyl ring, which has also been observed in the structure [46]. A second tailing spike appears around $\text{sign}(\lambda_2)\rho = 0.05$ is associated with the repulsion centered at the middle of pyrrole ring and located above and below the molecular plane. This disruption is basically due to the unpaired electrons of the nitrogen on the ring.

3.3. Vibrational Spectral Analysis

The title molecule has C_s symmetry when the planarity of the methyl group retained. There are 51 fundamental vibrational modes that can be distributed as $17A' + 34A''$ represented A' species in plane and A'' species out-of-plane modes. To make a comparison between the results of the theoretical and experimental, the infrared and Raman spectra of the 1MI are shown in Figure 4 where the calculated intensity is plotted against the wavenumbers. The observed and calculated vibrational wavenumbers with proposed assignments generated from TED calculation for the 1MI are presented in Table 2. The last column contains a detailed description of the fundamental modes obtained from their TED. The results of theory obtained by DFT/ B3LYP/6-311G(d,p) basis set are generally higher than their experimental data. The deviation can be a consequence of the anharmonicity and the general tendency of the quantum chemical methods to overestimate the force constants at the exact

equilibrium geometry. The other plausibility is the theoretical results have obtained in vacuum whereas experimental ones for solid phase. To minimize the overall deviation, the calculated frequencies were scaled by a scaling factor. After scaling, the results show better than older ones. The vibrational analyses of present molecule can supply helpful information about the fundamental bands, overtone, and combination bands. We also discuss following the fundamental modes of the molecule comparing their experimental data and similar structure.

The modes of C–H stretching are generally seen as multiply that in the region of $3000\text{--}3100\text{ cm}^{-1}$ [47]. The C–H stretching modes of indole were observed in the region from 3140 to 3051 cm^{-1} and computed to be between 3135 and 3044 cm^{-1} [48,49]. In this study, we observed ($\nu_1\text{--}\nu_6$) in the range of $3026\text{--}3121\text{ cm}^{-1}$ and predicted in the range of $3027\text{--}3114\text{ cm}^{-1}$ as pure modes by B3LYP functional of DFT as seen TED column in Table 2. C-H symmetric vibrations modes are seen higher than asymmetric ones in rings, while adverse situation is seen in methyl group.

The C–H modes of in plane and out-of-plane bending generally observed in aromatic compounds in the range of $1000\text{--}1300\text{ cm}^{-1}$ and $750\text{--}1000\text{ cm}^{-1}$, respectively [50]. The experimental C–H in-plane bending vibrations of 1MI are in the range of $1014\text{--}1488\text{ cm}^{-1}$ and generally mixed with C–C stretching modes according to their TED results. The C–H out-of-plane bending vibrations are calculated at $711\text{--}959\text{ cm}^{-1}$ region. The CH_3 group has nine fundamental vibrations, asymmetric and symmetric stretches, bending, rocking, and torsion modes [51]. The CH_3 asymmetric stretching vibrations are expected in the range of $3000\text{--}2925\text{ cm}^{-1}$ and the symmetric CH_3 vibrations in the range of $2940\text{--}2905\text{ cm}^{-1}$ [52].

The asymmetric stretch usually appears at higher wavenumbers than the symmetric stretching. Therefore, the CH_3 asymmetrical and symmetrical stretching occurs about 2900 cm^{-1} and 2800 cm^{-1} , respectively [53,54]. In this study, the CH_3 stretching modes were observed at 2885 cm^{-1} and 2941 cm^{-1} in FT-IR, and 2940 cm^{-1} in FT-Raman. The methyl group stretching modes were predicted at 2893 cm^{-1} (symmetric), and 2941 cm^{-1} and 2996 cm^{-1} (Asymmetric.). The other methyl group assignments of the molecule determined using GaussView 6 [34] program as wagging, scissoring, wagging, rocking, twisting etc. are given in Table 2. Methyl deformations modes of in-plane as known scissoring were defined at 1394 cm^{-1} and $1432\text{--}1460\text{ cm}^{-1}$, and rocking at 247 , and 1098 cm^{-1} .

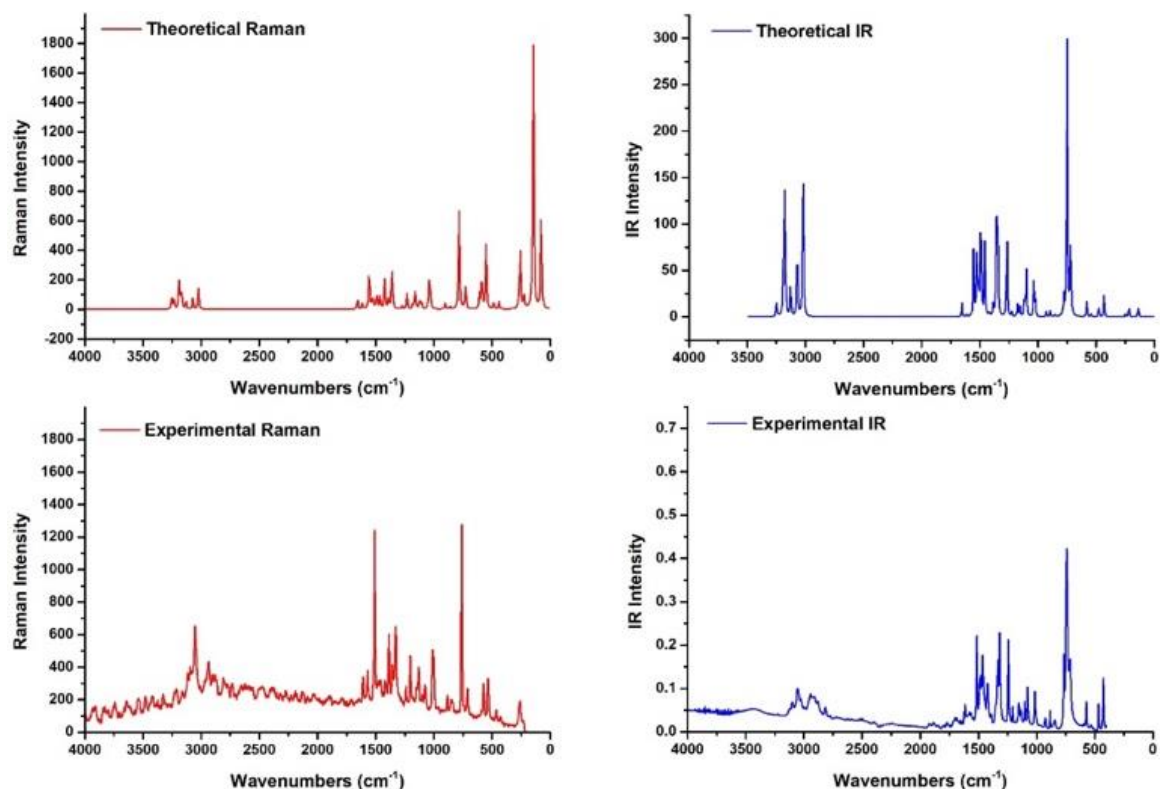


Figure 4. Theoretical and experimental FT-Raman and FT-IR spectra of 1MI.

Table 2. Comparison of the calculated harmonic frequencies and experimental (FT-IR and FT-Raman) wavenumbers (cm^{-1}) using by B3LYP method 6-311G(d,p) basis set of 1MI molecule.

Modes No	Sym. Species	Experimental		Theoretical		TED ^b (10%)
		FT-IR	FT-Raman	Unscaled freq.	Scaled freq. ^a	
v ₁	A'	3121		3250	3114	vCH _{sym} .(100) _{ring2}
v ₂	A'	3096		3231	3095	vCH _{asym} .(100) _{ring2}
v ₃	A'	3055	3053	3189	3055	vCH _{sym} .(100) _{ring1}
v ₄	A'			3178	3045	vCH _{asym} .(100) _{ring1}
v ₅	A'			3168	3035	vCH _{asym} .(100) _{ring1}
v ₆	A'	3026		3160	3027	vCH _{asym} .(100) _{ring1}
v ₇	A'			3127	2996	vCH _{asym} (100) _{methyl}
v ₈	A''	2941	2940	3069	2941	vCH _{asym} (100) _{methyl}
		2914				Overtone + Combination
		2906				Overtone + Combination
		2885				vCH _{sym} (100) _{methyl}
		2816				Overtone + Combination
v ₉	A'	2770		3020	2893	Overtone + Combination
		2518				Overtone + Combination
		2492				Overtone + Combination
		1920				Overtone + Combination
		1888				Overtone + Combination
		1799				Overtone + Combination
		1766				Overtone + Combination
1702		Overtone + Combination				



V ₁₀	A'	1616	1610	1654	1625	vCC(59) _{ring}
V ₁₁	A'	1578	1569	1612	1585	vCC(60) _{ring}
		1559				Overtone + Combination
V ₁₂	A'	1516	1513	1552	1526	vC=C(48), δNCH (11)
V ₁₃	A'			1525	1499	ωCH ₃ (63)
V ₁₄	A'	1488		1516	1490	ωCH ₃ (22), vCC(19), δCCH(19) _{ring1}
		1478				Overtone + Combination
V ₁₅	A'	1465	1465	1495	1469	vCC(25), δCCH(35) _{ring1}
V ₁₆	A''			1485	1460	ρCH ₃ (89)
V ₁₇	A'	1423	1418	1457	1432	ρCH ₃ (81)
V ₁₈	A'	1390	1387	1418	1394	vCC(39), vCN(15), δCCH(16) _{ring2}
V ₁₉	A'		1357	1385	1362	vCC(25), vCN(28), δCCH(32) _{ring1}
V ₂₀	A'	1331	1331	1357	1334	vCC(53) _{ring1} , vCN(19)
V ₂₁	A'	1315		1348	1325	vCC(21), vCN(18), δCCH(37)
V ₂₂	A'	1243	1239	1268	1247	vCC(18), δCCH(41), δNCH(10)
V ₂₃	A'	1206	1205	1227	1206	vCC(26), δCCH(37)
V ₂₄	A'	1154		1177	1157	vCC(18) _{ring1} , δCCH(69) _{ring1}
V ₂₅	A'	1134	1135	1157	1137	vCC(23) _{ring1} , δCCH(42) _{ring1}
V ₂₆	A''			1144	1125	ωCH ₃ (98)
V ₂₇	A'	1098	1098	1117	1098	vCC(11), δCCC(11), δCCH(16), ΓCH ₃ (26)
V ₂₈	A'	1079	1077	1101	1082	vCC(11), δCCH(42) _{ring1} , δNCH(25)
V ₂₉	A'	1014	1010	1036	1018	vCC(61) _{ring1} , δCCH(17)
V ₃₀	A'			1023	1006	vCN(23), δCCH(20), ΓCH ₃ (23)
V ₃₁	A''	959		973	957	γCH(88)
V ₃₂	A''	923		932	916	γCH(91)
V ₃₃	A'	881	881	896	881	vCC(13), δCCC(40), δCCH(16)
V ₃₄	A''	842	844	857	842	γCH(75)
V ₃₅	A''			853	838	γCH(78)
V ₃₆	A''			779	766	γCH(88)
V ₃₇	A'	761	763	777	764	vCC(47), vCN(10), δCCC(13)
V ₃₈	A''	737		750	737	γCH(88)
V ₃₉	A'	711	711	723	711	vC ₁₆ -N(25), δCCC(23), δCCH(14)
V ₄₀	A''			718	706	γCH(83)
V ₄₁	A''			602	591	φPyrrole(62)
V ₄₂	A''	573	573	583	573	φPhenyl(44), τCCCN(25)
V ₄₃	A'			581	571	vCC(12), δCCC(29), δCCN(26)
V ₄₄	A'	533	534	544	535	vCN(14), vCC(10), δCCC(35) _{ring1}
V ₄₅	A'	467	468	478	470	vCC(10), δCCC(34), δCNC(27) _{methyl}
V ₄₆	A''	426	426	433	426	γCH(86))
V ₄₇	A''		261	266	261	ωCH ₃ (69)
V ₄₈	A'			251	247	ΓCH ₃ (88)
V ₄₉	A''			219	215	Butterfly effect (71)
V ₅₀	A''			138	136	ωCH ₃ (88)
V ₅₁	A''			70	69	φCH ₃ (100)

^aWavenumbers in the ranges from 4000 to 1700 cm^{-1} and lower than 1700 cm^{-1} are scaled with 0.958 and 0.983, respectively.

^bTED: Total Energy Distribution ν ; stretching, γ ; out-of plane bending, δ ; in-plane-bending, τ ; torsion, ρ ; scissoring, ω ; wagging, ϕ ; twisting, Γ ; rocking.

Our previous study also supported this situation [55]. The twisting and wagging modes as known out-of-plane deformations of methyl group were determined at 69 cm^{-1} ϕCH_3 (twisting) and 261, 1125, 1490 and 1499 cm^{-1} ωCH_3 (twisting) modes of the heading molecule, observed nearly the same region, showing agreement. The C–N stretching vibrations modes are generally very difficult to determine due to mixing of other several modes. Silverstein et al. [56] defined the C–N stretching modes in the region of 1386–1266 cm^{-1} for aromatic amines. In the present work, the modes calculated at 535, 711, 764, 1006, 1325, 1334, and 1394 cm^{-1} have contribution from CN vibrations according to the TED analysis. These complex modes were observed at 533, 711, 761, 1014, 1315, 1331 and 1390 cm^{-1} in FT-IR and 534, 711, 763, 1010, 1331 and 1387 cm^{-1} in the FT-Raman experimentally. The theoretically scaled frequencies of C–N related bands by B3LYP method well correlates with experimental observation.

$$\delta_{\text{cal}} = 0.9692\delta_{\text{exp}} + 0.0362, R^2 = 0.9992 \quad (3.3)$$

$$\delta_{\text{cal}} = 0.9692\delta_{\text{exp}} + 0.0362, R^2 = 0.9992 \quad (3.4)$$

$$\delta_{\text{cal}} = 0.9692\delta_{\text{exp}} + 0.0362, R^2 = 0.9992 \quad (3.5)$$

The stretching vibrational modes of rings are highly important in the vibrational spectra of the aromatic compounds. The bands observed C–C stretching vibrations modes are of variable intensity and generally observed at 1625–1590, 1590–1575, 1540–1470, 1465–1430 and 1380–1280 cm^{-1} five bands in this region given by Varsányi [57]. Also ring carbon–carbon stretching vibrations appears in the region of 1400–1650 cm^{-1} in benzene derivatives [32,55,57]. In this study, C–C stretching modes were computed in the region of 1625–1526 cm^{-1} , 1490 cm^{-1} , 1469 cm^{-1} , 1394–1137 cm^{-1} , 1098–1018 cm^{-1} , 881, 764 cm^{-1} , and 571–470 cm^{-1} for the title molecule. The observed values are 1616–1516 cm^{-1} , 1488 cm^{-1} , 1465 cm^{-1} , 1390–1134 cm^{-1} , 1098–1014 cm^{-1} , 881, 761 cm^{-1} , 533 and 467 cm^{-1} in FT-IR spectra and 1610–1513 cm^{-1} , 1387–1135 cm^{-1} , 1098–1010 cm^{-1} , 881, 763, 534, and 468 cm^{-1} in FT-Raman spectra. The highest contribution of the C–C stretching vibrations stem from ν_{10} (%59) and ν_{11} (%60) were assigned nearly pure modes of the 1MI.

The infrared and Raman correlation graphics were plotted individually (in Figure S2), to see the relations between theoretical and experimental data. Also, all wavenumbers are described as linear for total (together IR and Raman) in Figure S3. These states were showed following equations and showed linearity.

3.4. Electronic Properties

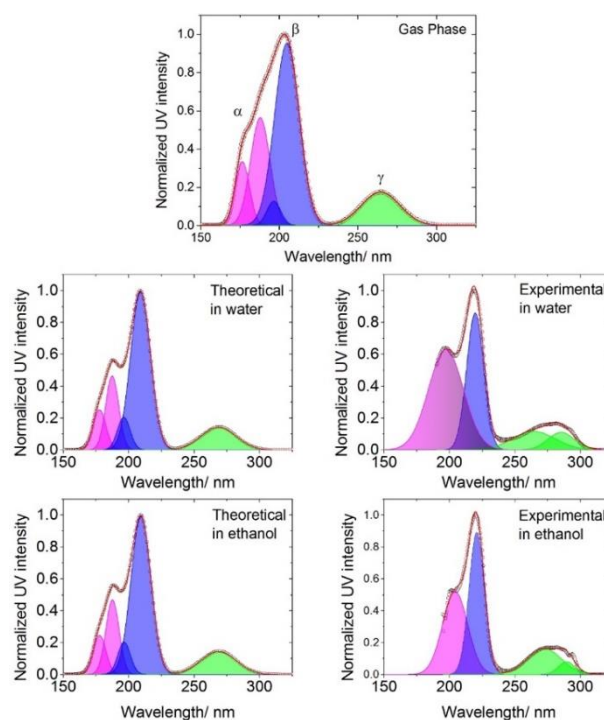


Figure 5. Theoretical and experimental UV spectra of 1MI in ethanol and water.

The experimental and calculated (using TD–DFT method) UV-Vis (electronic absorption) spectra predicted in gas phase, in water, and ethanol solvents, and measured in solvents were presented in Figure 5. The calculations were performed by using TD–DFT method, which is quite reasonable and computationally reliable, and suitable for medium size molecules [44,58]. Our theoretical calculations show that there should be five major transitions within the spectral range, the experimental spectra indicated four main peaks in the spectra. Simulated spectra can also reproduce the experimental spectra with embedded transition peaks underneath. Thus, the experimental UV-Vis spectra were quantified by multicomponent analysis method which has been used successfully in explanation of experimental UV spectra under the light of theoretical calculations [55,59]. In this method, the intensity, I , of the spectrum is modeled as a superposition of antisymmetrized Gaussian (AG) line shape functions given below, thus matches the peaks to major transition more accurately.

$$\delta_{\text{cal}} = 0.9692\delta_{\text{exp}} + 0.0362, R^2 = 0.9992 \quad (3.6)$$

Table 3. Experimental and calculated wavelengths λ (nm), excitation energies (eV), oscillator strengths (f) and electronic transitions of IMI for gas phase, in ethanol and water solutions.

		E (eV)	λ (nm)	f	Fitted-w	FWHM	Area	Major contributors
Gas Phase	$\alpha 1$	7.004	177.04	0.16	176.5	10.7	3.8	H-2 \rightarrow L (22%), H-1 \rightarrow L+4 (21%), H \rightarrow L+4 (42%)
	$\alpha 2$	6.600	187.88	0.26	187.8	14.6	8.8	H-2 \rightarrow L (27%), H-1 \rightarrow L+1 (36%), H \rightarrow L+4 (25%)
	$\beta 1$	6.274	197.64	0.29	196.6	10.5	1.4	H-2 \rightarrow L (28%), H-1 \rightarrow L+1 (40%), H \rightarrow L+1 (13%)
	$\beta 2$	5.983	207.24	0.37	204.8	18.6	18.8	H-1 \rightarrow L (26%), H-1 \rightarrow L+1 (11%), H \rightarrow L+1 (47%)
	γ	4.646	266.89	0.08	264.5	29	5.4	H \rightarrow L (85%)
Water Teo.	$\alpha 1$	6.989	177.42	0.15	177.6	11.7	3.2	H-2 \rightarrow L+1 (25%), H-1 \rightarrow L+3 (70%)
	$\alpha 2$	6.609	187.61	0.33	187.4	11.8	5.8	H-2 \rightarrow L (39%), H-1 \rightarrow L+1 (30%), H \rightarrow L+3 (22%)
	$\beta 1$	6.216	199.5	0.25	196.3	11.5	2.5	H-2 \rightarrow L (24%), H-1 \rightarrow L+1 (58%)
	$\beta 2$	5.897	210.26	0.63	209.1	17.9	18.9	H-1 \rightarrow L (30%), H \rightarrow L+1 (57%)
	γ	4.570	271.33	0.09	268.6	31.6	4.8	H \rightarrow L (90%)
Water Exp.	α	6.278			197.5	23	14.9	$\pi-\pi^*$
	β	5.649			219.5	15.4	14.1	$\pi-\pi^*$
	$\gamma 1$	4.688			264.5	38.9	4.8	$n-\pi^*$
	$\gamma 2$	4.351			285	23.8	2.8	$n-\pi^*$
Ethanol Teo.	$\alpha 1$	6.984	177.54		177.8	11.7	3.1	H-2 \rightarrow L+1 (25%), H-1 \rightarrow L+3 (70%)
	$\alpha 2$	6.602	187.81	0.34	187.6	11.9	5.9	H-2 \rightarrow L (39%), H-1 \rightarrow L+1 (29%), H \rightarrow L+3 (22%)
	$\beta 1$	6.213	199.58	0.25	196.6	11.4	2.5	H-2 \rightarrow L (24%), H-1 \rightarrow L+1 (59%)
	$\beta 2$	5.890	210.51	0.64	209.4	17.9	19	H-1 \rightarrow L (30%), H \rightarrow L+1 (57%)
	γ	4.571	271.3	0.09	268.6	31.7	4.9	H \rightarrow L (90%)
Ethanol Exp.	α	6.064			204.5	20.5	10.4	$\pi-\pi^*$
	β	5.624			220.5	13.9	13.3	$\pi-\pi^*$
	$\gamma 1$	4.550			272.5	30.7	5.3	$n-\pi^*$
	$\gamma 2$	4.283			289.5	14.8	1.2	$n-\pi^*$

The calculated UV-Vis spectra (using ethanol and water solutions) which is fragmented into contributions from different transitions are plotted Figure 5. The experimental and theoretical absorption wavelengths (λ), excitation energies (E) determined with oscillator strength (f) and major contributions of counterparts from theory were listed in Table 3 for gas phase, water, and ethanol solvent. The peaks were located at 197.5, 219.5, 264.5 and 285.0 nm for water solution, and at 204.5, 220.5, 272.5 and 289.5 nm for ethanol solution, experimentally. After fitting procedure, the theoretical transitions are almost well agree based on the experimental results, so the major contributions noted are fully taken into account. The fitting of experimental data is also at acceptable level with R^2 values of 0.9881 and

0.9906 for the spectra taken in ethanol and water, respectively. This fitting operation applied is quite remarkable. In fact, some fitted peaks are located exactly at the same energy for both spectra.

An intuitive way of analyzing electronic properties of molecules is to investigate the population of states, partial contributions of fragmental sections in the molecule, and overlapping regions. The most important application of the DOS [60–62] plots is to demonstrate molecule orbital (MO) compositions and their contributions to chemical bonding through the OPDOS plots, which are also referred in the literature as Crystal Orbital Overlap Population (COOP) diagrams.

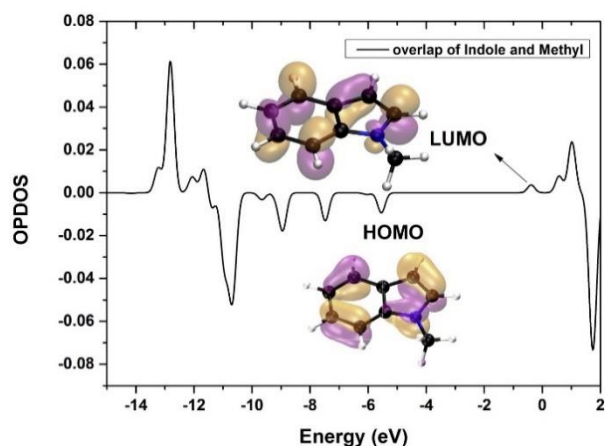


Figure 6. The OPDOS diagram of 1MI.

OPDOS is similar to DOS because it results from multiplying DOS by the overlap population. The OPDOS shows the bonding, anti-bonding, and nonbonding interaction of the two orbital's, atoms, or groups in a molecule. A positive value of the OPDOS indicates a bonding interaction, whereas negative value means an anti-bonding interaction, and zero value is for nonbonding interactions [63]. The OPDOS diagram for 1MI is shown in Figure 6 where the only overlapping between indole and methyl group is selected. Frontier occupied and virtual orbitals are shown in there. As can be seen from the OPDOS plot, a significant anti-bonding

character is observed in the HOMO and HOMO-1/-2/-3/-4/-5 molecular orbitals, and a bonding character in the LUMO and LUMO+1/+2/+3. This is a very nature of the covalently bonded systems where the population overlaps show negative character in low energy states below HOMO and positive character in high energies above LUMO and further. The overlap population value of the HOMO for indole with methyl is -0.0093 and LUMO value is 0.0036 . These values are relatively low compared to the fragmental interactions occur in molecules with electron donor/acceptor groups like carboxyl group [64]. Actually, this is an expected outcome if the molecular orbitals analyzed in terms of fractional contributions of each group. Fig. 7-a) shows the fragmental contributions to molecular orbitals, and Fig. 7-b) displays the combinations of fragmental orbitals of indole group and methyl group to create the molecular orbital. The indole orbitals play significant role in HOMO/-1/ and LUMO/+1 molecular orbital with 98/99 % and 99/95 % contributions, respectively. As for methyl orbitals, LUMO+2 orbital is localized with 30 % share as seen from Fig. 7-a). The HOMO orbital of the 1MI linked to indole's occupied frontier orbitals with 76% and 11% shares whereas no contributions from the occupied orbitals of the methyl group. On the other side, the LUMO orbital of 1MI accepts contributions from both groups. We infer that indole makes a larger contribution to the electron transfer in the ligand.

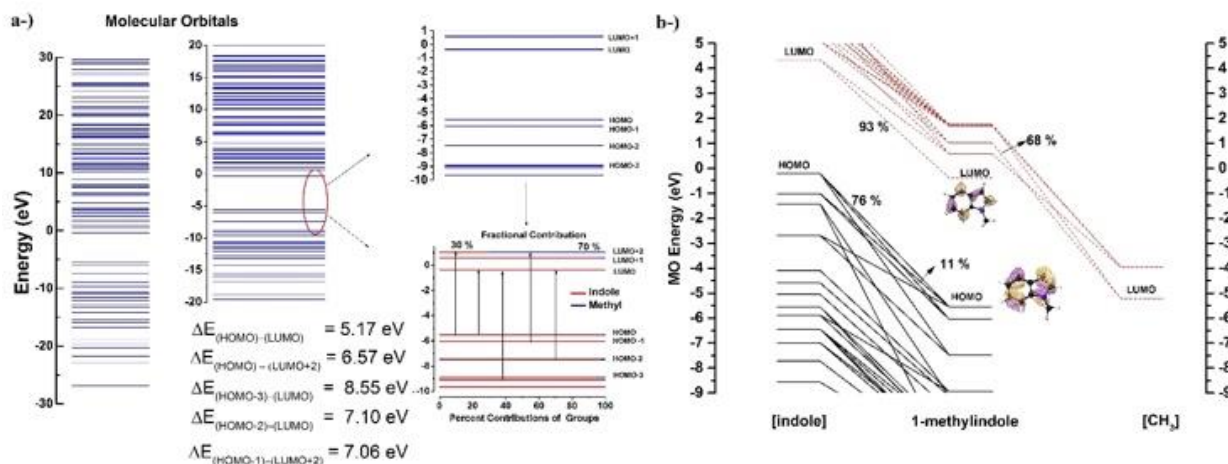


Figure 7. a) Molecular orbital energy levels of 1MI and fractional contributions from indole and methyl groups, b) Formation of frontier molecular orbitals of 1MI from fragmental combinations of indole and methyl groups.

The HOMO-LUMO energy is a critical parameter in determining molecular electrical transport properties because it is related to the electron conductivity [65]. The first most possible transition energies are also given in Fig 7-a) that ranges from 5.17 eV to 8.55 eV. Among these energy gaps, the $\Delta E_{(HOMO-LUMO)}$ is specifically important in determination of some physicochemical properties such as the order and the stability of molecular systems. The most prominent properties that can be calculated directly from the energy gaps are the chemical

potential (μ), electronegativity (χ), electrophilicity index (ω) and chemical hardness (η). These characteristic properties of 1MI in gas state and in water and ethanol solutions have been calculated using the formulas explained below and collated in Table S1 along with energies of molecular orbitals, energy gaps for first possible transitions.

The chemical hardness and the chemical potential are given by the following expression,

$$\delta_{\text{cal}} = 0.9692\delta_{\text{exp}} + 0.0362, R^2 = 0.9992 \quad (3.7)$$

$$\delta_{\text{cal}} = 0.9692\delta_{\text{exp}} + 0.0362, R^2 = 0.9992 \quad (3.8)$$

Where, I and H are ionization potential and electron affinity of a molecular system. Electrophilicity index (ω) which is a measure of the stabilization energy in terms of electronic chemical potential and the chemical hardness is calculated by the following expression,

$$\delta_{\text{cal}} = 0.9692\delta_{\text{exp}} + 0.0362, R^2 = 0.9992 \quad (3.9)$$

Finally, the electronegativity (χ) is given by

$$\delta_{\text{cal}} = 0.9692\delta_{\text{exp}} + 0.0362, R^2 = 0.9992 \quad (3.10)$$

These properties of the gas state are significantly different from that of solvents while they are nearly same for both solvents. This result is also consistent with the UV spectra being very similar in two solvents. Electron acceptance/donating properties for 1MI are found to be low in comparing to some other systems that contains other fractions rather than only methyl group [66].

Weak interactions in 1MI are only two kinds, either vdW or steric effects. The region marked by green-brown in Figure 3 b) can be identified as vdW interaction region

3.5. Nuclear Magnetic Resonance Spectral Analyses

The experimental ^{13}C and ^1H NMR spectra of 1MI in chloroform were given in Figure 8 and Figure 9 with assignments to the appropriate nuclei. The molecule has nine carbon atoms give rise to nine distinct NMR peaks, and nine protons showed in seven peaks because the protons on the methyl group are indistinguishable experimentally. In order to make a deeper explain of these observations, ^1H and ^{13}C NMR chemical shift values were calculated for the structure given in Figure 1 using a most widely used gauge including atomic orbital GIAO approach developed by Wolinski and Pulay [67] using the same method with the same level of theory used to optimize the structure. NMR calculations were performed for the gas state and chloroform solutions choosing IEFPCM for the solvent environment model. The isotropic chemical shifts, δ , values were calculated from the isotropic shielding values, σ , referencing to tetramethylsilane [TMS;(CH₃)₄Si] according to $\delta_{\text{iso}}^x = \sigma_{\text{iso}}^{\text{TMS}} - \sigma_{\text{iso}}^x$. The calculated and experimental ^{13}C and ^1H NMR chemical shifts values with determined assignments were collated in Table 4.

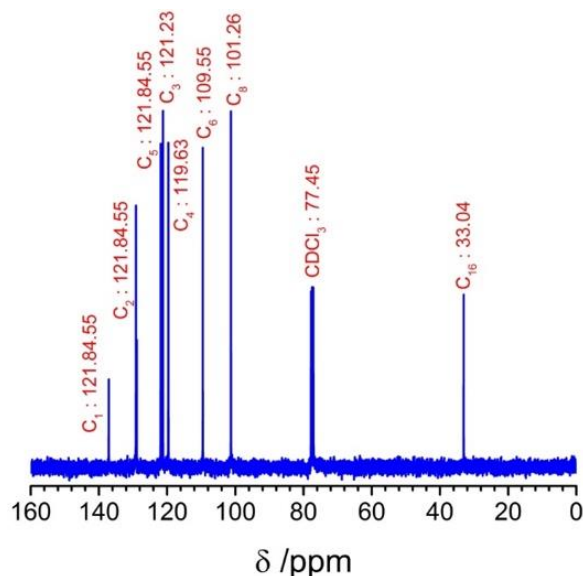


Figure 8. ^{13}C NMR spectra of the of 1MI molecule in CDCl_3 solution.

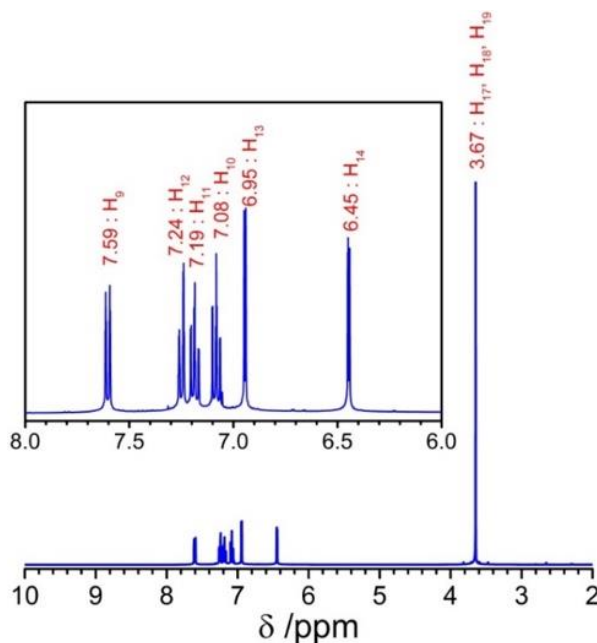


Figure 9. ^1H NMR spectra of the of 1MI molecule in CDCl_3 solution.

DFT calculations of the magnetic properties of 1MI give quite good results to compare experimental recordings with only one deficiency. The protons on the methyl group actually cannot be differentiated in experiments, however, the calculations provide two peaks for these three protons assuming only the H₁₇ and H₁₈ were the same and the H₁₉ differs from those. This is due to rigidity of the molecule in the calculations, which ignores the rotation of methyl group along its axes and breaking the symmetry during dynamic motion. Conformity of calculated results to experimental observations was analyzed and the correlation graphs in Figure S4 were created. ^{13}C and ^1H chemical shifts calculated in solution and in gas phase compared to the experimental values. In

all cases, the calculated shift values are slightly higher than observations, resulting in the slope of the linear fit to be lower than one. However, these deviations are not more than 1 ppm for the ^{13}C NMR and 0.1 ppm of the ^1H NMR calculated with the inclusion of solvent effect, as can be seen from the residual analysis at the top of each graph in Figure S4. These deviations doubles for the gas phase calculations despite seem to have the same trend in

curves. This shows that the solvent effect in NMR calculations must be included to obtain reliable supportive data.

Table 4. The experimental and calculated NMR chemical shifts (ppm) of 1MI.

^{13}C NMR	Calculated		Experimental
Atom Label	Gas	Chloroform	Chloroform
C16	32.7425	32.78	33.04
C8	104.505	103.08	101.26
C6	110.461	111.44	109.55
C4	123.230	122.63	119.63
C3	124.433	123.90	121.23
C5	124.790	124.27	121.84
C7	131.198	133.13	128.89
C2	134.230	133.78	129.13
C1	140.626	140.75	137.09
^1H NMR			
H19	3.4388	3.63	3.67
H18	3.6115	3.67	3.67
H17	3.6115	3.67	3.67
H14	6.4173	6.46	6.45
H13	6.7364	6.99	6.95
H10	7.1749	7.22	7.08
H11	7.1761	7.30	7.19
H12	7.2414	7.37	7.24
H9	7.6484	7.71	7.59

3.6. Nonlinear optical properties

Nonlinear optical (NLO) properties are substantial in terms of determination and classification of materials whether they are considerable as candidates in the applications where the light matter interactions violates linear superposition principle such as second harmonic generations, birefringent effects, and optical Kerr effect [68,69]. The most essential characteristics to investigate in this regard are the electronic dipole moment, μ , molecular polarizability, α , anisotropy of polarizability, $\Delta\alpha$, and molecular first hyperpolarizability, β , of the material. These properties can be calculated from the dipole moment μ_x, μ_y, μ_z , the polarizability $\alpha_{xx}, \alpha_{xy}, \alpha_{xz}, \alpha_{yy}, \alpha_{yz}, \alpha_{zz}$, and the first hyperpolarizability $\beta_{xxx}, \beta_{xxy}, \beta_{xyy}, \beta_{yyy}, \beta_{xxz}, \beta_{xyz}, \beta_{yyz}, \beta_{xzz}, \beta_{yzz}, \beta_{zyz}$ tensors obtained at the end of frequency job directly via equations 11-14

$$\mu = (\mu_x^2 + \mu_y^2 + \mu_z^2)^{\frac{1}{2}} \quad (3.11)$$

$$\alpha_0 = \frac{1}{3}(\alpha_{xx} + \alpha_{yy} + \alpha_{zz}) \quad (3.12)$$

$$\Delta\alpha = \frac{1}{\sqrt{2}} \left[(\alpha_{xx} - \alpha_{yy})^2 + (\alpha_{yy} - \alpha_{zz})^2 + (\alpha_{zz} - \alpha_{xx})^2 + 6\alpha_{xz}^2 + 6\alpha_{xy}^2 + 6\alpha_{yz}^2 \right]^{\frac{1}{2}} \quad (3.13)$$

$$\beta = \left[(\beta_{xxx} + \beta_{xyy} + \beta_{xzz})^2 + (\beta_{yyy} + \beta_{yzz} + \beta_{yxx})^2 + (\beta_{zzz} + \beta_{zxx} + \beta_{zyy})^2 \right]^{\frac{1}{2}} \quad (3.14)$$

The calculated values of the properties above for 1MI are tabulated in Table S2 and compared to that of urea as a limiting reference system for the materials to be considered as nonlinear optical in Table 5. A quick survey of the results shows that the title molecule has weak nonlinear optical properties; first hyperpolarizability of 1MI barely doubles that of urea, which is common for many organic compounds with any electron donor atom [55,59], and dipole moment of 1MI is even less than that of urea.

The average polarizability and the anisotropy of polarizability of IMI, on the other side, are reasonably high, nearly four times larger than that of urea. The highest contribution to the polarizability comes from the α_{xx} component. Because the molecular plane is located on the xy-plane and x-axis is along the two rings, polarizability being high in this direction is very natural due to high charge mobility through π -bonds. Polarizability on the y- and z- directions mostly results from the presence of the unpaired electrons on the nitrogen. As a results, IMI can be used as nonlinear optical material where the polarizability and anisotropy of polarizability are the main concerns rather than higher order properties.

Table 5. Comparison of optical properties of IMI with Urea.

Optical Properties	IMI	Urea	Ratio
$\beta = (\beta_x^2 + \beta_y^2 + \beta_z^2)^{1/2}$	1188.66	605.999	2.0
$\mu = (\mu_x^2 + \mu_y^2 + \mu_z^2)^{1/2}$	0.9643	1.4249	0.7
$\alpha_0 = (\alpha_{xx} + \alpha_{yy} + \alpha_{zz})/3$	15.1025	4.1496	3.6
$\Delta\alpha$	38.0410	8.8998	4.3

4. Conclusion

Geometrical structure, electronic transitional, vibrational, magnetic properties, and identifier characteristics of IMI were investigated experimentally and by DFT calculations. Theoretical results and experimental observations are found to be highly correlated. In this regard, UV-Vis and NMR calculations need to be done with the inclusion of solvent effect to produce more accurate and less dispersive data. Weak interactions in IMI are found to be only two kinds, either vdW or steric effects, and steric effects in rings in two sides of the molecule are quite different from each other. The vdW interactions play a role only in the region between methyl group and the nearest hydrogen of the benzene ring as visualized in both RDG analysis and ESP surface mapping. Vibrational properties of the molecule are in well agreement with the literature of similar compounds with only one difference; the vibrational modes that have contributions CN modes are highly complicated. Electronic transitional properties found to be nearly same for IMI dissolved in water or ethanol thus indicates that the IMI is not much under the influence of the solvent. IMI has some considerable nonlinear optical properties that can be taken into account in the applications involving the polarizability and anisotropy of polarizability

Ethics

There are no ethical issues after the publication of this manuscript.

Acknowledgement

The numerical calculations reported in this paper were fully/partially performed at TUBITAK ULAKBIM, High Performance and Grid Computing Center (TRUBA resources). The experiments in this paper were fully/partially performed at Manisa Celal Bayar University (TURKEY)- Applied Science and Research Center (DEFAM).

References

- [1]. Casapullo, A., Bifulco, G., Bruno, I., Riccio, R. New bisindole alkaloids of the topsentin and hamacanthin classes from the Mediterranean marine sponge *Rhaphisia lacazei*, 2000. *Journal of Natural Products*; 63: 447–451.
- [2]. Garbe, T.R., Kobayashi, M., Shimizu, N., Takesue, N., Ozawa, M., Yukawa, H. Indolyl Carboxylic Acids by Condensation of Indoles with α -Keto Acids, 2000. *Journal of Natural Products*; 63: 596–598.
- [3]. Vicente, R. Recent advances in indole syntheses: New routes for a classic target., 2011. *Organic & Biomolecular Chemistry*; 9: 6469–6480.
- [4]. Bao, B., Sun, Q., Yao, X., Hong, J., Lee, C.O., Sim, C.J., Im, K.S., Jung, J.H. Cytotoxic bisindole alkaloids from a marine sponge *Spongosorites* sp., 2005. *Journal of Natural Products*; 68: 711–715.
- [5]. Powell, B.J. 5,6-Dihydroxyindole-2-carboxylic acid: A first principles density functional study, 2005. *Chemical Physics Letters*; 402: 111–115.
- [6]. Powell, B.J., Baruah, T., Bernstein, N., Brake, K., McKenzie, R.H., Meredith, P., Pederson, M.R. A first-principles density-functional calculation of the electronic and vibrational structure of the key melanin monomers, 2004. *Journal of Chemical Physics*; 120: 8608–8615.
- [7]. Zhang, M.-Z., Mulholland, N., Beattie, D., Irwin, D., Gu, Y.-C., Chen, Q., Yang, G.-F., Clough, J. Synthesis and antifungal activity of 3-(1,3,4-oxadiazol-5-yl)-indoles and 3-(1,3,4-oxadiazol-5-yl)methyl-indoles, 2013. *European Journal of Medicinal Chemistry*; 63: 22–32.
- [8]. Xu, H., Wang, Q., Yang, W.-B. Antifungal activities of some indole derivatives., n.d. *Zeitschrift Fur Naturforschung. Teil C: Biochemie, Biophysik, Biologie, Virologie*; 65: 437–439.
- [9]. Da Silva, J.F.M., Garden, S.J., Pinto, A.C. The Chemistry of Isatins: A Review from 1975 to 1999, 2001. *Journal of the Brazilian Chemical Society*; 12: 273–324.
- [10]. Maj, J., Kołodziejczyk, K., Rogó, Z., Skuza, G. Roxindole, a potential antidepressant. I. Effect on the dopamine system, 1996. *Journal of Neural Transmission*; 103: 627–641.
- [11]. i Chen, Scott K. Spear, J.G.H. and R.D.R. Polyethylene glycol and solutions of polyethylene glycol as green reaction media, 2005. *Green Chemistry*; 7: 64.
- [12]. Smith, T.R., Sunshine, A., Stark, S.R., Littlefield, D.E., Spruill, S.E., Alexander, W.J. Sumatriptan and Naproxen Sodium for the Acute Treatment of Migraine, 2005. *Headache: The Journal of Head and Face Pain*; 45: 983–991.
- [13]. Budovská, M., Pilátová, M., Varinská, L., Mojžiš, J., Mezencev, R. The synthesis and anticancer activity of analogs of the indole phytoalexins brassinin, 1-methoxyspirobrassinol methyl ether and cyclobraassinin, 2013. *Bioorganic & Medicinal Chemistry*; 21: 6623–6633.
- [14]. Qin, X., Cui, X. Methyl-indole inhibits pancreatic cancer cell viability by down-regulating ZFX expression, 2020. *3 Biotech*; 10: 187.
- [15]. Billaud, D., Maarouf, E.B., Hannecart, E. Chemical oxidation and



- polymerization of indole, 1995. *Synthetic Metals*; 69: 571–572.
- [16]. Holze, R., Hamann, C.H. Electrosynthetic aspects of anodic reactions of anilines and indoles, 1991. *Tetrahedron*; 47: 737–746.
- [17]. Prakash, P.C.P.; R. Electrochemical Synthesis of Polyindole and Its Evaluation for Rechargeable Battery Applications, 1998. *Journal of The Electrochemical Society*; 145: 999–1003.
- [18]. Tourillon, G., Garnier, F. New electrochemically generated organic conducting polymers, 1982. *Journal of Electroanalytical Chemistry and Interfacial Electrochemistry*; 135: 173–178.
- [19]. Roychowdhury, P., Basak, B.S. The crystal structure of indole, 1975. *Acta Crystallographica Section B Structural Crystallography and Crystal Chemistry*; 31: 1559–1563.
- [20]. Catalán, J., de Paz, J.G. The molecular geometry of indole, 1997. *Journal of Molecular Structure: THEOCHEM*; 401: 189–192.
- [21]. Lin, J.L., Tzeng, W.B. Mass analyzed threshold ionization spectroscopy of 1-methylindole cation, 2003. *Chemical Physics Letters*; 377: 620–626.
- [22]. Karaca, C., Bardak, F., Kose, E., Atac, A. A comprehensive study on the effect of substitution position and solvent effect on absorption and emission characteristics of n-methylindoles via linear response and State-Specific formalisms, 2024. *Journal of Photochemistry and Photobiology A: Chemistry*; 450: 115469.
- [23]. Mourik, T. Van, Price, S.L., Clary, D.C. Ab initio calculations on indole–water, 1-methylindole–water and indole–(water)₂, 2000. *Chemical Physics Letters*; 331: 253–261.
- [24]. Muñoz, M. a., Carmona, C., Balón, M. FTIR and fluorescence studies on the ground and excited state hydrogen-bonding interactions between 1-methylindole and water in water–triethylamine mixtures, 2007. *Chemical Physics*; 335: 43–48.
- [25]. Muñoz, M.A., Galán, M., Carmona, C., Balón, M. Hydrogen-bonding interactions between 1-methylindole and alcohols, 2005. *Chemical Physics Letters*; 401: 109–114.
- [26]. Mons, M., Dimicoli, I., Tardivel, B., Piuze, F., Brenner, V., Millié, P. Site Dependence of the Binding Energy of Water to Indole: Microscopic Approach to the Side Chain Hydration of Tryptophan, 1999. *The Journal of Physical Chemistry A*; 103: 9958–9965.
- [27]. Karaca, C., Bardak, F., Kose, E., Atac, A. A comprehensive study on the effect of substitution position and solvent effect on absorption and emission characteristics of n-methylindoles via linear response and State-Specific formalisms, 2024. *Journal of Photochemistry and Photobiology A: Chemistry*; 450: 115469.
- [28]. Frisch, M.J., Trucks, G.W., Schlegel, H.B., Scuseria, G.E., Robb, M.A., Cheeseman, J.R., Scalmani, G., Barone, V., Mennucci, B., Petersson, G.A., Nakatsuji, H., Caricato, M., Li, X., Hratchian, H.P., Izmaylov, A.F., Bloino, J., Zheng, G., Sonnenberg, J.L., Hada, M., Ehara, M., Toyota, K., Fukuda, R., Hasegawa, J., Ishida, M., Nakajima, T., Honda, Y., Kitao, O., Nakai, H., Vreven, T., Montgomery Jr., J.A., Peralta, J.E., Ogliaro, F., Bearpark, M., Heyd, J.J., Brothers, E., Kudin, K.N., Staroverov, V.N., Kobayashi, R., Normand, J., Raghavachari, K., Rendell, A., Burant, J.C., Iyengar, S.S., Tomasi, J., Cossi, M., Rega, N., Millam, J.M., Klene, M., Knox, J.E., Cross, J.B., Bakken, V., Adamo, C., Jaramillo, J., Gomperts, R., Stratmann, R.E., Yazyev, O., Austin, A.J., Cammi, R., Pomelli, C., Ochterski, J.W., Martin, R.L., Morokuma, K., Zakrzewski, V.G., Voth, G.A., Salvador, P., Dannenberg, J.J., Dapprich, S., Daniels, A.D., Farkas, O., Foresman, J.B., Ortiz, J. V., Cioslowski, J., Fox, D.J., Gaussian 16 Revision A.03 (Gaussian, Inc., Wallingford CT,). Gaussian 16 Revision A.03, 2016.
- [29]. Perdew, J.P., Wang, Y. Accurate and simple analytic representation of the electron-gas correlation energy, 1992. *Physical Review B*; 45: 13244–13249.
- [30]. Lee, C., Yang, W., Parr, R.G. Development of the Colle-Salvetti correlation-energy formula into a functional of the electron density, 1988. *Physical Review B*; 37: 785–789.
- [31]. Becke, A.D. Density-functional thermochemistry.III. The role of exact exchange, 1993. *The Journal of Chemical Physics*; 98: 5648–5652.
- [32]. Sundaraganesan, N., Ilakiamani, S., Saleem, H., Wojciechowski, P.M., Michalska, D. FT-Raman and FT-IR spectra, vibrational assignments and density functional studies of 5-bromo-2-nitropyridine., 2005. *Spectrochimica Acta. Part A, Molecular and Biomolecular Spectroscopy*; 61: 2995–3001.
- [33]. Baker, J., Jarzecki, A.A., Pulay, P. Direct scaling of primitive valence force constants: An alternative approach to scaled quantum mechanical force fields, 1998. *Journal of Physical Chemistry A*; 102: 1412–1424.
- [34]. Dennington, R., Keith, T.A., Millam, J.M. GaussView Version 6, 2016.
- [35]. O’Boyle, N.M., Tenderholt, A.L., Langner, K.M. Software News and Updates cclib : A Library for Package-Independent Computational Chemistry Algorithms, 2008. *Journal of Computational Chemistry*; 29: 839–845.
- [36]. Bader, R. Atoms in Molecules: A Quantum Theory, Oxford University Press, Oxford (UK), 1994.
- [37]. Mayer, I. Improved definition of bond orders for correlated wave functions, 2012. *Chemical Physics Letters*; 544: 83–86.
- [38]. Mayer, I. Bond order and valence indices: A personal account, 2007. *Journal of Computational Chemistry*; 28: 204–221.
- [39]. Lu, T., Chen, F. Quantitative analysis of molecular surface based on improved Marching Tetrahedra algorithm, 2012. *Journal of Molecular Graphics and Modelling*; 38: 314–323.
- [40]. Lu, T., Chen, F. Multiwfn: A multifunctional wavefunction analyzer, 2012. *Journal of Computational Chemistry*; 33: 580–592.
- [41]. Karaca, C., Atac, A., Karabacak, M. Conformational analysis, spectroscopic study (FT-IR, FT-Raman, UV, ¹H and ¹³C NMR), molecular orbital energy and NLO properties of 5-iodosalicylic acid, 2015. *Spectrochimica Acta Part A: Molecular and Biomolecular Spectroscopy*; 136: 295–305.
- [42]. Gorelsky, S.I. Complexes with a single metal-metal bond as a sensitive probe of quality of exchange-correlation functionals, 2012. *Journal of Chemical Theory and Computation*; 8: 908–914.
- [43]. Johnson, E.R., Keinan, S., Mori-Sánchez, P., Contreras-García, J., Cohen, A.J., Yang, W. Revealing noncovalent interactions., 2010. *Journal of the American Chemical Society*; 132: 6498–506.
- [44]. Runge, E., Gross, E.K.U. Density-Functional Theory for Time-Dependent Systems, 1984. *Physical Review Letters*; 52: 997–1000.
- [45]. Humphrey, W., Dalke, A., Schulten, K. VMD: Visual molecular dynamics, 1996. *Journal of Molecular Graphics*; 14: 33–38.
- [46]. Atac, A., Karaca, C., Gunnaz, S., Karabacak, M. Vibrational (FT-IR and FT-Raman), electronic (UV–Vis), NMR (¹H and ¹³C) spectra and reactivity analyses of 4,5-dimethyl-o-phenylenediamine, 2014. *Spectrochimica Acta Part A: Molecular and Biomolecular Spectroscopy*; 130: 516–525.
- [47]. Socrates, G. Infrared and Raman Characteristic Group Frequencies: Tables and Charts, John Wiley & Sons Ltd., West Sussex, England, 2001.
- [48]. Collier, W., Klots, T. Heteroatom derivatives of indene. Part 1. Vibrational frequencies and a refined scaled overlay of the AM1 force field of indole, benzofuran benzothiophene, benzoxazole and benzothiazole, 1995. *Spectrochimica Acta Part A: Molecular and Biomolecular Spectroscopy*; 51: 1255–1272.
- [49]. Klots, T., Collier, W. Heteroatom derivatives of indene Part 3. Vibrational spectra of benzoxazole, benzofuran, and indole, 1995. *Spectrochimica Acta Part A: Molecular and Biomolecular Spectroscopy*; 51: 1291–1316.



- [50]. Silverstein, R.M., Webster, F.X., Kiemle, D.J. Spectrometric identification of organic compounds, John Wiley & Sons, 2005.
- [51]. Kalsi, P.S. Spectroscopy of Organic Compounds, Wiley Eastern Limited, New Delhi, 1995.
- [52]. Jeyavijayan, S., Arivazhagan, M. Study of density functional theory and vibrational spectra of hypoxanthine, 2010. *Indian Journal of Pure and Applied Physics*; 48: 869–874.
- [53]. Sundaraganesan, N., Joshua, B.D. Vibrational spectra and fundamental structural assignments from HF and DFT calculations of methyl benzoate., 2007. *Spectrochimica Acta. Part A, Molecular and Biomolecular Spectroscopy*; 68: 771–7.
- [54]. Ramalingam, S., Jayaprakash, a, Mohan, S., Karabacak, M. Vibrational investigation on FT-IR and FT-Raman spectra, IR intensity, Raman activity, peak resemblance, ideal estimation, standard deviation of computed frequencies analyses and electronic structure on 3-methyl-1,2-butadiene using HF and DFT (LSDA/B3LYP/, 2011. *Spectrochimica Acta. Part A, Molecular and Biomolecular Spectroscopy*; 82: 79–90.
- [55]. Kose, E., Atac, A., Bardak, F. The structural and spectroscopic investigation of 2-chloro-3-methylquinoline by DFT method and UV–Vis, NMR and vibrational spectral techniques combined with molecular docking analysis, 2018. *Journal of Molecular Structure*; 1163: 147–160.
- [56]. Silverstein, Robert M., Bassler, G. Clayton, Morrill, T.C. Spectrometric Identification of Organic Compounds, Wiley, New York, 1981.
- [57]. Varsányi, G., Kovner, M.A., Láng, L. Assignments for Vibrational Spectra of 700 Benzene Derivatives, 1973.
- [58]. Guillaumont, D., Nakamura, S. Calculation of the absorption wavelength of dyes using time-dependent density-functional theory (TD-DFT), 2000. *Dyes and Pigments*; 46: 85–92.
- [59]. Bardak, F., Karaca, C., Bilgili, S., Atac, A., Mavis, T., Asiri, A.M., Karabacak, M., Kose, E. Conformational, electronic, and spectroscopic characterization of isophthalic acid (monomer and dimer structures) experimentally and by DFT., 2016. *Spectrochimica Acta Part A: Molecular and Biomolecular Spectroscopy*; 165: 33–46.
- [60]. Hoffman, R. Solids and surfaces: a chemist's view of bonding in extended structures, 1988.
- [61]. Hughbanks, T., Hoffmann, R. Chains of trans-edge-sharing molybdenum octahedra: metal-metal bonding in extended systems, 1983. *Journal of the American Chemical Society*; 105: 3528–3537.
- [62]. Małecki, J.G. Synthesis, crystal, molecular and electronic structures of thiocyanate ruthenium complexes with pyridine and its derivatives as ligands, 2010. *Polyhedron*; 29: 1973–1979.
- [63]. Chen, M., Waghmare, U. V., Friend, C.M., Kaxiras, E. A density functional study of clean and hydrogen-covered α -MoO₃(010): Electronic structure and surface relaxation, 1998. *The Journal of Chemical Physics*; 109: 6854–6860.
- [64]. Babur Saş, E., Kurt, M., Can, M., Okur, S., İçli, S., Demic, S. Structural investigation of a self-assembled monolayer material 5-[(3-methylphenyl) (phenyl) amino] isophthalic acid for organic light-emitting devices, 2014. *Spectrochimica Acta Part A: Molecular and Biomolecular Spectroscopy*; 133: 307–317.
- [65]. Fukui, K. Role of frontier orbitals in chemical reactions., 1982. *Science (New York, N.Y.)*; 218: 747–754.
- [66]. Jayavarathanan, T., Sundaraganesan, N., Karabacak, M., Cinar, M., Kurt, M. Vibrational spectra, UV and NMR, first order hyperpolarizability and HOMO-LUMO analysis of 2-amino-4-chloro-6-methylpyrimidine, 2012. *Spectrochimica Acta - Part A: Molecular and Biomolecular Spectroscopy*; 97: 811–824.
- [67]. Wolinski, K., Hinton, J.F., Pulay, P. Efficient implementation of the gauge-independent atomic orbital method for NMR chemical shift calculations, 1990. *Journal of the American Chemical Society*; 112: 8251–8260.
- [68]. Sajan, D., Devi, T.U., Safakath, K., Philip, R., Némec, I., Karabacak, M. Ultrafast optical nonlinearity, electronic absorption, vibrational spectra and solvent effect studies of ninhydrin, 2013. *Spectrochimica Acta - Part A: Molecular and Biomolecular Spectroscopy*; 109: 331–343.
- [69]. Cho, M., Fleming, G.R., Mukamel, S. Nonlinear response functions for birefringence and dichroism measurements in condensed phases, 1993. *The Journal of Chemical Physics*; 98: 5314–5326.

Transforming University Life with Virtual Reality: Campus 2.0 – MetaCBU

Barıř ukurbaşı¹ , Ali Geriř^{2*} , Orkun Teke³ , Murat Kılın⁴ 

¹ Manisa Celal Bayar University, Manisa Technical Sciences Vocational School, Department of Computer Technologies, Manisa, Trkiye

² Manisa Celal Bayar University, Faculty of Education, Department of Computer Education & Instructional Technologies, Manisa, Trkiye

³ Manisa Celal Bayar University, Manisa Technical Sciences Vocational School, Department of Electric and Energy, Manisa, Trkiye

⁴ Karadeniz Technical University, Faculty of Economics and Administrative Sciences, Department of Management Information Systems, Trabzon, Trkiye

* ali.geris@cbu.edu.tr

* Orcid No: 0000-0003-2136-5490

Received: August 25, 2024

Accepted: December 9, 2024

DOI: 10.18466/cbayarfbe.1538384

Abstract

This study investigates the transformative potential of Virtual Reality (VR) and Extended Reality (XR) technologies in education, with a particular focus on the design and implementation of the MetaCBU virtual campus at Manisa Celal Bayar University. The primary research objectives are to examine how immersive VR platforms can enhance traditional educational methods by increasing student engagement, motivation, and collaboration, and to identify the technical and pedagogical challenges involved in their development. MetaCBU leverages advanced VR technologies to replicate and extend the capabilities of physical campuses, providing experiential learning opportunities that are otherwise difficult to achieve in conventional classrooms. Key challenges, such as optimizing system performance to mitigate issues like motion sickness and latency, were addressed using advanced rendering techniques, efficient server management, and iterative testing. The findings demonstrate that MetaCBU successfully integrates academic and social functionalities into a single platform, offering students a more interactive and engaging educational experience. The broader implications of this research suggest that VR and XR technologies are poised to revolutionize not only teaching methods but also the operational structures of educational institutions. Future studies are encouraged to explore the scalability of such platforms and their applications across diverse educational contexts and disciplines, ensuring that universities remain at the forefront of digital transformation. By addressing both technical and pedagogical dimensions, this study provides a comprehensive framework for the continued integration of VR in higher education.

Keywords: Artificial intelligence, Extended reality, Metaverse, Virtual classroom, Virtual reality.

1. Introduction

The rapid advancement of Virtual Reality (VR) and Extended Reality (XR) technologies has instigated a significant transformation in the development of virtual platforms, particularly within higher education. These technologies offer immersive and interactive environments that transcend the traditional boundaries of physical spaces, creating new opportunities for academic institutions to enhance both learning and operational processes. The COVID-19 pandemic further accelerated the adoption of digital transformation strategies,

compelling universities to explore innovative virtual solutions to maintain and improve educational delivery and campus experiences [1].

Unlike other digital transformation approaches, VR provides a unique value by combining interactivity, immersion, and personalization. This positions VR as an unparalleled tool for fostering student engagement, creativity, and collaboration. Studies in Environmental Design Education (EDE) have highlighted how VR enables students to engage with complex design concepts in ways that conventional methods cannot, fostering

problem-solving skills and enhancing experiential learning [2]. Similarly, in industrial operations, VR applications have demonstrated significant benefits in improving safety and operational efficiency, though these implementations also underscore the technical and organizational challenges of scaling such technologies [3].

A central challenge in implementing VR-based platforms in a university setting is the technical complexity involved in creating a scalable, multi-user environment that accurately replicates and enhances the physical campus. The design and development of such platforms require a meticulous integration of diverse software and hardware components to ensure high performance, user accessibility, and seamless interaction. This study focuses on the development of the MetaCBU virtual campus, a VR-based platform engineered to transform the traditional university experience by integrating cutting-edge VR technologies with academic and social functionalities. By leveraging advanced rendering techniques and robust server management, MetaCBU addresses common VR issues such as motion sickness and latency, creating an immersive and user-friendly experience.

The digital transformation of university environments through VR is not merely a conceptual exploration but a practical necessity, as evidenced by recent studies. While traditional online learning platforms often struggle to maintain engagement, VR offers unparalleled experiential opportunities that replicate and surpass physical classroom experiences. For example, VR has been shown to enhance deep learning and retention rates by creating interactive, multi-sensory environments that engage students in active learning [4].

MetaCBU exemplifies a comprehensive effort to address these challenges by creating a virtual campus that goes beyond merely replicating the physical university environment. The platform is designed to support a wide range of academic and extracurricular activities, from virtual classrooms to social spaces, thereby offering a holistic virtual campus experience. This study delves into the design and development process of MetaCBU, examining its potential to transform educational practices and how it addresses key challenges such as engagement, scalability, and accessibility. Furthermore, the innovative teaching strategies and collaborative learning opportunities provided by MetaCBU are explored in depth, positioning the platform as a model for future VR and XR applications in education.

The primary objective of this study is to comprehensively examine the potential applications of VR and XR technologies in education, with a particular focus on the virtual campus "MetaCBU" at Manisa Celal Bayar University. MetaCBU is designed as a multi-user learning environment based on VR and XR technologies.

This study details the design and development process of MetaCBU and investigates how such a virtual campus can transform educational processes and what advantages it offers compared to traditional educational methods. Additionally, the study explores how the innovative teaching strategies, user interactions, and collaborative learning experiences provided by MetaCBU could shape future trends in VR and XR applications in education. In this context, the potential of MetaCBU to revolutionize the field of education and its applicability across various disciplines, including engineering, health sciences, physics, chemistry, and information technology, is thoroughly examined.

By addressing the technical challenges associated with creating a comprehensive and scalable VR platform, MetaCBU not only replicates but also enhances the traditional university experience. This study contributes to the growing body of literature on the digital transformation of higher education, offering insights into the design, development, and implementation of VR platforms that can serve as a blueprint for future initiatives in this field.

2. Theoretical Framework

2.1. Virtual Reality

VR technology offers diverse applications that enable tracking of users' movements, thereby providing an immersive experience that significantly enhances user engagement [5]. As a rapidly emerging medium, VR and immersive technologies possess the potential to convey ideas and concepts in innovative ways [6]. The increasing sophistication of head-mounted display technologies is continually improving the perception of reality and seamlessly integrating virtual worlds into real life. VR is poised to revolutionize user interaction, paving the way for groundbreaking applications across various fields [6].

Recent studies have further emphasized the transformative role of VR in education, particularly in health sciences. For example, Kouame et al. [7] demonstrated that VR can be effectively utilized to provide immersive learning experiences in health sciences education, offering a unique opportunity for students to engage in experiential learning environments that traditional methods cannot replicate. This finding aligns with the broader trend of integrating VR into various educational domains, as reported by Zhao et al. [8] who highlighted that VR technologies are increasingly being adopted across diverse fields such as medicine, engineering, and the arts. The growing interest in VR's potential to enhance educational outcomes underscores the importance of continuous research and innovation in this area.

Given the ability of VR environments to effectively disengage users from their immediate reality, there has

been growing scholarly interest in exploring the potential of this technology. Educational researchers have been investigating the transformative potential of VR technologies, highlighting them as cutting-edge tools for effective training and education [9, 10]. Moreover, Mc Dermott et al. [11] pointed out that immersive technologies, including VR, are not only enhancing the student experience but also addressing the challenges associated with traditional learning environments. As VR continues to evolve, it is expected to play a crucial role in shaping the future of education by providing more engaging, interactive, and effective learning experiences.

2.2. Benefits of VR

With the progress of human-computer interaction technologies, VR has been integrated into various fields, leading to the future of educational processes [12]. VR technology offers an effective method to reduce training time, minimize or prevent errors in the application process, and improve product quality [13]. The interaction, immersion, and imagination feature it provides have led to the creation of virtual environments to overcome the limitations of traditional educational processes [12]. The high level of interest in immersive VR technologies for educational purposes and the wide range of fields that incorporate VR into teaching processes support this situation [14]. For instance, virtual assembly activities have emerged as the primary application of VR technology in industrial production and manufacturing sectors [12]. On the other hand, using VR technology is suggested to improve students' collaboration and communication skills [14]. In fact, many researchers have presented cases that highlight the benefits of using VR in education. Some of these benefits are summarized below:

- VR supports peer cooperative learning [8, 14].
- VR fosters the development of learners' problem-solving abilities and the discovery of new concepts [15-18].
- VR significantly increases student motivation [19, 20].
- VR offers a high level of interaction [21, 22].
- VR enables learners to acquire knowledge with less effort compared to traditional learning environments [11, 23].
- VR makes teaching processes more realistic and secure [24].
- VR enhances the quality of education in engineering fields by providing students with intuitive, multi-sensory experiences that improve deep learning and application processes [25].
- VR offers potential for innovative applications in architecture and urban design education, enabling students to engage with design concepts in a virtual, interactive space [26].

- VR provides immersive experiential learning opportunities in health sciences, allowing students to practice and master skills in a safe and controlled virtual environment [7, 27].
- VR provides innovative assessment tools by enabling automated analysis of student-created content, allowing educators to evaluate learning outcomes with greater precision and efficiency [28].

In addition to these benefits, Geriş et al. [23] highlight that VR environments, when optimized for performance and comfort, can significantly enhance the overall educational experience. Their study emphasizes the importance of maintaining high frames per second (FPS) and low latency to minimize discomfort such as motion sickness, thereby improving user engagement and learning outcomes. The research also points out that optimizing batch processing and rendering techniques within VR can lead to more immersive and seamless experiences, which are crucial for maintaining student attention and fostering an effective learning environment. As VR technology continues to evolve, these technical optimizations are essential to fully realizing its educational potential.

2.3. Next Generation of VR

VR is an innovative technology that offers exceptional opportunities for science education by immersing students in a virtual world where students can engage directly with scientific phenomena [5]. Embodied VR devices intensify sensory stimulation, which in turn directly affects affective and behavioral responses [29]. However, it has been observed that in the development of VR applications in higher education, learning theories are often overlooked, and the evaluation of educational VR applications tends to focus mainly on their usability while the incorporation of VR-based learning activities into the curriculum is not adequately explained [14]. Furthermore, it is recommended that the issues pertinent to virtual reality technologies be taken into consideration, especially in educational settings [30].

In more recent developments, the integration of 360-degree learning environments and telepresence capabilities, supported by emerging 6G networks, represents the cutting-edge of educational technology. These innovations allow students to explore remote locations and complex environments as if they were physically present, significantly enhancing the realism and engagement of virtual learning [31]. Zhao et al. [8] further emphasize that the growing adoption of VR and AR across multiple disciplines, including education, medicine, and engineering, is revolutionizing the way educational content is delivered and experienced.

Recent advancements in XR technologies, encompassing XR, Augmented Reality (AR), and Mixed Reality (MR),

are shaping the future landscape of education. These technologies collectively push the boundaries of traditional learning environments by merging elements of real and virtual worlds. XR technologies, which began with foundational VR platforms, have now expanded to include AR—overlying digital content onto the physical world—and MR, which interactively merges real and virtual objects [32]. As these technologies evolved, their application in education has also grown, offering more immersive and interactive learning experiences [33]. Moreover, the integration of machine learning (ML) and business intelligence (BI) techniques into VR systems has provided new dimensions for data-driven educational experiences. By analyzing vast amounts of data generated within virtual environments, such as in the MetaPortal application developed at Manisa Celal Bayar University, these tools enable more personalized and effective educational interventions [34]. Similar approaches have been explored in other contexts, demonstrating how AI and ML can optimize VR experiences by enhancing user interactions and learning outcomes [35, 36].

3. Method

3.1. Design and Development Process

The development of the MetaCBU virtual campus follows a specific set of procedural steps, which are organized in a cyclical and iterative flowchart. Furthermore, the platform is continuously refined through multiple rounds of testing and expert feedback. A graphical representation of the MetaCBU virtual campus development process shown in Figure 1.

During the implementation of the MetaCBU project according to the phases depicted in Figure 1, an advanced hardware infrastructure was employed. The graphical processing unit (GPU) of the computer system used played a crucial role in this infrastructure, while the central processing unit (CPU) power also proved to be significant. Furthermore, various types of virtual reality headsets were employed to ensure platform integration. The hardware infrastructure utilized during the study is outlined below. However, it should be noted that it showcases the features required for the optimal design and development of a virtual reality-based system, rather than the features necessary to experience the platform:

- Computer: Intel i7 12700 CPU, 32GB RAM, NVIDIA RTX 3080 12GB GPU, 1TB SSD.
- Oculus/Meta Quest 2: Qualcomm Snapdragon XR2 Platform, Single Fast-Switch LCD 1832×1920 px per eye, 72Hz (default), 6GB RAM.
- Oculus/Meta Quest 3:
- HTC Vive Pro: 1440 x 1600 px per eye, 90Hz (default), 110 degrees view, Dual OLED 3.5" diagonal panel.

- HTC Vive XR Elite: Qualcomm Snapdragon XR2 Platform, LCD RGB 1920×1920 px per eye, 90Hz (default), 110 degrees view, 12GB RAM.
- Pico 4: Qualcomm Snapdragon XR2 Platform, LCD Pancake lenses 2160×2160 px per eye, 90Hz (default), 105 degrees view, 8GB RAM.

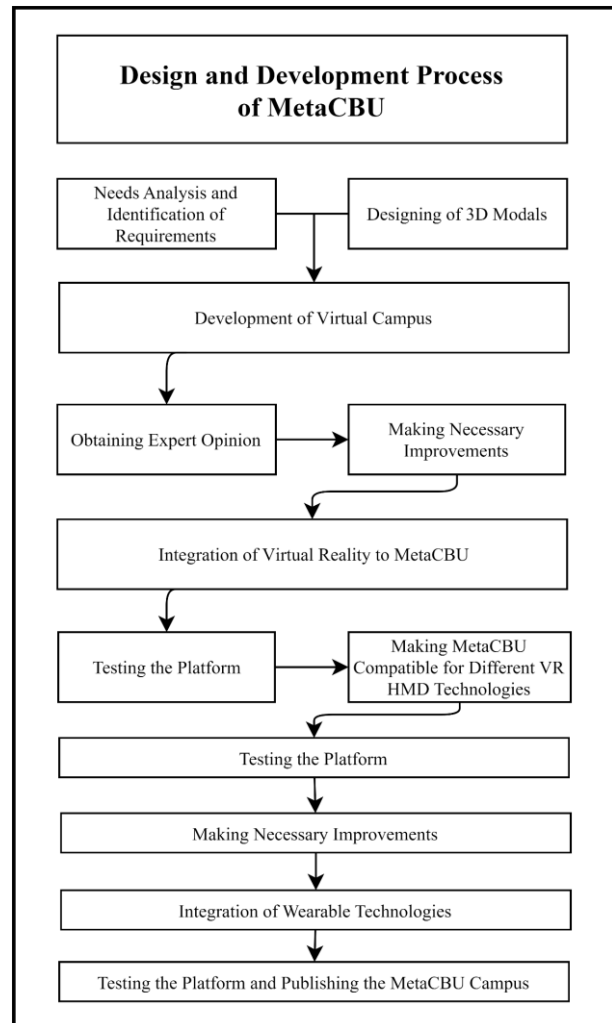


Figure 1. Design And Development Process of MetaCBU

In the fourth and fifth sections of this study, the technical infrastructure, and visual characteristics of the MetaCBU virtual campus are elaborated upon. The Visual Structure section encompasses a detailed description of the campus's visual properties, modeling techniques, and examples of screenshots taken from within the campus. On the other hand, the Technical Infrastructure section outlines the software, plugins, libraries, assets, and server information that were utilized during the development process of the virtual campus.

3.2. Visual Structure

The MetaCBU virtual campus was developed using the MetaCBU Unity Game Engine, while three-dimensional models integrated into the campus were created using programs such as Blender, Solidworks, and 3DSMax. Prior to the development of the virtual campus, a storyboard outlining the general structure of the campus was prepared during the needs analysis phase, and the design process was conducted accordingly. The virtual campus was designed to include various structures, such as academic units, classrooms, social areas, clinic, library, sports fields, and a conference center. The design process of these structures has been completed, and an overview of the general structure of the virtual campus can be seen in Figure 2.

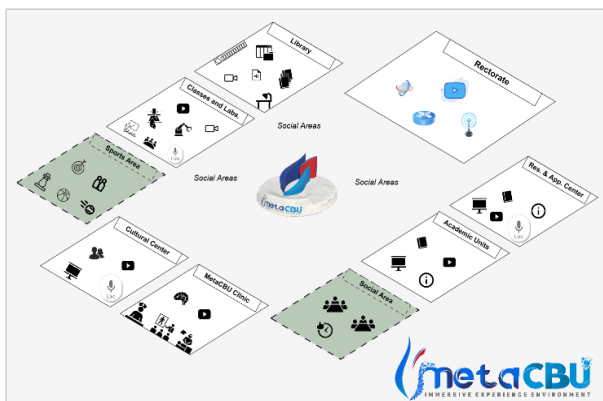


Figure 2. MetaCBU General Structure

The MetaCBU virtual campus serves as a convergence point for a multitude of university departments and systems. Among its many features are a central building which houses promotional units, classrooms, academic units, a library, social areas, a conference center, sports fields, and a clinic. The virtual campus is designed to be as authentic and realistic as possible, featuring a detailed, unit-based organization.



Figure 3. MetaCBU Library

Both live and pre-existing lectures can be accessed within the academic units and classrooms of the MetaCBU campus, with a plethora of educational materials will be integrated into the platform through 360-degree videos

potentially. The library represents a critical component of the platform, where users can physically engage with books and enjoy unrestricted access to their contents in a database and cloud storage unit. This allows users to read PDFs of desired books while on the MetaCBU platform (Figure 3).



Figure 4. MetaCBU Screenshots

The MetaCBU campus has been designed to provide educational environments for a variety of academic units. One of the most significant components is the MetaCBU Clinic, which has been specifically developed for the field of health education. This feature includes a dedicated section for medical educators and students, allowing them to interact with various objects and incorporate different learning materials. The system also integrates models of various medical devices, instruments, organs, and non-living mannequins. In addition to academic units, areas that promote socialization and physical activity have been incorporated into the system. Examples of such areas include a chess playground, a conference center, and a basketball court. The accompanying visuals of these features are presented in Figure 4.

3.3. Technical Structure

The MetaCBU virtual campus is designed to be used in both virtual reality head-mounted displays and desktop mode. MetaCBU has been configured to work with Oculus, HTC, and Pico virtual reality glasses. In this process, the platform integrates several packages, including Oculus, SteamVR, OpenVR, Unity XR, and VRTK. Furthermore, MetaCBU has been optimized to work with numerous desktop computers. Additionally, the platform includes a multiplayer feature, allowing users to see what other participants are doing, communicate with them, or interact with them. To enhance the participants' sense of presence and integration into the environment, a realistic full-body avatar system has been integrated into the platform. This integration is achieved using the Ready Player Me avatar system and libraries, with Final IK and Unity Body System packages used to control the avatars and their skeletal systems.

MetaCBU also incorporates a structure that allows participants to interact with many objects. To achieve this, numerous code libraries and packages have been utilized, particularly in facilitating interaction processes in the sports field, social areas, educational materials, and library. Packages such as Unity Interaction, Oculus, Tilia, and Zinnia have been integrated into the platform to provide various types of interaction. As a result, a multi-layered structure has been developed to support diverse interaction types. The technical structure of the MetaCBU platform is presented in Table 1.

Table 1. Technical Structure of MetaCBU

Specification	Package
Game Engine	Unity
Server	Photon, Photon Voice, Pun 2
VR / XR	Oculus, SteamVR, OpenVR, Unity XR, VRTK
Optimized HMD's	Oculus/Meta Quest 2, Oculus/Meta Quest 3, HTC VIVE Pro, HTC VIVE XR Elite, Pico 4
Interaction	Unity Interaction, SteamVR, Tilia & Zinnia, Unity XR
Avatar System	Ready Player Me
Avatar Controls	Final IK, Unity Body System
Modeling Tools	Blender, Solidworks, 3DS Max
Graphic Tools	Adobe Photoshop, Adobe Illustrator

During the development of the MetaCBU platform, careful consideration was given to the quality of the 3D models utilized and their impact on the system. To maximize the positive effects of the virtual reality environment on the participants, it is crucial to maintain an optimum Frame Per Second (FPS) value. Therefore, optimizing the processor latency and polygon values in the 3D models is essential for maintaining the desired FPS level. Special attention was paid to the polygon numbers of the 3D models used in the platform, and care was taken to ensure that they were developed and integrated into the platform without creating an excessive load on the system.

Various server structures were employed to enable multiplayer use of the MetaCBU platform, user registration, data collection, and interaction between users. Photon Server (S1), depicted in Figure 5, was used

for the processes of registration, login, and inclusion of users in the MetaCBU campus. The platform's integration with the first server was achieved using Photon and Pun 2 infrastructure. All users included in the MetaCBU campus connect to this server, regardless of whether they are using a desktop or HMD. Server 1 facilitates multiplayer interaction within the virtual environment.

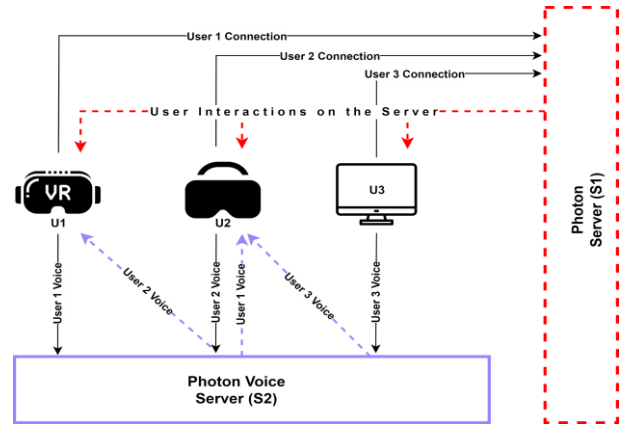


Figure 5. MetaCBU Server Structure

The second server structure (S2) is dedicated to facilitating voice-based communication between users. Unlike the first server, which utilizes the Photon infrastructure, S2 employs the Photon Voice infrastructure to enable voice interactions between users. Upon logging in to the first server, users are automatically logged into S2 as well. However, S2 is exclusively responsible for transmitting voice interactions between users.

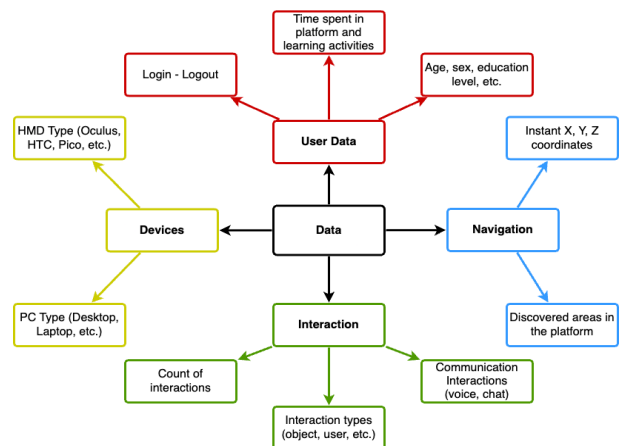


Figure 6. MetaCBU Data Types

The server infrastructure integrated into the MetaCBU platform enables the recording of various user variables, such as entry and exit records, interaction with objects or other users, duration of education, success rate, and location, in databases. By storing virtually all user actions in data warehouses with server connections, a significant data flow can be generated, and studies can be conducted

to improve the platform. Additionally, the training materials provided on the platform can be customized and updated according to the user preferences, using the data obtained from the users within MetaCBU. Furthermore, the data collected from the users can be continually updated, and new additions or deletions can be made as necessary. Figure 6 displays some of the data information extracted from the current version of the platform.

4. Discussion & Implications

This study has explored the transformative potential of Virtual Reality (VR) and Extended Reality (XR) technologies within the educational landscape, with a particular focus on the development of the MetaCBU virtual campus at Manisa Celal Bayar University. The MetaCBU project offers a unique and innovative learning environment that has the potential to not only complement but also surpass traditional educational methods in several key areas. By leveraging the immersive and interactive capabilities of VR and XR, MetaCBU significantly enhances student engagement, motivation, and collaboration, providing experiential learning opportunities that are otherwise challenging to achieve in conventional classrooms.

The implementation of VR and XR technologies in educational settings marks a significant advancement in how immersive learning environments can be designed and utilized. These technologies have been demonstrated to provide students with highly interactive platforms that simulate real-world scenarios, thereby enhancing the overall learning experience. For instance, VR-based cooperative learning strategies have been shown to significantly improve student engagement and learning outcomes, particularly in disciplines requiring intricate spatial understanding, such as anatomy and engineering [37]. Similarly, VR's capacity for experiential learning has been validated in surgical training environments, where participants demonstrate improved retention and mastery of complex skills compared to traditional methods [38, 39]. Research consistently shows that VR and XR can significantly improve student engagement and learning outcomes by offering environments that traditional methods cannot replicate [14, 40, 41]. This study builds upon this foundation by systematically applying these advanced technologies to create comprehensive educational platforms that address the evolving needs of modern education.

However, the development of MetaCBU was not without its challenges. One of the key technical hurdles was ensuring optimal performance to prevent issues like motion sickness and latency, which are common in VR environments. Motion sickness, primarily caused by sensory mismatches between visual and vestibular cues, can be mitigated through advanced rendering techniques such as polygon optimization and maintaining high frame

rates of 90Hz or above [42, 43]. Moreover, latency—a major contributor to simulator sickness—was addressed using robust server infrastructures and load balancing methods, achieving display update latencies below 20ms, which are critical for user comfort [44]. The integration of artificial intelligence to synchronize visual and vestibular cues has also emerged as a promising solution to reduce cybersickness in VR environments [45]. The platform's success in overcoming these challenges through the optimization of processing power and the careful management of 3D model rendering highlights the importance of technical precision in the development of immersive educational tools. This aspect of the project underscores the necessity for continuous refinement and adaptation of VR technologies to meet the high standards required for educational use.

Moreover, while the educational benefits of VR and XR are well-documented, this study also highlights the critical role these technologies play in transforming the infrastructure of educational institutions. The MetaCBU platform exemplifies how a well-designed virtual campus can offer more than just a replica of a physical university; it can create a dynamic and interactive space that enhances the educational process in ways that traditional campuses cannot. For example, MetaCBU fosters student collaboration and critical thinking by enabling immersive group activities that are difficult to replicate in physical settings [46]. Additionally, VR environments allow for safe, controlled practice of skills, such as medical procedures or engineering simulations, which would otherwise pose risks or logistical challenges [38]. The ability of VR and XR to provide multi-sensory, interactive learning environments represents a paradigm shift in educational methodology, where students are no longer passive recipients of information but active participants in their learning journey.

The integration of XR in various disciplines, particularly engineering and health sciences, has shown to significantly enhance the retention of complex concepts by allowing students to engage with practical lessons in a controlled virtual environment. In these settings, students report higher levels of motivation and satisfaction due to the immersive nature of the learning experiences, which traditional methods often fail to achieve [37, 39]. This aligns with broader educational trends, where XR technologies are increasingly being adopted to support interdisciplinary learning, providing a more holistic educational experience [47, 48]. Furthermore, recent advancements such as the XR Vest and e-skin technology have expanded the boundaries of immersive learning by integrating tactile, thermal, and olfactory sensations, thereby bridging the gap between physical and virtual worlds [49, 50].

In addition to these technological advancements, the use of VR and XR in education has been systematically optimized through the integration of learning analytics,

which provides actionable insights into the learning process. This integration enables educators to tailor educational experiences to individual student needs, thereby enhancing learning effectiveness and providing new opportunities for research and practice [17]. The theoretical frameworks supporting the use of VR and AR in STEM education further reinforce the value of these technologies in enhancing cognitive skills and learning outcomes [51].

However, it is important to acknowledge the limitations of this study. The scalability of MetaCBU and its broader applicability across different educational contexts remain areas for further exploration. Additionally, while the technical challenges were successfully addressed, ongoing developments in VR and XR technologies necessitate continuous updates to the platform to incorporate new features and maintain high levels of user engagement.

Overall, the findings of this study not only highlight the current impact of VR and XR technologies on educational practices but also suggest a promising future where these technologies could become integral to the development of more effective and engaging educational environments. The continued exploration and integration of VR and XR in education are likely to lead to significant advancements in how we approach teaching and learning across various disciplines, offering new opportunities to enhance the educational process in ways previously unimaginable.

5. Conclusion

This study has demonstrated the significant potential of Virtual Reality (VR) and Extended Reality (XR) technologies in transforming the educational landscape, particularly through the development and implementation of the MetaCBU virtual campus. By providing an immersive and interactive environment, MetaCBU has shown the ability to enhance student engagement, motivation, and collaboration—elements that are often limited in traditional educational settings. The successful integration of these technologies into a multi-user, virtual campus highlights their capacity not only to replicate but also to extend the capabilities of physical educational environments.

The technical challenges encountered during the development of MetaCBU, such as optimizing system performance and ensuring user comfort, underscore the complexity of creating scalable and effective VR platforms. However, the solutions implemented in this study, including advanced rendering techniques and robust infrastructure management, provide a valuable blueprint for future projects seeking to incorporate VR and XR technologies into educational frameworks.

Moreover, the implications of this study extend beyond the immediate application of MetaCBU, offering insights into the broader potential of VR and XR technologies across various disciplines. The findings suggest that these technologies are poised to play a crucial role in the future of education, enabling more personalized, engaging, and effective learning experiences. As educational institutions continue to explore digital transformation, the integration of VR and XR will likely become a central component of innovative educational strategies.

Looking ahead, further research is needed to explore the scalability of platforms like MetaCBU and their applicability across different educational contexts. Additionally, ongoing advancements in VR and XR technologies should be continuously monitored and integrated to maintain the relevance and effectiveness of these virtual environments. By embracing these emerging technologies, the education sector can unlock new possibilities for teaching and learning, ultimately shaping a more dynamic and accessible educational future.

Acknowledgement

This study was prepared within the scope of the project numbered 2022-077 supported by Manisa Celal Bayar University Scientific Research Projects Coordination Unit.

Author's Contributions

Barış Çukurbaşı: Supervised the experiment's progress, result interpretation and helped in manuscript preparation.

Ali Geriş: Drafted and wrote the manuscript, performed the experiment and result analysis.

Orkun Teke: Assisted in analytical analysis on the structure and helped in manuscript preparation.

Murat Kılınç: Assisted in analytical analysis on the structure and helped in manuscript preparation.

Ethics

There are no ethical issues after the publication of this manuscript.

References

- [1]. Ćwiertniak, R., et al., *Addressing students' perceived value with the virtual university concept*. e-mentor, 2022. **94**(2): p. 65-76.
- [2]. Liu, X., *Digital Transformation of Environmental Design Education and Application of Virtual Reality*. Journal of Education and Educational Research, 2023. **5**(3): p. 53-56.
- [3]. Saghafian, M., et al., *Application of human factors in the development process of immersive visual technologies: challenges and future improvements*. Frontiers in psychology, 2021. **12**: p. 634352.

- [4]. Bellalouna, F., *Industrial case studies for digital transformation of engineering processes using the virtual reality technology*. Procedia CIRP, 2020. **90**: p. 636-641.
- [5]. Hite, R., *Virtual reality: Flight of fancy or feasible? Ways to use virtual reality technologies to enhance students' science learning*. The American Biology Teacher, 2022. **84**(2): p. 106-108.
- [6]. Rubio-Tamayo, J.L., M. Gertrudix Barrio, and F. García García, *Immersive environments and virtual reality: Systematic review and advances in communication, interaction and simulation*. Multimodal technologies and interaction, 2017. **1**(4): p. 21.
- [7]. Kouame, G., J. Davis, and L. Smith, *Providing health sciences education through virtual reality experiences*. Journal of the Medical Library Association, 2023. **111**(4): p. 833-834.
- [8]. Zhao, X., Y. Ren, and K.S. Cheah, *Leading Virtual Reality (VR) and Augmented Reality (AR) in education: bibliometric and content analysis from the web of science (2018–2022)*. SAGE Open, 2023. **13**(3): p. 21582440231190821.
- [9]. Fowler, C., *Virtual reality and learning: Where is the pedagogy?* British journal of educational technology, 2015. **46**(2): p. 412-422.
- [10]. Kamińska, D., et al., *Virtual reality and its applications in education: Survey*. Information, 2019. **10**(10): p. 318.
- [11]. McGermott, G., et al., *Exploring the use of immersive technologies to enhance the student experience*. Ubiquity Proceedings, 2023.
- [12]. Jiang, Z., et al. *Virtual reality training environment for electric systems*. in *2021 IEEE 7th International Conference on Virtual Reality (ICVR)*. 2021. IEEE.
- [13]. Dixken, M., et al. *Distributed, collaborative virtual reality application for product development with simple avatar calibration method*. in *2019 IEEE Conference on Virtual Reality and 3D User Interfaces (VR)*. 2019. IEEE.
- [14]. Radianti, J., et al., *A systematic review of immersive virtual reality applications for higher education: Design elements, lessons learned, and research agenda*. Computers & education, 2020. **147**: p. 103778.
- [15]. Gonzalez Lopez, J.M., et al., *Incorporating virtual reality into the teaching and training of grid-tie photovoltaic power plants design*. Applied sciences, 2019. **9**(21): p. 4480.
- [16]. Huang, T.-K., et al., *Augmented reality (AR) and virtual reality (VR) applied in dentistry*. The Kaohsiung journal of medical sciences, 2018. **34**(4): p. 243-248.
- [17]. Heinemann, B., S. Görzen, and U. Schroeder. *Systematic design for effective learning in virtual reality*. in *2022 International Conference on Advanced Learning Technologies (ICALT)*. 2022. IEEE.
- [18]. Kim, D. and T. Im, *A Systematic Review of Virtual Reality-Based Education Research Using Latent Dirichlet Allocation: Focus on Topic Modeling Technique*. Mobile Information Systems, 2022. **2022**(1): p. 1201852.
- [19]. Cabero-Almenara, J., et al., *Degree of acceptance of virtual reality by health sciences students*. International Journal of Environmental Research and Public Health, 2023. **20**(8): p. 5571.
20. Regal, G., et al., *Challenges in virtual reality training for CBRN events*. Multimodal Technologies and Interaction, 2023. **7**(9): p. 88.
- [20]. Tacgin, Z., *Immersive virtual reality as an action: measuring approach and learning status of learners after planning myVOR*. Educational Media International, 2020. **57**(4): p. 353-371.
- [21]. Cho, B., *Domestic University Virtual Reality (VR) Utilization Education Research Trend*. Journal of Learner-Centered Curriculum and Instruction, 2023. **23**(9): p. 47-57.
- [22]. Geriş, A. and N. Özdener, *Design, development, and evaluation of educational virtual reality environment: EVRECA*. Educational technology research and development, 2024. **72**(2): p. 915-945.
- [23]. Pimentel, D., et al., *An introduction to learning in the metaverse*. Meridian Treehouse, 2022. **3**(4): p. 348-352.
- [24]. Han, Y. *Virtual reality in engineering education*. in *SHS web of conferences*. 2023. EDP Sciences.
- [25]. Fathallah, N.A., et al. *Virtual reality: A paradigm shift in architecture and urban design education*. in *2022 IEEE 1st Industrial Electronics Society Annual On-Line Conference (ONCON)*. 2022. IEEE.
- [26]. Lie, S.S., et al., *Implementation of virtual reality in health professions education: scoping review*. JMIR medical education, 2023. **9**: p. e41589.
- [27]. Ng, J.T., et al. *Automated Analysis of Text in Student-Created Virtual Reality Content*. in *2023 IEEE International Conference on Advanced Learning Technologies (ICALT)*. 2023. IEEE.
- [28]. Flavián, C., S. Ibáñez-Sánchez, and C. Orús, *The influence of scent on virtual reality experiences: The role of aroma-content congruence*. Journal of Business Research, 2021. **123**: p. 289-301.
- [29]. Geriş, A. and Y. Tunga, *Sanal Gerçeklik Ortamlarında Bulunma Hissi*. Manisa Celal Bayar Üniversitesi Sosyal Bilimler Dergisi, 2020. **18**(4): p. 261-282.
- [30]. Sharrab, Y.O., et al., *Toward Smart and Immersive Classroom based on AI, VR, and 6G*. Int. J. Emerg. Technol. Learn., 2023. **18**(2): p. 4-16.
- [31]. Mills, K.A., *Potentials and challenges of extended reality technologies for language learning*. Anglistik, 2022. **33**(1): p. 147-163.
- [32]. Cibulška, E. and K. Boločko. *Virtual reality in education: structural design of an adaptable virtual reality system*. in *2022 6th International Conference on Computer, Software and Modeling (ICCSM)*. 2022. IEEE.
- [33]. Kilinc, M., et al. *MetaPortal: Business Intelligence and Machine Learning Approach for VR Data*. in *2023 Innovations in Intelligent Systems and Applications Conference (ASYU)*. 2023. IEEE.
- [34]. Ribeiro de Oliveira, T., et al., *Virtual reality solutions employing artificial intelligence methods: A systematic literature review*. ACM Computing Surveys, 2023. **55**(10): p. 1-29.
- [35]. Sindu, I.G.P., et al., *Systematic literature review of machine learning in virtual reality and augmented reality*. Jurnal Nasional Pendidikan Teknik Informatika: JANAPATI, 2023. **12**(1): p. 108-118.
- [36]. Wang, C.-Y., et al., *Enhancing anatomy education through cooperative learning: harnessing virtual reality for effective gross anatomy learning*. Journal of Microbiology and Biology Education, 2023. **24**(3): p. e00100-23.
- [37]. Lohre, R., et al., *Improved complex skill acquisition by immersive virtual reality training: a randomized controlled trial*. JBJS, 2020. **102**(6): p. e26.
- [38]. Seymour, N.E., et al., *Virtual reality training improves operating room performance: results of a randomized, double-blinded study*. Annals of surgery, 2002. **236**(4): p. 458-464.

- [39]. AlGerafi, M.A., et al., *Unlocking the potential: A comprehensive evaluation of augmented reality and virtual reality in education*. Electronics, 2023. **12**(18): p. 3953.
- [40]. Sofiadin, A. *Extended Reality for Experiential Learning from Students' Perspective*. in *2023 IEEE 8th International Conference on Engineering Technologies and Applied Sciences (ICETAS)*. 2023. IEEE.
- [41]. Takata, R., et al., *Improvement of three-dimensional motion sickness using a virtual reality simulator for robot-assisted surgery in undergraduate medical students: A prospective observational study*. BMC Medical Education, 2021. **21**: p. 1-7.
- [42]. Kemeny, A., F. Colombet, and T. Denoual. *How to avoid simulation sickness in virtual environments during user displacement*. in *The Engineering Reality of Virtual Reality 2015*. 2015. SPIE.
- [43]. Tošić, I., D. Hoffman, and N. Balram, *Effect of latency on simulator sickness in smartphone virtual reality*. Journal of the Society for Information Display, 2021. **29**(7): p. 561-572.
- [44]. Arshad, I., et al., *Reducing cybersickness in 360-degree virtual reality*. Multisensory Research, 2021. **35**(2): p. 203-219.
- [45]. Ranasinghe, N., et al. *Exploring the use of olfactory stimuli towards reducing visually induced motion sickness in virtual reality*. in *Proceedings of the 2020 ACM Symposium on Spatial User Interaction*. 2020.
- [46]. Mouttalib, H., M. Tabaa, and M. Youssefi, *Revolutionizing engineering education: Creating a web-based teaching platform for immersive learning experiences*. Journal of Smart Cities and Society, 2023(Preprint): p. 1-12.
- [47]. Alnagrat, A., et al., *A review of extended reality (XR) technologies in the future of human education: Current trend and future opportunity*. Journal of Human Centered Technology, 2022. **1**(2): p. 81-96.
- [48]. Bayro, A., B. Havens, and H. Jeong, *Xr vest: A novel system for demonstration-based learning of safety skills*. IEEE Transactions on Learning Technologies, 2023. **17**: p. 63-72.
- [49]. Wang, J. and S. Gao, *Electronic Skin for Virtual Sensation Generation in Immersive Virtual and Augmented Reality*. IEEE Open Journal on Immersive Displays, 2023.
- [50]. Christopoulos, A. and N. Pellas. *Theoretical foundations of Virtual and Augmented reality-supported learning analytics*. in *2020 11th International Conference on Information, Intelligence, Systems and Applications (IISA)*. 2020. IEEE.

Improvement of Mechanical and Viscoelastic Properties of Polypropylene with Wood and Wollastonite Fillers

Mustafa Öncül^{1*} , Kutlay Sever¹ 

¹ İzmir Katip Çelebi University, Department of Mechanical Engineering, İzmir, Türkiye

* mustafa.oncul@ikcu.edu.tr

* Orcid No: 0000-0002-4441-6353

Received: October 11, 2024

Accepted: December 28, 2024

DOI: 10.18466/cbayarfbe.1565156

Abstract

In recent years, polypropylene has become one of the most popular thermoplastic polymers due to its excellent properties, chemical resistance, affordability, and easy processing. When reinforced with glass fibers, wood fibers, or mineral fillers, polypropylene composites exhibit enhanced mechanical strength, stiffness, and durability. This makes them suitable for applications where high performance and specific mechanical properties are required, such as in automotive interior parts, building materials, and consumer goods. This research analyzes the effects of wood fibers as an organic filler and wollastonite mineral as an inorganic filler on the mechanical and viscoelastic properties of polypropylene. Various weight ratios of these fillers were added into polypropylene to produce hybrid biocomposites using a laboratory-type high-speed thermokinetic mixer and a heated-cooled hydraulic press. The mechanical properties were determined by tensile and three-point bending tests, and viscoelastic properties were analyzed using dynamic mechanical analysis. The test results indicated that the polypropylene composite sample containing 7% by weight of silane-treated wollastonite and 3% by weight of wood fibers showed the best results among all samples. The storage and loss moduli of the sample are approximately 25% and 22% higher than those of the polypropylene, respectively. Overall, hybrid biocomposites filled with silane-treated wollastonite exhibited enhanced mechanical and viscoelastic properties compared to those filled with untreated wollastonite, as supported by the experimental data.

Keywords: Organic and inorganic fillers, Hybrid composites, Mechanical properties, Polypropylene, Silane-treated wollastonite, Viscoelastic properties

1. Introduction

The increasing demand for sustainable and environmentally friendly materials has led to a significant increase in interest in biocomposites, which are composites manufactured from natural fibers and bio-based matrices. These materials offer a number of advantages over conventional composites, including a reduced environmental impact, biodegradability and a lower cost [1]. The use of biocomposites is becoming increasingly prevalent across a range of industries, including automotive, construction and packaging. This is due to the favorable mechanical properties exhibited by these materials, which include a high strength-to-weight ratio and good thermal stability [2]. Among biocomposites, hybrid composites, which combine two

or more types of fibers or fillers, have attracted considerable attention due to their potential to enhance performance characteristics while maintaining environmental benefits. The selection of appropriate fibers and fillers allows the creation of hybrid composites that can be tailored to achieve a balance between mechanical strength, stiffness, and other desired properties [3, 4]. The utilization of hybrid composites incorporating natural fillers, such as wood flour or wood fibers, in conjunction with mineral fillers, including wollastonite, can present distinctive benefits, including enhanced stiffness, improved dimensional stability and reduced water absorption [5].

Wollastonite, a naturally occurring calcium silicate mineral, has been effectively used as a filler in composite materials due to its ability to improve mechanical properties, thermal stability and fire resistance [6]. When incorporated into hybrid composites, wollastonite can

provide significant improvements in wear resistance and thermal performance, which are crucial for applications in automotive components and construction materials [7]. Similarly, wood fibers, derived from renewable sources, are gaining popularity due to their low density, high availability, and biodegradability, making them ideal for eco-friendly composite applications [8–10]. The combination of wood fibers and wollastonite in hybrid biocomposites represents a promising avenue for the development of advanced materials with enhanced mechanical, thermal, and environmental properties. These hybrid composites offer a more sustainable alternative to traditional synthetic composites and align with the increasing regulatory and consumer demands for greener and more sustainable products [11, 12]. The objective of this paper is to examine the potential of hybrid biocomposites reinforced with wollastonite and wood fibers, with a focus on their properties, processing methods, and potential applications in various industries.

There is a growing need for materials that offer both high performance and sustainability. Polypropylene (PP) is a popular thermoplastic due to its chemical resistance, low cost, and ease of processing. When reinforced with fillers like glass fibers, wood fibers, or minerals, PP composites become stronger and more durable, making them ideal for use in automotive parts, construction, and consumer products. This study explores the effects of adding wood fibers and wollastonite, a mineral filler, to PP to create hybrid biocomposites. By examining how different amounts of these fillers affect the mechanical and viscoelastic properties of PP, this research aims to find new ways to improve material performance while using more sustainable resources.

This work observes the impact of incorporating wood fibers and wollastonite, a mineral filler, into PP to create hybrid biocomposites. The objective of this research is to identify new methods of enhancing the mechanical and viscoelastic properties of PP while utilizing more sustainable resources. To achieve this, an examination was conducted on the effects of varying quantities of fillers on the properties of PP.

2. Materials and Methods

2.1. Materials

The PP-copolymer (LG Chem M1500) used in this work that has a density of 0.9 g/cm³. Untreated wollastonite (Tremin 939-300) and silane-treated wollastonite (Tremin 939-300 AST), both with needle-like morphology, a density of 2.85 g/cm³, and a Mohs hardness of 4.5, were obtained from Kaolin Minerals, Türkiye. The woods were supplied from the products left as pruning waste from a cherry tree plant field in Konya, Türkiye. To make wood fibers suitable for composite production, branches were broken into small pieces then ground with a laboratory-type grinder. Then, wood fibers were passed through sieves. Particles, under 100

micrometer sizes, were used to produce composites. The production of polymer composites was carried out to a high-speed thermokinetic mixer and a heated-cooled hydraulic press. The nomenclature of the produced samples is provided in Table 1 for reference.

Table 1. The nomenclature of the composite samples

Name	Rates (wt. %)
PP	100% Polypropylene
3UTW-7WF	3% Untreated wollastonite + 7% Wood fiber + 90% PP
7UTW-3WF	7% Untreated wollastonite + 3% Wood fiber + 90% PP
3STW-7WF	3% Silane-treated wollastonite + 7% Wood fiber + 90% PP
7STW-3WF	7% Silane-treated wollastonite + 3% Wood fiber + 90% PP

2.2. Methods

The mechanical properties—including tensile strength, tensile modulus, flexural strength, and flexural modulus—of the samples were measured using a tensile testing machine (Shimadzu AGS-X, 5 kN, Japan). Tensile tests were conducted following ASTM D638-14, "Standard Test Method for Tensile Properties of Plastics," with a cross-head speed of 50 mm/min. Flexural tests adhered to ASTM D790-17, "Standard Test Methods for Flexural Properties of Unreinforced and Reinforced Plastics and Electrical Insulating Materials," with a cross-head speed of 1 mm/min. Each test was repeated at least five times for each material type to ensure accuracy and reliability. Dynamic mechanical properties, including storage modulus and loss modulus, were measured using a dynamic mechanical analyzer (TA Instruments Inc., USA). The analyses were conducted with a single-point holder over a temperature range of 35-130°C, with a heating rate set to 3°C/min.

3. Results and Discussion

3.1. Tensile Test

The tensile test results illustrated in Figure 1. The tensile strength of PP was found to be 23.16 ± 0.18 MPa, as given in Figure 1.a. Among the composites, the 7STW-3WF sample exhibited a tensile strength of 23.06 ± 0.67 MPa, which is in close proximity to that of PP. These findings suggest that the incorporation of 7% silane-treated wollastonite maintains the tensile strength of PP, with the addition of wood fiber having a negligible effect. In contrast, composites comprising untreated wollastonite (3UTW-7WF and 7UTW-3WF) exhibited slightly reduced tensile strengths of 21.02 ± 0.21 MPa and 21.89 ± 0.07 MPa, respectively. This indicates that silane treatment enhances tensile strength by improving interfacial adhesion between the wollastonite and the PP matrix [6,13].

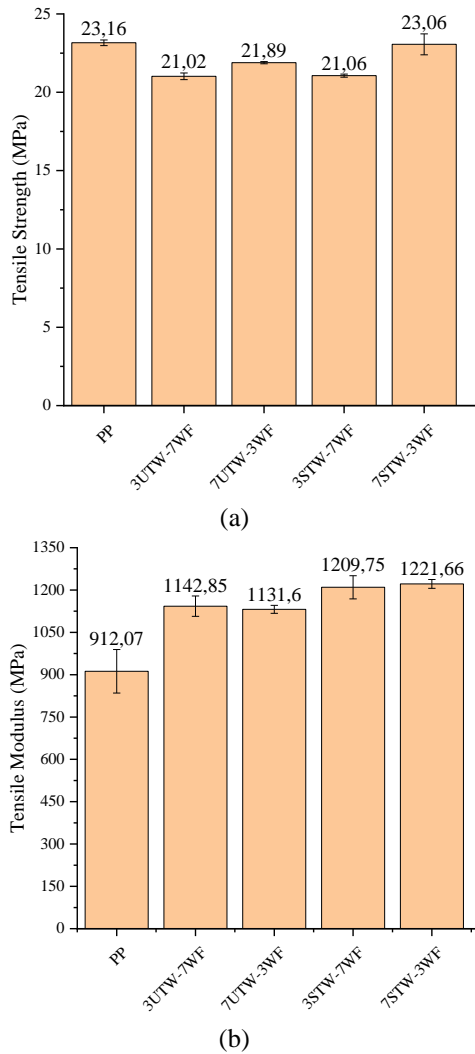


Figure 1. a) Tensile strength and b) Tensile modulus

The incorporation of fillers resulted in a notable enhancement in the tensile modulus of the composites, as seen in Figure 1.b, in comparison to PP, which exhibited a tensile modulus of 912.07 ± 76.97 MPa. The highest tensile modulus was observed in the 7STW-3WF sample, with a value of 1221.66 ± 15.78 MPa, indicating that the addition of 7% silane-treated wollastonite effectively increases the stiffness of the composite. This improvement in stiffness is likely due to enhanced bonding between the treated wollastonite and the PP matrix, which restricts the mobility of the polymer chains [14]. The tensile modulus values for the composites with untreated wollastonite (3UTW-7WF and 7UTW-3WF) were also higher (1142.85 ± 36.2 MPa and 1131.60 ± 14.26 MPa, respectively) than those of the pure PP, although these values were slightly lower than those of the silane-treated samples. This indicates that silane treatment has a beneficial effect on tensile properties.

3.2. Flexural Test

The flexural test results demonstrated in Figure 2. The flexural strength of PP was determined to be 32.63 ± 0.7

MPa, as shown in Figure 2.a. The incorporation of fillers led to an enhancement in flexural strength, with the 7STW-3WF composite exhibiting the highest value of 39.25 ± 0.62 MPa. This increase can be attributed to the reinforcing effect of both the silane-treated wollastonite and wood fibers, which enhance the load distribution across the composite matrix [6]. The 3UTW-7WF and 7UTW-3WF samples also exhibited enhanced flexural strengths (38.23 ± 0.7 MPa and 37.46 ± 1.59 MPa, respectively) in comparison to PP. However, these increments were less pronounced than those observed in the silane-treated samples. This highlights the efficacy of surface treatment in enhancing interfacial bonding and optimizing composite performance.

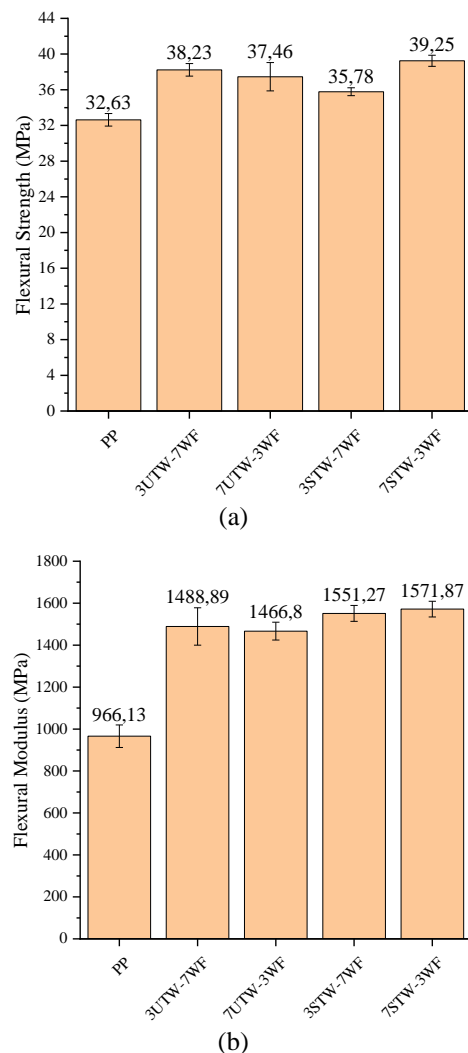


Figure 2. (a) Flexural strength and (b) Flexural modulus

The flexural modulus, which reflects the material's resistance to bending, was significantly enhanced in all composite samples compared to PP, which had a modulus of 966.13 ± 53.69 MPa (Figure 2.b). The 7STW-3WF sample exhibited the highest flexural modulus at 1571.87 ± 37.43 MPa, followed closely by the 3STW-7WF sample at 1551.27 ± 37.81 MPa. Composites with untreated wollastonite (3UTW-7WF

and 7UTW-3WF) also demonstrated considerable improvements in flexural modulus (1488.89 ± 88.95 MPa and 1466.8 ± 42.53 MPa, respectively), though these values were slightly lower than those of the silane-treated samples. The increased flexural moduli in the silane-treated composites are likely due to better compatibility and stress transfer between the fillers and the PP matrix, which reduces deformation under bending loads [12].

The research indicates that incorporating silane-treated wollastonite into PP composites significantly improves their tensile and flexural properties compared to using untreated wollastonite. The 7STW-3WF composite, in particular, achieved the best overall mechanical performance, indicating an optimal balance of filler content for reinforcing PP while maintaining cost-effectiveness and environmental sustainability. These findings are consistent with previous research demonstrating that surface treatment of fillers enhances their interfacial bonding with the polymer matrix, leading to improved mechanical properties [3].

3.3 Dynamic Mechanical Analysis (DMA)

Figure 3 illustrates the variation of both the storage modulus and loss modulus with temperature for PP and various hybrid biocomposites reinforced with untreated and silane-treated wollastonite and wood fibers. The storage modulus, representing the material's stiffness, indicates its ability to store energy elastically under deformation, providing insight into the viscoelastic behavior of the composites under different temperatures—a key factor in their real-world performance. In contrast, the loss modulus measures the energy dissipated as heat during deformation, reflecting the material's damping characteristics and viscous response to stress. This parameter is essential for understanding the energy absorption and internal friction behavior of the composites under dynamic loading conditions.

Figure 3.a illustrates that as the temperature increases, the storage modulus of PP decreases significantly, starting from around 1000 MPa at 30°C and declining steadily to about 200 MPa at 160°C, which reflects the typical thermal softening behavior of thermoplastic polymers as they become less stiff and more compliant due to increased molecular mobility [15]. The 3UTW-7WF composite exhibits a higher initial storage modulus than PP, starting at around 1200 MPa at 30°C, indicating that the addition of untreated wollastonite and wood fiber enhances the stiffness of the composite at lower temperatures due to the reinforcing effects of the fillers [16]. However, as the temperature increases, the modulus decreases at a rate similar to that of PP, showing a notable reduction in stiffness at higher temperatures. In comparison, the 7UTW-3WF sample starts with a slightly higher initial storage modulus of around 1300 MPa at 30°C, suggesting that a greater content of

wollastonite contributes more effectively to stiffness. Although its modulus also decreases with increasing temperature, this composite retains higher stiffness than both the 3UTW-7WF and PP throughout the temperature range, emphasizing the role of wollastonite in maintaining the material's stiffness.

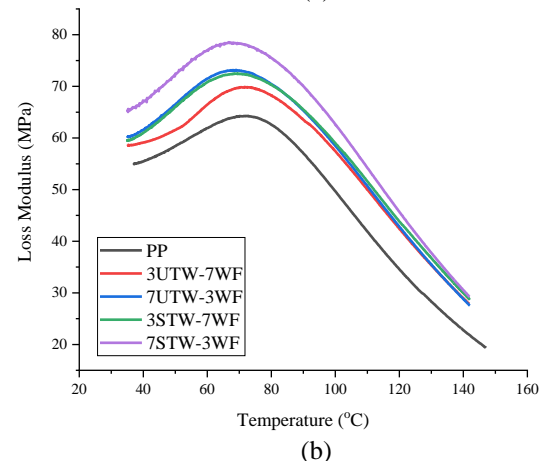
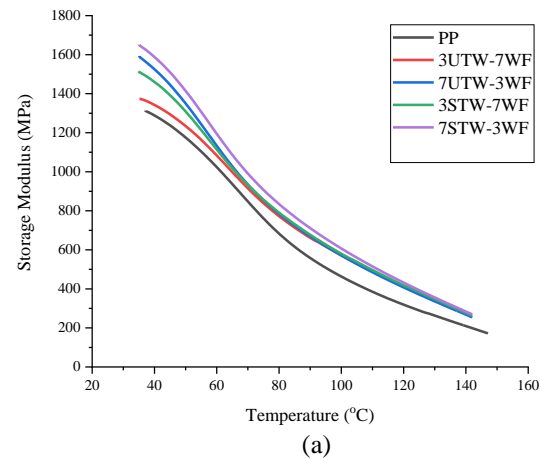


Figure 3. (a) Storage modulus and (b) Loss modulus

The 3STW-7WF composite shows a higher initial storage modulus than its untreated counterparts, starting at approximately 1350 MPa at 30°C. This increase is attributed to the silane treatment, which enhances interfacial adhesion between the wollastonite particles and the PP matrix, leading to improved stress transfer and increased stiffness [17]. As the temperature rises, the modulus decreases, but it remains consistently higher than that of the untreated composites, indicating superior thermal stability. The 7STW-3WF sample shows the highest initial storage modulus of all samples, beginning around 1400 MPa at 30°C, and demonstrates the slowest rate of decline in modulus with increasing temperature, maintaining a significantly higher modulus than all other samples even at 160°C. These findings clearly highlight the combined effect of higher wollastonite content and silane treatment in enhancing both the stiffness and thermal stability of the composite material.

The loss modulus of PP, given in Figure 3.b, shows a characteristic peak around 90°C, corresponding to the glass transition temperature (T_g) of the polymer, where there is a marked increase in molecular mobility leading to maximum energy dissipation. Beyond the T_g , the loss modulus decreases steadily as the polymer transitions into a rubbery state, becoming more flexible and less resistant to deformation [15].

The 3UTW-7WF composite exhibits a higher loss modulus than PP, with a peak value slightly shifted to around 95°C, suggesting that the addition of untreated fillers enhances the energy dissipation capacity of the composite, likely due to increased internal friction between the matrix and the fillers. However, the peak height indicates that while the composite dissipates more energy, it also experiences increased internal friction, which could negatively affect its dynamic mechanical performance at elevated temperatures [16]. Similarly, the 7UTW-3WF composite shows an even higher loss modulus compared to PP, with a peak similar to that of 3UTW-7WF but slightly greater, implying that a higher wollastonite content contributes to increased damping properties. This may result from the rigid nature of wollastonite particles, which provide more resistance to deformation and, consequently, greater energy dissipation.

The 3STW-7WF sample exhibits a peak loss modulus that is higher than those of both the untreated composites and PP, with the peak occurring around 100°C, slightly above that of the untreated counterparts. This shift and increase in peak height indicate improved interfacial bonding between the matrix and the treated filler due to the silane treatment, which enhances stress distribution and increases frictional damping within the composite [17]. The 7STW-3WF sample shows the highest peak loss modulus, also occurring around 100°C. This elevated peak and shift further highlight the effectiveness of silane treatment in enhancing the composite's damping properties. The higher wollastonite content in this composite results in a greater interfacial area and more pronounced interaction with the polymer matrix, leading to increased energy dissipation and improved thermal stability [18].

The results show that the addition of both untreated and silane-treated wollastonite and wood fibers enhances the stiffness and damping properties of PP composites, with silane-treated wollastonite showing superior performance in both aspects. The 7STW-3WF composite exhibited the highest storage modulus across all temperatures tested, making it the most suitable candidate for applications requiring high stiffness and thermal stability. This improved performance can be attributed to better interfacial bonding provided by the silane treatment, which facilitates effective load transfer between the filler and the polymer matrix [18]. Additionally, the higher wollastonite content (7%)

consistently results in greater stiffness compared to a higher wood fiber content (7%) in both treated and untreated groups, suggesting that wollastonite is a more effective reinforcement than wood fiber [19]. Similarly, silane-treated fillers enhance the loss modulus of the composites, with the 7STW-3WF composite showing the highest loss modulus and the most significant shift in T_g , indicating superior damping capacity and energy dissipation. This improved damping behavior is likely due to better adhesion between the filler and the matrix, which facilitates more efficient stress transfer and energy dissipation [20]. The findings suggest that wollastonite's rigid structure and surface characteristics make it more effective in improving both the stiffness and damping properties of PP composites compared to wood fiber.

4. Conclusion

The study demonstrates that the incorporation of both untreated and silane-treated wollastonite and wood fibers enhances the mechanical and viscoelastic properties of PP composites. The incorporation of these fillers has been observed to enhance the tensile and flexural modulus, thereby indicating an increase in stiffness and load-bearing capacity when compared to PP. Among the results, composites with silane-treated wollastonite (3STW-7WF and 7STW-3WF) exhibited superior mechanical performance, with the highest tensile and flexural moduli. This indicates that surface treatment facilitates improved interfacial bonding between the filler and the matrix, enabling effective stress transfer and resulting in enhanced mechanical properties. Furthermore, dynamic mechanical analysis confirms these findings, demonstrating that silane-treated wollastonite composites exhibit elevated storage and loss moduli across the investigated temperature range. This suggests enhanced energy storage and dissipation capabilities due to augmented matrix-filler interaction. Furthermore, the shift in the glass transition temperature (T_g) to higher values in treated composites indicates enhanced thermal stability and reduced mobility of polymer chains, which can be attributed to the formation of strong interfacial bonds between the fillers and the matrix. In conclusion, the results indicate that silane treatment of wollastonite is an effective strategy for enhancing the mechanical and dynamic properties of PP composites. Composites with higher wollastonite content, particularly the 7STW-3WF formulation, exhibit the most promising performance, combining high stiffness, strength, and damping properties. This makes them suitable for applications requiring higher mechanical and viscoelastic properties, such as automotive components, construction materials, and consumer products. Further studies could concentrate on optimizing filler content and investigating additional surface treatments with a view to enhancing the performance of these hybrid biocomposites.

Acknowledgement

The authors would like to thank KAOLIN Industrial Minerals, Türkiye, for the wollastonite supply.

Author's Contributions

Mustafa Öncül: Performed the experiment and result analysis, drafted and wrote the manuscript.

Kutlay Sever: supervised the experiment's progress, result interpretation and helped in manuscript preparation.

Ethics

There are no ethical issues after the publication of this manuscript.

References

- [1]. Ashori A. Wood-plastic composites as promising green-composites for automotive industries! *Bioresour Technol.* 2008; 99(11):4661-7.
- [2]. Faruk O, Bledzki AK, Fink HP, Sain M. Biocomposites reinforced with natural fibers: 2000-2010. *Top Issue Polym Biomater.* 2012 Nov 1; 37(11):1552-96.
- [3]. Koronis G, Silva A, Fontul M. Green composites: A review of adequate materials for automotive applications. *Compos Part B Eng.* 2013; 44(1):120-7.
- [4]. Savran M, Öncül M, Yılmaz M, Aydın L, Sever K. Modeling and optimization of dynamic-mechanical properties of hybrid polymer composites by multiple nonlinear neuro-regression method. *Sigma J Eng Nat Sci.* 2023; 41(6):1243-54.
- [5]. Mohan Sharma A. Mechanical Behaviour, Water Absorption and Morphology of Wheat Straw, Talc, Mica and Wollastonite filled Polypropylene Composites [Internet] [Master's Thesis]. University of Waterloo; 2012 [cited 2024 Sep 10]. Available from: <https://uwspace.uwaterloo.ca/handle/10012/6772>
- [6]. Chan JX, Wong JF, Hassan A, Mohamad Z, Othman N. Mechanical properties of wollastonite reinforced thermoplastic composites: A review. *Polym Compos.* 2020 Feb; 41(2):395-429.
- [7]. Karagöz İ, Büyükkaya K, Demirer H, Mudu M, Kartal İ. Mechanical and thermal characterization of elastomer modified polypropylene hybrid composites reinforced with hazelnut shell and wollastonite fillers. *J Appl Polym Sci.* 2024 Aug 10; 141(30):e55710.
- [8]. Atagür M, Kaya N, Uysalman T, Durmuşkahya C, Sarikanat M, Sever K, et al. A detailed characterization of sandalwood-filled high-density polyethylene composites. *J Thermoplast Compos Mater.* 2020 Jul 31; 089270572093915.
- [9]. Savran M, Yılmaz M, Öncül M, Sever K. Manufacturing and Modeling of Polypropylene-based Hybrid Composites by Using Multiple-Nonlinear Regression Analysis. *Sci Res Commun.* 2022 Jan 30; 2(1):1-15.
- [10]. Sever K, Yılmaz M. Evaluation of Mechanical and Thermal Properties of Artichoke Filled Polypropylene Composites: Influence of Wollastonite Hybridization. *Emerg Mater Res.* 2020 Jun 1;9(2):1-6.
- [11]. Geissdoerfer M, Savaget P, Bocken NM, Hultink EJ. The Circular Economy—A new sustainability paradigm? *J Clean Prod.* 2017; 143:757-68.
- [12]. Mohanty AK, Misra M, Drzal LT. Natural fibers, biopolymers, and biocomposites. CRC press; 2005.
- [13]. Chen M, Wan C, Shou W, Zhang Y, Zhang Y, Zhang J. Effects of interfacial adhesion on properties of polypropylene/Wollastonite composites. *J Appl Polym Sci.* 2008 Feb 5; 107(3):1718-23.
- [14]. Wong JF, Chan JX, Hassan AB, Mohamad ZB, Othman NB. Thermal and flammability properties of wollastonite-filled thermoplastic composites: a review. *J Mater Sci.* 2021 May; 56(15):8911-50.
- [15]. Andradý AL. Science and technology of polymer nanofibers [Internet]. John Wiley & Sons; 2008 [cited 2024 Sep 10]. Available from: <https://books.google.com/books?hl=en&lr=&id=KOdoYIuFHZAC&oi=fnd&pg=PR7&dq=Science+and+Technology+of+Polymer+Nanofibers&ots=ue1XtfEz3l&sig=HkcLBWLddnWjU5ezGCQL4INGYYY>
- [16]. Joseph P, Joseph K, Thomas S, Pillai C, Prasad V, Groeninckx G, et al. The thermal and crystallisation studies of short sisal fibre reinforced polypropylene composites. *Compos Part Appl Sci Manuf.* 2003; 34(3):253-66.
- [17]. Luyt AS, Dramićanin MD, Antić Ž, Djoković V. Morphology, mechanical and thermal properties of composites of polypropylene and nanostructured wollastonite filler. *Polym Test.* 2009; 28(3):348-56.
- [18]. Fu SY, Lauke B, Mäder E, Yue CY, Hu X. Tensile properties of short-glass-fiber-and short-carbon-fiber-reinforced polypropylene composites. *Compos Part Appl Sci Manuf.* 2000; 31(10):1117-25.
- [19]. Lee SY, Kang IA, Doh GH, Yoon HG, Park BD, Qinglin Wu. Thermal and Mechanical Properties of Wood Flour/Talc-filled Poly(lactic Acid) Composites: Effect of Filler Content and Coupling Treatment. *J Thermoplast Compos Mater.* 2008 May; 21(3):209-23.
- [20]. Malkapuram R, Kumar V, Yuvraj Singh Negi. Recent Development in Natural Fiber Reinforced Polypropylene Composites. *J Reinf Plast Compos.* 2009 May; 28(10):1169-89.

Naringenin-Based Oximes and Hydrazones: Synthesis, Molecular Docking with Bovine Serum Albumin and Drug-Likeness, Admet Profiling Studies

Ferhat Melihcan Abay¹ , Hafize Özcan^{2*} , Ayşen Şuekinci Yılmaz² , Ömer Zaim² 

¹ Trakya University, Institute of Natural and Applied Sciences, Edirne, 22030, Türkiye

² Trakya University, Faculty of Science, Department of Chemistry, Edirne, 22030, Türkiye

* hafizeozcan@trakya.edu.tr

* Orcid No: 0000-0002-8031-6755

Received: September 19, 2024

Accepted: January 13, 2025

DOI: 10.18466/cbayarfbe.1552978

Abstract

Scientists are now increasingly interested in the flavonoid molecule naringenin due to the broad spectrum of biological roles it conducts. Oximes and hydrazones were created employing derivatives of the naringenin-active substances 7-piperidinethoxy and 7-morpholinethoxy to contribute to this research. The ability of the produced compounds to bind to BSA was determined by molecular docking and their potential as medications was assessed using various methods. Based on Lipinski's rule of five, none of the substances were hazardous or carcinogenic, and their blood-brain barrier crossing values were all within permissible limits.

Keywords: BSA, Flavonoid, Hydrazones, Lipinski, Oximes

1. Introduction

Naturally occurring in citrus fruits, naringenin (4',5,7-trihydroxyflavone) belongs to the flavanone class of flavonoid compounds. Many biological and pharmacological activity studies with flavonoids have been going on for many years and have had impressive results [1-3]. In light of this relatively small amount of studies, scientists have started to research and find effective results on this flavanone skeleton namely naringenin which is well-known for its use in biochemistry, food chemistry, medicine, and cosmetics [4-6]. Based on their activities, many naringenin derivatives have been produced and their biological effects have been studied in various areas. Studies on them showed that they have antiviral, anticancer, antioxidant, anti-inflammatory, antidiabetic, and anti-atherogenic activities [7-10].

The C-7- derivatives of naringenin are the most studied ones. Research with these derivatives has shown that C-7-alkyl derivatives exhibit significant biological activity against many microorganisms and anticancer cell lines [7, 11]. Morpholine or piperazine-linked 7-O-naringenin derivatives were chosen as this study's starting material. Literature investigations indicated that the biological activities of naringenin derivatives were further boosted

by the carbonyl group converted to oxime in addition to the alkyl groups [12, 13]. In this direction, we first aimed to synthesize the oximes and hydrazones of 7-O-naringenin derivatives (**3a** and **3b**) whose activity was shown previously (Figure 1).

The interaction of the molecules with the proteins in the blood plasma determines their pharmacological and pharmacokinetic characteristics. Serum albumins, one of the most essential proteins, account for 60 percent of all plasma proteins. These proteins carry out physiological tasks such as transporting endogenous and exogenous substances, maintaining osmotic blood pressure, and helping to keep blood pH [14]. The binding interaction of serum albumin with drugs controls pharmaceuticals' transportation, distribution, and metabolism in vivo. Stronger serum albumin-drug interactions are generally thought to result in a reduction in the concentration of free medication in plasma. In contrast, weaker interactions may result in a shorter half-life or inadequate pharmaceutical dispersion in vivo. Understanding how a drug interacts with and binds to serum albumin provides crucial insight into how it works in vivo [15]. Bovine serum albumin (BSA) has become among the most extensively researched proteins due to its accessibility, low cost, and 75.8% similarity to human serum albumin (HSA). BSA is heart-shaped and made up three main

domains (I, II, and III) and their sub-domains (A and B). Research on the relationship between flavonoids and serum albumin has become increasingly important in the pharmaceutical industry, and a variety of papers are available in the literature on this topic. [16].

Regarding this viewpoint, the purpose of the current study was to clarify the molecular docking-based interactions and binding of two oximes and two hydrazone derivatives of the 7-O-alkyl naringenin with BSA. Additionally, in-silico investigations of the synthesized compounds' ADMET (Absorption, Distribution, Metabolism, Excretion, Toxicity) were carried out, and Lipinski's rule of five filters was used to calculate their drug potentials.

2. Materials and Methods

2.1. General

All reagents were purchased from Sigma-Aldrich or Merck. Merck silica gel (60 mesh) was used for column chromatography and Merck silica gel plates (60F-254) for TLC analysis. Reactions were mainly carried out in an inert atmosphere. The progress of the reactions was monitored using TLC with methanol and chloroform as eluents. The IR spectra were recorded using an FT-IR spectrophotometer, and the ^1H NMR spectra were acquired in DMSO- d_6 using a Varian Mercury Plus 400 MHz spectrometer. ^{13}C NMR spectra were acquired at room temperature using a 100 MHz spectrometer. In ^1H NMR, the following acronyms are used: s = singlet, br. s = broad singlet, d = doublet, dd = doublet of doublets, t = triplet, qui = quintet, and m = multiplet. High-resolution mass spectra (HR-MS) were obtained in AB SCIEX 4600 Q-TOF (Ab Sciex, USA) in m/z (rel.%).

2.2. Synthesis of 7-(2-Bromoethoxy)-5-hydroxy-2-(4-hydroxyphenyl) chroman-4-one (2)

7-(2-bromoethoxy)-5-hydroxy-2-(4-hydroxyphenyl) chroman-4-one was synthesized via a procedure that we utilized previously [7].

2.3. General Procedure for Preparation of Naringenin Alkylamines (3a-3b)

In a solution of compound **2** (300 mg, 0.79 mmol, 1 eq.) in dry acetonitrile (45 mL), piperidine or morpholine (0.87 mmol, 1.1 eq.) and potassium carbonate (0.87 mmol, 1.1 eq.) were added, and the temperature was brought to 70°C. The progress of the reaction was monitored by TLC. After the reaction was terminated, acetonitrile was evaporated and the crude product was purified with flash column chromatography on silica gel using dichloromethane: methanol (19:1). The spectroscopic data were in agreement with literature values [7].

2.4. General Procedure for Preparation of Naringenin Oximes and Hydrazones

0.525 mmol of compound **3a** or **3b** and 1.25 mmol of sodium acetate were mixed with 5 mL of methanol using a magnetic stirrer in a nitrogen atmosphere. Hydroxylamine or hydrazine (1.28 mmol) was added to the solution and stirred at 40 °C for 24 hours. It was then refluxed for a day. The resulting mixture was poured into ice water, and the solids were filtered and dried.

2.4.1. (E)-7-(2-piperidinoethoxy)-5-hydroxy-2-(4-hydroxyphenyl) chroman-4-hydrazone (4a)

Yield 50%, ^1H NMR (400 MHz, DMSO- d_6 , δ , ppm): 12.91 (s, 1H), 9.54 (s, 1H), 7.27 (d, $J = 8.5$ Hz, 2H), 6.76 (d, $J = 8.5$ Hz, 2H), 6.35 (s, 2H), 5.95 (m, 2H), 5.04 (dd, $J = 11.9$, 3.1 Hz, 1H), 4.04 (t, $J = 5.9$ Hz, 2H), 3.1 (dd, $J = 11.9$ Hz, 3.1 Hz, 1H), 2.58 (m, 3H), 2.38 (t, $J = 5.5$ Hz, 4H), 1.46 (m, 4H), 1.35 (qui, $J = 5.9$ Hz, 2H). ^{13}C NMR (100 MHz, DMSO- d_6 , δ , ppm): 160.2, 159.9, 157.9, 157.4, 145.7, 130.6, 128.4, 115.51, 100.6, 96.1, 93.9, 76.4, 65.9, 57.6, 54.6, 30.7, 25.8, 24.2. IR (cm^{-1}): 2938, (C-H), 1616(C=N), 1598, 1446 (C=C), 1199 (C-O), 1160 (C-N). HRMS: m/z $\text{C}_{22}\text{H}_{28}\text{N}_3\text{O}_4$ (M+H) $^+$ found: 398.2071; calc. 398.2080.

2.4.2. (E)-7-(2-morpholinoethoxy)-5-hydroxy-2-(4-hydroxyphenyl) chroman-4-hydrazone (4b)

Yield 57%, ^1H NMR (400 MHz, DMSO- d_6 , δ , ppm): 12.91 (s, 1H), 9.51 (s, 1H), 7.28 (d, $J = 8.1$ Hz, 2H), 6.77 (d, 2H), 6.35 (s, 2H), 6.00 – 5.93 (m, 2H), 5.02 (dd, $J = 11.8$, 3.1 Hz, 1H), 4.03 (t, $J = 5.9$ Hz, 2H), 3.55 (d, $J = 4.7$ Hz, 5H), 3.1 (dd, $J = 11.9$, 3.1 Hz, 1H), 2.6 (m, 3H), 2.42 (t, $J = 4.6$ Hz, 4H). ^{13}C NMR (100 MHz, DMSO- d_6 , δ , ppm): 160.12, 159.9, 157.8, 157.4, 145.8, 130.6, 128.4, 115.5, 100.6, 96.1, 94.2, 76.4, 66.7, 65.9, 57.3, 53.8, 30.4. IR (cm^{-1}): 2973, 2868 (C-H), 1614 (C=N), 1595, 1457 (C=C), 1202 (C-O), 1159 (C-N). HRMS: m/z $\text{C}_{21}\text{H}_{26}\text{N}_3\text{O}_5$ (M+H) $^+$ found: 400.1864; calc. 400.1872.

2.4.3. (E)-7-(2-piperidinoethoxy)-5-hydroxy-2-(4-hydroxyphenyl) chroman-4-oxime (5a)

Yield 27%, ^1H NMR (400 MHz, DMSO- d_6 , δ , ppm): 11.35 (s, 1H), 11.32 (s, 1H), 9.55 (d, $J = 8.4$ Hz, 1H) 7.27 (d, $J = 8.4$ Hz, 2H), 6.77 (dd, $J = 8.4$, 2.1 Hz, 2H), 6.08 (d, $J = 12.4$ Hz, 2H), 5.02 (d, $J = 11.5$ Hz, 1H), 4.25 (m, 2 H), 3.27 (m, 5H), 2.81(dd, $J = 7.2$, 11.8 Hz, 2H), 2.48 (m,2H), 1.76-1.61 (m, 3H), 1.48 (m, 2H). ^{13}C NMR (100 MHz, DMSO- d_6 , δ , ppm): 160.6, 159.4, 158.3, 157.8, 146.5, 130.1, 128.4, 115.48, 106.19, 95.79, 94.15, 76.5, 61.24, 54.36, 52.9, 29.7, 28.7, 22.6. IR (cm^{-1}): 3229 (O-H) 2988, 2902 (C-H), 1616 (C=N), 1577, 1457, 1373 (C=C), 1199 (C-O), 1156 (C-N). HRMS: m/z $\text{C}_{22}\text{H}_{27}\text{N}_2\text{O}_5$ (M+H) $^+$ found:399.1916; calc. 399.1919.

2.4.4. (*E*)-7-(2-morpholinoethoxy)-5-hydroxy-2-(4-hydroxyphenyl) chroman-4-oxime (**5b**)

Yield 90%, ¹H NMR (400 MHz, DMSO-d₆, δ, ppm): 11.31 (s, 1H), 11.24 (s, 1H), 9.5 (s, 1H), 7.2 (d, *J* = 8.4 Hz, 2H), 6.7 (d, *J* = 8.4 Hz, 2H), 5.99 (d, *J* = 4.6 Hz, 2H), 4.99 (dd, *J* = 11.7, 3.1 Hz, 1H), 4.02 (s, 2H), 3.54 (m, 5H), 3.3 (dd, *J* = 17.1, 3.2 Hz, 1H), 2.73 (dd, *J* = 17.1, 11.7 Hz, 2H), 2.49 (s, 4H). ¹³C NMR (100 MHz, DMSO-d₆, δ, ppm): 161.2, 159.4, 158.3, 157.95, 153.4, 130.1, 128.5, 115.6, 98.8, 96.1, 94.8, 76.4, 66.2, 56.9, 53.6, 43.2, 29.4. IR (cm⁻¹): 3240 (O-H), 2971, (C-H), 1614 (C=N), 1568, 1455, (C=C), 1196 (C-O), 1160 (C-N). HRMS: *m/z* C₂₁H₂₅N₂O₆ (M+H)⁺ found:401.1707; calc. 401.1712.

2.5. Molecular Docking

Molecular docking can be employed to replicate the ligand-protein interaction at the atomic level thereby it possible for us to better understand fundamental biological processes and identify how a ligand functions at the binding site of target proteins. Utilizing Auto Dock Tools 1. 5. 6 [17], molecular docking simulations of synthesized compounds were performed. BSA's crystal structure was obtained from Protein Databank (PDB ID:3V03). To prepare the protein for docking analysis, water molecules were deleted, and polar hydrogens and Kollman charges were added. The ligands were prepared for docking via the Chem3D program's molecular mechanics (MM2), which minimized their energy. The grid box was initially set to 126x126x126 for x, y, and z, respectively, and the best binding site was identified. The interactions were then thoroughly explored by readjusting the grid box to 60x60x60 for x, y, and z, respectively. Docking studies were carried out using the Lamarckian Genetic Algorithm (LGA). Eventually, among the nine docking interactions, the lowest energy ligand-protein binding was selected and analyzed. Ligand-protein interactions were simulated in Pymol [18] and Biovia Studio [19] programs.

2.6. Drug-Likeness Prediction

SwissADME was used to determine the drug-likeness study by computing the pharmacokinetic parameters of the compounds, eliminating and screening those that are incompatible. The Lipinski filter (Pfizer), which classifies small molecules based on physicochemical factors which includes Mw, H-bond acceptors, H-bond donors, TPSA, and log P is employed for this purpose [20]. The SwissADME program's Lipinski filter (Pfizer) was employed to examine the synthetic compounds' pharmacological similarities.

2.7. ADMET

ADMET server analyzes parameters such as Human

intestinal absorption (HIA), Metabolism, (CYP450) Inhibitors, carcinogenesis, Biodegradation of the test compound. (<http://lmm.d.ecust.edu.cn/admetserver/>). Using several models, the server predicts more than 50 ADMET parameters [21].

3. Results and Discussion

3.1. Chemistry

Naringenin contains three hydroxyl groups. The 4- and 7-hydroxy groups are easily available for O-substitutions, whereas the 5-hydroxy group is less accessible. When we compare the hydroxy groups, the 7-hydroxy group has more acidic hydrogen than the 4'-hydroxy group due to the hydroxy group's conjugation with the ketone. Starting with this knowledge, 1,2-dibromoethane was added to the mixture of (±)-naringenin (**1**) in acetone, resulting in a fair yield of 7-(2-Bromoethoxy)-5-hydroxy-2-(4-hydroxyphenyl)-chroman-4-one (**2**) with existing procedures [7] and then using the compound **2** and the proper amines (morpholine or piperazine) in acetonitrile, we started preparing two derivatives of 7-O-naringenin-amine. Next, to boost the molecule's ability to form more hydrogen bonds and to distinguish between its contacts, hydrazone and oxime derivatives of the related substance were created from each product. Oxime and hydrazone derivatives were obtained by adding sodium acetate along with hydroxylamine or hydrazine to morpholine and piperidine-containing derivatives of racemic naringenin, respectively. The spectral data of the synthesized molecules were evaluated by comparing them with naringenin oximes and hydrazones reported in the literature [13,22,23]. It was reported that when the ketone compound was converted to the oxime derivative, the carbonyl carbon and α carbon signals shifted to the upper field, and for α carbon, the ¹H and ¹³C δ-values of the *E*-configuration were lower than the *Z*-configuration. Based on these findings and the comparison of our NMR values with the *E* and *Z* naringenin oximes available in the literature, we believe that the configuration of the molecules we synthesized is *E* [22]. In addition, the NMR data of the obtained hydrazones were similar to the *E*-naringenin hydrazones in the literature [23].

For **4a**, (Figure 1) in the ¹H-NMR spectrum (Figure S1), the singlet 2H peak at 6.35 ppm represents the hydrogens in the N-NH₂ structure. The structure description of the rest of the molecule was detailed in our previous work [9]. The absence of a peak at 200-190 ppm in the ¹³C-NMR spectrum (Figure S2) proves the conversion of the carbonyl group to the imine structure, and the imine bond with the peak at 145.7 ppm is proven. The absence of a peak between 1800-1650 cm⁻¹ in the IR spectrum proves that the carbonyl group in **4a** has disappeared, while the

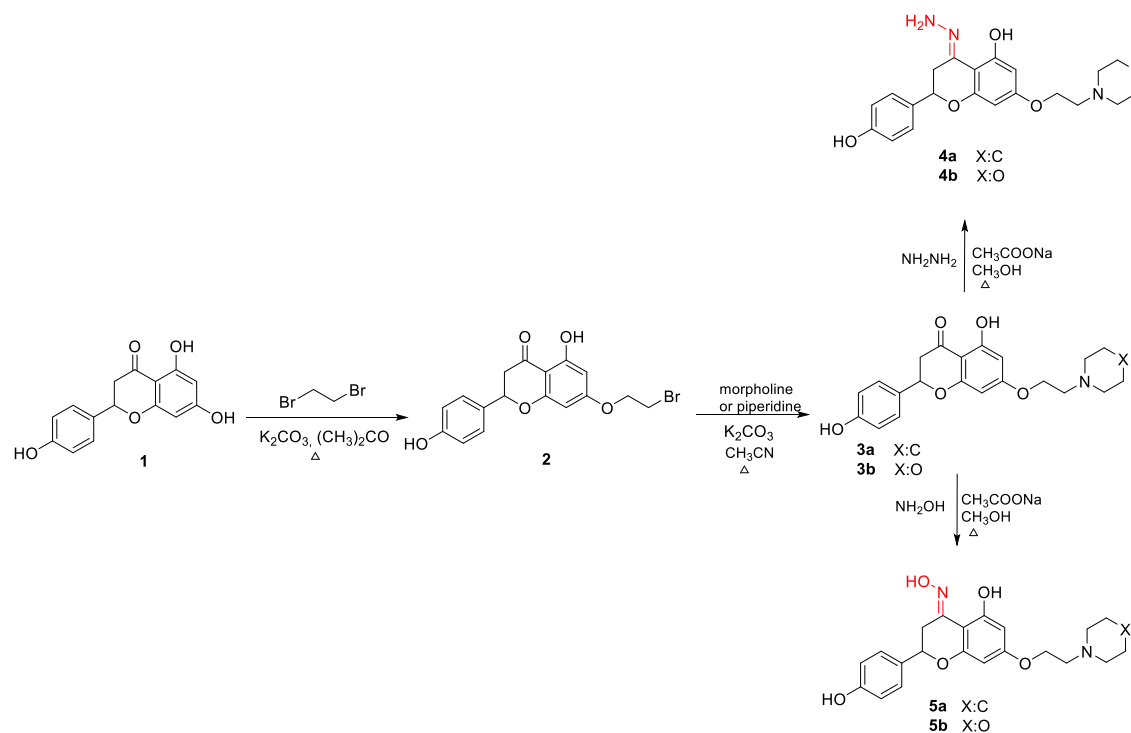


Figure 1. Synthesis of target oximes and hydrazones **4a-b** and **5a-b**

peak seen in the IR spectrum of 1616 cm^{-1} proves that the imine bond is formed. The MS value of the substance whose mass analysis was performed was found to be 398.2071 [M+H] and the value found is in agreement with the calculated value.

Similarly, for **5b**, it expresses the oxime -OH of the singlet peak at 11.31 ppm, and C5-OH of the singlet at 11.24 ppm in the $^1\text{H-NMR}$ spectrum. The singlet C5-OH peak, which was recorded at 12.08 ppm (for **3b**), moved to 11.24 ppm (for **5b**) after the C=O group was converted to the C=N group. This is because of the difference in the atom with which the H in C5-OH forms the H-bond. (Figure S13). In the $^{13}\text{C-NMR}$ spectrum (Figure S14), the peak showing the carbonyl group at 200-190 ppm disappeared, while the peak observed at 157.95 ppm corresponds to the oxime carbon. The absence of a peak between $1800\text{-}1650\text{ cm}^{-1}$ in the IR spectrum indicates the loss of the carbonyl group in the structure. The peak seen at 1614 cm^{-1} in the IR spectrum proves the formation of an oxime bond. 399.1916 observed in the mass spectrum was seen as [M+H] and the structure was confirmed.

Similar data were obtained for compounds **4b** and **5a**, consistent with the expected oxime and hydrazine structures.

3.2. Molecular Docking Analysis

The use of molecular docking simulations is a very efficient method for determining the structural compatibility of the investigated compounds and the

target macromolecules, their mode of interaction, binding energy, and chemical environment [24]. When the binding potential of flavonoids with BSA is examined, it was shown that different substituents greatly affect the binding ability of the molecules to BSA. Studies employing naringenin, which lacks functional groups, indicated that the binding energy to BSA was higher, whereas the binding energy of derivatives that could create more hydrogen bonds decreased. The molecules subject to our research can make more H-bonds and the molecular docking results of them with BSA, provide insights into the structural activity of them docked to a target biomolecule.

In the study of Hu et al. [25] the specific interaction of naringenin and BSA was investigated by spectroscopic methods including fluorescence spectroscopy and UV-visible absorption spectroscopy, and it was found that naringenin binds to BSA via hydrophobic interactions. Liu et al. [26] reported that naringenin's binding energy to BSA protein was 7.6 kcal/mol, it did not form hydrogen bonds, and it bound to the BSA through hydrophobic interactions. When the docking data were compared, it was seen that the oxime and hydrazone components of the designed naringenin derivatives reduced the binding energy by forming multiple hydrogen bonds.

The configurations of the naringenin derivatives-BSA complexes with the lowest binding energy are shown in Figure 2. Docking results revealed that all compounds bound inside the binding pocket in subdomain IB of BSA

Table 1. Binding energy and interactions of the compounds with BSA protein.

Docked Comp.	Binding Energy (kcal/mol)	Interacted residues	
		H-bond	Non-bonded
4a	-8.9	Asp108 O with H-N Asp108 O with H-N Leu112 N-H with O Leu112 O with H-O	Pro110, Arg144 π -Alkyl His145, Ala193 Alkyl Ser109 Amide- π Glu424 π -Anion Arg458 π -Cation
4b	-8.6	Leu112, N-H with O His145 N-H with O His145 N-H with N Ser192 O with H-N Ser192 H with O	Pro110, Arg144 π -Alkyl His145, Ala193 Alkyl Ala193 π -Sigma Arg458 π -Cation
5a	-8.8	Asp108 O with H-O Arg458 O with H-O Leu112 N-H with O Leu112 O with H-O	Pro110, Arg144 π -Alkyl His145, Ala193, Leu454, Ile455 Alkyl Ser109 Amide- π Glu424 π -Anion Arg458 π -Cation
5b	-8.5	Asp108 O with H-O Leu112 O with H-O	Pro110, Arg144 π -Alkyl His145, Ala193 Alkyl Ser109 Amide- π Glu424 π -Anion Asp458 π -Cation Arg458 N-H with H-O Arg458 N-H with H-O unfavorable donor-donor

with close binding energy (in the range of -8.5 / -8.9 kcal/mol). Amino acids in BSA bond with molecules via hydrogen bonds and hydrophobic interactions, as shown in Table 1. **4a** interacts with Asp108 and Leu112 via four hydrogen bonds, and **4b** interacts with Leu112, His145, and Ser192 amino acids via five hydrogen bonds. **5a** interacts with Asp108, Leu112, and Arg458 amino acids via four hydrogen bonds; **5b** interacts with Asp108 and Leu112 amino acids via two hydrogen bonds. We found that compounds **4a**, **5a**, and **5b** primarily functioned as hydrogen bond acceptors, whereas compound **4b** primarily functioned as a hydrogen bond donor. All molecules are surrounded by the Pro110 and Arg144 amino acids through π -alkyl interactions, His145 and Ala193 amino acids through alkyl interactions, and Ser109 amino acid through amide- π interactions. Additionally, although **4a**, **5a**, and **5b** interact with Glu424 amino acid via π -anion all compounds interact with Arg458 amino acid via π -cation. Finally, **5b** interacts with Arg458 amino acid through two unfavorable donor-donor interactions, so its binding energy is higher than other molecules. Multiple connections between derivatives and the BSA structure imply strong interactions and suggest that these substances can be delivered as medicinal products.

3.3. Drug-likeness Profiles

The druggability of the compounds and the corresponding radar plots are listed in Table 2. The six parameters studied by SwissADME [27], including lipophilicity, size, polarity, insolubility, saturation, and elasticity, are within the desired range as seen on the radar chart for all compounds.

In addition, all compounds obey Lipinski's rule of five [16]: number of H bond donors ≤ 5 , H bond acceptor ≤ 10 , molecular weight ≤ 500 , TPSA $\leq 140 \text{ \AA}^2$, $\log P \leq 5$. Compounds have enough hydrogen bond acceptors and donors to form hydrogen bonds. The mass of the compounds is within the desired range, and the presence of five rotatable bonds (should be less than ten) suggests molecular flexibility. They show strong permeability to the blood-brain barrier (BBB) and cellular plasma membrane, as topological polar surface area (TPSA) values are less than 140 \AA^2 . Octanol-water distribution coefficient (Log P), a metric for the hydrophilicity or hydrophobicity of molecules, shows that molecules with $\log P < 0$ have poor lipid bilayer permeability and those with $\log P > 3$ have poor water solubility. Log P values for them, which vary from 1.79 to 2.89, show that they are soluble in both water and lipids.

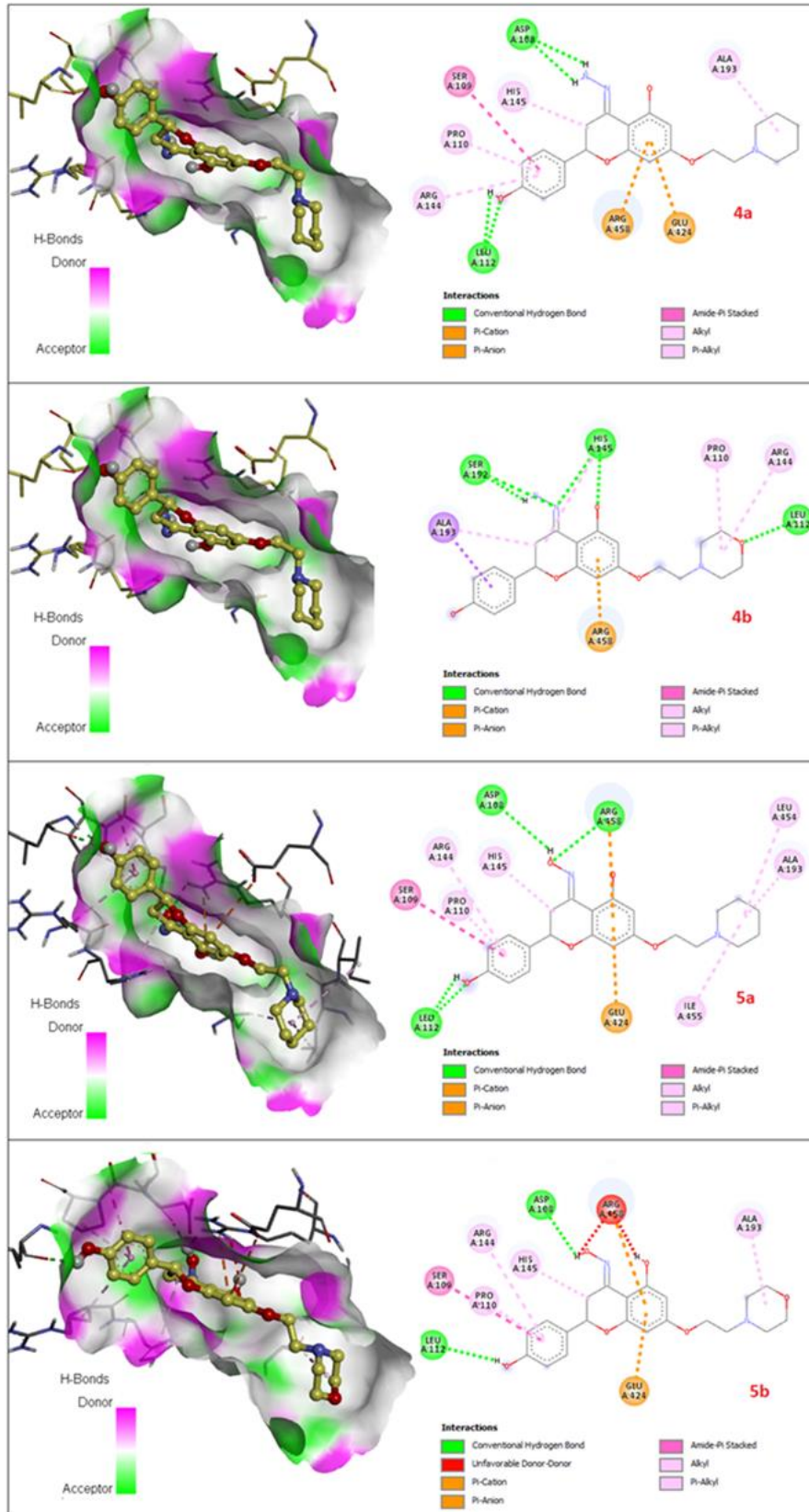
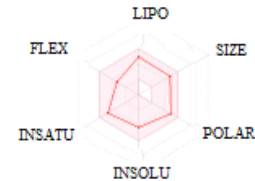
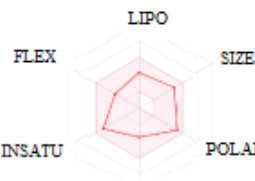
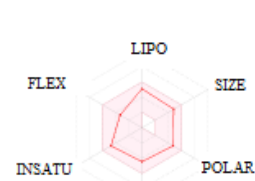
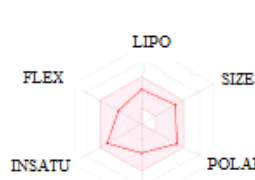


Figure 2. The lowest energy docked poses and 2D representations of the interactions of the **4a**, **4b**, **5a**, **5b** with bovine serum albumin.

Table 2. Druggability of Compounds.

Comp.	HBD ^[a]	HBA ^[b]	nROTB ^[c]	Lipinski, violation	TPSA ^[d] (Å ²)	MW ^[e]	logP ^[f]	Radar Chart
4a	3	6	5	Yes, 0	100.54	397.47	2.66	
4b	3	7	5	Yes, 0	109.77	399.44	1.79	
5a	3	7	5	Yes, 0	94.75	398,45	2.89	
5b	3	8	5	Yes, 0	103.98	400.43	2.03	

^[a] the number of H-bond donors, ^[b] the number of H-bond acceptors, ^[c] nROTB: the number of rotatable bonds, ^[d] Topological polar surface area, ^[e] Molecular Weight, ^[f] the octanol-water partition coefficient. In radar charts, the pink color shows the ideal range.

Table 3. ADMET profiling of the compounds.

	Absorption	Distribution	Metabolism (CYP450) Inhibitor					Excretion		Toxicity		
	HIA ^[a]	BBB ^[b]	2C19	3A4	2C9	2D6	1A2	B.D. ^[c]	C. ^[d]	Hp.T ^[e]	S.S ^[f]	AOT ^[g]
4a	82.30 (+)	0.675 (+)	No	No	No	No	No	NB ^[h]	No	No	No	III
4b	82.30 (+)	0.675 (+)	No	No	No	No	No	NB	No	No	No	III
5a	79.17 (+)	0.65 (+)	No	No	No	No	No	NB	No	No	No	III
5b	79.17 (+)	0.65 (+)	No	No	No	Yes	No	NB	No	No	No	III

^[a] Human Intestinal Absorption, ^[b] Blood Brain Barrier, ^[c] Biodegradation, ^[d] Carcinogenicity, ^[e] Hepatotoxicity, ^[f] Skin Sensitization, ^[g] Acute Oral Toxicity, ^[h] Non-biodegradable

3.4. ADMET Properties

The *in silico* predictions of the ADMET properties of the compounds are shown in Table 3. They can be absorbed by the human intestine and can cross the blood-brain barrier. This indicates the compounds have good potential for dispersion and absorption. The metabolic activity of the compounds was evaluated using a microsomal enzyme (Cytochrome P450 inhibitors), which catalyzes crucial drug metabolism processes. It can be seen from Table 3 that the compounds do not inhibit cytochrome P450, such as CYP: 1A2, 2C19, 2C9, 2D6, and 3A4, which cause drug interactions. The compounds are non-biodegradable nevertheless, they present no carcinogenicity, hepatotoxicity, or skin sensitization. They have type III (slightly toxic) acute oral toxicity (LD50) values, which are easily converted to type IV (nontoxic) during hit-lead optimization. According to the results, they have a good ADMET profile and are ideal candidates for medications.

4. Conclusion

In the study, two oximes and two hydrazones as derivatives of naringenin were synthesized, their geometries were clarified, and the binding interaction of each structure with BSA was investigated by molecular docking. The binding energies of the compounds were found to be in the range of -8.5 - 8.9 kcal/mol and the values were more effective than the molecular docking interactions of naringenin with BSA. In addition, the drug potentials of the molecules were investigated with SwissADME and admetSAR. The molecules complied with Lipinski's five rules, are not carcinogenic, hepatotoxic, skin-sensitizing properties, and the BBB values were within the range.

Acknowledgement

We gratefully acknowledge the financial support of the scientific research project commission of Trakya University (TÜBAP 2018/232).

Author's Contributions

Ferhat Melihcan Abay: Oxime and Hydrazone Preparation.

Hafize Ozcan: Data Analysis, Original draft preparation, Writing.

Ayşen Şuekinçi Yılmaz: Molecular Docking, ADMET predictions, Writing.

Ömer Zaim: Supervision, Reviewing and Editing.

Ethics

There are no ethical issues after the publication of this manuscript.

References

- [1]. Formica, J, Regelson, W. 1995. Review of the biology of quercetin and related bioflavonoids. *Food and Chemical Toxicology*; 33(12):1061-1080. [https://doi.org/10.1016/0278-6915\(95\)00077-1](https://doi.org/10.1016/0278-6915(95)00077-1).
- [2]. Cazarolli, LH, Zanatta, L, Alberton, EH, Bonorino, Figueiredo, MSR, Folador, P, Damazio, RG, et al. 2008. Flavonoids: prospective drug candidates. *Mini Reviews in Medicinal Chemistry*; 8(13):1429-1440. <https://doi.org/10.2174/138955708786369564>.
- [3]. Cushnie, TT, Lamb, AJ. 2011. Recent advances in understanding the antibacterial properties of flavonoids. *International Journal of Antimicrobial Agents*; 38(2):99-107. <https://doi.org/10.1016/j.ijantimicag.2011.02.014>.
- [4]. Miller, E, Schreier, P. Studies on flavonol degradation by peroxidase (donor: H₂O₂-oxidoreductase, EC 1.11. 1.7): Part 1—Kaempferol. *Food Chemistry*; 17(2):143-154. [https://doi.org/10.1016/0308-8146\(85\)90083-4](https://doi.org/10.1016/0308-8146(85)90083-4).
- [5]. Wiseman, H. 1996. Dietary influences on membrane function: importance in protection against oxidative damage and disease. *The Journal of Nutritional Biochemistry*; 7(1):2-15. [https://doi.org/10.1016/0955-2863\(95\)00152-2](https://doi.org/10.1016/0955-2863(95)00152-2).
- [6]. Hollman, P, Hertog, M, Katan, M. 1996. Role of dietary flavonoids in protection against cancer and coronary heart disease. *Biochemical Society Transactions*; 24:785-789. <https://doi.org/10.1042/bst0240785>.
- [7]. Zaim, Ö, Doğanlar, O, Zreigh, MM, Doğanlar, ZB, Özcan, H. 2018. Synthesis, Cancer-Selective Antiproliferative and Apoptotic Effects of Some (±)-Naringenin Cycloaminoethyl Derivatives. *Chemistry & Biodiversity*; 15(7):e1800016. <https://doi.org/10.1002/cbdv.201800016>.
- [8]. Hodek, P, Trefil, P, Stiborová, M. 2002. Flavonoids-potent and versatile biologically active compounds interacting with cytochromes P450. *Chemico-Biological Interactions*, 139(1):1-21. [https://doi.org/10.1016/S0009-2797\(01\)00285-X](https://doi.org/10.1016/S0009-2797(01)00285-X).
- [9]. Ahmadi, A, Hassandarvish, P, Lani, R, Yadollahi, P, Jokar, A, Bakar, SA, et al. 2016. Inhibition of chikungunya virus replication by hesperetin and naringenin. *RSC Advances*; 6(73):69421-69430. <https://doi.org/10.1039/C6RA16640G>.
- [10]. Denaro, M, Smeriglio, A, Trombetta, D. 2021. Antioxidant and anti-inflammatory activity of citrus flavanones mix and its stability after in vitro simulated digestion. *Antioxidants*; 10(2):140. <https://doi.org/10.3390/antiox10020140>.
- [11]. Babu, KS, Babu, TH, Srinivas, P, Kishore, KH, Murthy, U, Rao, JM. 2006. Synthesis and biological evaluation of novel C (7) modified chrysin analogues as antibacterial agents. *Bioorganic & Medicinal Chemistry Letters*; 16(1):221-2244. <https://doi.org/10.1016/j.bmcl.2005.09.009>.
- [12]. Zaim, Ö, Doğanlar, O, Doğanlar, ZB, Özcan, H, Zreigh, MM, Kurtdere, K. 2022. Novel synthesis naringenin-benzyl piperazine derivatives prevent glioblastoma invasion by inhibiting the hypoxia-induced IL6/JAK2/STAT3 axis and activating caspase-dependent apoptosis. *Bioorganic Chemistry*; 129:106209. <https://doi.org/10.1016/j.bioorg.2022.106209>.
- [13]. Türkkân, B, Özyürek, M, Bener, M, Güçlü, K, Apak, R. 2012. Synthesis, characterization and antioxidant capacity of naringenin-oxime. *Spectrochimica Acta Part A: Molecular and Biomolecular Spectroscopy*; 85(1):235-240. <https://doi.org/10.1016/j.saa.2011.09.066>.

- [14]. Carter, DC, Ho, JX. 1994. Structure of serum albumin. *Advances in Protein Chemistry*; 45:153-203.
[https://doi.org/10.1016/S0065-3233\(08\)60640-3](https://doi.org/10.1016/S0065-3233(08)60640-3).
- [15]. Otagiri, M. 2005. A molecular functional study on the interactions of drugs with plasma proteins. *Drug Metabolism and Pharmacokinetics*, 20(5):309-323.
<https://doi.org/10.2133/dmpk.20.309>.
- [16]. Zhang, G, Chen, X, Guo, J, Wang, J. 2009. Spectroscopic investigation of the interaction between chrysin and bovine serum albumin. *Journal of Molecular Structure*; 921(1-3):346-351.
<https://doi.org/10.1016/j.molstruc.2009.01.036>.
- [17]. Trott, O, Olson, AJ. 2010. AutoDock Vina: improving the speed and accuracy of docking with a new scoring function, efficient optimization, and multithreading. *Journal of Computational Chemistry*; 31(2):455-461.
<https://doi.org/10.1002/jcc.21334>.
- [18]. Masand, VH, Rastija, V. 2017. PyDescriptor: A new PyMOL plugin for calculating thousands of easily understandable molecular descriptors. *Chemometrics and Intelligent Laboratory Systems* 169:12-18. <https://doi.org/10.1016/j.chemolab.2017.08.003>.
- [19]. Studio D. 2008. "Discovery studio" Accelrys [21]. 2008. <https://discover.3ds.com/discovery-studio-visualizer-download>.
- [20]. Lipinski, CA. 2004. Lead-and drug-like compounds: the rule-of-five revolution. *Drug Discovery Today: Technologies*; 1(4):337-341.
<https://doi.org/10.1016/j.ddtec.2004.11.007>.
- [21]. Job, P. 1928. Job's plot analyses for the 2-CG and 3-CG complexes were consistent with 1: 1 stoichiometry. *Annalen der Chemie*; 9:113-34.
- [22]. Latif, A. D., Gonda, T., Vágvölgyi, M., Kúsz, N., Kulmány, Á., Ocsosvski, I., Hunyadi, A. 2019. Synthesis and in vitro antitumor activity of naringenin oxime and oxime ether derivatives. *International Journal of Molecular Sciences*; 20(9), 2184.
<https://doi.org/10.3390/ijms20092184>
- [23]. Ferreira, R. J., Gajdacs, M., Kincses, A., Spengler, G., Dos Santos, D. J., Ferreira, M. J. U. 2020. Nitrogen-containing naringenin derivatives for reversing multidrug resistance in cancer. *Bioorganic & Medicinal Chemistry*, 28(23), 115798.
<https://doi.org/10.1016/j.bmc.2020.115798>
- [24]. Yılmaz, AŞ, Uluçam, G. 2023. Novel N-benzyl-2-oxo-1, 2-dihydrofuro [3, 4-d] pyrimidine-3 (4H)-carboxamide as anticancer agent: Synthesis, drug-likeness, ADMET profile, DFT and molecular modelling against EGFR target. *Heliyon*; e12948.
<https://doi.org/10.1016/j.heliyon.2023.e12948>.
- [25]. Hu, Y. J., Wang, Y., Ou-Yang, Y., Zhou, J., & Liu, Y. 2010. Characterize the interaction between naringenin and bovine serum albumin using spectroscopic approach. *Journal of Luminescence*, 130(8), 1394-1399.
<https://doi.org/10.1016/j.jlumin.2010.02.053>
- [26]. Liu, J., Yang, Z., Cheng, Y., Wu, Q., He, Y., Li, Q., & Cao, X. 2020. Eriodictyol and naringenin inhibit the formation of AGEs: An in vitro and molecular interaction study. *Journal of Molecular Recognition*, 33(1), e2814.
<https://doi.org/10.1002/jmr.2814>
- [27]. Daina, A, Michielin, O, Zoete, V. 2017. SwissADME: a free web tool to evaluate pharmacokinetics, drug-likeness and medicinal chemistry friendliness of small molecules. *Scientific Reports*; 7(1):42717.
<https://www.nature.com/articles/srep42717>.

Integrating GIS and Fuzzy BWM for Solar PV Power Plant Site Selection: A Case Study of Konya, Turkey

Ömer Öztaş¹ , Bilal Ervural^{2*} 

1 Department of Industrial Engineering, OSTIM Technical University, 06374 Ankara, Türkiye

2 Department of Industrial Engineering, Necmettin Erbakan University, 42090 Konya, Türkiye

* bervural@erbakan.edu.tr

* Orcid No: 0000-0002-5206-7632

Received: November 22, 2024

Accepted: February 4, 2025

DOI: 10.18466/cbayarfbe.1589809

Abstract

The global demand for energy continues to rise, driving the need for sustainable and efficient energy solutions. This study presents a comprehensive framework that combines the fuzzy best-worst method (BWM) with geographic information systems (GIS) to optimize solar power plant site selection. Eight criteria, including solar irradiation, slope, aspect, and proximity to infrastructure and water resources, were evaluated using the fuzzy BWM approach. These weighted criteria were integrated into GIS to create a suitability map, categorized into five levels of potential. The proposed framework was applied to Konya, Türkiye, a region with abundant solar energy resources, and highly suitable sites for solar photovoltaic (PV) power plant development were successfully identified. Furthermore, a sensitivity analysis was conducted to validate the robustness of the results. The findings demonstrate the framework's potential as a reliable decision-support tool for energy planners and policymakers, offering a replicable model for regions with similar characteristics.

Keywords: Best-Worst Method, Fuzzy Logic, GIS, MCDM, Renewable Energy, Solar.

1. Introduction

The energy demand is growing globally due to an increasing population and intensive industrial activities. This has emphasized the need for sustainable and efficient energy solutions [1]. As a result, there has been a noticeable shift towards exploring alternative energy sources, with a particular focus on renewable energy. This shift is motivated by the environmental consequences and limitations of conventional fossil fuels. Solar energy is considered a leading candidate among renewable options because of its renewable nature and consistent availability [2].

Today, the utilization of solar energy has experienced a surge in global popularity. In alignment with this global trend, Türkiye is directing its attention toward optimizing the use of renewable resources, with a particular emphasis on solar energy, as a strategic approach to efficiently address its expanding energy requirements. According to Türkiye's National Energy Plan [3], Türkiye aims to achieve net zero emissions by 2053. The

plan outlines strategic actions until 2035 and anticipates that Türkiye's primary energy consumption,

which was 147.2 million tons of oil equivalent in 2020, is expected to increase to 205.3 million tons of oil equivalent by 2035. Electricity consumption of Türkiye, displaying an average annual increase of 4.4 percent during the period spanning 2000 to 2020, is projected to sustain an average annual growth rate of 3.5 percent through 2035, culminating in a total of 510.5 TWh (terawatt-hours). The proportion of electricity in final energy consumption, constituting 21.8 percent in 2020, is expected to rise to 24.9 percent by 2035. The installed electricity capacity in Türkiye, standing at 95.9 GW (gigawatt) after 2020, is forecasted to attain 189.7 GW by 2035, with renewable energy sources increasing their share, rising from 52 percent in 2020 to 64.7 percent in 2035 (see Fig. 1). Notably, renewable energy sources are planned to contribute 74.3 percent to the anticipated 96.9 gigawatts of new electricity capacity to be commissioned by 2035. The most significant increase in investment in renewable resources is allocated to solar energy. The installed solar power capacity in Türkiye, which is quantified at 6.7 GW at the end of 2020, is projected to

rise to 52.9 GW by 2035. This significant increase represents almost five times the 9.32 GW recorded in 2022. Once the capacity is realized in 2035, solar energy will have the highest share of Türkiye's total installed capacity, displacing other sources.

The initial step in establishing solar power plants involves identifying regions with high solar energy potential by considering environmental, economic, and social factors. Proper site selection is critical for maximizing energy generation, minimizing costs, and ensuring the long-term sustainability of renewable energy projects. The integration of multi-criteria

decision-making (MCDM) methodologies with geographic information system (GIS) techniques has proven highly effective for renewable energy planning [4–9]. Through this integration, decision-makers can employ GIS as a dominant tool for handling spatial solar energy data, while MCDM methods aid in assessing alternative solar power plant locations [10]. The techniques of MCDM enable the weighting and identification of the most suitable areas by considering many criteria. Various approaches, including their fuzzy versions, are employed in selecting locations for photovoltaic energy plants.

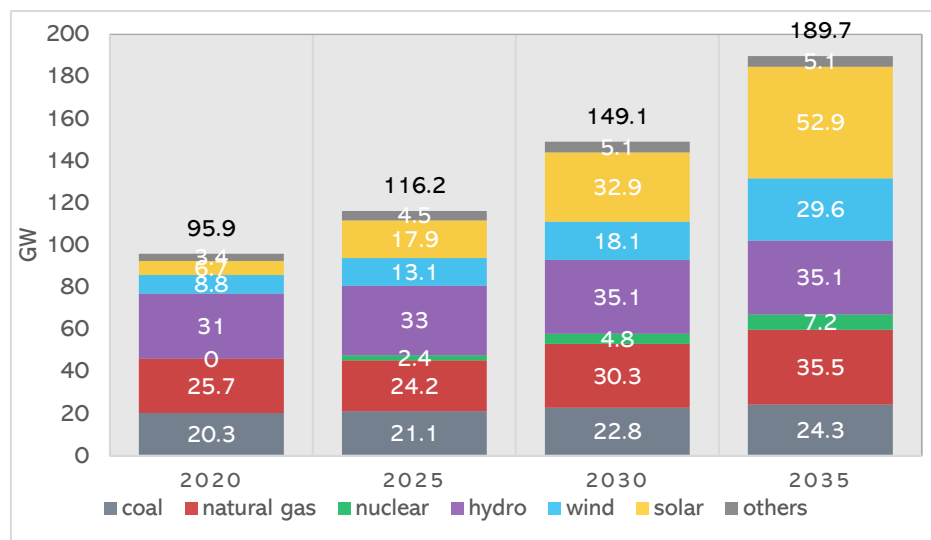


Figure 1. Installed capacity by source in Türkiye [2]

The literature underscores the importance of integrating GIS with MCDM methods for solar PV power plant site selection. The analytic hierarchy process (AHP) is widely applied among these methods. Akkas et al. [11] utilized AHP alongside methods such as ELECTRE, TOPSIS, and VIKOR for site selection in Central Anatolia, Türkiye, while Aktas and Kabak [12] integrated AHP with TOPSIS to evaluate solar plant sites across Türkiye. Aragonés-Beltrán et al. [13] used AHP for PV solar power plant investment decisions in Spain, and Colak et al. [14] employed GIS-AHP for optimal site selection in Malatya province of Türkiye. Similarly, Al Garni and Awasthi [15] adopted a GIS-AHP approach for site selection in Saudi Arabia, further demonstrating the adaptability of AHP-based models across regions.

GIS integration in solar PV power plant site selection extends beyond AHP to various other MCDM methods. Lee et al. [16] employed a hybrid MCDM approach, using the fuzzy analytic network process (ANP) and VIKOR for PV solar plant site selection in Taiwan. Shorabeh et al. [10] utilized a GIS-based method for solar power plant site selection in Iran, emphasizing the pivotal role of geographical information in decision-making. Hybrid models that combine multiple decision-making

methods are emerging as an intriguing aspect. Badi et al. [17] introduced a hybrid SWARA-DEMATEL model for solar park site selection in Libya, demonstrating the versatility of hybrid models in considering financial, social, and environmental dimensions in decision-making processes. Beyond MCDM methods, fuzzy logic has found application in certain studies. Zoghi et al. [18], in their case study in Isfahan, Iran, employed a fuzzy logic model and weighted linear combination method for solar site selection, demonstrating the adaptability of fuzzy logic in decision support systems. Noorollahi et al. [1] designed a decision support tool for suitable sites for a solar photovoltaic power plant in Iran, using Fuzzy and Boolean logic, AHP, and GIS. The literature emphasizes the integration of GIS with various fuzzy techniques for effective solar energy plant site selection. These studies highlight the critical role of fuzzy techniques in enhancing the robustness of renewable energy planning by managing uncertainties inherent in the decision-making process [19–22].

While AHP has been a dominant tool for prioritizing criteria in renewable energy site selection, the best-worst method (BWM) has recently emerged as a robust alternative. Its crisp version has been successfully

applied in various renewable energy contexts, including assessing renewable energy sources [23], wind and solar power plant sites [20,24], solar panel technology [25], sites for wind-powered hydrogen production [26], and onshore wind plants [27]. However, the integration of fuzzy BWM with GIS remains underexplored. Fard et al. [28] demonstrated the use of fuzzy BWM with GIS for solar site selection, applying the version proposed by Guo and Zhao [29]. However, our study adopts the improved fuzzy BWM methodology developed by Dong et al. [30], which addresses the key limitations of the earlier method and provides more accurate and reliable results.

This study focuses on the need for site selection in Konya, Türkiye, to utilize its vast solar energy potential for PV projects. Despite having enormous potential, there has been a lack of comprehensive studies focusing on site selection for such regional projects. This research aims to fill this gap by thoroughly analyzing potential sites using a methodological framework outlined in Fig. 2. The study provides valuable insights for renewable energy planning and development in Konya. This study uses the improved fuzzy BWM method to weight the evaluation criteria. This method allows for the representation of vague or imprecise information, enhancing the robustness and comprehensiveness of the decision-making process. The study identifies highly suitable areas within Konya through a systematic investigation, including criterion weighting, GIS analysis, suitability mapping, and sensitivity analysis. This demonstrates the model's efficacy in addressing the complexities of site selection for solar PV projects. The research provides information

to aid decision-makers in selecting the most suitable sites for solar energy infrastructure development in Konya.

Based on the characteristics mentioned above, the proposed methodology offers the following contributions:

- Firstly, the study uses tailored criteria reflecting Konya's geographical and environmental characteristics. These criteria are weighted with the fuzzy BWM method to yield more accurate results in uncertain conditions.
- Secondly, a comprehensive sensitivity analysis is conducted within the GIS environment to evaluate the robustness of the results and to understand the impact of individual criteria on the overall suitability map.
- Finally, the study proposes a sustainable and adaptable approach by developing a framework that can be applied to other regions with similar characteristics, even though it is specifically tailored for Konya.

The remainder of this study is organized as follows: Section 2 delineates the study area and identifies the criteria and restriction factors. The fuzzy BWM is then introduced as a methodology. Sections 3 and 4 present the results and discuss findings from the study. This includes calculating the criteria weights using fuzzy BWM and conducting suitability and sensitivity analysis. Finally, Section 5 concludes the study, highlighting its limitations and providing suggestions for further research.

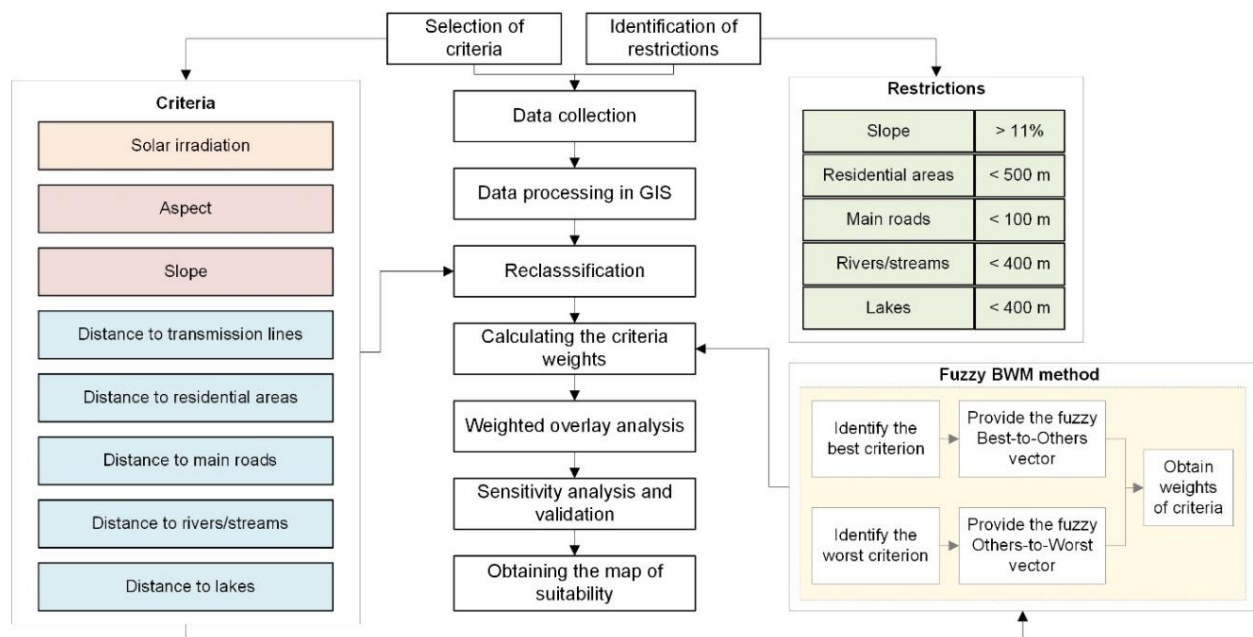


Figure 2. Schematic representation for the solar PV site selection.

2. Materials and Methods

The primary aim of this study is to evaluate site alternatives to determine optimal locations for solar PV projects in Konya, Turkey, which is renowned for its significant solar energy potential. Data for this investigation were gathered from various sources, including governmental institutions, open-access databases, and existing literature. This section provides information regarding the study area, the criteria, and the methodological framework used. The methodological framework employed in this study is depicted in Fig. 2.

2.1 Study Area

The study area is Konya province, with an area of 40,838 km² in southwest Central Anatolia, Turkey. It is located between the latitudes of 36°41' and 39°16' N and the longitudes of 31°14' and 34°26' E and is recognized as the largest province in the country. Konya boasts a robust solar resource, surpassing many other regions. With high global horizontal irradiance (GHI) levels, Konya has the potential for efficient and cost-effective solar power generation. The region's favorable weather further enhances the feasibility of solar PV systems. As of 2020, Konya's annual electricity consumption was 8.4 TWh (Terawatt-hour) [31]. The province of Konya in Turkey is identified as possessing significant solar energy potential, as indicated by the Solar Energy Potential Atlas (GEPA) [32], as shown in Fig. 3.

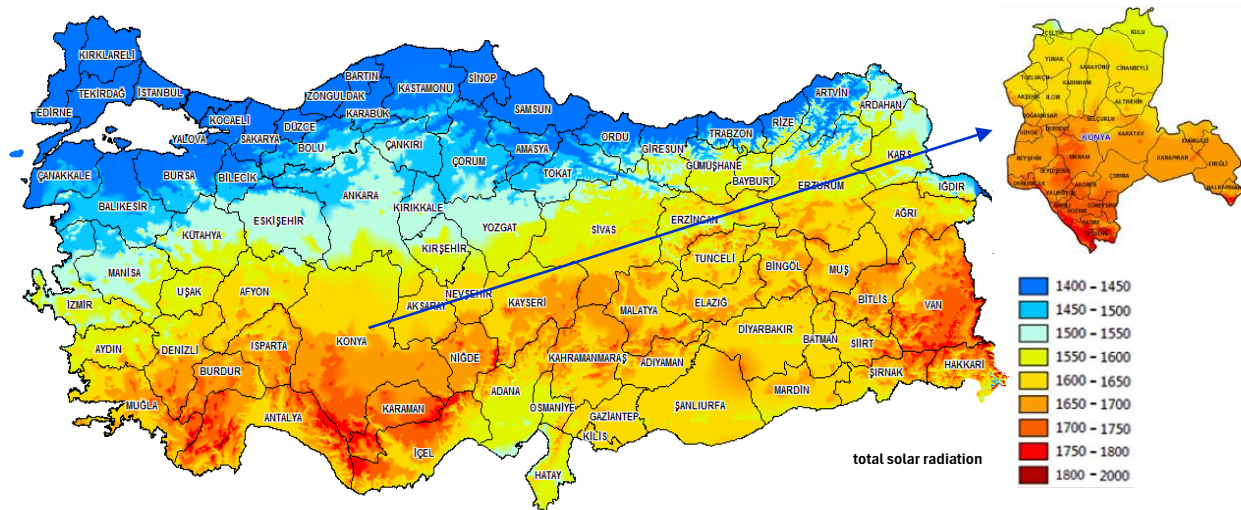


Figure 3. Solar energy potential map of Turkey [32].

Global radiation values and sunshine hours for the Konya Province are shown in Fig. 4. Konya, Turkey, boasts a substantial solar resource, outperforming many other regions in Turkey regarding sunlight availability. In comparison to other areas with lower solar irradiance, Konya has the potential to generate solar power efficiently and cost-effectively. The region's solar potential suggests it could achieve a significant power

output, potentially requiring fewer PV modules and less installation space than locations with lower solar irradiance levels. In addition, Konya benefits from favorable weather conditions conducive to PV development, including low cloudiness and a limited number of days with precipitation [33]. These weather characteristics enhance the feasibility and effectiveness of solar PV systems in the region.

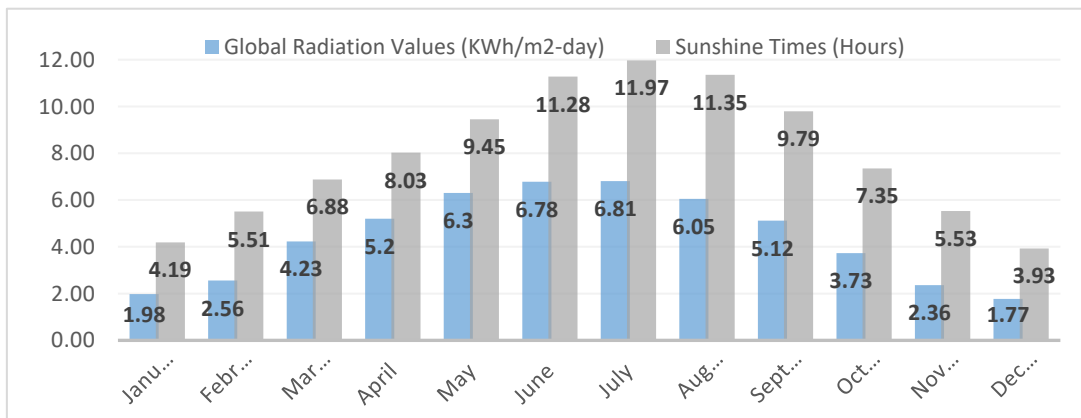


Figure 4. Global radiation values and sunshine times in Konya province.

2.2 Identification of criteria and restriction factors

Careful consideration of specific conditions is essential to establish a solar power plant and ensure its optimal functionality. The criteria for selecting suitable areas vary depending on the solar power plant's intended purpose and geographic location. To identify regions unsuitable for such installations, a comprehensive literature review was conducted, enabling the recognition of critical conditions that require attention. Based on these conditions, eight distinct criteria have been established: solar radiation levels, distance to power transmission infrastructure, aspect orientation, slope, distance to residential areas, distance to main roads, distance to rivers/streams, and distance to lakes. These factors collectively contribute significantly to a comprehensive framework for placing solar PV projects. The study encompasses various constraints, including ensuring that the slope gradient remains below 11%, maintaining a minimum distance of 400 m from rivers and lakes, maintaining a distance of at least 100 m from highways and railways, and locating the farms at a distance greater than 500 m from residential areas. The regions characterized by spatial suitability scores of 0, denoting restricted areas for each criterion, are delineated in Table 1. This tabular presentation also provides the threshold limits alongside their corresponding spatial suitability scores, including categories very high suitability (5), high suitability (4), moderate suitability (3), low suitability (2), and very low suitability (1). The determination of these limitation values for all pertinent factors influencing solar photovoltaic (PV) site selection is derived from expert consensus and literature. The following subsections elaborate on each criterion, demonstrating their relative importance.

2.2.1 Solar Irradiation

Solar irradiance refers to the amount of solar radiation absorbed within a given area influenced by factors such as latitude, longitude, time of day, humidity, evaporation, air temperature, sun angle, and other variables. It is usually measured per unit area by a specific surface area (expressed in watts per square meter, W/m^2). It is the most significant parameter in assessing the potential for energy generation within a solar PV power plant [5,34]. Selecting a location with low solar energy potential can lead to inefficiencies in establishing and operating a power plant. The reclassified solar irradiation map of Konya is shown in Fig.5 (a).

2.2.2 Aspect

The aspect of the land plays a crucial role in the site selection process for solar PV power plants, particularly concerning the land slope. Evaluating slope orientations necessitates the creation of an aspect map, which is derived from elevation maps and provides insights into the topography of the terrain. Understanding the terrain

ensures optimal use of sunlight, contributing to the efficiency of solar power generation systems [8,35,36]. The aspect map of Konya is presented in Fig.5 (b).

2.2.3 Slope

Highly sloping and rough terrain is critical when installing a solar PV power plant. Generally, areas with slopes above 11% are considered unsuitable, whereas slopes of 4% and below are deemed appropriate [37,38]. An excessive slope can lead to shading between solar panels, potentially affecting efficiency. In addition, failure to meet the specified slope requirements may necessitate excavation or filling operations in the area, leading to potential setbacks in terms of time and cost [1,17,35]. Fig.5 (c) shows the reclassified slope map of Konya.

2.2.4 Distance to the transmission lines

Ensuring efficient transmission and distribution of electricity with minimal loss is vital. While traditional power structures are typically reliable, areas with solar PV power plants can present installation cost challenges for power infrastructure [39]. Therefore, situating solar PV power plants near existing power lines aids in reducing transmission losses and enhancing overall reliability [8,35,40]. It's important to maximize the utilization of current power lines to avoid additional associated with introducing new ones. Moreover, locating solar PV power generation near a transformer center proves advantageous, as it reduces expenses by negating the need to construct new transformers. The transmission line map is depicted in Fig.5 (d).

2.2.5 Distance to residential areas

The construction of a solar PV power plant within a prospective residential zone can be avoided by considering the anticipated development trajectory of these areas. Simultaneously, positioning solar power plants close to settlements becomes essential to meet the region's energy demands while addressing cost considerations [14,15,36,41]. Fig.5 (e) shows the map of the reclassified distance to residential areas.

2.2.6 Distance to the main roads

Transportation is crucial in regional investments, especially in the installation of solar PV power plants. This significance arises from the substantial transportation needs linked to solar energy infrastructure [6,17,18]. To establish these plants, it is essential to carefully assess the existing road network. Introducing new roads increases expenses, particularly in areas without established transportation systems. Therefore, the feasibility of solar energy plant installation hinges on the condition and accessibility of the road network. Fig.5 (f) shows the reclassified distance to the main road map.

Table 1. Evaluation criteria and suitability scores

Criteria	References	Unit	Classes	Scores
C1 - Solar Irradiation	[10,17,38,42,43]	kWh/m ²	< 1200	1
			1200 – 1300	2
			1300 – 1400	3
			1400 – 1500	4
			> 1500	5
C2 - Aspect	[6,9,39,42,44]	direction	North	1
			Northeast, Northwest	2
			East, West	3
			Southeast, Southwest	4
			South	5
C3 - Slope	[1,5,7,44]	%	< 1	5
			1 – 4	4
			4 – 7	3
			7 – 9	2
			9 – 11	1
			> 11	0
C4 - Distance to transmission lines	[38,41,45]	km	0 – 2	5
			2 – 4	4
			4 – 6	3
			6 – 10	2
			> 10	1
C5 - Distance to residential areas	[14,15,40]	km	0 – 0.5	0
			0.5 – 0.75	1
			0.75 – 1	2
			1 – 2	3
			2 – 5	4
			> 5	5
C6 - Distance to main roads	[6,15,17,18]	km	0 – 0.1	0
			0.1 – 1	5
			1 – 2	4
			2 – 5	3
			5 – 10	2
			> 10	1
C7 - Distance to rivers/streams	[42,44,45]	km	< 0.4	0
			0.4 – 2	5
			2 – 5	4
			5 – 7.5	3
			7.5 – 10	2
			> 10	1
C8 - Distance to lakes	[14,35,46]	km	< 0.4	0
			0.4 – 2	5
			2 – 5	4
			5 – 7.5	3
			7.5 – 10	2
			> 10	1

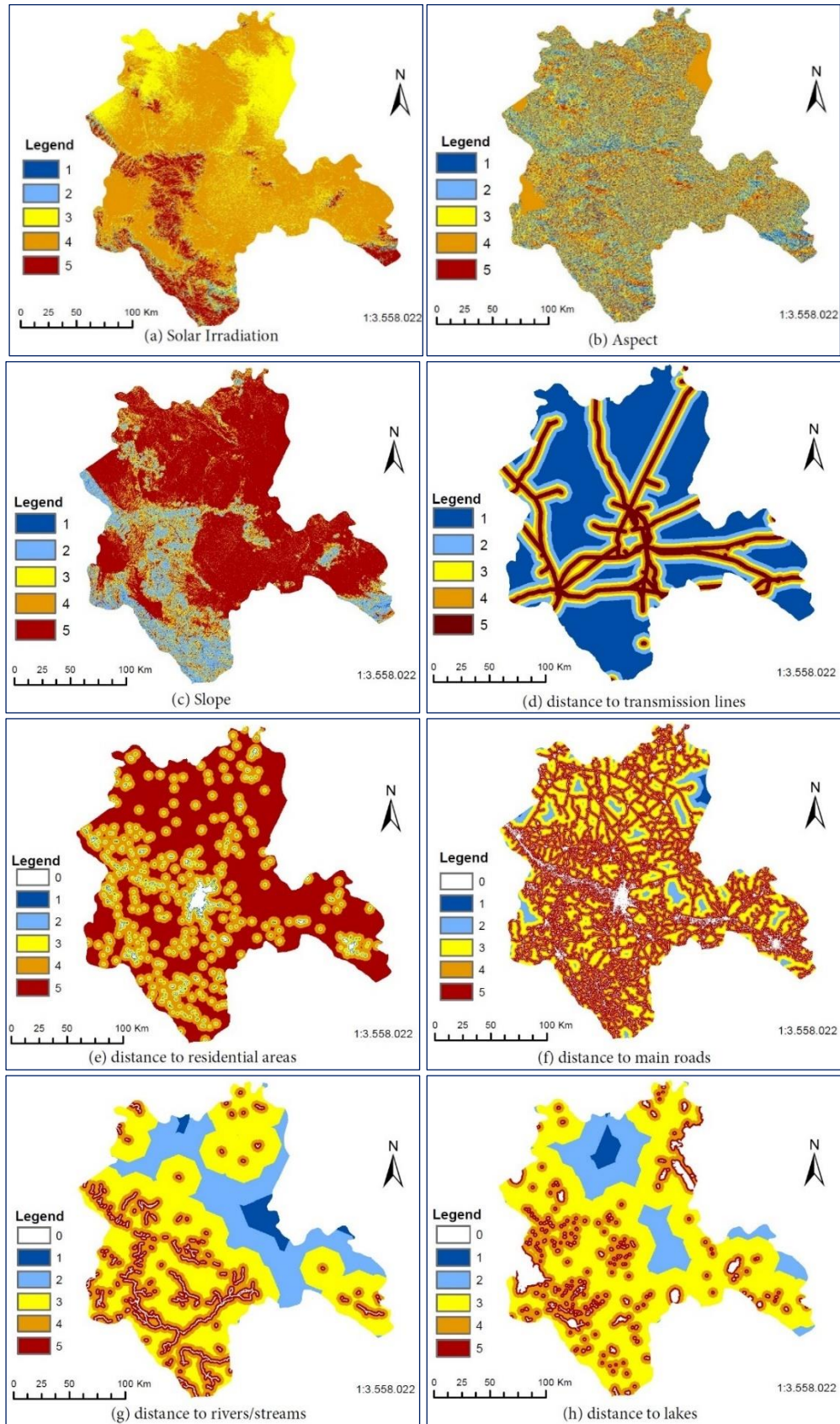


Figure 5. Reclassified layers of evaluation criteria: (a) solar irradiation; (b) aspect; (c) slope; (d) distance to transmission lines; (e) distance to residential areas; (f) distance to main roads; (g) distance to rivers/streams; (h) distance to lakes.

2.2.7 Distance to rivers/streams

The location of land near rivers or streams carries a notable risk of substantial material losses, particularly during winter floods. Hence, the criteria for considering proximity to rivers and streams are of utmost importance, as natural disasters in such areas can severely damage the facility [44,45]. This scenario can elevate operational costs and impede electricity generation. Furthermore, establishing a power plant in a river or stream region has been found to negatively impact efficiency due to factors such as fog, evaporation, and humidity risks, which are believed to influence the overall effectiveness of the plants. The reclassified distance to the river map is presented in Fig. 5 (g).

2.2.8 Distance to the lakes

To ensure safety and prevent environmental pollution caused by the potential adverse effects of floods due to variations in the volumes of lakes at different times of the year, it is recommended that solar power plants be located at a minimum distance of 400 m from lakes. This precautionary measure mitigates the impact of potential flooding and protects the surrounding environment [14,35,46]. The reclassified space in the lake map of Konya is presented in Fig. 5 (h).

2.3 Fuzzy BWM

In this study, fuzzy Best Worst Method (BWM) is adopted to ascertain the weights of the criteria within a fuzzy framework. Initially introduced by Rezaei in [47], classical BWM is a relatively recent technique that has successfully addressed various MCDM problems, such as firms' R&D performance evaluation [48], comparing communication technologies [49], and measuring the importance of logistics performance indicators [50]. Compared to other subjective weighting methods, such as AHP, BWM is notable for its ease of implementation. The methodology presents various advantages, particularly concerning the number of pairwise comparisons required, consistency, and reliability. Notably, BWM necessitates only $(2n - 3)$ pairwise comparisons, which is a notably lower number compared to AHP, which demands $n(n - 1)$ pairwise comparisons. The abundance of pairwise comparisons and extensive data involvement in AHP often leads to inconsistent results. Rezaei [47,51] demonstrated that BWM is more consistent than AHP, emphasizing its reliability as a preferred method for MCDM applications.

In decision-making under uncertainty, expressing preferences using crisp numbers can be challenging, especially when decision-makers compare alternatives with inherent vagueness or ambiguity. To address these challenges, Dong et al. [30] proposed an enhanced fuzzy BWM approach based on triangular fuzzy numbers, which incorporates fuzzy logic into the BWM

framework. This method overcomes the limitations of traditional methods by offering greater flexibility and improved reliability in capturing decision-makers' preferences.

For this study, criteria weights were calculated using the neutral decision-maker model, one of the three approaches outlined by Dong et al. [30]. This model is specifically designed to strike a balance between optimistic and pessimistic decision-making tendencies, making it well-suited for neutral contexts (mixed approach). The neutral model ensures a robust and balanced evaluation by integrating the adaptability of fuzzy BWM with improved consistency in weight estimation. The mathematical formulation and detailed application of this approach are thoroughly presented by Dong et al. [30].

The fuzzy comparison scale delineated in Table 2 serves as a tool for converting the linguistic assessments provided by experts into fuzzy ratings (represented by TFNs). The procedural framework of the fuzzy-BWM approach proposed by Dong et al. [30] encompasses the following steps:

Table 2. Linguistic scale for criteria weighting

Linguistic Terms	TFN scale
Equally important (EI)	(1,1,1)
Weakly important (WI)	(2/3,1,3/2)
Fairly important (FI)	(3/2,2,5/2)
Very important (VI)	(5/2,3,7/2)
Absolutely important (AI)	(7/2,4,9/2)

Step 1. Define a set of decision criteria denoted as $C = \{C_1, C_2, \dots, C_n\}$.

Step 2. Identify the best criterion (C_B) which is considered the most important, and the worst criterion (C_W), regarded as the least important.

Step 3. Provide preference for the best criterion over all other criteria. Let $\tilde{a}_{Bj} = (a_{Bj}^l, a_{Bj}^m, a_{Bj}^u)$ be the triangular fuzzy preference of the best criterion C_B over criterion C_j , satisfying $\tilde{a}_{BB} = (1,1,1)$. Formulate the best-to-others vector as follows:

$$\tilde{A}_B = [\tilde{a}_{B1}, \tilde{a}_{B2}, \dots, \tilde{a}_{Bn}]$$

Step 4. Provide preference for all criteria over the worst criterion. Let $\tilde{a}_{jW} = (a_{jW}^l, a_{jW}^m, a_{jW}^u)$ be the triangular fuzzy preference of a criterion C_j over the worst criterion C_W , satisfying $\tilde{a}_{WW} = (1,1,1)$. Formulate the Others-to-Worst vector as follows:

$$\tilde{A}_W = [\tilde{a}_{1W}, \tilde{a}_{2W}, \dots, \tilde{a}_{nW}]$$

Step 5. Determine appropriate values for the tolerance parameters (d_j^t and q_j^t) within the interval [1, 9] according to expert preferences and the specific characteristics of the problem. This study calculates the global optimum solution by using tolerance parameter 1.

Step 6. Derive the optimal weight vector $\tilde{w}^* = [\tilde{w}_1^*, \tilde{w}_2^*, \dots, \tilde{w}_n^*]$ and the optimal satisfaction degree β . In

$$\begin{aligned} & \max \beta \\ \text{s.t.} & \begin{cases} 1 - \frac{w_B^t - w_j^t a_{Bj}^t}{d_j^t} \geq \beta, & 0 \leq w_B^t - w_j^t a_{Bj}^t \leq d_j^t \quad (j = 1, 2, \dots, n; t = l, m, u) \\ 1 + \frac{w_j^t - a_{jw}^t w_w^t}{q_j^t} \geq \beta, & -q_j^t \leq w_j^t - a_{jw}^t w_w^t \leq 0 \quad (j = 1, 2, \dots, n; t = l, m, u) \\ 0 \leq \beta \leq 1 \\ \sum_{i=1}^n w_i^m = 1, & w_j^u + \sum_{i=1, i \neq j}^n w_i^l \leq 1, \quad w_j^l + \sum_{i=1, i \neq j}^n w_i^u \geq 1 \quad (j = 1, 2, \dots, n) \end{cases} \end{aligned} \quad (1)$$

Then, the optimal weight vector (\tilde{w}^*) based on the TFNs is converted to crisp weights using Eq. (2).

$$R(\tilde{a}) = \frac{1}{6} (a^l + 4a^m + a^u) \quad (2)$$

Step 7. Compute the fuzzy deviation of the comparisons $\tilde{\xi}^* = (\xi^{*l}, \xi^{*m}, \xi^{*u})$.

$$\begin{aligned} \xi^{*l} &= \frac{1}{2n} \sum_{j=1}^n (|w_B^{*l} - w_j^{*l} a_{Bj}^l| + |w_j^{*l} - a_{jw}^l w_w^{*l}|) \\ \xi^{*m} &= \frac{1}{2n} \sum_{j=1}^n (|w_B^{*m} - w_j^{*m} a_{Bj}^m| + |w_j^{*m} - a_{jw}^m w_w^{*m}|) \end{aligned} \quad (3)$$

this study, the Mixed Approach-I for obtaining the weights of the criteria from the perspective of a neutral decision-maker is employed. Eq. (1) presents the linear programming model used to compute the criteria weights under the neutral decision-making assumption, ensuring a balanced and robust evaluation framework.

$$\xi^{*u} = \frac{1}{2n} \sum_{j=1}^n (|w_B^{*u} - w_j^{*u} a_{Bj}^u| + |w_j^{*u} - a_{jw}^u w_w^{*u}|)$$

where ξ^{*l} , ξ^{*m} and ξ^{*u} denote the possible lower bound, possible mode and possible upper bound of the fuzzy deviation ($\tilde{\xi}^*$), respectively.

Step 8: Calculate the fuzzy consistency ratio (FCR) using Eq. (4).

$$FCR = \frac{\tilde{\xi}^*}{\tilde{\zeta}} = \frac{(\xi^{*l}, \xi^{*m}, \xi^{*u})}{(\zeta^l, \zeta^m, \zeta^u)} = \left(\frac{\xi^{*l}}{\zeta^u}, \frac{\xi^{*m}}{\zeta^m}, \frac{\xi^{*u}}{\zeta^l} \right) \quad (4)$$

where fuzzy consistency index, $\tilde{\zeta} = (\zeta^l, \zeta^m, \zeta^u)$, is obtained using Table 3.

Table 3. Fuzzy Consistency Index (FCI) for Fuzzy BWM

Linguistic Terms	Equally important (EI)	Weakly important (WI)	Fairly important (FI)	Very important (VI)	Absolutely important (AI)
\tilde{a}_{BW}	(1,1,1)	(2/3,1,3/2)	(3/2,2,5/2)	(5/2,3,7/2)	(7/2,4,9/2)
FCI ($\tilde{\zeta}$)	(0, 0, 0)	(0, 0, 1.36)	(0.34, 0.44, 2.16)	(0.71, 1, 4.29)	(1.31, 1.63, 5.69)

Step 9. Compute the graded mean integration representation (GMIR) of FCR, i.e., $R(FCR)$, to check consistency using Eq. (5).

$$R(FCR) = \frac{1}{6} \left(\frac{\xi^{*l}}{\zeta^u} + \frac{4\xi^{*m}}{\zeta^m} + \frac{\xi^{*u}}{\zeta^l} \right) \quad (5)$$

If $R(FCR) \leq 0.1$, the fuzzy pairwise comparisons are considered acceptable consistent; however, if $R(FCR) > 0.1$, the comparisons are not consistent.

3. Results

3.1 Calculating the weights of the criteria using fuzzy BWM

After selecting relevant criteria, a team of experts evaluates the importance of these criteria using fuzzy BWM. Section 2.3 provides an overview of the implementation of the fuzzy BWM method suggested by Dong et al. [30]. The optimal overall weights of the criteria are determined through pairwise comparisons from the standpoint of an impartial decision-maker, taking into account mixed approach-I and all tolerance parameters (d_j^f) 1.

In the initial stage of the fuzzy BWM process, experts begin by choosing the most favorable (best) and least

favorable (worst) criteria from a preset list. After identifying these, experts are assigned the task of providing assessments involving comparisons among the criteria using fuzzy numbers. The comparisons of the best criterion with the other criteria (\tilde{a}_{Bj}) and all the criteria with the worst criterion (\tilde{a}_{jW}) are systematically displayed in Table 4.

Upon identifying the best-to-others (\tilde{A}_B) and others-to-worst vectors (\tilde{A}_W), we utilized the Lingo 19.0 optimization software to solve the linear programming (LP) model in Eq. (1) in order to calculate the optimal weight vector. The resulting fuzzy weights, which were obtained from the LP model, are detailed in Table 5. Furthermore, Eq. (2) was employed to determine the crisp weights for TFNs.

Table 4. Collective preferences of experts

Best Criterion	Worst Criterion	TFN preferences								
		C1	C2	C3	C4	C5	C6	C7	C8	
C1	C8	\tilde{a}_{Bj}	EI (1,1,1)	FI (3/2,2,5/2)	FI (3/2,2,5/2)	VI (5/2,3,7/2)	AI (7/2,4,9/2)	VI (5/2,3,7/2)	AI (7/2,4,9/2)	AI (7/2,4,9/2)
		\tilde{a}_{jW}	AI (7/2,4,9/2)	VI (5/2,3,7/2)	VI (5/2,3,7/2)	FI (3/2,2,5/2)	FI (3/2,2,5/2)	FI (3/2,2,5/2)	WI (2/3,1,3/2)	EI (1,1,1)

Table 5. Weights of the criteria

	Solar Irradiation (C1)	Aspect (C2)	Slope (C3)	Distance to the transmission lines (C4)	Distance to residential areas (C5)	Distance to the main roads (C6)	Distance to rivers/streams (C7)	Distance to lakes (C8)
Fuzzy weights	(0.13, 0.304, 0.34)	(0, 0.137, 0.137)	(0, 0.137, 0.137)	(0, 0.098, 0.098)	(0, 0.076, 0.076)	(0, 0.098, 0.098)	(0.025, 0.08, 0.08)	(0.037, 0.08, 0.08)
Crisp Weights	0.32	0.13	0.13	0.09	0.07	0.09	0.08	0.08

Table 6 provides essential metrics, including the minimal acceptance degree (β), fuzzy deviations ($\tilde{\xi}^*$), fuzzy consistency index ($\tilde{\zeta}$) and $R(FCR)$ value. As observed in Table 6, the $R(FCR)$ value is less than 0.1, indicating that the comparisons are reasonably consistent.

Table 6. Consistency values

β^*	0.8709
$\tilde{\xi}^*$	(0.0281, 0.0348, 0.0656)
$\tilde{\zeta}$	(1.31, 1.63, 5.69)
FCR	(0.0049, 0.0213, 0.05)
$R(FCR)$	0.0234

3.2 Suitability Analysis

In the context of suitability analysis, the input criterion layers used in overlay analysis necessitate reclassification into raster layers. Hence, the initial preparation and reclassification of the input criterion layers were executed, as illustrated in Fig. 5 (a-h), to delineate the eight resultant maps. Comprehensive class intervals alongside corresponding suitability values are elaborated in Table 1.

Following the reclassification of input criterion layers and the determination of weights through fuzzy BWM, a weighted overlay analysis technique was applied. This method integrated the derived weights with raster layers corresponding to the eight identified criteria. In line with previous studies, the suitability map in this study was

divided into six categories, including restricted areas, to ensure consistency with the literature and enhance interpretability. This classification approach provided a well-structured differentiation among varying suitability levels while effectively capturing the spatial characteristics of the study area. The outcome of this process generated a suitability map that classifies areas into six discrete categories: 'unsuitable,' 'very low suitability,' 'low suitability,' 'moderate suitability,' 'high suitability,' and 'very high suitability.' Sequential values

spanning from 0 to 5 were assigned to these suitability classes to facilitate the overlay analysis. The criterion layers underwent stacking via the weighted sum tool. Subsequent to this, the output layer, featuring values ranging from 0 to 5, underwent division utilizing the reclassify tool, thereby partitioning it into five equally spaced suitability classes. Following this step, restriction factors were considered, and unsuitable areas were removed from the map. The resulting suitability map, created using ArcGIS software, is shown in Fig. 6.

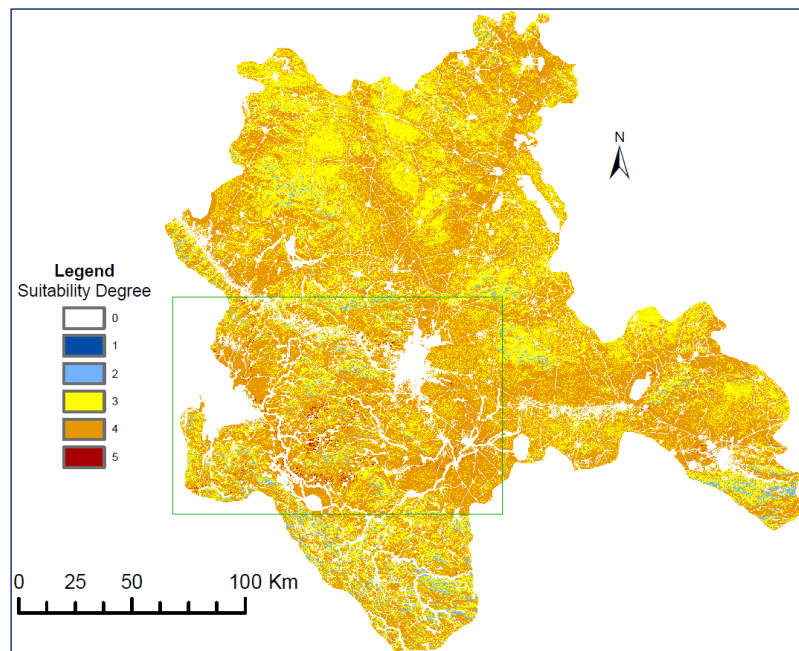


Figure 6. Suitability map results using fuzzy BWM weights.

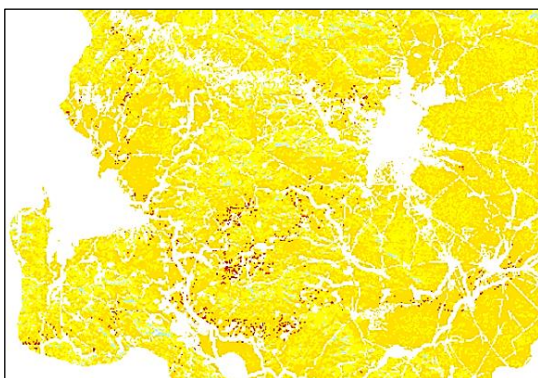


Figure 7. A close-up view of areas with the highest suitability.

Notably, approximately half of the entire area exhibits high potential for solar PV installations, with 137.03 km² (0.3%) classified as 'very high suitable'. The regions

identified as exhibiting the highest suitability are predominantly situated within the city's central belt, notably in its central and western sectors (as delineated within the enclosed area in Fig. 6). This concentration is further elucidated in a distinct graphical representation showcased in Fig. 7, where enhanced contrast has been applied to facilitate more precise visualization.

Fig. 8 shows the spatial distribution of the three photovoltaic facilities with the highest installed capacity in Konya. As shown in Figure 8, the Karapınar solar power plant, with an installed capacity of 1,000 MW and occupying an area of 27.18 km², is located in an area with high suitability and above. Similarly, the Alibeyhoyugu (18-MW) and Apa (13-MW) facilities are also situated in high suitability areas. It reveals a robust correlation between potentially suitable areas and current installations. This correlation underscores the validity of the methodology employed in this study.

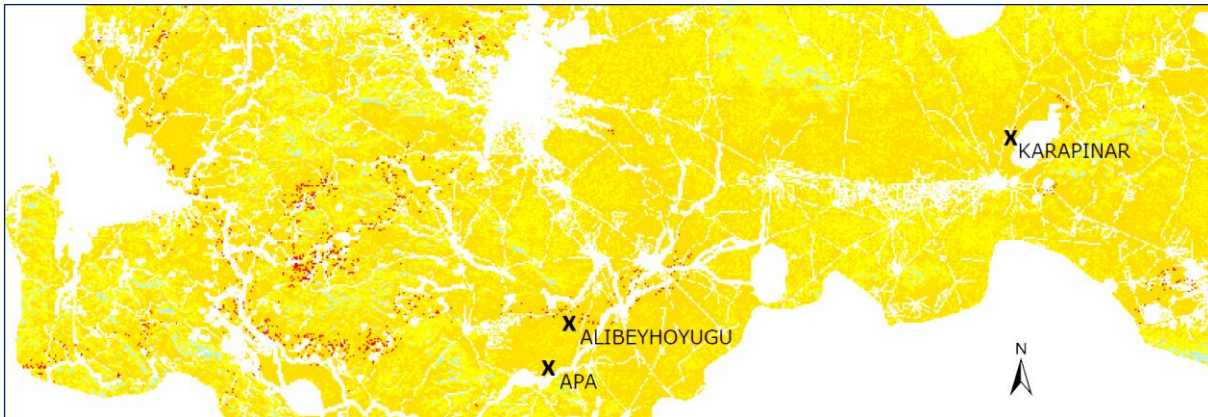


Figure 8. Current solar PV plants.

3.3 Sensitivity Analysis

In this section, a sensitivity analysis was conducted by changing the criterion weights and examining the changes in the suitability map to assess the robustness of the proposed fuzzy BWM-GIS approach. For this purpose, three scenarios were developed.

Scenario 1 assumes equal importance of all criteria and assigns equal weights to them. Scenario 2 disregarded distance criteria (C4-C6), while Scenario 3 excluded the evaluation of distance criteria to rivers and lakes (C7, C8), ensuring the proportional distribution of weights to the remaining criteria. Table 7 presents all scenarios and their associated weights.

Table 7. Sensitivity analysis scenarios and criteria weights

Scenarios	Criteria Weights							
	Solar Irradiation (C1)	Aspect (C2)	Slope (C3)	Distance to the transmission lines (C4)	Distance to residential areas (C5)	Distance to the main roads (C6)	Distance to rivers/streams (C7)	Distance to the lakes (C8)
Current situation (Fuzzy BWM)	0.322	0.131	0.131	0.093	0.073	0.093	0.077	0.080
Scenario 1 - Equal weighting	0.125	0.125	0.125	0.125	0.125	0.125	0.125	0.125
Scenario 2- Ignore distance criteria (C4-C6)	0.435	0.177	0.177	-	-	-	0.104	0.108
Scenario 3- Ignore distance to rivers/lakes criteria (C7, C8)	0.382	0.155	0.155	0.110	0.087	0.110	-	-

The results of this analysis are presented in detail in Fig. 9. The most straightforward method, equal weighting (Scenario 1), which allows avoidance of risks and disregards the relative importance already known, yielded the lowest percentage of “very high suitable” areas (206.26 km², 0.3%). Because the weight of the solar radiation criterion is significantly reduced in Scenario 1, it helps us observe the impact of this criterion. In this scenario, while the percentage of “highly suitable” areas decreases by approximately 10% compared with the

current situation, the area covered by “moderate suitable” areas increases by 10%. In Scenario 2, when distances to transmission lines, residential areas, and main roads are disregarded, the percentage of “very high suitable” areas increases to 1.3% (543.76 km²). In Scenario 3, when distance to the lakes and rivers criteria are excluded, the percentage of “high suitable” areas rises to 1.8% (718.56 km²).

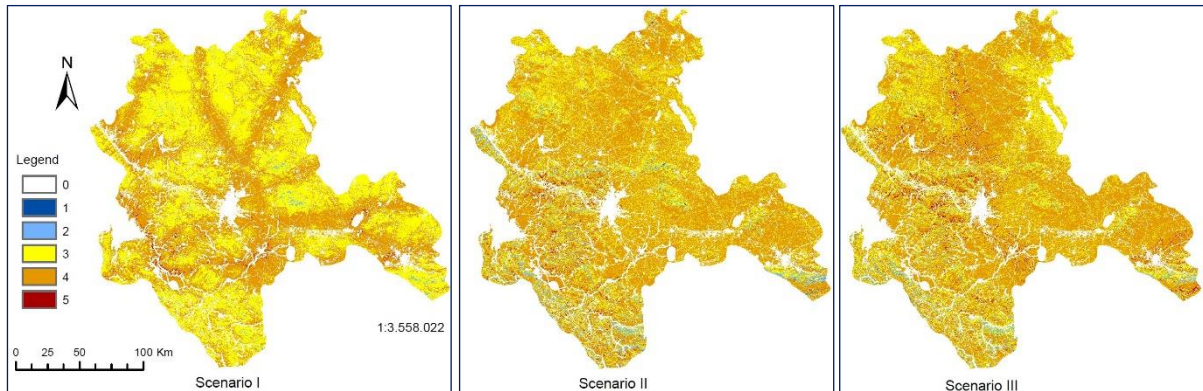


Figure 9. Sensitivity analysis results considering scenarios.

4. Discussion

The findings of this study highlight the significant potential of Konya for solar PV power plant deployment. By integrating fuzzy BWM with GIS-based suitability mapping, the research provides a systematic framework for selecting optimal solar energy sites. The analysis revealed that approximately 50.02% of the study area is classified as highly suitable, while 137.03 square kilometers (0.3%) of the region is considered very highly suitable, emphasizing the region's viability for large-scale solar investments. The methodology effectively addresses uncertainties in decision-making by incorporating expert judgments and spatial data, ensuring a comprehensive evaluation of site suitability.

From a policy and industry perspective, the findings offer valuable insights for decision-makers, urban planners, and investors in the renewable energy sector. Policymakers can leverage this study to design incentive programs for solar energy investments, streamline land-use regulations, and develop infrastructure in high-suitability zones. Energy stakeholders can use this framework to minimize project risks, optimize investment strategies, and accelerate the integration of solar energy into Türkiye's energy mix.

5. Conclusions

The increasing global demand for sustainable energy has accelerated the need for systematic site selection methodologies for solar power projects. This study introduced a fuzzy BWM-GIS framework to identify optimal locations for solar PV installations in Konya, Türkiye. By integrating MCDM techniques with geospatial analysis, this research ensures a comprehensive and adaptable approach for renewable energy site selection.

A key contribution of this study is the incorporation of neutral decision-making in the fuzzy BWM process, which balances optimistic and pessimistic biases in expert evaluations. Additionally, the study employs a customized set of eight criteria, tailored to Konya's

geographical and environmental conditions. Furthermore, the use of sensitivity analysis enhances the robustness of the decision-making process, demonstrating the model's applicability across different regions and scenarios.

Despite its strengths, this study has some limitations that should be addressed in future research. The accuracy of the site suitability analysis is highly dependent on the quality and availability of geospatial data, which may impact the precision of the results. Incorporating real-time solar radiation data and economic feasibility analysis could enhance the decision-making process by providing more dynamic and financially viable site recommendations. Additionally, while this study offers a structured methodological foundation, further research should integrate financial cost-benefit analysis to assess the economic viability of solar PV deployment.

Overall, this research contributes to both academic literature and practical applications, offering a reliable decision-support tool for advancing renewable energy planning in Türkiye and beyond. By systematically addressing site selection complexities, this study aligns with Türkiye's National Energy Plan, reinforcing efforts to enhance sustainability and energy security in the transition toward a low-carbon future.

Author's Contributions

Ömer Öztaş: Drafted and wrote the manuscript, performed the experiment and result analysis.

Bilal Ervural: Assisted in analytical analysis of the structure, supervised the experiment's progress and result interpretation, and studied manuscript preparation.

Note

This study is based on the master's thesis titled 'A GIS Based Hybrid Approach for Solar PV Power Plant Site Selection' conducted by Ömer Öztaş at Necmettin Erbakan University, Institute of Science and Technology,

Department of Industrial Engineering, under the supervision of Dr. Bilal Ervural.

Ethics

There are no ethical issues after the publication of this manuscript.

References

- [1]. Noorollahi Y, Ghenaatpisheh Senani A, Fadaei A, Simaee M, Moltames R. 2022. A framework for GIS-based site selection and technical potential evaluation of PV solar farm using Fuzzy-Boolean logic and AHP multi-criteria decision-making approach. *Renew. Energy*;186: 89.
- [2]. Arvizu D et al. 2011. Renewable Energy Sources and Climate Change Mitigation: Direct Solar Energy. *Renew. Energy Sources Clim. Chang. Mitig.*;333.
- [3]. ENR. Turkey National Energy Plan. Ankara. 2022.
- [4]. Bandira PNA et al. 2022. Optimal Solar Farm Site Selection in the George Town Conurbation Using GIS-Based Multi-Criteria Decision Making (MCDM) and NASA POWER Data. *Atmos.*;13(12): 2105.
- [5]. Khan A, Ali Y, Pamucar D. 2023. Solar PV power plant site selection using a GIS-based non-linear multi-criteria optimization technique. *Environ. Sci. Pollut. Res.*;30(20): 57378.
- [6]. Hooshangi N, Mahdizadeh Gharakhanlou N, Ghaffari Razin SR. 2023. Evaluation of potential sites in Iran to localize solar farms using a GIS-based Fermatean Fuzzy TOPSIS. *J. Clean. Prod.*;384: 135481.
- [7]. Heo J, Moon H, Chang S, Han S, Lee DE. 2021. Case study of solar photovoltaic power-plant site selection for infrastructure planning using a bim-gis-based approach. *Appl. Sci.*;11(18): 8785.
- [8]. Kocabaldır C, Yücel MA. 2023. GIS-based multicriteria decision analysis for spatial planning of solar photovoltaic power plants in Çanakkale province, Turkey. *Renew. Energy*;212: 455.
- [9]. Türk S, Koç A, Şahin G. 2021. Multi-criteria of PV solar site selection problem using GIS-intuitionistic fuzzy based approach in Erzurum province/Turkey. *Sci. Rep.*;11(1): 5034.
- [10]. Shorabeh SN, Firozjaei MK, Nematollahi O, Firozjaei HK, Jelokhani-Niaraki M. 2019. A risk-based multi-criteria spatial decision analysis for solar power plant site selection in different climates: A case study in Iran. *Renew. Energy*;143: 958.
- [11]. Akkas OP, Erten MY, Cam E, Inanc N. 2017. Optimal Site Selection for a Solar Power Plant in the Central Anatolian Region of Turkey. *Int. J. Photoenergy*;2017: 1.
- [12]. Aktas A, Kabak M. 2019. A Hybrid Hesitant Fuzzy Decision-Making Approach for Evaluating Solar Power Plant Location Sites. *Arab. J. Sci. Eng.*;44(8): 7235.
- [13]. Aragonés-Beltrán P, Chaparro-González F, Pastor-Ferrando JP, Rodríguez-Pozo F. 2010. An ANP-based approach for the selection of photovoltaic solar power plant investment projects. *Renew. Sustain. Energy Rev.*;14(1): 249.
- [14]. Colak HE, Memisoglu T, Gercek Y. 2020. Optimal site selection for solar photovoltaic (PV) power plants using GIS and AHP: A case study of Malatya Province, Turkey. *Renew. Energy*;149: 565.
- [15]. Al Garni HZ, Awasthi A. 2017. Solar PV power plant site selection using a GIS-AHP based approach with application in Saudi Arabia. *Appl. Energy*;206: 1225.
- [16]. Lee AHI, Kang HY, Liou YJ. 2017. A Hybrid Multiple-Criteria Decision-Making Approach for Photovoltaic Solar Plant Location Selection. *Sustain.* 2017, Vol. 9, Page 184;9(2): 184.
- [17]. Badi I, Pamucar D, Gigović L, Tatirović S. 2021. Optimal site selection for sitting a solar park using a novel GIS- SWA`TEL model: A case study in Libya. *Int. J. Green Energy*;18(4): 336.
- [18]. Zoghi M, Houshang Ehsani A, Sadat M, javad Amiri M, Karimi S. 2017. Optimization solar site selection by fuzzy logic model and weighted linear combination method in arid and semi-arid region: A case study Isfahan-IRAN. *Renew. Sustain. Energy Rev.*;68: 986.
- [19]. Alipour M, Alighaleh S, Hafezi R, Omranievardi M. 2017. A new hybrid decision framework for prioritizing funding allocation to Iran's energy sector. *Energy*;121: 388.
- [20]. Aghaloo K, Ali T, Chiu YR, Sharifi A. 2023. Optimal site selection for the solar-wind hybrid renewable energy systems in Bangladesh using an integrated GIS-based BWM-fuzzy logic method. *Energy Convers. Manag.*;283: 116899.
- [21]. Onar SC, Oztaysi B, Otay İ, Kahraman C. 2015. Multi-expert wind energy technology selection using interval-valued intuitionistic fuzzy sets. *Energy*;90, Part 1: 274.
- [22]. Hocine A, Kouaissah N, Bettahar S, Benbouziane M. 2018. Optimizing renewable energy portfolios under uncertainty: A multi-segment fuzzy goal programming approach. *Renew. Energy*;129: 540.
- [23]. Alshamrani A, Majumder P, Das A, Hezam IM, Božanić D. 2023. An Integrated BWM-TOPSIS-I Approach to Determine the Ranking of Alternatives and Application of Sustainability Analysis of Renewable Energy. *Axioms* 2023, Vol. 12, Page 159;12(2): 159.
- [24]. Konurhan Z, Yucesan M, Gul M. 2023. A GIS-Based BWM Approach for the Location Selection of Solar Power Plant in Tunceli Province (Turkey). *Lect. Notes Oper. Res.*;87.
- [25]. Shayani Mehr P, Hafezalkotob A, Fardi K, Seiti H, Movahedi Sobhani F, Hafezalkotob A. 2022. A comprehensive framework for solar panel technology selection: A BWM- MULTIMOOSRAL approach. *Energy Sci. Eng.*;10(12): 4595.
- [26]. Mostafaeipour A, Hosseini Dehshiri SS, Hosseini Dehshiri SJ, Almutairi K, Taher R, Issakhov A, Techato K. 2021. A thorough analysis of renewable hydrogen projects development in Uzbekistan using MCDM methods. *Int. J. Hydrogen Energy*;46(61): 31174.
- [27]. Ecer F. 2021. Sustainability assessment of existing onshore wind plants in the context of triple bottom line: a best-worst method (BWM) based MCDM framework. *Environ. Sci. Pollut. Res.*;28(16): 19677.
- [28]. Besharati Fard M, Moradian P, Emarati M, Ebadi M, Gholamzadeh Chofreh A, Klemeš JJ. 2022. Ground-mounted photovoltaic power station site selection and economic analysis based on a hybrid fuzzy best-worst method and geographic information system: A case study Guilan province. *Renew. Sustain. Energy Rev.*;169: 112923.
- [29]. Guo S, Zhao H. 2017. Fuzzy best-worst multi-criteria decision-making method and its applications. *Knowledge-Based Syst.*;121: 23.
- [30]. Dong J, Wan S, Chen SM. 2021. Fuzzy best-worst method based on triangular fuzzy numbers for multi-criteria decision-making. *Inf. Sci. (Ny)*;547: 1080.
- [31]. KMM. Konya Annual Electricity Consumption in Industry and Residential.2020.
- [32]. GEPA. 2024. Solar Energy Potential Atlas. *Repub. Türkiye Minist. Energy Nat. Resour.*;https://gepa.enerji.gov.tr/MyCalculator/.
- [33]. MGM. 2024. Seasonal normals for provinces in Turkey. *Turkish State Meteorol. Serv.*;https://www.mgm.gov.tr/eng/forecast-cities.aspx?m=KONYA.
- [34]. Deveci M, Cali U, Pamucar D. 2021. Evaluation of criteria for site selection of solar photovoltaic (PV) projects using fuzzy logarithmic

additive estimation of weight coefficients. *Energy Reports*;7: 8805.

[35]. Tercan E, Eymen A, Urfalı T, Saracoglu BO. 2021. A sustainable framework for spatial planning of photovoltaic solar farms using GIS and multi-criteria assessment approach in Central Anatolia, Turkey. *Land use policy*;102: 105272.

[36]. Günen MA. 2021. A comprehensive framework based on GIS-AHP for the installation of solar PV farms in Kahramanmaraş, Turkey. *Renew. Energy*;178: 212.

[37]. Doorga JRS, Rughooputh SDDV, Boojhawon R. 2019. Multi-criteria GIS-based modelling technique for identifying potential solar farm sites: A case study in Mauritius. *Renew. Energy*;133: 1201.

[38]. Günen MA. 2021. Determination of the suitable sites for constructing solar photovoltaic (PV) power plants in Kayseri, Turkey using GIS-based ranking and AHP methods. *Environ. Sci. Pollut. Res.*;28(40): 57232.

[39]. Rios R, Duarte S. 2021. Selection of ideal sites for the development of large-scale solar photovoltaic projects through Analytical Hierarchical Process – Geographic information systems (AHP-GIS) in Peru. *Renew. Sustain. Energy Rev.*;149: 111310.

[40]. Uyan M. 2017. Optimal site selection for solar power plants using multi-criteria evaluation: A case study from the Ayranci region in Karaman, Turkey. *Clean Technol. Environ. Policy*;19(9): 2231.

[41]. Akinci H, Özalp AY. 2022. Optimal site selection for solar photovoltaic power plants using geographical information systems and fuzzy logic approach: a case study in Artvin, Turkey. *Arab. J. Geosci.* 2022 159;15(9): 1.

[42]. Giamalaki M, Tsoutsos T. 2019. Sustainable siting of solar power installations in Mediterranean using a GIS/AHP approach. *Renew. Energy*;141: 64.

[43]. Sun L, Jiang Y, Guo Q, Ji L, Xie Y, Qiao Q, Huang G, Xiao K. 2021. A GIS-based multi-criteria decision making method for the potential assessment and suitable sites selection of PV and CSP plants. *Resour. Conserv. Recycl.*;168: 105306.

[44]. Coruhlu YE, Solgun N, Baser V, Terzi F. 2022. Revealing the solar energy potential by integration of GIS and AHP in order to compare decisions of the land use on the environmental plans. *Land use policy*;113: 105899.

[45]. Alami Merrouni A, Elwali Elalaoi F, Mezrhah A, Mezrhah A, Ghennioui A. 2018. Large scale PV sites selection by combining GIS and Analytical Hierarchy Process. Case study: Eastern Morocco. *Renew. Energy*;119: 863.

[46]. Yushchenko A, de Bono A, Chatenoux B, Patel MK, Ray N. 2018. GIS-based assessment of photovoltaic (PV) and concentrated solar power (CSP) generation potential in West Africa. *Renew. Sustain. Energy Rev.*;81: 2088.

[47]. Rezaei J. 2015. Best-worst multi-criteria decision-making method. *Omega (United Kingdom)*;53: 49.


[48]. Salimi N, Rezaei J. 2018. Evaluating firms' R&D performance using best worst method. *Eval. Program Plann.*;66: 147.

[49]. van de Kaa G, Fens T, Rezaei J, Kaynak D, Hatun Z, Tsilimeni-Archangelidi A. 2019. Realizing smart meter connectivity: Analyzing the competing technologies Power line communication, mobile telephony, and radio frequency using the best worst method. *Renew. Sustain. Energy Rev.*;103: 320.

[50]. Rezaei J, van Roekel WS, Tavasszy L. 2018. Measuring the relative importance of the logistics performance index indicators using Best Worst Method. *Transp. Policy*;68: 158.

[51]. Rezaei J. 2016. Best-worst multi-criteria decision-making method: Some properties and a linear model. *Omega (United Kingdom)*;64: 126.

Analysis of Level-Off Flight Segments of Descending Aircraft for Busy Terminal Maneuvering Areas

Ramazan Kürşat Cecen¹ 

¹Eskisehir Osmangazi University, Motor Vehicles and Transportation Technology Department, Eskisehir, Türkiye.

* ramazankursat.cecen@ogu.edu.tr

* Orcid No: 0000-0002-6580-2894

Received: May 5, 2024

Accepted: February 11, 2025

DOI: 10.18466/cbayarfbe.1478719

Abstract

The demand for air transportation increases significantly worldwide, and the number of aircraft and passengers is also rising. This situation directly affects the major airports and their surrounding Terminal Manoeuvring Areas (TMAs) because they launch new destinations and increase flight frequency. However, airport and airspace structures have some difficulty meeting this increasing demand. Therefore, there is an increase in airborne delay in air traffic congestion. Airborne delay severely affects TMAs operations since they have several entry points, yet all arrival traffic lands mainly at the same airport. This problem also expands the flight duration within TMAs. Air traffic controllers regulate the arrival traffic with separation and sequencing methods, including vectoring, point merge approach or holding manoeuvres. These are generally implemented at a constant flight level. Therefore, they generate level-off flight segments during the descending profile of arrival aircraft. The level-off segments directly increase the fuel consumption and emissions values because of engine configurations. Therefore, this study aims to expose the level-off segments for the London Heathrow, Amsterdam Schiphol, Paris Charles de Gaulle and Istanbul airports. The results show that Amsterdam Schiphol has the lowest level-off time to total descent time ratio of 12.8% among other airports.

Keywords: Continuous descent operations, Vertical profile inefficiency, Airborne delay, Air traffic management, Terminal Maneuvering Areas Operations

1. Introduction

Civil aviation plays a crucial role in modern society, contributing significantly to various aspects of economic, social, and cultural development. Besides, air transportation connects people, businesses, and countries worldwide and international cooperation. It enables rapid movement of goods, services, and people across borders, facilitating global supply chains and enhancing global integration. Rapid developments have caused increases in air traffic operations. According to Eurocontrol's optimistic anticipation, the flight growth is expected to average 2.0% per year, with a range of ± 1.4 percentage points. By 2030, the number of flights is projected to exceed 12 million [1]. While increasing air traffic operations signifies economic vitality and connectivity, it also presents challenges such as airspace congestion, environmental concerns, and infrastructure constraints. Therefore, effective planning, collaboration among stakeholders, and sustainable growth strategies are essential to manage the growth of air traffic operations

responsibly. Air traffic congestion can adversely affect various aspects of the aviation industry, the economy, the environment, and society. It can cause flight delays and cancellations, leading to lost productivity, missed connections, and increased costs for airlines and passengers [2-5]. It can also increase fuel consumption and emissions, contributing to climate change and air pollution [6,7]. Additionally, air traffic congestion can affect other industries that rely on air transportation, such as tourism and international trade. Aircraft delays can be absorbed for the departure aircraft by updating the expected departure time, which helps to minimize fuel consumption and decrease ground traffic duration [8,9]. Furthermore, aircraft scheduling can be affected due to the congestion of airports and Terminal Manoeuvring Areas (TMAs), weather conditions, and air traffic control (ATC) Restrictions. Continuous Descent Operation (CDO) is introduced to ease the aircraft operation within the TMAs. CDO aims to operate aircraft to follow a flexible, optimum flight path that delivers significant environmental and economic benefits. These benefits

include reduced fuel burn, gaseous emissions, noise, and fuel costs without adversely affecting safety [1]. When employing CDO, arriving aircraft use their optimal climb engine thrust and speed [10]. With this approach, the aircraft decides the top of the descent (TOD) point, affecting engine thrust configurations. This technique also significantly reduces intermediate level-offs, resulting in more time spent at higher cruising levels, which are more fuel-efficient [11, 12]. This situation reduces fuel burn, lower emissions, and lower fuel costs. Air traffic controls (ATCOs) use vector manoeuvring [13, 14] and point merge system (PMS) [15, 16] approaches generally implemented in constant flight levels to maintain safe separation and provide efficient aircraft sequencing. When an aircraft enters the TMAs, It can experience level-offs during the descent phase. These level-offs can occur when aircraft enter holding patterns [17], wait for clearance to approach and land, or obey altitude restrictions while transitioning from en route airspace to terminal airspace. These procedures are necessary for ATCOs to maintain safe separation between aircraft and ensure a smooth and efficient arrival process. During the level-off segments, aircraft must keep their altitude and change idle thrust settings to level flight thrust settings. Airbus says aerodynamic and engine characteristics usually deteriorate over time due to various factors, including maintenance actions [18]. Also, weather conditions, temperature and pressure differences create different idle descent arrival trajectories for each aircraft. Therefore, applying uninterrupted CDO for each aircraft, especially busy airspaces, is impossible due to traffic numbers. This study aims to investigate level-off flight segments for London Heathrow, Amsterdam Schiphol, Paris Charles de Gaulle and Istanbul airports, the most used airport TMA in Europe.

Some studies have been conducted on selected airports [19-21]. Several studies have analyzed aircraft vertical profiles for descending operations. Lemetti et al. analyzed the TMA of Stockholm Arlanda Airport for arrival operations and showed the vertical inefficiency of descending profiles. It could lead to additional fuel burn, a vital cost and environmental impact to consider [22]. Aksoy et al. presented a study about the arrival of aircraft descending the profile of Trabzon Airport. They showed that arriving aircraft have vertical efficiency problems after 6000 feet of TOD points [11]. Gui et al. proposed a path-stretching method to eliminate level-off segments during the TMA operations of Guangzhou Baiyun International Airport. Their results showed that they reduced the total fuel consumption and total flight time for the selected airspace [23]. Saez et al. presented a method for managing terminal airspace traffic using two zones: a Pre-Sequencing Area, where 4D trajectory synchronization occurs, and a Dynamic-Trajectories Area, where adaptive arrival routes are created. These routes enable fuel-efficient CDOs with idle thrust and no speed-brake use [24]. Lui et al. presented a study

comparing the PMS and trombone route systems. PMS supports the CDO, and the results showed that PMS increased the arrival capacity [25]. Kaplan et al. presented a mixed-integer nonlinear programming model for aircraft sequencing and scheduling problems using vector manoeuvring and CDO approach [13].

2. Materials and Methods

This study uses Automatic Dependent Surveillance-Broadcast (ADS-B) data sets for the aircraft descending profile analysis. ADS-B data set, an Excel format, includes aircraft identification, position, altitude, velocity, and other flight parameters. They enable researchers to identify the flight phases of an aircraft for the entire flight operation. ADS-B data also presents valuable parameters for calculating the aircraft flight time within the TMA using time of position and altitude. A filtering algorithm is developed in Python to reveal the level-off duration for arrival aircraft. Four significant TMAs were selected among the top four airports that provide the most service in Europe [26]. Hourly arrival traffic number for each airport was considered, as shown in Figure 1. Blue, orange, grey and yellow lines represent London Heathrow, Istanbul, Paris Charles de Gaulle Airport and Amsterdam Schiphol airports.

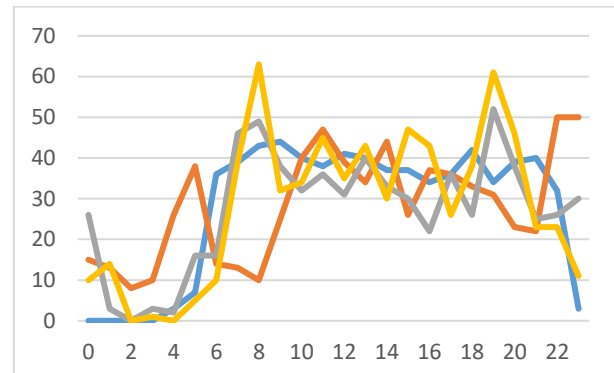


Figure 1. Hourly arrival traffic numbers for the selected airports

According to the traffic numbers, the 17:00-18:00 time duration was selected for London Heathrow, Paris Charles de Gaulle, and Istanbul airports. Also, 18:00-19:00 was chosen for the Amsterdam Schiphol airport. All the airports served almost equivalent traffic numbers per hour for the selected time durations. After determining the duration, we collected the ADS-B data from the Flightradar 24 website in Excel CVS format. Several traffic numbers were evaluated for the selected duration between 15-18 April 2024. The final arrival traffic numbers are 80, 77, 88 and 79 for London Heathrow, Paris Charles de Gaulle, Amsterdam Schiphol, and Istanbul airports for the selected days and periods. The flight phase consists of ground taxiing, take-off, climb, en-route, descend, approach, landing, and arrival taxiing. The entire flight profile is shown in Figure 2.

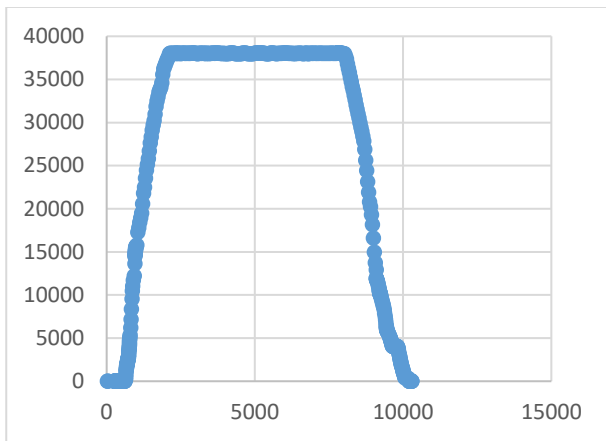


Figure 2. An entire flight profile for an aircraft landing at Paris Charles de Gaulle Airport.

In Figure 2, the vertical axis represents the altitude in feet, and the horizontal axis represents the flight time in seconds. Level-off segments are determined using information on aircraft flight phase, altitude, and rate of descent value. Our algorithm first analyzes the flight profile and finds the TOD point in the filtering mechanism, a critical point for descending operations. After determining the TOD, the algorithm focuses on altitudes below 25000 feet and above 3000 feet. An example of the arrival of aircraft ADS-B data is given in Figure 3.

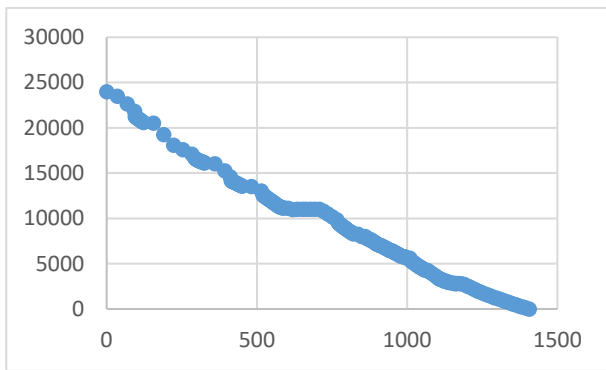


Figure 3. Descending profile of an aircraft landing at Heathrow Airport in the TMA.

The algorithm searches for every altitude change after 25000 feet to determine the rate of descent value. Suppose it finds a value as a zero. It shows that the aircraft performs a level-off flight within the selected TMA. Level-off durations for each selected TMA are analyzed carefully according to the detailed altitude distribution and the level-off time percentage regarding the entire descending operation.

3. Results and Discussion

The proposed algorithm detected the level-off segments for each TMA of the airports. The average level-off duration is presented in Table 1 for the selected traffic numbers.

Table 1. Average descending and level-off duration for each airport (sec).

Airport	Average Descending Duration	Average Level-off Duration
London Heathrow	1261.6	161.5
Paris Charles de Gaulle Airport	1216.2	176.7
Amsterdam Schiphol	1155.8	151.1
Istanbul	1259.8	218.3

The results showed that the minimum level-off duration occurred at the Amsterdam Schiphol Airport. The average level of duration is 12.8% of the entire descending operation. The rest are 13.1%, 14.5% and 17.3% for the Amsterdam Schiphol, Paris Charles de Gaulle Airport, and Istanbul Airport. While ATCOs aims to provide effective and safe aircraft sequencing, they need instructions to maintain safe separation among the aircraft set. These can be vector manoeuvre, holding, and point merge systems. ATCOs generally apply these constant flight-level methods. Furthermore, the need for separation techniques can arise more than once, according to the demand for air traffic in this airspace and airport. Altitude distributions for level-off flight are presented in Figure 4.

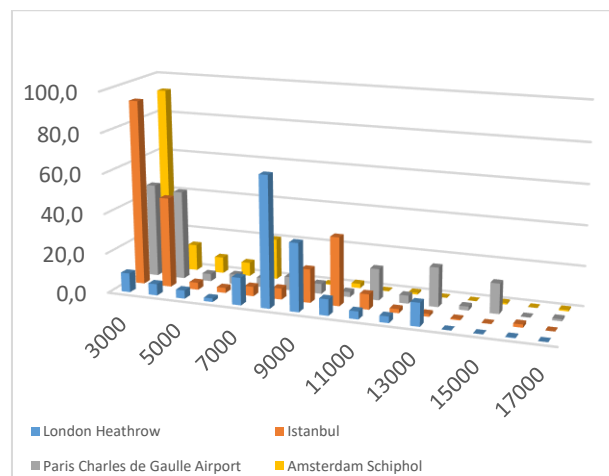


Figure 4. Level-off distributions for each airport.

The outputs showed that arrival aircraft generally fly about 3000 feet for the final sequencing of Istanbul and Amsterdam Schiphol. Also, arrival traffic for Istanbul and Paris Charles de Gaulle used 4000 feet for constant level flight for approximately the same duration. London

Heathrow arrival traffic performs level-off flight segments, mostly 8000 and 9000 feet. Paris Charles de Gaulle airport also utilizes high flight levels, such as 13000 and 15000 feet. Istanbul TMA has a point merge system; therefore, aircraft use sequencing legs located at 9000 and 10000 feet. In addition to this, the need for an extra level-off segment emerges due to the runway assignment strategy. This situation mainly occurs to maintain safe separation before flight level differences maintain the final approach point. This situation raises the level-off segment percentage for Istanbul Airport. Amsterdam Schiphol Airport uses a dynamically changing runway system. They can operate different runways for arrival and departure operations to optimize airport and airspace operations. Similarly, London Heathrow and Amsterdam Schiphol adopted a time-based separation system using intelligent approach tools. The results prove London Heathrow and Amsterdam Schiphol airports have a lower value of level-off flight duration in Europe.

4. Conclusion

The level-off flight segments during the TMA operations are investigated in this study for the most popular airports. We analyzed the results and found that London Heathrow and Amsterdam Schiphol have lower level-off segments. More than 40% of the arrival traffic performed level-off of segment no longer than two minutes for Amsterdam Schiphol and Paris Charles de Gaulle. The aircraft ratio, which has a level-off duration of less than a minute, is approximately %24, 16%, 31% and 5% for London Heathrow, Paris Charles de Gaulle, Amsterdam Schiphol, and Istanbul Airports, respectively. While level-off flight within a TMA is necessary to maintain safe separation between aircraft and ensure efficient traffic flow, it poses some disadvantages. Finally, level-off flights pose several challenges related to congestion, fuel burn, increased workload, traffic conflicts, and noise pollution. However, efforts to improve airspace management, optimize routing, and implement new technologies like CDO can help mitigate some of these disadvantages. By reducing the time aircraft spend level-off, CDO improves fuel efficiency, reduces noise pollution, and minimizes traffic conflicts. Furthermore, optimizing arrival routes and using advanced surveillance systems can help controllers manage airspace more effectively and reduce congestion while improving safety and efficiency for all aircraft. For further research, we can explore how the level-off segments affect fuel consumption and noise pollution. Additionally, we can investigate how to design TMA airspace to reduce or eliminate level-off segments effectively.

Acknowledgement

There are no financial declarations. This work does not grant funded.

Author's Contributions

Ramazan Kursat Cecen: Drafted and wrote the manuscript, supervised the progress of the experiment, and performed the experiment and results analysis.

Ethics

There are no ethical issues after the publication of this manuscript.

References

- [1]. Eurocontrol. Continuous climb and descent operations. Available online: <https://www.eurocontrol.int/concept/continuous-climb-and-descent-operations> (accessed on 04.05.2024).
- [2]. Vlachos, I, Lin, Z. 2014. Drivers of airline loyalty: Evidence from the business travelers in China. *Transportation Research Part E: Logistics and Transportation Review*, 71:1-17.
- [3]. Kafle, N, Zou, B. 2016. Modeling flight delay propagation: A new analytical-econometric approach. *Transportation Research Part B: Methodological*, 93:520-542.
- [4]. AhmadBeygi, S, Cohn, A, Guan, Y, Belobaba, P. 2008. Analysis of the potential for delay propagation in passenger airline networks. *Journal Of Air Transport Management*, 14(5) : 221-236.
- [5]. Kim, M, Park, S. 2021. Airport and route classification by modelling flight delay propagation. *Journal of Air Transport Management*, 93: 102045.
- [6]. Kwasiborska, A, Skorupski, J. 2021. Assessment of the method of merging landing aircraft streams in the context of fuel consumption in the airspace. *Sustainability*, 13(22): 12859.
- [7]. Irvine, D, Budd, L, Ison, S, Kitching, G. 2016. The environmental effects of peak hour air traffic congestion: the case of London Heathrow Airport. *Research in Transportation Economics*, 55: 67-73.
- [8]. Montlaur, A, Delgado, L. 2017. Flight and passenger delay assignment optimization strategies. *Transportation Research Part C: Emerging Technologies*. 81:99-117.
- [9]. Dönmez, K. 2023 Aircraft sequencing under the uncertainty of the runway occupancy times of arrivals during the backtrack procedure. *The Aeronautical Journal*, 127(1310): 562-580.
- [10]. ICAO, "Continuous Descent Operations (CDO) Manual – Doc 9931/AN/476," Montreal, 1st edition, 2010
- [11]. Aksoy, H, Turgut, ET, Usanmaz, Ö. 2021. The design and analysis of optimal descent profiles using real flight data. *Transportation Research Part D: Transport and Environment*, 100:103028
- [12]. Turgut, ET, Usanmaz, O, Ozan Canarslanlar, A, Sahin, O. 2010. Energy and emission assessments of continuous descent approach. *Aircraft Engineering and Aerospace Technology*, 82(1): 32-38.
- [13]. Kaplan, Z, Çetek, C, Saraç, T. 2024. A multi-objective nonlinear integer programming model for mixed runway operations within the TMAs. *The Aeronautical Journal*, 128(1320) : 340-370.

- [14]. Omer, J. 2015. A space-discretized mixed-integer linear model for air-conflict resolution with speed and heading maneuvers. *Computers & Operations Research*, 58: 75-86.
- [15]. Demirel, S. 2023 Comparison of RECAT-EU and ICAO wake turbulence category on the Point Merge System. *The Aeronautical Journal*, 127(1315): 1623-1637.
- [16]. Dönmez, K., Çetek, C, Kaya, O. 2022. Air traffic management in parallel-point merge systems under wind uncertainties. *Journal of Air Transport Management*, 104: 102268.
- [17]. Dönmez, K. 2023. Evaluation of the performance of the multi-objective scalarization methods for the aircraft sequencing and scheduling problem using multi-criteria decision-making. *Aircraft Engineering and Aerospace Technology*, 95(4): 501-511.
- [18]. Airbus, L. (2002). Getting to grips with Aircraft Performance Monitoring.
- [19]. Olive, X, Sun, J, Basora, L, Spinielli, E. 2023. Environmental inefficiencies for arrival flights at European airports. *Plos one*, 18(6): e0287612.
- [20]. Scala, P, Mota, MM, Delahaye, D. 2021. Air Traffic Management during Rare Events Such as a Pandemic: Paris Charles de Gaulle Case Study. *Aerospace*, 8(6): 155.
- [21]. Dönmez, K, Çetek, C, Kaya, O. 2022. Aircraft sequencing and scheduling in parallel-point merge systems for multiple parallel runways. *Transportation Research Record*, 2676(3): 108-124.
- [22]. Lemetti, A, Polishchuk, T, Sáez, R, Prats, X. Evaluation of flight efficiency for Stockholm Arlanda airport arrivals. In 2019 IEEE/AIAA 38th Digital Avionics Systems Conference. 2019. IEEE.
- [23]. Gui, D, Le, M, Huang, Z, Zhang, J, D'Ariano, A. 2023. Optimal aircraft arrival scheduling with continuous descent operations in busy terminal maneuvering areas. *Journal of Air Transport Management*, 107:102344.
- [24]. Sáez, R, Polishchuk, T, Schmidt, C, Hardell, H, Smetanová, L, Polishchuk, V, Prats, X. 2021. Automated sequencing and merging with dynamic aircraft arrival routes and speed management for continuous descent operations. *Transportation Research Part C: Emerging Technologies*, 132: 103402.
- [25]. Liu, W, Delahaye, D, Cetek, FA, Zhao, Q, Notry, P. 2024. Comparison of performance between PMS and trombone arrival route topologies in terminal maneuvering area. *Journal of Air Transport Management*, 115: 102532.
- [26]. OAG: Flight Database & Statistics | Aviation Analytics Available online: <https://www.oag.com/blog/europes-busiest-airports> (accessed on 04.05.2024).

Antireflection Coating for MWIR on Calcium Fluoride Using Ion-Assisted E-Beam Deposition

Yusuf Dogan^{1,2} , İlhan Erdogan^{1,2*} 

¹ Department of Electrical and Electronics Engineering, Sivas University of Science and Technology, Sivas, Türkiye

² Optical Excellence Application and Research Center, Sivas University of Science and Technology, Sivas, Türkiye

* ilhan.erdogan@sivas.edu.tr

* Orcid No: 0000-0002-2774-1349

Received: July 28, 2024

Accepted: March 3, 2025

DOI: 10.18466/cbayarfbe.1523797

Abstract

This research outlines the design, analysis, and fabrication of a multilayer anti-reflective coating on a calcium fluoride (CaF₂) substrate, specifically for mid-wavelength infrared uses, employing the ion-assisted electron-beam evaporation method. A 2-layered multilayer structure in the form of SiO₂/Ge was created on CaF₂, consisting of low refractive index silicon dioxide (SiO₂) and high refractive index germanium (Ge) thin films with a total thickness below 1 µm. The design was optimized for the 3.6-4.9 µm MWIR range, and an average transmission of 98.39% and an average reflectance of 0.93% were simulated at a broadband spectral width of 1300 nm. After the fabrication process using the ion-assisted physical vapour deposition (IAPVD) technique, the experimental results showed an average transmission of 98.13% and a reflectance value of 1.19% within the 3.6-4.9 µm range. The simulation design and experimental results were found to be very close to each other, with a difference of only 0.26%. This work provides a high-efficiency solution for AR coatings in the MWIR region on CaF₂ surfaces. To our knowledge, the Ge/SiO₂ multilayer structure on CaF₂ has not been reported before in the literature and the results obtained will be an alternative for CaF₂-based optical systems.

Keywords: Mid-wave infrared (MWIR), Calcium fluoride, Optical thin films, Anti-reflective coating, Ion-assisted e-beam deposition

1. Introduction

Antireflective (AR) coatings are thin films applied to optical components to minimize reflections and maximize light transmission. These coatings are essential and indispensable in various fields due to their broad range of applications, from infrared sensors to everyday eyeglasses. By reducing reflections, AR coatings enhance the transmission of light through optical elements, improving sensitivity, accuracy, and overall system performance [1]. In solar panels, AR coatings enhance energy efficiency by allowing more sunlight to be absorbed and converted into electricity. On eyeglasses, AR coatings reduce glare and reflections, improving visual clarity and comfort. For camera lenses, they minimize reflections and lens flare, resulting in sharper, higher-quality photographs. On display screens like those on smartphones and monitors, AR coatings reduce ambient light glare, improving visibility and user experience. In microscopes, AR coatings improve light

transmission and image contrast, enabling clearer and more detailed observations in scientific research [2-5]. AR coatings are particularly important for applications involving infrared radiation, which covers wavelengths longer than visible light but shorter than microwaves. Mid-wavelength infrared (MWIR) range (3-5 µm) being particularly important for applications such as thermal imaging, night vision, space, and environmental monitoring [6, 7]. In electro-optical systems, AR coatings increase light transmission through optical elements, enhance image quality, and improve overall system performance by minimizing signal loss and glare. This enhancement is critical for detecting temperature differences in thermal imaging and other similar applications.

The multilayer structure of AR coatings is essential for achieving optimal performance, as each layer is designed to target specific wavelengths, further reducing reflections and enhancing light transmission across a broad spectrum [8]. These coatings are designed to

minimize reflectance within this specific range by carefully selecting materials and controlling each layer's thickness and refractive index. Germanium (Ge) and silicon dioxide (SiO₂) are crucial optical materials in this range due to their effective AR properties and common use in infrared thin films. SiO₂, with a low refractive index of 1.44 at 4 μm, is favored for its availability, chemical stability, high-temperature resistance, cost-effectiveness, low dispersion, eco-friendliness, excellent adhesion to various surfaces, and good transmission in both visible and infrared ranges, along with notable scratch resistance [9, 10]. Meanwhile, Ge, a high-index material with a refractive index of 4.0 at 4 μm, offers benefits such as insolubility, effective transmission, chemical inertness, low dispersion, non-toxicity, good thermal conductivity, and durability within the infrared range [7, 11, 12]. Calcium fluoride (CaF₂) is an ideal substrate for optical thin films due to its excellent optical properties and chemical stability. It has a wide transmission range from deep ultraviolet (UV) to infrared (IR), making it suitable for diverse optical applications [13, 14]. CaF₂'s low refractive index minimizes reflection losses, which is beneficial in multi-layer coatings for maintaining high transmittance. It also has a high laser damage threshold, making it suitable for high-power laser applications. Its low solubility in water and resistance to chemical attack ensure the durability and longevity of optical components. These properties make CaF₂ a preferred substrate for spectroscopy, lithography, and other advanced optical systems. Moreover, its transparency range, low refractive index, chemical stability, and resistance to moisture make it advantageous for AR coatings, offering a non-toxic and durable solution for precision optical components [15, 16].

AR thin films can be produced through various methods including physical vapor deposition (PVD), chemical vapor deposition (CVD), magnetron sputtering, and the sol-gel process [4, 17-19]. The ion-assisted electron-beam (e-beam) deposition technique provides better control, higher film quality, reduced contamination, and greater process flexibility compared to traditional e-beam evaporation methods. In this study, an ion-assisted e-beam PVD technique was employed for the experiment. So far, numerous studies have fabricated and developed high-performance AR coatings in the MWIR spectrum range using the e-beam PVD technique. Various multilayer stacks have been implemented on different substrates such as Si [6, 7, 9, 20, 21], Ge [7, 22, 23], ZnS [24], and ZnSe [25]. Studies in the literature mainly focused on Si and Ge substrates for the MWIR region. However, the literature on CaF₂ substrates is limited, and among the studies conducted in the MWIR region with CaF₂ substrates, one focuses on a ZnS/YbF₃/Y₂O₃ 5-layer multilayer stack, presented [26] as a conference proceeding. In addition, Yenisoy et al. [27] proposed a multilayer stack of aluminum oxide (Al₂O₃) and Ge on a CaF₂ substrate. In this study, we proposed a Ge/SiO₂

multilayer stack on a CaF₂ substrate which has not been presented in the literature before.

This research details the development and manufacture of a wideband AR multilayer coating intended for CaF₂ optics, specifically targeting the MWIR spectrum. The coating was created using ion-assisted e-beam physical vapor deposition. Before the fabrication, OptiLayer software is used to design and optimize the SiO₂/Ge/CaF₂ Substrate/Ge/SiO₂ multilayer structure, and average transmission (T_{av}) of 98.39% and an average reflection (R_{av}) of 0.93% values are simulated. After the e-beam evaporation process, an average transmission (T_{av}) of 98.13% and an average reflection (R_{av}) of 1.19% is achieved through the double-sided coated structure. The study demonstrates superior transmission performance on CaF₂ optics within the 3.6-4.9 μm MWIR range, marking it as a noteworthy advancement. Moreover, the proposed AR multilayer structure is noted for its cost-effectiveness, attributed to its overall thickness and layer count.

2. Materials and Methods

Multilayer thin film coatings are essential in AR coatings because they can manipulate light precisely, enhancing the performance of optical systems by improving reflection, and transmission as needed. In these coatings, the desired transmission or reflection characteristics are achieved by optimizing the thickness of layers with high and low refractive indices. Compared to single-layer coatings, multilayer structures offer better control, a broader wavelength range, and superior performance, making them more suitable for complex applications such as narrow-band filters, high-performance mirrors, and dual/triple-band structures [1, 5]. Coating materials are chosen based on their refractive index, physical stability, transparency in the targeted wavelength regions, and thermal expansion coefficients. A multilayer stack of optical thin film coatings, comprising alternating layers of materials with different refractive indices, is deposited on a substrate. The thickness of each layer is precisely controlled to the nanometer scale to regulate light transmission and reflection through constructive and destructive interference. The multilayer design was simulated using OptiLayer software which is a specialized software suite essential for designing, analyzing, and optimizing optical coatings. It enables the creation and simulation of complex multilayer structures, using advanced algorithms and a comprehensive material database to achieve desired optical properties efficiently. The software provides detailed spectral analysis and simulates performance at different angles of incidence. It supports manufacturing processes by assessing production tolerances, enabling reverse engineering, and integrating with deposition equipment for real-time monitoring. The target design consists of 100% transmittance and 0% reflectance values distributed over 126 linearly spaced spectral points at a 0° incident angle

in the 3.6-4.9 μm wavelength range. Target interpolation was performed to align the desired spectral characteristics with the material design parameters. To achieve this, an optimization method was selected, employing the Modified Damped Least Squares (Modified DLS) algorithm. This method is particularly effective, offering rapid convergence during the initial stages of the refinement process. The Modified DLS algorithm remains a robust choice for refining intricate optical designs with high precision. The termination criteria for the Gradual Evolution setup are defined to ensure an optimized design process. The merit function is set to a threshold value of 0.5, which serves as a key indicator of convergence during the optimization.

The designed Ge/SiO₂ thin film stacks on both sides of the CaF₂ substrate have been implemented, as shown in Figure 1. In this multilayer stack, SiO₂ and Ge are used as the low (nL) and high (nH) refractive index materials, respectively. AR coatings are designed to ensure a 180° relative phase shift between the beams reflected at the top and bottom surfaces of a thin film. This results in destructive interference, which cancels out both reflected beams. The optical thickness of the coating must be an odd multiple of $\lambda/4$, where λ represents the design wavelength. This configuration is essential to create a path difference of $\lambda/2$ between the reflected beams, leading to their cancellation. The refractive index of the thin film required to achieve complete beam cancellation can be calculated using the refractive indices of the incident medium and the substrate. In the design of AR coatings, the fundamental principle for single-layer films relies on the refractive index matching between the coating material, the incident medium, and the substrate. This relationship is described by the following equation:

$$n_{film} = \sqrt{n_{medium} \cdot n_{substrate}} \quad (1)$$

For single-layer thin films, optimal antireflection is achieved when the optical thickness corresponds to a quarter wavelength of light. In contrast, for multilayer coatings, the layers are typically arranged to have optical thicknesses of either quarter-wavelength or half-wavelength according to their refractive index values. Multilayer structures are designed to provide enhanced reflection control over a broader spectral range and to achieve the desired optical performance. This design approach requires careful optimization of both the refractive index and the thickness of each layer.

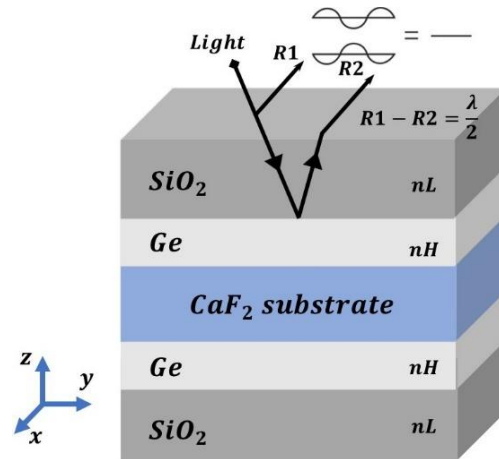


Figure 1. Schematic representation of double-sided multilayer structure

Due to its high melting and boiling points, low thermal expansion coefficient, substantial hardness, and excellent mechanical stability, CaF₂ is an ideal material for various optical applications, ensuring durability and reliability in demanding environments. The technical specifications of CaF₂ are provided in Table 1.

Table 1. Technical specifications of the CaF₂ substrate

Property	Value	Unit	Ref.
Transmission Range	0.3-11	-	[28]
Refractive Index	1.3-1.48	-	[29]
Density	3.18	g/cm ³	[30]
Melting Point	1418	C°	[31]
Boiling Point	2533	C°	[32]
Laser damage threshold	10	J/cm ²	[33]
Thermal Expansion Coefficient	18.85	1/ C°	[30]
	$\times 10^{-6}$		
Knoop's hardness, HK ₃₀₀	152-159	kg/mm ²	[30]
Young's modulus	75.8	GPa	[34]
Abbe number	95.13	-	[29]

The Hartmann dispersion equation is a mathematical representation used to describe the wavelength-dependent refractive index of optical materials [35]. This equation, often applied in the field of optics, allows for the precise characterization of materials by relating the refractive index to the wavelength of light passing through the material. The equation typically includes parameters that account for the material's intrinsic properties, such as dispersion coefficients. The dispersion formula is an empirical relationship used to describe how the refractive index of Ge and SiO₂ thin films and CaF₂ substrate varies with wavelength. The equation is given by

$$n(\lambda) = A_0 + \frac{A_1}{\lambda - A_2} \quad (2)$$

where $n(\lambda)$ is the refractive index at wavelength λ , A_0 , A_1 and A_2 are coefficients specific to the material. The Hartmann constants for a 1 mm thick CaF_2 substrate are found as 0.10, 187.98, and -139.6, for A_0 , A_1 , and A_2 , respectively. The values for the constants in the Hartmann dispersion equation were obtained by fitting experimental transmission measurements of the CaF_2 substrate. The experimental and modeled transmission and reflection spectra for a CaF_2 substrate over the MWIR range are shown in Figure 2 (a) and (b). These data exhibit a strong correlation, indicating that the theoretical model accurately represents the observed transmission and reflection spectra for the CaF_2 substrate in the MWIR range. The measurements were taken using a PerkinElmer FT-IR (Fourier-transform infrared spectroscopy) device.

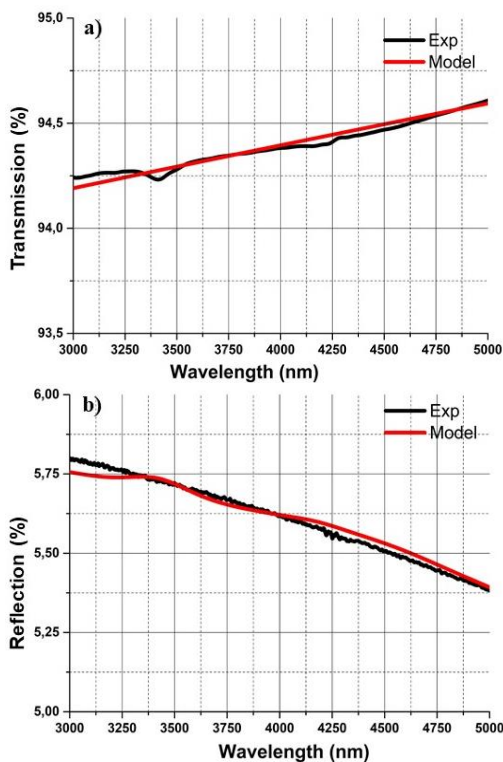


Figure 2. Experimental and modeled transmission and reflection spectra for CaF_2 substrate

Before initiating the multilayer design process, it is crucial to analyze the optical properties of individual layers comprehensively. Such evaluations are indispensable for understanding and optimizing the interactions between the layers in a multilayer structure. Each layer may be composed of distinct optical materials, each contributing uniquely to the overall optical performance. By examining these properties independently, designers can ensure proper refractive

index matching, thickness control, and spectral behavior, which are critical for achieving the desired functionality in the final multilayer configuration. To accurately simulate the refractive index dispersions in thin films, a 300 nm thick Ge film on a CaF_2 substrate and a 400 nm thick SiO_2 film on a Ge substrate are coated via e-beam evaporation. Figure 3 (a) depicts the transmission curves of 300 nm Ge and 400 nm SiO_2 thin films. The dispersion coefficients for the Ge film and SiO_2 film were determined as $A_0=4.258$, $A_1=0.003$, and $A_2=2.78$. and $A_0=0.1$, $A_1=75.64$, and $A_2=-51.73$, respectively. The dispersion coefficients A_0 , A_1 , and A_2 were calculated by fitting experimental transmission measurements of Ge and SiO_2 coated substrates. These coefficients facilitate the prediction of refractive indices across different wavelengths, enabling the customization and enhancement of optical thin film coatings with specific desired characteristics. The refractive index dispersions of Ge and SiO_2 thin films and CaF_2 substrate are illustrated in Figure 3 (b).

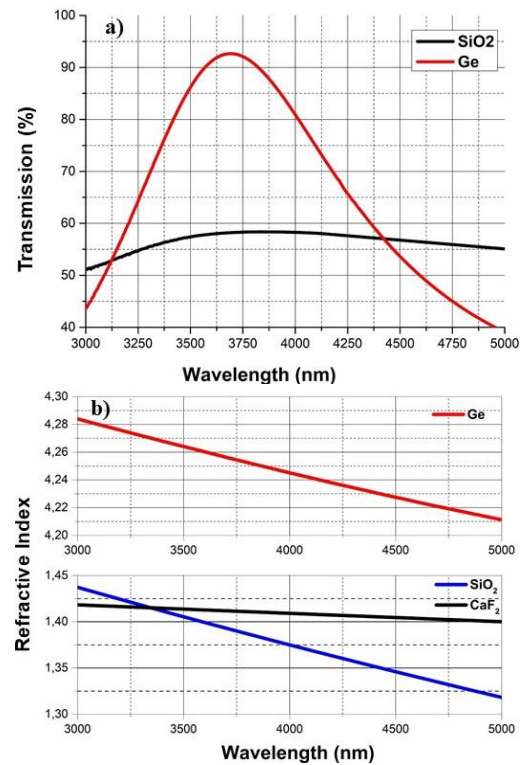


Figure 3. a) Transmission spectra of SiO_2 and Ge b) Refractive index dispersions of Ge film, SiO_2 film, and CaF_2 substrate

Refractive index distribution models were defined for the substrate and layer materials, and the multilayer AR coating design for the wavelength range of 3.6 to 4.9 μm was obtained using the Optilayer software. Thanks to gradual and needle optimizations, the optimized design reached R_{av} and T_{av} values of 0.93% and 98.39%, respectively. The optimized total thickness of the multilayer stack is approximately 889.79 nm. The quarter wavelength optical thickness (QWOT) of the layer

materials was defined for a control wavelength of 4 μm . The refractive indices of Ge, SiO₂, and CaF₂ at a center wavelength of 4 μm are found to be 4.245, 1.375, and 1.41, respectively. Table 2 shows the materials RI and layer thicknesses of the designed multilayer structure.

Table 2. Optical parameters of the designed multilayer AR coating

Material	Optical		
	Thickness (nm)	QWOT	RI at 4 μm
SiO ₂	852,787	1,193	1.375
Ge	37,003	0,148	4.245
CaF ₂	1 (mm)		1.41

The deposition of the thin films was carried out using the e-beam evaporation technique, with an ion plasma source. The e-beam PVD system used in this study is equipped with a dual electron beam configuration, consisting of a continuous single-pocket system and a six-pocket crucible system, enabling the deposition of various materials without interrupting the process for material changes. By combining the vaporized coating material with ion bombardment, the system enhances the density and adhesion of the thin film, resulting in a higher quality and more durable coating. To generate the ion plasma necessary for the deposition process, Argon (Ar) gas was introduced into the vacuum chamber. The use of argon facilitates the creation of a stable plasma, which is critical for the effective evaporation and deposition of the thin films to improve the adhesion and quality of the coating. The chamber's temperature was controlled and maintained uniformly using halogen heaters, ensuring a stable thermal environment essential for high-quality film growth. To monitor and control the deposition rate and the thickness of the deposited layers, a 6 MHz gold piezoelectric Quartz Crystal Microbalance (QCM) was employed. Figure 4 illustrates the inner chamber of the ion-assisted electron beam deposition system used in this study, showcasing its advanced design and functional versatility tailored for thin film fabrication.

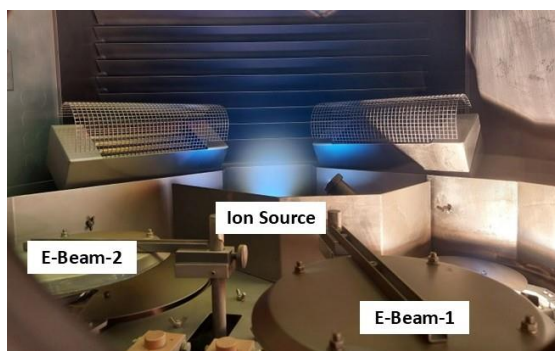


Figure 4: Inner chamber of ion-assisted E-beam PVD system

By optimizing the deposition conditions, including the ion plasma generation, temperature regulation, and real-time monitoring, high-quality Ge and SiO₂ thin films with refractive index distributions were successfully fabricated. Optical analysis is conducted to assess the coating's transmission, reflection, and surface quality. Upon detecting deviations from the expected outputs, an optimization process is commenced by modifying deposition parameters such as gas flow rates, deposition rates, temperature, ion parameters, and e-gun parameters. This iterative procedure guarantees an AR coating with desired optical characteristics. The flow chart of the AR coating process is depicted in Figure 5.

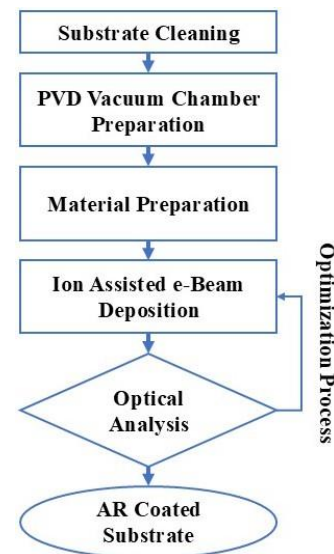


Figure 5: Flow chart of the PVD deposition process

Before deposition, the 1-inch CaF₂ substrate underwent a precleaning process to remove native oxide and contaminants, involving a rinse with acetone followed by nitrogen gas drying. During deposition, the base vacuum level was maintained at 2×10^{-7} Torr, while the process vacuum level was controlled at about 2×10^{-4} Torr, and the chamber temperature was kept at 200 °C. High-purity Ge (99.999%) and SiO₂ (99.99%) granules were placed into the crucible in the water-cooled hearth. The vaporization sequence for SiO₂ and Ge materials was followed precisely, with deposition rates of 1 nm/s for both. To ensure uniform coating, the sample holder was continuously rotated at 20 rpm. During SiO₂ vaporization, oxygen gas was introduced into the PVD chamber at a flow rate of 10 sccm, which was critical for maintaining the purity and quality of the SiO₂ layer. The optical properties of the coated multilayer AR coatings were evaluated using an FT-IR spectrometer to measure transmission and reflectance at a 10° incidence angle. Additionally, the surface roughness of the coated multilayer AR coatings was assessed using a Profilm 3D white light interferometry (WLI) profiler equipped with a 20x Michelson objective.

3. Results and Discussion

The CaF₂ substrate surfaces were thoroughly cleaned using deionized water and acetone, and then dried with nitrogen to remove any dust or natural oxides. After cleaning, a white light interferometer (Filmetrics, 3D) was used to assess how deposition affected the surface quality of the samples. Figure 6 illustrates the surface roughness profiles of the CaF₂ substrate before (a) and after (b) applying multiple layers, with a scan area of 1x1 mm. The surface roughness (Sq) values were measured as 3.04 nm (standard deviation 0.17) for the uncoated surface and 2.45 nm (standard deviation 0.07) for the coated surface.

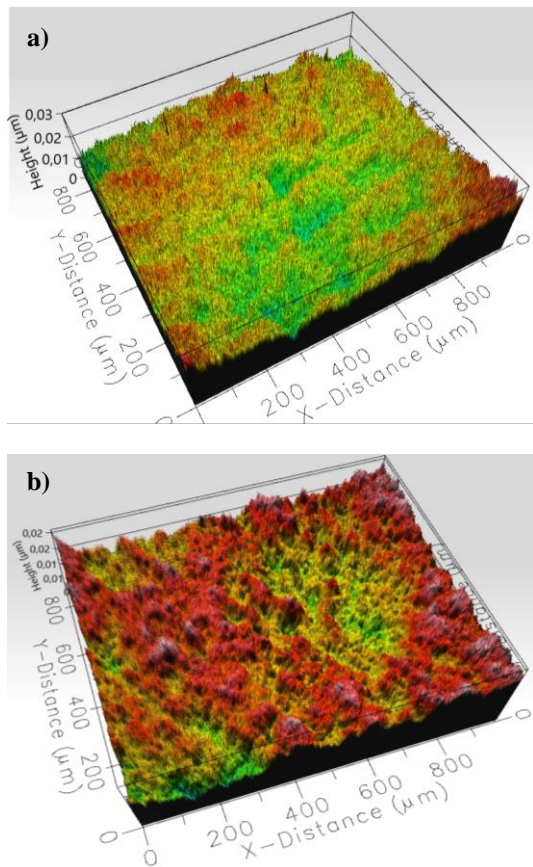


Figure 6. Surface profiles of CaF₂ substrate a) before and b) after multilayer deposition

Following the predefined process parameters, a multi-stack of SiO₂ and Ge materials was coated onto a CaF₂ substrate. Identical layer sequences and process conditions were applied to both sides of the CaF₂ substrate to reduce reflections from the rear surface. Figure 7 displays the transmission and reflection spectra of the double-side multilayer (SiO₂/Ge/CaF₂ Substrate/Ge/SiO₂) AR coating within the 3-5 μm MWIR range. Figure 7 (a) shows that the simulated transmission spectrum closely matches the measured transmission, indicating a good correlation. Minor deviations can be attributed to variations in material thickness and inherent

absorbance properties, which affect the optical path length and cause energy loss at specific wavelengths, leading to the observed discrepancies. In the 3.6-4.9 μm MWIR range, the average transmission (T) is 98.39% for the simulated data and 98.13% for the measured data. The peak transmission values are 98.98% at 4196 nm for the measured data and 99% at 3983 nm for the simulated data. Similarly, as shown in Figure 7 (b), the simulated reflection spectrum closely aligns with the measured reflection, demonstrating a strong agreement. In the 3.6-4.9 μm MWIR range, the average reflection (Rav) is 0.93% for the simulated data and 1.19% for the measured data. The minimum reflection values are 0.1% at 4120 nm for the simulated data and 0.46% at 4112 nm for the measured data.

Additionally, the inherent absorbance properties of the materials, which can cause energy loss at specific wavelengths, contribute to the observed deviations. These factors highlight the sensitivity of the spectra to physical and material parameters, emphasizing the importance of precise control and characterization in experimental setups. Moreover, the discrepancy in measured reflection values compared to the simulated data is due to the difference in incident angles between the design (AOI=0°) and the FTIR measurement (AOI=10°). Table 3 presents the Rav and Tav values of the simulated and measured curves.

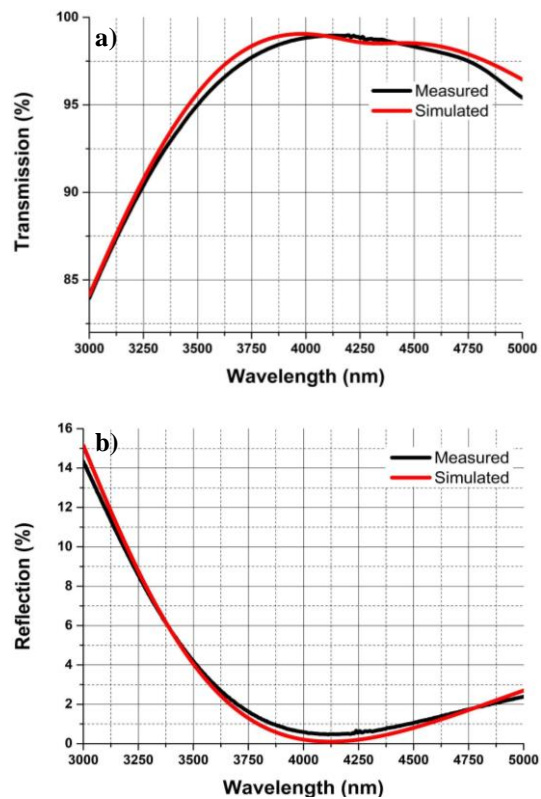


Figure 7. Measured and simulated spectra of the double-side multilayer (SiO₂/Ge/CaF₂ Substrate/Ge/SiO₂) AR coating a) Transmission b) Reflection

Table 3. Simulated and measured values of the double side multilayer (SiO₂/Ge/CaF₂ Substrate/Ge/SiO₂) AR coating for Tav and Rav in 3.6-4.9 μm.

Parameters	Simulated %	Real %
Tav	98.39	98.13
Rav	0.93	1.19

4. Conclusion

This study successfully demonstrated the design and fabrication of a highly efficient broad-band multilayer AR coating on a CaF₂ substrate, targeting the 3.6-4.9 μm wavelengths of the MWIR spectrum. The coating was applied using the ion-assisted e-beam evaporation technique, ensuring precise layer deposition and optimal optical performance. The experimental results showed a close match between the simulated and measured transmission and reflection spectra, with minor deviations attributed to thickness variations and absorbance effects. In the 3.6-4.9 μm range, the average transmission (Tav) was 98.39% for simulations 98.13% for measured data, while the average reflection (Rav) was 0.93% and 1.19%, respectively. Additionally, this study is particularly significant due to the shortage of multilayer AR coating research on CaF₂ substrates. The successful implementation of this bi-layer (SiO₂/Ge/CaF₂ Substrate/Ge/SiO₂) AR multilayer structure on a CaF₂ substrate marks a significant advancement, offering an effective coating solution for high-performance CaF₂-based optical components in MWIR electro-optical applications. Our study emphasizes the use of SiO₂, an eco-friendly, chemically stable material, combined with Ge in a simplified bilayer design, providing a cost-effective, highly applicable, easy-to-replicate, and innovative MWIR AR coating compared with the more resource-intensive other designs. Moreover, the reduced number of layers and thinner total thickness in our study make the production process significantly easier and more efficient compared to the thicker, 5-layer structures, which are inherently more complex and challenging to manufacture. The findings from this study contribute to the ongoing development of advanced AR coating designs, setting the stage for future research to explore new materials, deposition techniques, and innovative designs to further enhance AR coating technology in the MWIR region.

Author's Contributions

Yusuf Dogan: Supervision, Writing – review & editing, Writing – original draft, Methodology

İlhan Erdogan: Writing – review & editing, Writing – original draft, Software.

Ethics

There are no ethical issues after the publication of this manuscript.

References

- [1]. Raut, H. K., Ganesh, V. A., Nair, A. S., Ramakrishna, S. 2011. Anti-reflective coatings: A critical, in-depth review. *Energy & Environmental Science*; 4(10): 3779-3804. doi: 10.1039/C1EE01297E.
- [2]. Ji, C., et al. Recent Applications of Antireflection Coatings in Solar Cells. *Photonics*; 9(12). doi: 10.3390/photonics9120906.
- [3]. Bouhafs, D., Moussi, A., Chikouche, A., Ruiz, J. M. 1998. Design and simulation of antireflection coating systems for optoelectronic devices: Application to silicon solar cells. *Solar Energy Materials and Solar Cells*; 52(1): 79-93. doi: 10.1016/S0927-0248(97)00273-0.
- [4]. Chen, D. 2001. Anti-reflection (AR) coatings made by sol-gel processes: A review. *Solar Energy Materials and Solar Cells*; 68(3): 313-336. doi: 10.1016/S0927-0248(00)00365-2.
- [5]. Kaminski, P. M., Lisco, F., Walls, J. M. 2014. Multilayer Broadband Antireflective Coatings for More Efficient Thin Film CdTe Solar Cells. *IEEE Journal of Photovoltaics*; 4(1): 452-456. doi: 10.1109/JPHOTOV.2013.2284064.
- [6]. Yenisoy, A., Yeşilyaprak, C., Tüzemen, S. 2019. High efficient ultra-broadband anti-reflection coating on silicon for infrared applications. *Infrared Physics & Technology*; 100: 82-86. doi: 10.1016/j.infrared.2019.05.014.
- [7]. Bhatt, M., Nautiyal, B. B., Bandyopadhyay, P. K. 2010. High efficiency antireflection coating in MWIR region (3.6–4.9 μm) simultaneously effective for Germanium and Silicon optics. *Infrared Physics & Technology*; 53(1): 33-36. doi: 10.1016/j.infrared.2009.08.006.
- [8]. Valiei, M., Shaibani, P. M., Abdizadeh, H., Kolahdouz, M., Asl Soleimani, E., Poursafar, J. 2022. Design and optimization of single, double and multilayer anti-reflection coatings on planar and textured surface of silicon solar cells. *Materials Today Communications*; 32: 104144. doi: 10.1016/j.mtcomm.2022.104144.
- [9]. Kala, M. B., Bandyopadhyay, P. K., Nautiyal, B. B. 2012. Thorium free antireflection coating in MWIR region on Silicon optics. *Infrared Physics & Technology*; 55(5): 409-411. doi: 10.1016/j.infrared.2012.05.005.
- [10]. Amirzada, M. R., Khan, Y., Ehsan, M. K., Rehman, A. U., Jamali, A. A., Khatri, A. R. Prediction of Surface Roughness as a Function of Temperature for SiO₂ Thin-Film in PECVD Process. *Micromachines*; 13(2). doi: 10.3390/mi13020314.
- [11]. Melcher, F., Buchholz, P. 2014. Germanium. In: Gunn, A. G. (ed.) *Critical Metals Handbook*; Wiley, pp. 177-203.
- [12]. Harris, D. C. 1999. *Materials for Infrared Windows and Domes: Properties and Performance*. SPIE Press.
- [13]. Thomas, I. M. 1988. Porous fluoride antireflective coatings. *Applied Optics*; 27(16): 3356-3358. doi: 10.1364/AO.27.003356.
- [14]. Deng, C.-Z., et al. 2019. Two-pair multilayer Bloch surface wave platform in the near- and mid-infrared regions. *Applied Physics Letters*; 115(9): 091102. doi: 10.1063/1.5101008.
- [15]. Yan, J., Syoji, K., Tamaki, J. I. 2003. Crystallographic effects in micro/nanomachining of single-crystal calcium fluoride. *Journal of Vacuum Science & Technology B: Microelectronics and Nanometer Structures Processing, Measurement, and Phenomena*; 22(1): 46-51. doi: 10.1116/1.1633770.

- [16]. Çetin, N. E., et al. 2013. The structural, optical and morphological properties of CaF₂ thin films by using Thermionic Vacuum Arc (TVA). *Materials Letters*; 91: 175-178. doi: 10.1016/j.matlet.2012.07.086.
- [17]. Zambrano, D. F., et al. 2021. Mechanical and microstructural properties of broadband anti-reflective TiO₂/SiO₂ coatings for photovoltaic applications fabricated by magnetron sputtering. *Solar Energy Materials and Solar Cells*; 220: 110841. doi: 10.1016/j.solmat.2020.110841.
- [18]. Varade, A., Krishna, A., Reddy, K. N., Chellamalai, M., Shashikumar, P. V. 2014. Diamond-like Carbon Coating Made by RF Plasma Enhanced Chemical Vapour Deposition for Protective Antireflective Coatings on Germanium. *Procedia Materials Science*; 5: 1015-1019. doi: 10.1016/j.mspro.2014.07.390.
- [19]. Choi, W. S., Kim, K., Yi, J., Hong, B. 2008. Diamond-like carbon protective anti-reflection coating for Si solar cell. *Materials Letters*; 62(4): 577-580. doi: 10.1016/j.matlet.2007.06.019.
- [20]. Duris, M., Deubel, D., Bodiou, L., Vaudry, C., Keromnes, J. C., Charrier, J. 2021. Fabrication of Ge-ZnS multilayered optical filters for mid-infrared applications. *Thin Solid Films*; 719: 138488. doi: 10.1016/j.tsf.2020.138488.
- [21]. Zhu, Z., et al. 2023. Scratch-resistant antireflective coating for mid-wave infrared band. *Infrared Physics & Technology*; 133: 104807. doi: 10.1016/j.infrared.2023.104807.
- [22]. Yenisoy, A., Yesilyaprak, C., Ruzgar, K., Tuzemen, S. 2019. Ultra-broad band antireflection coating at mid wave infrared for high efficient germanium optics. *Optical Materials Express*; 9(7): 3123-3131. doi: 10.1364/OME.9.003123.
- [23]. Dogan, Y., Erdogan, İ., Altuntepe, A. 2024. Design and fabrication of highly efficient antireflective coating in MWIR on germanium using ion-assisted e-beam deposition. *Optical Materials*; 157: 116362. doi: 10.1016/j.optmat.2024.116362.
- [24]. Awasthi, S., Nautiyal, B. B., Kumar, R., Bandyopadhyay, P. K. 2012. Multi-spectral antireflection coating on zinc sulphide simultaneously effective in visible, eye safe laser wavelength and MWIR region. *Infrared Physics & Technology*; 55(5): 395-398. doi: 10.1016/j.infrared.2012.06.003.
- [25]. Lemarquis, F., Marchand, G., Amra, C. 1998. Design and manufacture of low-absorption ZnS-YF₃ antireflection coatings in the 3.5–16- μ m spectral range. *Applied Optics*; 37(19): 4239-4244. doi: 10.1364/AO.37.004239.
- [26]. Yao-ping, Z., Jun-qi, F., Hong, X. 2012. Anti-reflection coating on calcium fluoride substrate using ion-assisted deposition. In: *Proceedings of SPIE*; 8416: 84161Q. doi: 10.1117/12.976048.
- [27]. Yenisoy, A., Tüzemen, S. 2020. Development of high efficient and ultra-broadband antireflection coating on calcium fluoride for electro-optical applications. *Surface Engineering*; 36(4): 364-370. doi: 10.1080/02670844.2019.1644936.
- [28]. Michael, E. C. 2001. Challenges in IR optics. In: *Proceedings of SPIE*; 4369: 649-661. doi: 10.1117/12.445327.
- [29]. Malitson, I. H. 1963. A Redetermination of Some Optical Properties of Calcium Fluoride. *Applied Optics*; 2(11): 1103-1107. doi: 10.1364/AO.2.001103.
- [30]. Retherford, R. S., Sabia, R., Sokira, V. P. 2001. Effect of surface quality on transmission performance for (111) CaF₂. *Applied Surface Science*; 183(3): 264-269. doi: 10.1016/S0169-4332(01)00587-6.
- [31]. Jacob, R., Sergeev, D., Yazhenskikh, E., Müller, M. 2023. Evaluation of the calcium chloride-calcium fluoride system for high temperature thermal energy storage. *Journal of Energy Storage*; 72: 108521. doi: 10.1016/j.est.2023.108521.
- [32]. Choi, J. H., Na, H., Park, J., Kim, H.-J. 2019. Plasma corrosion resistance of aluminosilicate glasses containing Ca, Y and B under fluorocarbon plasma with Ar+. *Journal of Non-Crystalline Solids*; 521: 119498. doi: 10.1016/j.jnoncrysol.2019.119498.
- [33]. Bezuidenhout, D. F. 1997. Calcium Fluoride (CaF₂). In: Palik, E. D. (ed.) *Handbook of Optical Constants of Solids*; Academic Press: Burlington, pp. 815-835.
- [34]. Zhan, J., Guo, Y., Wang, H. 2024. Electro-plastic effect on the indentation of calcium fluoride. *International Journal of Mechanical Sciences*; 261: 108693. doi: 10.1016/j.ijmecsci.2023.108693.
- [35]. Lee, H. W. 1926. The Hartmann formula for the dispersion of glass. *Transactions of the Optical Society*; 28(3): 161. doi: 10.1088/1475-4878/28/3/303.

A Contribution To Solve A Linear Equation With One Variable And Reverse A Matrix In 3-Cyclic Refined Neutrosophic Ring

Hamiyet Merkepçi¹ 

¹ Department of Mathematics, University of Gaziantep, Gaziantep, Türkiye.

* hamiyetmerkepci@hotmail.com

* Orcid No: 0000-0003-4302-1162

Received: May 22, 2024

Accepted: March 5, 2025

DOI: 10.18466/cbayarfbe.1488451

Abstract

n-cyclic refined neutrosophic rings have become the focus of scientific research and various applications in recent years. Due to the complexity and versatile uses of these structures, much research and development is still needed. There are many open problems waiting to be solved in this field. This article focuses on solving some of these problems. In particular, 3-cyclic refined neutrosophic rings are emphasized and the solution of some basic problems in this context is discussed. First, a linear equation is solved and then the inverse of 2x2 matrices is found. In order to do all these, the inverse of an element taken from this ring is used. There is a need for convenience for this. Therefore, the algorithm developed to easily find the inverse of an element in 3-cycle refined neutrosophic rings is presented.

Keywords: Neutrosophic Ring, n-Cyclic Refined Neutrosophic Ring, 3-Cyclic Refined Neutrosophic Ring, 3-Cyclic Refined Neutrosophic equation, Inverse of 3-Cyclic Refined Neutrosophic Real Number.

1. Introduction

Neutrosophy is an important concept in philosophy and has formed the basis of the widely used neutrosophic set theory. Thanks to the contributions of this theory to classical set theory, new algebraic structures and topologies such as neutrosophic groups, rings, spaces and modules have been defined and applied in various fields. The wide use of neutrosophic clusters is clearly evident in various studies. These clusters are used as an important tool, especially in the analysis of situations such as uncertainty, inconsistency and incompleteness [1,2,3,4,6,7,9,10,11]. Recent advances in this field include the introduction of improved neutrosophic clusters, as in [8]. The results of these developments are notable in the study of refined neutrosophic rings as well as refined neutrosophic modules and spaces [5, 12, 13]. Florentin Smarandache [21] refined the concept of literal indeterminacy I as I_1, I_2, \dots, I_n and defined a different multiplication on them called n-cyclic refined neutrosophic ring. The introduction of n-refined neutrosophic clusters reflects an effort to capture and analyze the complexities of uncertainty in more detail. The elements in any n-refined neutrosophic ring and an n-cyclic refined neutrosophic ring are equivalent. Despite this equality in elements, the multiplication of elements differs significantly based on the defined

operation between sub-indeterminacies. This differentiation leads to the emergence of a new class of refined neutrosophic rings [14]. n-cyclic refined neutrosophic rings'' has become a widely studied in [15-23]. Due to the complexity and versatile uses of these structures, much research and development is still needed. There are many open problems waiting to be solved in this field. This article focuses on solving some of these problems. Particularly, 3-cyclic refined neutrosophic rings are focused on and the solution of some basic problems in this context is discussed. First, a linear equation is solved, then the inverse of the 2x2 matrices is found. To do all this, the inverse of an element taken from this ring is used. To facilitate this process, an algorithm is presented to easily find the inverse of an element in 3-cyclic refined neutrosophic rings.

2. Materials and Methods

Definition 2.1: [4] Let R be a ring and I_1, I_2, \dots, I_n be n sub-indeterminacies. $R_n(I) = \{a_0 + a_1 I_1 + \dots + a_n I_n : a_i \in R, i=1,2,\dots,n\}$ is called n-cyclic refined neutrosophic ring with the following operations:

$$\sum_{i=0}^n x_i I_i + \sum_{i=0}^n y_i I_i = \sum_{i=0}^n (x_i + y_i) I_i,$$

$$\sum_{i=0}^n x_i I_i \cdot \sum_{i=0}^n y_i I_i = \sum_{i,j=0}^n (x_i \cdot y_j) I_i I_j = \sum_{i,j=0}^n (x_i \cdot y_j) I_{(i+j \bmod n)}.$$

$$A^{-1} = \frac{1}{2} + I_1 \left[\frac{3}{1.1} \right] + I_2 \left[\frac{-(-3) - 2}{2.1} + \frac{-3}{1.1} \right] \Rightarrow$$

$$A^{-1} = \frac{1}{2} + 3I_1 - \frac{5}{2} I_2$$

Now, solve one variable equation given in example 2.5

$$AX + B = 0 \Rightarrow X = A^{-1} \cdot B$$

$$\Rightarrow X = \left(\frac{1}{2} + 3I_1 - \frac{5}{2} I_2 \right) \cdot (-1 + 4I_1 - 2I_2)$$

$$\Rightarrow X = -\frac{1}{2} + I_1 [2 - 3 - 6 - 10] + I_2 \left[-1 + 12 + \frac{5}{2} + 5 \right]$$

$$\text{So, the solution is } X = -\frac{1}{2} - 17I_1 + \frac{37}{2} I_2.$$

Definition 2.2: Let R be a ring. $R_3(I)$ is called 3-cyclic refined neutrosophic ring defined by $R_3(I) = \{m_0 + m_1 I_1 + m_2 I_2 + m_3 I_3 : m_i \in R, i = 1, 2, 3\}$

.It is commutative if $\forall m, n \in R_3(I), mn = nm$. If

there is $1 \in R_3(I)$ and $1 \cdot m = m \cdot 1 = m$, then it is called an 3-cyclic refined neutrosophic ring with unity.

Theorem 2.3: [12]

$R_2(I) = \{m_0 + m_1 I_1 + m_2 I_2 : m_i \in R\}$ be 2-cyclic refined neutrosophic ring of real numbers. Let

$A = m_0 + m_1 I_1 + m_2 I_2 \in R_2(I)$. Then, the algorithm of invers of A is given the following:

$$A^{-1} = \frac{1}{m_0} + I_1 \left[\frac{-m_1}{(m_0 - m_1 + m_2)(m_0 + m_1 + m_2)} \right] + I_2 \left[\frac{-m_1 - m_2}{m_0(m_0 + m_1 + m_2)} + \frac{m_1}{(m_0 + m_1 + m_2)(m_0 - m_1 + m_2)} \right]$$

where $m_0 \neq 0, m_2 \neq 0, m_0 - m_1 + m_2 \neq 0$.

Remark 2.4: A linear 2-cyclic refined neutrosophic equation with one variable $AX + B = 0$ can be solved easily by using above algorithm of the inverse of a 2-cyclic refined neutrosophic real number A .

Example 2.5: By getting 2-cyclic refined neutrosophic linear equation:

$$(2 - 3I_1 + 2I_2)X + (1 - 4I_1 + 2I_2) = 0$$

Let us solve this linear equation.

Solution: Let $AX + B = 0$ be a linear 2-cyclic refined neutrosophic equation with one variable, where

$$A = 2 - 3I_1 + 2I_2, B = 1 - 4I_1 + 2I_2,$$

$X = x_0 + x_1 I_1 + x_2 I_2$. We compute A^{-1} with the algorithm given in theorem 2.3.

For $a_0 = 2 \neq 0, a_2 = 2 \neq 0, a_0 - a_1 + a_2 = 1 \neq 0,$

3.Results and Discussion

Definition 3.1: Let R be any ring with unity and $R_3(I) = \{a_0 + a_1 I_1 + a_2 I_2 + a_3 I_3 : a_i \in R, i = 1, 2, 3\}$

be the 3-cyclic refined neutrosophic ring. Then

$A = a_0 + a_1 I_1 + a_2 I_2 + a_3 I_3 \in R_3(I)$ is called

invertible (unit) if and only if there exists

$A^{-1} = K = k_0 + k_1 I_1 + k_2 I_2 + k_3 I_3 \in R_3(I)$ such

that $A \cdot A^{-1} = A \cdot K = 1$.

Theorem 3.2: Let R be any ring of real numbers with unit and $R_3(I) = \{a_0 + a_1 I_1 + a_2 I_2 + a_3 I_3 : a_i \in R\}$

be the 3-cyclic refined neutrosophic ring of real numbers. Then, $A = a_0 + a_1 I_1 + a_2 I_2 + a_3 I_3$ is

invertible if and only if the following Diophantine equation is true:

equation is true:

$$(a_0 + a_3)^3 + (a_1)^3 + (a_2)^3 - 3a_1 a_2 (a_0 + a_3) \neq 0$$

Proof: The invertibility of A means that compute the 3-cyclic refined neutrosophic equation $A \cdot A^{-1} = 1$, where

$$A = a_0 + a_1 I_1 + a_2 I_2 + a_3 I_3 \in R_3(I) \text{ and}$$

$$A^{-1} = K = k_0 + k_1 I_1 + k_2 I_2 + k_3 I_3 \in R_3(I).$$

$$A \cdot K = a_0 k_0 + I_1 [a_0 k_1 + a_1 k_0 + a_1 k_3 + a_3 k_1 + a_2 k_2]$$

$$+ I_2 [a_0 k_2 + a_2 k_0 + a_2 k_3 + a_3 k_2 + a_1 k_1]$$

$$+ I_3 [a_0 k_3 + a_3 k_0 + a_1 k_2 + a_2 k_1 + a_3 k_3] = 1$$

This implies that;

$$\begin{aligned} a_0 k_0 &= 1, & (a_0 + a_3)k_1 + a_2 k_2 + a_1 k_3 &= -a_1 k_0 \\ a_1 k_1 + (a_0 + a_3)k_2 + a_2 k_3 &= -a_2 k_0 \\ a_2 k_1 + a_1 k_2 + (a_0 + a_3)k_3 &= -a_3 k_0 \end{aligned}$$

Get three linear equations with three variables k_1, k_2, k_3 and write the following system:

$$\begin{bmatrix} (a_0 + a_3) & a_2 & a_1 \\ a_1 & (a_0 + a_3) & a_2 \\ a_2 & a_1 & (a_0 + a_3) \end{bmatrix} \begin{bmatrix} k_1 \\ k_2 \\ k_3 \end{bmatrix} = \begin{bmatrix} -a_1/a_0 \\ -a_2/a_0 \\ -a_3/a_0 \end{bmatrix}$$

Where the coefficients matrix is called M. The system is solvable uniquely if and only if the determinant of the coefficients matrix M is invertible, that is,

$$\det M = \begin{vmatrix} a_0 + a_3 & a_2 & a_1 \\ a_1 & a_0 + a_3 & a_2 \\ a_2 & a_1 & a_0 + a_3 \end{vmatrix} \neq 0$$

By easy computing the determinant of the coefficients matrix, we get the equations

$$(a_0 + a_3)^3 + (a_1)^3 + (a_2)^3 - 3a_1 a_2 (a_0 + a_3) \neq 0$$

Theorem 3.3: Let R be any ring of real numbers with unity and

$$R_3(I) = \{a_0 + a_1 I_1 + a_2 I_2 + a_3 I_3 : a_i \in R\}$$

be the 3-cyclic refined neutrosophic ring of real numbers. Let $A = a_0 + a_1 I_1 + a_2 I_2 + a_3 I_3 \in R_3(I)$

and $A^{-1} = K = k_0 + k_1 I_1 + k_2 I_2 + k_3 I_3 \in R_3(I)$

Then, find the following algorithm of $A^{-1} = K$ is true.

$$\begin{aligned} A^{-1} = K &= \frac{1}{a_0} + \left(\frac{a_2^2 - a_1(a_0 + a_3)}{N} \right) I_1 + \left(\frac{a_1^2 + a_2(a_0 + a_3)}{N} \right) I_2 \\ &+ \left(\frac{-(a_1^3 + a_2^3 + a_3^3) + a_1 a_2 (2a_0 + 3a_3) - a_0 a_3 (a_0 + 2a_3)}{a_0 N} \right) I_3 \end{aligned}$$

Where $N = \det M \neq 0$ and $a_0 \neq 0$.

$$AdjM = \begin{bmatrix} \begin{vmatrix} (a_0 + a_3) & a_2 \\ a_1 & (a_0 + a_3) \end{vmatrix} & -\begin{vmatrix} a_1 & a_2 \\ a_2 & (a_0 + a_3) \end{vmatrix} & \begin{vmatrix} a_1 & (a_0 + a_3) \\ a_2 & a_1 \end{vmatrix} \\ -\begin{vmatrix} a_2 & a_1 \\ a_1 & (a_0 + a_3) \end{vmatrix} & \begin{vmatrix} (a_0 + a_3) & a_1 \\ a_2 & (a_0 + a_3) \end{vmatrix} & -\begin{vmatrix} (a_0 + a_3) & a_2 \\ a_2 & a_1 \end{vmatrix} \\ \begin{vmatrix} a_2 & a_1 \\ (a_0 + a_3) & a_2 \end{vmatrix} & -\begin{vmatrix} (a_0 + a_3) & a_1 \\ a_1 & a_2 \end{vmatrix} & \begin{vmatrix} (a_0 + a_3) & a_2 \\ a_1 & (a_0 + a_3) \end{vmatrix} \end{bmatrix}^T$$

Proof: Let $A = a_0 + a_1 I_1 + a_2 I_2 + a_3 I_3 \in R_3(I)$ and $A^{-1} = K = k_0 + k_1 I_1 + k_2 I_2 + k_3 I_3 \in R_3(I)$.

Compute $A.K = 1$.

$$\begin{aligned} A.K &= a_0 k_0 + I_1 [a_0 k_1 + a_1 k_0 + a_1 k_3 + a_3 k_1 + a_2 k_2] \\ &+ I_2 [a_0 k_2 + a_2 k_0 + a_2 k_3 + a_3 k_2 + a_1 k_1] \\ &+ I_3 [a_0 k_3 + a_3 k_0 + a_1 k_2 + a_2 k_1 + a_3 k_3] = 1 \end{aligned}$$

$$\Rightarrow a_0 k_0 = 1,$$

$$a_0 k_1 + a_1 k_0 + a_1 k_3 + a_3 k_1 + a_2 k_2 = 0$$

$$a_0 k_2 + a_2 k_0 + a_2 k_3 + a_3 k_2 + a_1 k_1 = 0$$

$$a_0 k_3 + a_3 k_0 + a_1 k_2 + a_2 k_1 + a_3 k_3 = 0$$

$$\Rightarrow (a_0 + a_3)k_1 + a_2 k_2 + a_1 k_3 = -\frac{a_1}{a_0}$$

$$a_1 k_1 + (a_0 + a_3)k_2 + a_2 k_3 = -\frac{a_2}{a_0}$$

$$a_2 k_1 + a_1 k_2 + (a_0 + a_3)k_3 = -\frac{a_3}{a_0}$$

Then write the following system;

$$\begin{bmatrix} (a_0 + a_3) & a_2 & a_1 \\ a_1 & (a_0 + a_3) & a_2 \\ a_2 & a_1 & (a_0 + a_3) \end{bmatrix} \begin{bmatrix} k_1 \\ k_2 \\ k_3 \end{bmatrix} = \begin{bmatrix} -a_1/a_0 \\ -a_2/a_0 \\ -a_3/a_0 \end{bmatrix}$$

(1)

Where the coefficients matrix is called M. By multiplying above system from the right and left by the inverse of M, obtain the coefficients of K, that is, find an algorithm of $A^{-1} = K$.

Now, compute $M^{-1} = \frac{1}{\det M} AdjM$.

Where

$$\det M = (a_0 + a_3)^3 + (a_1)^3 + (a_2)^3 - 3a_1 a_2 (a_0 + a_3) \neq 0$$

$$AdjM = \begin{bmatrix} (a_0 + a_3)^2 - a_1a_2 & -a_1(a_0 + a_3) + a_2^2 & a_1^2 - a_2(a_0 + a_3) \\ -a_2(a_0 + a_3) + a_1^2 & (a_0 + a_3)^2 - a_1a_2 & -a_1(a_0 + a_3) + a_2^2 \\ a_2^2 - a_1(a_0 + a_3) & -a_2(a_0 + a_3) + a_1^2 & (a_0 + a_3)^2 - a_1a_2 \end{bmatrix}^T$$

$$AdjM = \begin{bmatrix} (a_0 + a_3)^2 - a_1a_2 & -a_2(a_0 + a_3) + a_1^2 & a_2^2 - a_1(a_0 + a_3) \\ -a_1(a_0 + a_3) + a_2^2 & (a_0 + a_3)^2 - a_1a_2 & -a_2(a_0 + a_3) + a_1^2 \\ a_1^2 - a_2(a_0 + a_3) & -a_1(a_0 + a_3) + a_2^2 & (a_0 + a_3)^2 - a_1a_2 \end{bmatrix}$$

By easy computing , write the following matrix is inverse of M;

$$M^{-1} = \begin{bmatrix} \frac{(a_0 + a_3)^2 - a_1a_2}{(a_0 + a_3)^3 + a_1^3 + a_2^3 - 3a_1a_2(a_0 + a_3)} & \frac{-a_2(a_0 + a_3) + a_1^2}{(a_0 + a_3)^3 + a_1^3 + a_2^3 - 3a_1a_2(a_0 + a_3)} & \frac{a_2^2 - a_1(a_0 + a_3)}{(a_0 + a_3)^3 + a_1^3 + a_2^3 - 3a_1a_2(a_0 + a_3)} \\ \frac{-a_1(a_0 + a_3) + a_2^2}{(a_0 + a_3)^3 + a_1^3 + a_2^3 - 3a_1a_2(a_0 + a_3)} & \frac{(a_0 + a_3)^2 - a_1a_2}{(a_0 + a_3)^3 + a_1^3 + a_2^3 - 3a_1a_2(a_0 + a_3)} & \frac{-a_2(a_0 + a_3) + a_1^2}{(a_0 + a_3)^3 + a_1^3 + a_2^3 - 3a_1a_2(a_0 + a_3)} \\ \frac{a_1^2 - a_2(a_0 + a_3)}{(a_0 + a_3)^3 + a_1^3 + a_2^3 - 3a_1a_2(a_0 + a_3)} & \frac{-a_1(a_0 + a_3) + a_2^2}{(a_0 + a_3)^3 + a_1^3 + a_2^3 - 3a_1a_2(a_0 + a_3)} & \frac{(a_0 + a_3)^2 - a_1a_2}{(a_0 + a_3)^3 + a_1^3 + a_2^3 - 3a_1a_2(a_0 + a_3)} \end{bmatrix}$$

By multiplying the system (I) from the right and left by M^{-1} , obtain the coefficients of K . So,

$$k_0 = \frac{1}{a_0}, \quad k_1 = \frac{a_2^2 - a_1(a_0 + a_3)}{N}, \quad k_2 = \frac{a_1^2 - a_2(a_0 + a_3)}{N}, \quad k_3 = \frac{-(a_1^3 + a_2^3 + a_3^3) + a_1a_2(2a_0 + 3a_3) - a_0a_3(a_0 + 2a_3)}{a_0N}$$

Where $N = \det M \neq 0$ and $a_0 \neq 0$.

Finally, the algorithm of $A^{-1} = K$;

$$K = \frac{1}{a_0} + \left(\frac{a_2^2 - a_1(a_0 + a_3)}{N} \right) I_1 + \left(\frac{a_1^2 - a_2(a_0 + a_3)}{N} \right) I_2 + \left(\frac{-(a_1^3 + a_2^3 + a_3^3) + a_1a_2(2a_0 + 3a_3) - a_0a_3(a_0 + 2a_3)}{a_0N} \right) I_3$$

4. Numerical Application

Problem 4.1: Take the following 3-cyclic refined neutrosophic linear equation:

$(2 + I_1 - 3I_2 + I_3)X + I_1 - I_2 - I_3 = 0$. Let us solve this linear equation.

Solution: This problem is a linear 3-cyclic refined neutrosophic equation with one variable $AX + B = 0$, where

$A = 2 + I_1 - 3I_2 + I_3$, $X = x_0 + x_1I_1 + x_2I_2 + x_3I_3$ and $B = I_1 - I_2 - I_3$. Firstly, Let us check whether A is invertible or not. So that, use the algorithm given in theorem 3.2.

$$\Rightarrow (a_0 + a_3)^3 + a_1^3 + a_2^3 - 3a_1a_2(a_0 + a_3) \neq 0$$

$$\Rightarrow (2+1)^3 + 1^3 + (-3)^3 - 3.1.(-3).(2+1) = 28 \neq 0$$

So, A is invertible.

Now, compute A^{-1} with the algorithm given in theorem 3.3.

$$A^{-1} = \frac{1}{2} + \left(\frac{(-3)^2 - 1(2+1)}{28} \right) I_1 + \left(\frac{1^2 - (-3)(2+1)}{28} \right) I_2$$

$$+ \left(\frac{-\left(1^3 + (-3)^3 + 1^3\right) + 1(-3)(2.2+3.1) - 2.1(2+2.1)}{2.28} \right) I_3$$

$$A^{-1} = \frac{1}{2} + \frac{3}{14} I_1 + \frac{5}{14} I_2 - \frac{1}{14} I_3$$

Finally, solve one variable equation given in problem:

$$AX + B = 0 \Rightarrow X = A^{-1}B$$

$$\Rightarrow X = \left(\frac{1}{2} + \frac{3}{14} I_1 + \frac{5}{14} I_2 - \frac{1}{14} I_3 \right) \cdot (-I_1 + I_2 + I_3)$$

$$\Rightarrow X = \left(-\frac{1}{2} + \frac{3}{14} + \frac{5}{14} + \frac{1}{14} \right) I_1$$

$$+ \left(\frac{1}{2} - \frac{3}{14} + \frac{5}{14} - \frac{1}{14} \right) I_2 + \left(\frac{1}{3} + \frac{3}{14} - \frac{5}{14} - \frac{1}{14} \right) I_3$$

$$\Rightarrow X = \frac{1}{7} I_1 + \frac{4}{7} I_2 + \frac{2}{7} I_3$$

Problem 4.2. Let $A = \begin{bmatrix} 1 & -2I_2 \\ I_1 & 1 - I_3 \end{bmatrix} \in R_3(I)$. Is it invertible?

Solution: Let us solve the problem using the found algorithms. Compute A^{-1} .

$$A^{-1} = \frac{1}{\det A} \text{Adj}A \Rightarrow \det A = 1 + I_3$$

Let $\frac{1}{\det A} = B$. Using the algorithm of an element in

$$R_3(I) \text{ in theorem 3.3, get } B = 1 - \frac{1}{2} I_3.$$

$$\text{Adj}A = \begin{bmatrix} 1 - I_3 & 2I_2 \\ -I_1 & 1 \end{bmatrix}$$

$$\Rightarrow A^{-1} = \left(1 - \frac{1}{2} I_3 \right) \begin{bmatrix} 1 - I_3 & 2I_2 \\ -I_1 & 1 \end{bmatrix}$$

$$\Rightarrow A^{-1} = \begin{bmatrix} 1 - I_3 & I_2 \\ -\frac{1}{2} I_1 & 1 - \frac{1}{2} I_3 \end{bmatrix}$$

So, the inverse of a given matrix in $R_3(I)$ can be found easily using algorithms.

5. Conclusion

In this article, methods for solving basic mathematical problems in 3-cycle refined neutrosophic rings are developed and applied. Operations such as finding the inverse of elements, solving linear equations and calculating the inverse of 2x2 matrices are examined in detail. These solutions provide a basis for more complex problems in this field and open new avenues for researchers.

Author's Contributions

Hamiyet Merkepçi: Drafted and wrote the manuscript, performed the experiment and result analysis.

Ethics

There are no ethical issues after the publication of this manuscript.

References

- [1]. Abobala, M., "AH-Subspaces in Neutrosophic Vector Spaces", *International Journal of Neutrosophic Science*, Vol. 6 , pp. 80-86, 2020.
- [2]. Abobala, M., "Classical Homomorphisms Between Refined Neutrosophic Rings and Neutrosophic Rings", *International Journal of Neutrosophic Science*, Vol. 5, pp. 72-75, 2020.
- [3]. Abobala, M., "On Some Special Substructures of Neutrosophic Rings and Their Properties", *International Journal of Neutrosophic Science*", Vol. 4 , pp. 72-81, 2020.
- [4]. Abobala M., "n-Cyclic Refined Neutrosophic Algebraic Systems Of Sub-Indeterminacies, An Application To Rings and Modules", *International Journal of Neutrosophic Science*, Vol. 12, 2020. pp. 81-95 .
- [5]. Abobala, M., "On Some Special Substructures of Refined Neutrosophic Rings", *International Journal of Neutrosophic Science*, Vol. 5, pp. 59-66, 2020.
- [6]. Agboola, A.A.A., Akwu, A.D., and Oyebo, Y.T., "Neutrosophic Groups and Subgroups", *International .J. Math. Combin*, Vol. 3, pp. 1-9, 2012.
- [7]. Agboola, A.A.A., and Akinleye, S.A., "Neutrosophic Vector Spaces", *Neutrosophic Sets and Systems*, Vol. 4 , pp. 9-17, 2014.
- [8]. Agboola, A.A.A., "On Refined Neutrosophic Algebraic Structures", *Neutrosophic Sets and Systems*, Vol.10, pp. 99-101, 2015.
- [9]. Alhamido, R., and Abobala, M., "AH-Substructures in Neutrosophic Modules", *International Journal of Neutrosophic Science*, Vol. 7, pp. 79-86 , 2020.
- [10]. Alhamido, R., and Gharibah, T., "Neutrosophic Crisp Tri-Topological Spaces", *Journal of New Theory*, Vol. 23 , pp.13-21, 2018.
- [11]. A. Alrida Basheer , Katy D. Ahmad , Rozina Ali., "Examples on Some Novel Diophantine Equations Derived from the Group of Units Problem in n-Cyclic Refined Neutrosophic Rings of Integers",



Galoitica Journal Of Mathematical Structures And Applications,
Vol.3, 2022.

[12]. Basheer Abd Al Rida Sadiq., A Contribution to the Group of Units' Problem in Some 2- Cyclic Refined Neutrosophic Rings, *Journal Of Neutrosophic And Fuzzy Systems*, Vol.18, No.3, pp.48-58, 2022.

[13]. Basheer, A., Ahmad, K., and Ali, R., " A Short Contribution To Von Shtawzen's Abelian Group In n-Cyclic Refined Neutrosophic Rings", *Journal Of Neutrosophic And Fuzzy Systems*, 2022.

[14]. Basheer, A., Ahmad, K., and Ali, R., " On Some Open Problems About n-Cyclic Refined Neutrosophic Rings and Number Theory", *Journal Of Neutrosophic And Fuzzy Systems*, 2022.

[15]. Hatip, A., Alhamido, R., and Abobala, M., "A Contribution to Neutrosophic Groups", *International Journal of Neutrosophic Science*", Vol. 0, pp. 67-76 , 2019.

[16]. Hatip, A., and Olgun, N., " On Refined Neutrosophic R-Module", *International Journal of Neutrosophic Science*, Vol. 7, pp.87-96, 2020.

[17]. Hatip, A., and Abobala, M., "AH-Substructures In Strong Refined Neutrosophic Modules", *International Journal of Neutrosophic Science*, Vol. 9, pp. 110-116 , 2020.

[18]. Sankari, H., and Abobala, M., " On The Group of Units Classification In 3-Cyclic and 4-cyclic Refined Rings of Integers And The Proof of Von Shtawzens' Conjectures", *International Journal of Neutrosophic Science*, 2023.

[19]. Sankari, H., and Abobala, M., "On The Classification of The Group of Units of Rational and Real 2-Cyclic Refined Neutrosophic Rings", *Neutrosophic Sets and Systems*, 2023.

[20]. Sankari, H., and Abobala, M., "On the Algebraic Homomorphisms between Symbolic 2-plithogenic Rings and 2-cyclic Refined Rings", *Neutrosophic Sets and Systems*, 2023.

[21]. Smarandache, F., and Abobala, M., "n-Refined neutrosophic Rings", *International Journal of Neutrosophic Science*, Vol. 5, pp. 83-90, 2020.

[22]. Von Shtawzen, O., " Conjectures For Invertible Diophantine Equations Of 3-Cyclic and 4-Cyclic Refined Integers", *Journal Of Neutrosophic And Fuzzy Systems*, Vol.3, 2022.

[23]. Von Shtawzen, O., " On A Novel Group Derived From A Generalization Of Integer Exponents and Open Problems", *Galoitica journal Of Mathematical Structures and Applications*, Vol 1, 2022.

Investigation of Salinity Tolerance Related Gene Expression in Rice (*Oryza sativa* L.)

Atilla Salman¹ , Sinan Meriç¹ , Tamer Gümüş¹ , Çimen Atak¹ , Alp Ayan^{1*} 

¹Department of Molecular Biology and Genetics, Istanbul Kültür University, Istanbul, Türkiye
* a.ayan@iku.edu.tr

*Orcid No: 0000-0003-3749-0472

Received: August 7, 2024

Accepted: November 27, 2024

DOI: 10.18466/cbayarfb.1529138

Abstract

Rice ranks second with the highest consumption rate after corn in world production. As a result of various biotic and abiotic stress factors exposed during production, plants quit normal growth. Under such conditions, plants have developed survival mechanisms at the molecular level in order to maintain their existence. Phenotypic data is widely used to evaluate plant tolerance with assistance of gene expression analysis that interprets the source of tolerance. In this study, Osmancık-97 rice variety which is extensively cultivated in Türkiye was grown under four different salt (NaCl) concentrations (60, 90, 120 mM and control) in *in vivo* conditions. The study aimed to determine the expression differences of the TPS1, NHX1, SOS1 and HKT2;1 genes under increasing salinity conditions. In the highest applied NaCl concentration (120 mM), TPS1, NHX1, SOS1 and HKT2;1 gene expression decreased 78.2, 74.0, 78.3, and 73.5% compared to the control, respectively. In the same concentration, parameters of photosynthetic pigment content, average plant length, fresh and dry weight, and root length decreased significantly. In contrast, proline accumulation and TBARS content presented significant increases. The difference in ion homeostasis and salt tolerance among species or varieties is related to the expression of regulatory genes. Rice, a moderately salt sensitive crop, has complex responses to salt stress and its sensitivity varies according to species, variety, growth and development stages and the duration of stress to which it is exposed.

Keywords: Abiotic Stress, *Oryza sativa*, OsHKT2;1, OsNHX1, OsSOS1, OsTPS1, Salinity

1. Introduction

Rice, which belongs to the *Oryza* genus, is a member of the Poaceae family. The genus has two cultivated species (*Oryza sativa* and *Oryza glaberrima*) and twenty-two wild-type varieties [1]. The wild-type varieties are distributed around South America, Australia, Asia and Africa, while as one of the cultivated varieties, *O. glaberrima*, is restricted to Africa. On the other hand, the second cultivated variety, *O. sativa*, is the most common variety grown in about 112 countries around the world [2]. Rice (*O. sativa* L.), which was first cultivated in China and India, is one of the earliest cultivated plants [3]. Rice has been consumed by humans for about 5000 years due to its carbohydrates, rich content of vitamins (A, E, B1 and B2), protein, minerals (calcium, phosphorus, sodium, magnesium, zinc) and low production costs [4]. Therefore, rice ranks second after maize in terms of production and share of cultivation in the world [5].

According to 2018 data from the Food and Agriculture Organization (FAO), the average annual market share of rice production in the world is 996.1 million tons. China was ranked first with 426.2 million tons, India ranked second with 172.6 million tons and Indonesia ranked third with 83 million tons. As of 2018, Türkiye produced 940 thousand tons and ranked 38th in the world [6].

Anatolia was introduced to rice 500 years ago, through Egypt and its agriculture was first practiced in Tosya, Kastamonu district [7].

Rice, as a monocot plant, is the only cereal that can grow in water as it can utilize dissolved oxygen in water. It can grow in a wide variety of geographically diverse terrains up to 2500 m altitude and below sea level in elevation [8]. It is sensitive to temperature changes and day length. Rice production requires 3000 - 5000 kg of water per kilogram yield and 80% of this water is fresh water [9].

Despite the high share of rice for feeding the growing population in our country, its cultivation area is only 0.80% of the total cereal cultivation areas. The global value for rice cultivation area is 0.11% [10]. The annual per capita rice consumption in Türkiye has increased from 3.2 kg in 1964 to 4.4 kg in 1970, 6.5 kg in 2010-2011 and 8.3 kg in 2013. In terms of production, the yield in the 1920s was 30,000-40,000 tons on less than 100,000 decares of land, while production was 225 thousand tons in the nineties. It reached 830 thousand tons in 2014 which indicates the amount of rice production in Türkiye has increased 3.9 times over the past decades [10]. However, 5-year average of rough rice production was calculated as 862 thousand tons from 2019 to 2024 [11].

Türkiye is very favorable for rice production in terms of both climate and soil structure. Regionally, East and West Marmara, Western Black Sea and Southeastern Anatolia regions and provincially Balıkesir, Çanakkale, Çorum, Edirne and Samsun have the highest production capacity [12]. In Türkiye, Marmara Region has 70%, Black Sea Region has 25% and other regions have 5% share in total rice production [13]. Of the world's total land area (13.4 billion hectares), 11% (1.5 billion hectares) can be used for agricultural activities. This corresponds to only 36% of the fertile land available for agriculture. In the world, 80% of the food needs are met by cereal crops. Rice is one of the staple crops that is the only food source of 50% of the world population. One fourth of the daily energy need per capita is met by rice, and, if the world population increases in the recent trend, a 50% increase in cultivated areas will be needed for cultivation by 2030 in order to meet the energy needs of the increasing population [10, 14].

In the last decade, factors such as increasing population, climatic and environmental problems, and intensive industrial activities have increased the negative effects of abiotic stress factors such as salinity, frost, drought and temperature fluctuation on plants and disrupted their vital functions. Therefore, increasing crop production is a very important topic for the nutritional sustainability of the world population. The first method that can be applied for this purpose is to increase the production areas. However, this method indirectly brings more negative aspects instead of being part of the solution. The second method is to increase the yield per unit area. The genotype of the cultivated plant and ecological factors are the primary properties affecting the yield per unit area [15].

Salinity is one of the most important abiotic stresses for plants. It disrupts the intracellular ion balance and prevents the water uptake at optimum levels. Hence, it leads to physiological drought. During prolonged stress, plants may suffer from decline and deterioration in energy, carbohydrate and lipid metabolism, disruptions in photosynthetic activities and protein synthesis mechanisms, and deterioration in leaf structure. In total,

these effects lead the plant to yield loss. If the severity and/or duration of stress increases, it may even lead to plant death [16].

Salinity stress generally occurs in areas where the annual precipitation is below 300 mm. In these areas, excessive evaporation due to high temperatures leads to the accumulation of dissolved salts from water in the soil. Also, uncontrolled irrigation practices such as surface and flood irrigation contribute to the problem. Improper drainage properties of the fields may cause an increase in the concentration of ions such as K^+ and Na^+ in the root zone of plants and may also cause decreases in yield. In soils with high salt concentration, plants are categorized under two main groups according to their tolerance. The first group is glycophytic plants which represent the group of plants with low salt tolerance. Most plants belong to the glycophytic group, and when the concentration of salt in the soil exceeds the threshold value, their growth and development stops. Halophytes, which constitute the second group, can maintain their vital activities at high salt concentrations [17]. The amount of salinity in agricultural areas can be measured by the electrical conductivity of the soil. Salt sensitive plants can survive in soils with an electrical conductivity of 1.5 - 3 dS/m (approximately 15 - 30 mM NaCl concentration), while highly salt tolerant plants can survive in soil with an electrical conductivity of 5 - 10 dS/m (approximately 50 - 100 mM NaCl concentration) [18].

According to 2014 data of Turkish Statistical Institute (TUIK), the distribution of saline soils in Türkiye, covers a total area of 1.5 million hectares. Of this value, 599 thousand hectares are slightly saline, 508 thousand hectares are saline, 15 thousand hectares are sodic, 127 thousand hectares are slightly saline - sodic, and 268 thousand hectares are saline - sodic soils [19].

Salinity tolerance is a multigenic trait including free-radical scavenging, osmotic regulation, cellular ion homeostasis and more. Osmoprotectants such as trehalose (Tre) which is a non-reducing disaccharide of glucose, are key components of salinity tolerance in plants. As well as providing an energy source to plants, Tre has unique physicochemical properties for stabilizing dehydrated enzymes, proteins, and lipid membranes, under osmotic stress conditions. Besides Tre takes part in cellular signaling. It is also known to act as an elicitor for stress response genes [20]. TPS gene encoding trehalose -6-phosphate synthase has a crucial role in trehalose biosynthesis.

The salt overly sensitive (SOS) pathway, which evolved to maintain salinity tolerance, consists of SOS1, SOS2 and SOS3. SOS1 gene encodes Na^+/H^+ antiporter protein in plasma membrane which excludes Na^+ out of cytoplasm. It takes part in cellular signaling regulation through mediating ion homeostasis under saline

conditions along with other SOS components. Particularly, SOS1 is a key component for salinity tolerance in plants. Sequestration of Na⁺ ions instead of exclusion is another strategy for maintaining cell turgor pressure under saline conditions. Na⁺/H⁺ antiporters (NHXs) exchange protons and Na⁺ ions particularly across vacuole membranes in plants, algae, and fungi. Therefore, both SOS1 and NHX1 have been reported to improve salinity tolerance in numerous plants [21, 22]. Moreover, HKT transporters are found in plants and microorganisms. Especially, class II of HKT transporters (HKT2s) mediate Na⁺/K⁺ transport activity. There is substantial evidence on the physiological significance of HKTs for growth and development of plants under saline conditions. The HKT2;1 transporter has unique functions among class II HKTs which is determined to be mediating the nutritional Na⁺ absorption and Na⁺ uptake to compensate K⁺ deficiency conditions [23].

In the present study, Osmancık-97 rice variety, which is extensively cultivated in Türkiye, was grown. Osmancık-97 comprises 80% of rice production of Türkiye along with Rocca and Baldo. It is a hybrid of Rocca x Europa and registered in 1997. Since then, it has high yield potential and adapted to various ecological condition in different regions of Türkiye. Therefore, it is a suitable candidate for abiotic stress tolerance investigations. Plants were grown under four different salt concentrations (60, 90, and 120 mM and control) in *in vivo* conditions. The study aimed to determine the expression differences of the TPS1, NHX1, SOS1 and HKT2;1 genes under increasing salinity conditions as the components of osmotic adjustment (osmoprotectants and ion exclusion/sequestration) mechanism and to evaluate growth and biochemical parameters.

2. Materials and Methods

2.1. Plant Material and Experimental Design

Osmancık-97 rice variety was obtained from the Directorate of Trakya Agricultural Research Institute (Edirne, Türkiye) and was grown in the Plant Biotechnology Laboratory of Molecular Biology and Genetics Department of T.C. Istanbul Kültür University. Seeds of the control group and each salinity treatment group were sown in plastic plant growth containers with perlite as filler. Sowing was carried out with a total of 60 seeds per experimental group as 10 seeds per plastic container. The sown seeds were germinated in plastic containers filled with distilled water for one week. At the end of the first week, irrigation with Yoshida nutrient solution was continued. On the 28th day of germination, 60, 90 and 120 mM NaCl were added to the Yoshida solution except the control group. Salinity conditions were determined according to the preliminary test conducted. After 10 days of stress treatment, the leaves were harvested. The developmental differences of the harvested plants were evaluated based on average plant

height, average root length, average fresh and dry weight (shoot and root) parameters [16].

2.2. Lipid Peroxidation Analysis

The amount of thiobarbituric acid reactive substances (TBARS) which are the products of lipid peroxidation caused by salinity stress induced oxidative stress in rice plants, was determined colorimetrically according to the method of Stewart and Bewley [24]. For each sample, 0.1 g of rice leaves was homogenized in sterile mortars with 1 mL sterile distilled water. One mL of 0.5% (v/w) thiobarbituric acid including 20% trichloroacetic acid was added on all homogenates. The samples were incubated at 95°C for 30 minutes and then the reaction was stopped by placing the tubes in an ice bath for 5 minutes. The homogenates were centrifuged at +4 °C for 30 minutes at 10.000 × g and the absorbance values were measured at 532 and 600 nm wavelengths. The results were calculated and presented as μmol TBARS/g.FW. The experiment was performed in three replicates.

2.3. Proline Accumulation

The proline accumulation caused by salt stress in rice plants was calculated according to the method of Bates et al. [25]. Rice leaf tissue (0.1 g) was homogenized with 2 mL of 3% (w/v) sulfosalicylic acid. After centrifugation at 10.000 × g for 15 minutes at +4 °C, 2 mL of each sample was transferred to a glass tube. Ninhydrin reagent was added to the samples and the reaction was carried out in an incubator at 100 °C for an hour. At the end of the duration, the samples were kept on ice to terminate the reactions. 4 mL toluene were added to each tube and vortexed. After phase separation, the supernatants of samples were measured spectrophotometrically at 520 nm wavelength. The results were calculated and presented as μmol proline/g.FW according to the standard calibration curve. The experiment was performed in three replicates.

2.4. Photosynthetic Pigment Content

Effects of salinity stress on photosynthetic pigment content of rice plants were determined according to the method of Arnon [26]. Rice leaf tissues (0.1 g) were homogenized with 80% (v/v) cold acetone. The samples were then centrifuged at 10.000 × g for 15 minutes at +4 °C. Supernatants were measured at 470, 645 and 663 nm wavelengths. The experiment was performed in three replicates. Photosynthetic pigment contents were calculated according to the equations below and presented as μg/g.FW.

$$\text{Chlorophyll } a = 11.24 \times A_{663} - 2.04 \times A_{645}$$

$$\text{Chlorophyll } b = 20.13 \times A_{645} - 4.19 \times A_{663}$$

$$\text{Total Chlorophyll} = 7.05 \times A_{663} + 13.09 \times A_{645}$$

$$\text{Carotenoid} = \frac{(1000 \times A_{470}) - (1.9 \times \text{Chl } a) - (63.14 \times \text{Chl } b)}{214}$$

2.5. RNA Extraction

Plant leaves (0.3 g) were homogenized in sterile mortars with liquid nitrogen and transferred to 2 mL tubes. One mL TRIzol reagent was added. The samples were mixed gently for 20 seconds and kept at room temperature for 5 minutes. After the duration, 0.2 mL of chloroform was added, and the samples were kept at room temperature for 4 minutes after shaking for 20 seconds. Then centrifugation was performed at +4 °C, 12.000 × g for 15 minutes. 450 µL of supernatant was transferred to new sterile tubes and 450 µL of isopropanol was added in equal volume. After 10 minutes at room temperature, the samples were centrifuged at 12.000 × g for 10 minutes at 4 °C. The supernatants were discarded. One mL of 75% RNAase-free ethanol was added, and samples were centrifuged at 7500 × g for 5 minutes at +4 °C. The supernatant was discarded, and the tubes were kept at room temperature until the ethanol evaporated. Finally, 40 µL of RNAase-free water was added and RNA unwinding was performed. After the extraction, the concentration and purity of the obtained RNAs were measured in Nanodrop Implen NP80 device [16]. The experiment was performed in three replicates.

2.6. cDNA Synthesis

cDNA synthesis was performed using the iScript cDNA Isolation Kit. Components were used following the recommendations by the manufacturer: 4 µL 5X iScript cDNA buffer, 1 µL iScript Reverse Transcriptase, 14 µL nuclease-free water and 1 µL RNA (300 µg) sample in a total volume of 20 µl. The reaction was performed at the times and temperatures indicated in **Table 1**.

Table 1. cDNA synthesis PCR reaction protocol.

Step	Time (min.)	Temperature (°C)
Priming	5	25
Reverse Transcription	20	46
RT inactivation	1	95
Hold	-	4

2.7. Gradient PCR

The primer sequences designed for the target genes are given in **Table 2**. Thermo Scientific PCR Master Mix (2X) was used for the gradient PCR step. Mixture of 12.5 µL mix, 9.5 µL Thermo Fisher DEPC-treated water, 1 µL cDNA, 1 µL Forward Primer, 1 µL Reverse Primer were placed in a 200 µL PCR tube and vortexed. The protocol was carried out with Prima - Duo™ Hi-Media PCR device at the times and temperatures given in **Table 3**. Associated optimum binding temperatures of the primers were determined by agarose gel electrophoresis analysis of amplification products.

Table 2. Target genes, accessions, products sizes and primer sequences.

Target Genes	Accession	Forward Primer (5' → 3')	Reverse Primer (5' → 3')	Product length (bp)
OsTPS1	HM050424	CTGATGAGAGA GAAAAGCGACA T	GACTAGGGAGA TCAGGTGGAAC T	153
OsNHX1	XM_015789089	CTGGATTGCTCA GTGCATACATA	ACCACAGAAGA ATACGGTGAGA A	155
OsHKT2;1	AJ491852	GTC AACCTCTGC TCTGACACTTT	GAAA ACTCTGG GTTGTGCTTA TG	168
OsSOS1	KY752550	GGCTTCCTTCT CTGCTCTAATGT	ACTGCATCACTA GCACGCTTAAC	185

OsTPS1: Trehalose 6 Phosphate Synthase 1, OsNHX1: Na⁺/H⁺ antiporter, OsHKT2;1: High Affinity K⁺ transporters, OsSOS1: Salt Overly Sensitive 1

Table 3. Gradient PCR protocol.

Step	Time (min.)	Temperature (°C)	Cycles
Initial Denaturation	3	95	1
Denaturation	0.5	95	
Annealing	0.5	54, 56, 58, 60, 62, 64, 66, 68	35
Extension	1	72	
Final Extension	10	72	1

2.8. Quantitative Real Time PCR Analysis

Gene expression analysis was performed by following the BIO-RAD iQ™ SYBR® Green Supermix protocol. The reaction mixture containing BIO-RAD iQ™ SYBR® Green Supermix (2X) 10 µL, 1 µL forward primer, 1 µL reverse primer, 1 µL cDNA and 7 µL Thermo Fisher DEPC-treated water was used. The reactions were carried out on BIO-RAD CFX Connect Real-Time PCR device. Ubiquitin 5 primer was selected as endogenous control. Reaction times and temperatures are presented in **Table 4**.

Table 4. Quantitative real-time PCR protocol.

Step	Time (sec.)	Temperature (°C)	Cycles
Polymerase activation and DNA denaturation	180	95	1
Denaturation	15	95	
Annealing / Extension and Plate Read at Optimum Temperature	45	60	39
Melting Curve Analysis	5	65 - 95	1

2.9. Statistical Analysis

The data obtained from the evaluation of morphological damage and biochemical analysis (lipid peroxidation, proline accumulation, photosynthetic pigment), plant height, root length, fresh weight and fresh length of the control and experimental groups of rice plants treated with different concentrations of NaCl were statistically analyzed by using GraphPad Prism 8 (<https://www.graphpad.com>) statistical program. One-way ANOVA test was performed, and the comparison of the groups found to be statistically significant in the test were further analyzed by Student- Newman Keuls post-test. The experiments were performed in three biological and technical replicates.

3. Results and Discussion

In this study, proline accumulation levels, TBARS levels, photosynthetic pigment content, plant fresh and dry weights, root lengths, plant lengths and salt stress response gene expression profiles of Osmancık-97 rice variety were analyzed under increasing salinity stress conditions (no salt as control, 60, 90, and 120 mM NaCl for salinity stress).

In all salinity treatment groups of Osmancık-97 rice variety, with increasing NaCl concentration, root lengths, average plant weights and average plant lengths decreased, significantly (**Figure 3**). In Osmancık-97 variety, the average root length in the control group was 7.80 cm, while the root length of plants exposed to 60 mM salinity stress decreased by 1 cm to 6.80 cm. The average root length in plants exposed to 90 mM and 120 mM NaCl decreased to 6.60 cm and 6.30 cm, respectively. The root lengths of the group exposed to 120 mM salt decreased by 19% compared to the control (**Figure 1**). Similarly, it was reported that salinity application (50 mM NaCl) significantly reduced shoot and root growth morphological indices of two rice varieties, and especially in certain varieties, salinity application for 8 - 10 days significantly reduced root biomass in rice plants [2].

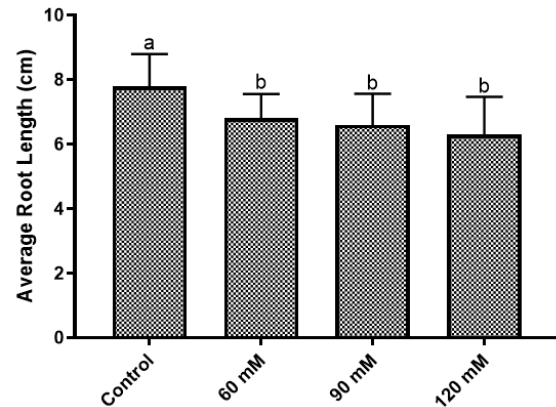


Figure 1. Effect of increasing NaCl concentrations on average root length of Osmancık-97 rice variety.

Similarly, in a study performed with salinity tolerant Pokkali and susceptible IR-28 rice varieties, it was reported that short-term salt stress negatively affected root lengths on all varieties, but IR-28 variety was much more affected by the stress factor compared to Pokkali [27]. In another study performed with tolerant Pokkali and sensitive IR-28, it was emphasized that increasing salinity stress (60 or 120 mol m⁻³ NaCl) had negative effects on IR-28 root lengths, but this change was not significant for both varieties [28]. In another study, it was reported that root length and root total volume presented a decreasing trend during the salinity treatment (50 mM) period in Huanghuazhan rice variety compared to the control, and root length and root total volume decreased by 30.08% and 40.8% on the 10th day of treatment, respectively [29]. The reduced root surface area under salt stress reduces nutrient uptake and water absorption and further inhibits the cell division process. As a result, it causes a decrease in root length and root biomass [30].

In Osmancık-97 variety, statistically significant decreases were measured gradually in the fresh and dry weights following the salinity treatment (60, 90, and 120 mM NaCl) compared to the control group. The average fresh weight of the plants in the control group was 0.45 g, while the dry weight was 0.12 g. The average fresh weight of the plants exposed to 60 mM salinity stress was measured as 0.39 g and dry weight as 0.11 g. The fresh weight and dry weight of the rice plants exposed to 90 mM salinity decreased to 0.30 and 0.09 g, respectively. Similarly, in plants exposed to 120 mM NaCl, the fresh weight was measured as 0.30 g, while the dry weight was measured as 0.09 g (**Figure 2**).

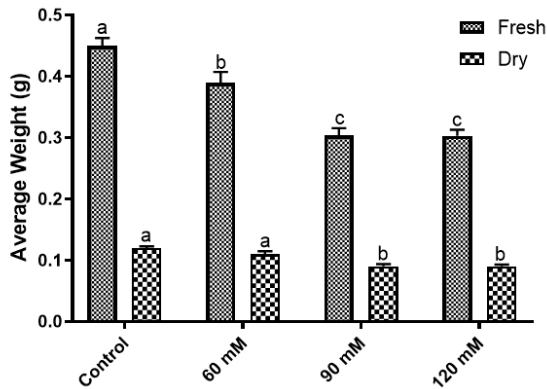


Figure 2. Effect of increasing NaCl concentrations on average fresh and dry weights of Osmancik-97 rice variety plants.

In the study performed by Chen et al. [29], in Chaoyouqianhao rice variety, shoot dry weight was decreased under salinity treatment compared to the control. Especially, stronger decrease was occurred between 6th and 10th days. In the same study, it was reported that both total dry weight and root dry weight were strongly inhibited during the salinity treatment period of Huanghuazhan rice variety compared to the control (18.86% and 19.09%, respectively). When the fresh weights were evaluated, despite the 0.06 g decrease between the control group and 60 mM salinity-treated rice plants, the highest difference occurred between 60 mM and 90 mM salinity-treated rice plants by 0.09 g. In the highest applied 120 mM NaCl treated group, 33% decrease occurred compared to the control group.

In Osmancik-97 variety, the average plant length in the control group was 23.8 cm, while the length of plants exposed to 60 mM salinity stress was 1.7 cm shorter, decreasing to 22.1 cm. The average length of plants exposed to 90 mM salinity was 19.8 cm, while the average plant length in plants exposed to 120 mM NaCl stress was 19.2 cm. The decrease in the length of plants treated with 120 mM salinity compared to the control group was 19% (Figure 3).

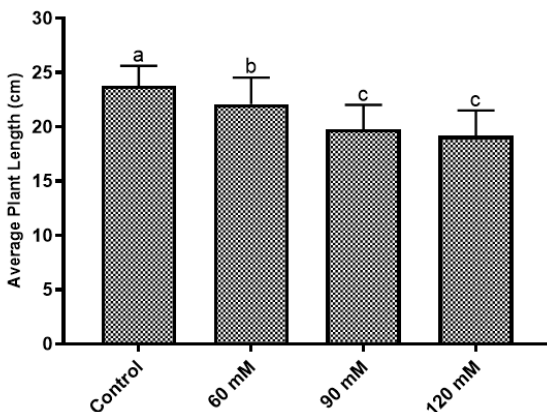


Figure 3. Effect of increasing NaCl concentrations on average plant length of Osmancik-97 rice variety.

In a study performed with Mekongga, Banyuasın, Madura, Ciherang, Inpara-3 and Inpari 13 rice varieties, 50, 100, 150, and 200 mM levels of NaCl were applied to the varieties together with the control group for four weeks. As a result, it was determined that there was a decrease in plant length in all rice varieties [31]. Similarly, plant length of Chaoyouqianhao and Huanghuazhan rice varieties gradually decreased during the 10-days salinity treatment, and presented a decrease of 17.7% and 11.5% on the 10th day of the treatment, respectively [29].

In Osmancik-97 variety, the effects of increasing salinity stress (60, 90, and 120 mM NaCl) on the photosynthetic pigment contents were measured spectrophotometrically. Following the increase in salinity concentrations, decreases in the amounts of chlorophyll a, chlorophyll b, total chlorophyll and carotenoids were detected (Figure 4).

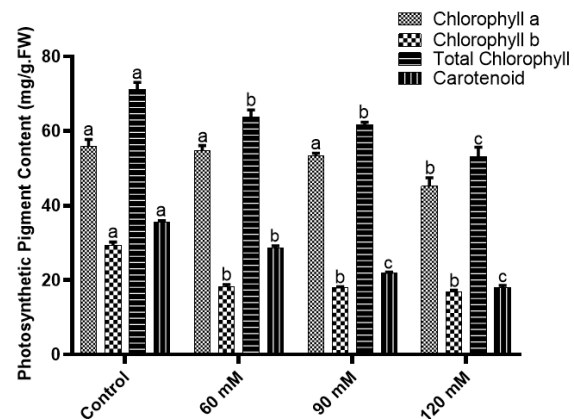


Figure 4. Effect of increasing NaCl concentrations on photosynthetic pigment content of Osmancik-97 rice variety.

Since salt stress largely inhibits biomass accumulation, it reduces leaf area and photosynthetic parameters [32]. Numerous salinity stress studies have reported significant decreases in chlorophyll concentration as the intensity of salinity stress increases [33, 34] In our study, there was no significant difference between control and 60 mM, 90 mM salinity applied plants for chlorophyll a pigment in Osmancik-97 variety similar to the results of the study conducted by Chen et al. in which they applied 50 mM salt to rice plants [29]. In some salt applications (80 mM NaCl), it was reported that chlorophyll a, b and total chlorophyll contents increased in rice seedlings [35]. Chlorophyll content may temporary increase during the growing period under 100 Mm NaCl salinity treatment, which was indicated to be mainly due to the stimulating effect of stress conditions [36].

The highest alteration of chlorophyll a concentration was observed in 120 mM salinity applied group. When we compared the chlorophyll a concentrations between control and 120 mM salinity stress, an 18% decrease was

measured with increasing salinity. For chlorophyll b, 45% initial concentration loss was measured. When the difference in carotenoid concentration between control and 120 mM was evaluated, 48.5% concentration loss was measured. When the total chlorophyll amount was evaluated, a decrease was observed in Osmancık-97 rice plants exposed to 60 and 90 mM salinity compared to the control, while the greatest change occurred between control plants and rice plants applied with 120 mM salinity. The change in total chlorophyll concentration resulted in a loss of 25% between control and 120 mM. Similarly, it was reported that chlorophyll a (11.34% and 15.84%), chlorophyll b (12.71% and 19.48%), carotenoid (10.86% and 17.73%) and total chlorophyll contents (11.71% and 16.78%) of two rice varieties decreased significantly under salinity treatment compared to the control [29]. In another study, it was reported that chlorophyll a, chlorophyll b and total chlorophyll concentrations of Gala and Edirne rice varieties decreased under 300 mM salinity stress [37].

The most important energy source for plants is photosynthesis. Although the tolerance of plants to salt stress varies, photosynthetic pigment determination is used as a biochemical marker in abiotic stress factor tolerance [38]. There is sufficient evidence to report that exposure of plants to stressful environments such as salinity reduces chlorophyll content, which leads to general growth retardation. Short-term exposure to salt induces osmotic stress in plants, which results in reduced water absorption, redox imbalance, stomatal closure, and inhibition of new leaf growth and root system development. However, long-term exposure to salt causes ionic toxicity due to Na^+ accumulation in mature leaves. This reduces the rate of photosynthesis and nutrient accumulation, resulting in premature senescence [39]. Excessive salinity significantly inhibits plant growth and biomass accumulation, and causes a decrease in photosynthetic parameters [40]. In addition, the decrease in photosynthetic pigments can be explained by the increase in chlorophyll-ase activity caused by salinity and the degradation of chlorophyll [41].

The change in proline concentration in Osmancık-97 variety under 60, 90 and 120 mM NaCl treatment compared to the control is represented in **Figure 5**. High salt concentration limits water uptake for plants and thus osmotic stress occurs. Plants store compatible solutes such as proline in order to protect themselves from osmotic stress [42]. A statistically significant increase was observed between the control group (0.64 $\mu\text{mol} / \text{g.FW}$) and the 90, 120 mM NaCl treated rice plants (0.86 $\mu\text{mol} / \text{g.FW}$ and 1.07 $\mu\text{mol} / \text{g.FW}$, respectively). Especially, when the proline amounts in the control group and the 120 mM salinity treated rice plants were examined, an increase of 40% was determined.

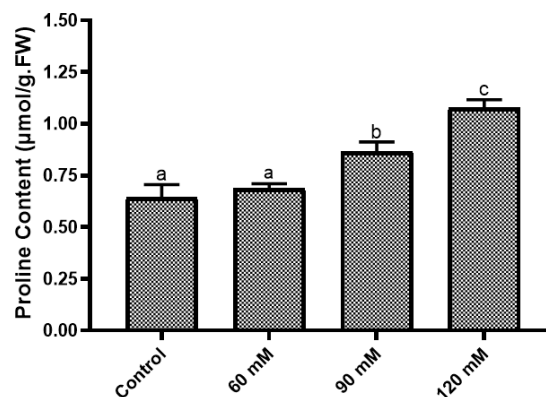


Figure 5. Effect of increasing NaCl concentrations on proline accumulation of Osmancık-97 rice variety.

In a study performed with salt sensitive IR-29, tolerant Pokkali and 12 other rice varieties, an increase in proline accumulation was observed in all groups compared to the control at all salinity concentrations [43]. In another study, it was reported that proline demonstrated a gradual accumulation in accordance with increasing NaCl concentrations. In the same study, plants exposed to 150 and 210 mM NaCl had the highest proline content with 4.47 and 4.81 fold increase over the control, respectively [16].

In Osmancık-97 rice variety, an increase in TBARS levels was measured and found to be directly proportional to the increasing salinity (**Figure 6**). Salt stress leads to membrane damage and stomatal closure. This process leads to a decrease in carbon dioxide fixation and hydrolase activity, and an increase in lipid peroxidation levels. The formation of reactive oxygen species such as O_2^- , H_2O_2 and OH^- can be stimulated. ROS can cause oxidative damage to cell membranes, proteins, DNA and lipids, and can also cause TBARS accumulation, disrupting various biochemical and metabolic processes in plants [44]. In particular, unsaturated fatty acids in the plant cell membrane are subjected to lipid peroxidation by reactive oxygen species formed as a result of abiotic and biotic stresses. Thus, ion transport systems and proteins in the membrane and cell membrane structure are damaged. TBARS, which is the product of this damage, has been used as an indicator of oxidative damage in membranes [45]. While the value obtained as a result of colorimetric measurement of TBARS amounts in the Osmancık-97 rice control group was 0.004 $\mu\text{mol} / \text{g.FW}$, this value increased to 0.0063 $\mu\text{mol} / \text{g.FW}$ in proportion to stress in the 60 mM group. The amount of TBARS in rice plants exposed to 90 mM salt was very close to the 60 mM salt treated group and was determined as 0.0064 $\mu\text{mol} / \text{g.FW}$, while this value presented the highest increase in the 120 mM salinity group and was measured as 0.011 $\mu\text{mol} / \text{g.FW}$. In our study, TBARS concentrations increased by 60% in plants exposed to 120 mM NaCl compared to the control group.

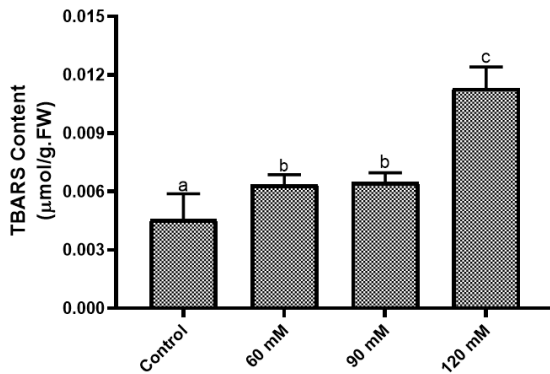


Figure 6. Effect of increasing NaCl concentrations on TBARS content of Osmancık-97 rice variety.

Similarly, it was indicated that TBARS concentration in plants increases in direct proportion to salinity stress [46–48]. Hossen et al. [48] indicated that the MDA content in 150 mM NaCl-treated rice seedlings increased by 98%. In another study, TBARS amount was found to be particularly high in a salt-sensitive variety, while it was detected at low levels in a tolerant variety [45]. In tolerant rice genotypes, the positive relationship between the Na^+/K^+ ratio and hydrogen peroxide (H_2O_2), TBARS and the activity of antioxidant enzymes indicates that they are important in improving salinity tolerance. Salt tolerant rice varieties demonstrated lower Na^+/K^+ ratio, higher proline accumulation, lower H_2O_2 accumulation and TBARS content, and higher catalase and ascorbate peroxidase activities [45]. Wu et al. demonstrated that overexpression of the MADS-box gene *OsMADS57* plays an important role in response to salinity stress and improves salt tolerance via antioxidant mechanism in rice. In this process, TBARS content was also significantly decreased in *OsMADS57* overexpressing lines compared to controls [49].

Plants should develop different strategies to reduce the harmful effects of salt stress and protect themselves from the harmful effects of ROS. Salt stress is among the environmental stress factors that lead to the accumulation of ROS at toxic levels. Antioxidant mechanisms are one of the most important mechanisms that protect cells from the harmful effects of reactive oxygen species (ROS). In previous studies, the responses of 14-day-old seedlings of Osmancık-97 rice (*Oryza sativa* L.) variety to NaCl stress were shown by transcriptional analyses of genes responsible for antioxidant enzymes (Cyt-APX, CAT A, Cyt-GR1 and proline metabolism-related genes). It was reported that these genes were expressed differently between the two rice varieties under different salt concentrations [50]. Salt stress responsive genes including TPS1, NHX1, SOS1 and HKT2 genes are another important part of this effective strategy. In the present study, we analyzed the expression of NHX1, HKT2 and SOS1 genes, which are members of the three main Na^+ transporter gene families that play an important role in salinity tolerance, under different salt concentrations. We also examined the expression profile

of the TPS1 gene, which belongs to trehalose metabolism and is also associated with salt tolerance. The gene expression levels of target genes were determined by qRT-PCR.

In Osmancık-97 variety, expression of *OsTPS1* gene was examined in 60, 90, and 120 mM salinity conditions (Figure 7). *OsTPS1* gene expression in 60 mM salinity treated rice demonstrated 63.3% decrease compared to the control. *OsTPS1* gene expression decreased by 85% in 90 mM salinity treated rice, while a 78.2% decrease was detected in 120 mM salinity group. Trehalose is a non-reducing disaccharide that protects cellular proteins and membranes against abiotic stress factors. Trehalose production in plants occurs through trehalose-6-phosphate synthase (TPS) / trehalose-6-phosphate phosphatase (TPP). In Arabidopsis seedlings grown in medium containing trehalose and without sucrose, increased expression of the starch synthesis gene *ApL3*, excessive starch accumulation in cotyledons and inhibition of root growth were observed [51].

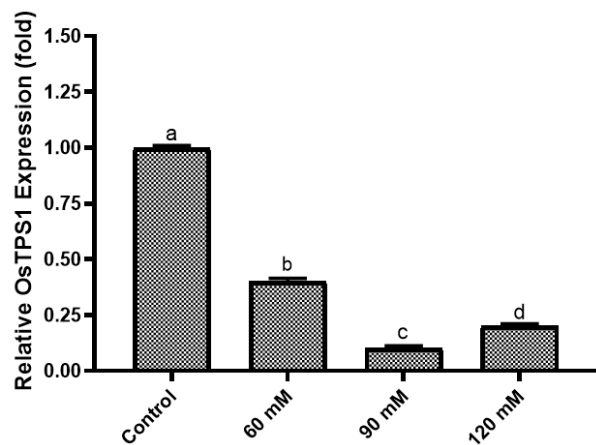


Figure 7. Effect of increasing NaCl concentrations on *OsTPS1* gene expression of Osmancık-97 rice variety.

In our study, as a result of statistically significant decreases in the expression of *OsTPS1* gene at increasing salinity concentrations in Osmancık-97 rice variety, it was hypothesized that our variety may be tolerant to salinity. There are two different cases in the literature regarding the TSP1 gene expression under stress conditions. It has been stated that both increase and decrease in TSP1 gene expression in different plant species or varieties are associated with stress tolerance. In a previous study, bioinformatics analyses including co-expression network, gene expression, chromosomal map analysis of cis element and phylogenetic relationships of 11 *OsTPS* gene sequences downloaded from NCBI were performed in *O. sativa*. Similar to our study, it was reported that the expression of *OsTPS1* gene was downregulated in abiotic stresses of dehydration, cold and drought and in biotic stresses of *X. oryzae* [52]. Also, it was shown that the expression levels of genes related to trehalose biosynthesis (TPS1, TPS2, TPP1 and TPP2) in tomato seedlings were reduced under NaCl

application [53]. In the same study, molecular evidence has revealed that the up regulation of TPS1, TPS2, TPP1 and TPP2 genes in tomato plants is only realized through plant hormone strigolactones and then supports tomato seedling growth. In another study, it was indicated that increased expression of OsTPS1 gene in rice plants has an important role in developing tolerance to salinity, drought and low temperature [54]. Similarly, in study performed with *Arabidopsis thaliana* plant, high expression of AtTPS1 gene was associated with drought stress [55].

In our study, OsNHX1 gene expression in 60 mM salinity treated rice plants decreased by 51.9% compared to the control. OsNHX1 gene expression decreased by 79.1% in 90 mM salinity treated rice, while a 74% decrease was detected in 120 mM salinity group (**Figure 8**). NHX antiporters regulate salt and pH levels by providing cation/H⁺ balance in the cell. In a study performed with transgenic rice plants, it was reported that salt tolerance improved as a result of increased expression of Na⁺, K⁺/H⁺ antiporter gene (OsNHX1) [56]. In another study, it was shown that OsNHX gene provided intracellular Na⁺ balance in transgenic corn plants and improved salt tolerance by providing Na⁺ ion transport to vacuoles [57]. K⁺ is the basic macronutrient found in the cell cytosol. The presence of Na⁺ ion in high concentrations inside the cell disrupts the cell water balance and changes the cell ion charge balance by competing with K⁺ ion. Studies have reported that NHX1 type transporters generate tolerance to salt stress by removing Na⁺ ion in wheat, rice and *Arabidopsis* plants [22, 58, 59]. It has been reported that the NHX1 gene was statistically down-regulated in salt-tolerant plant shoots under NaCl treatment (75 mM) for 14 days compared to the control, and statistically significantly up-regulated in salt-sensitive plant shoot. On the contrary, the NHX1 gene was statistically significantly up-regulated in the salt-tolerant plant roots under salinity stress compared to the control, while it was statistically significantly down-regulated in the salt-sensitive plant roots [60].

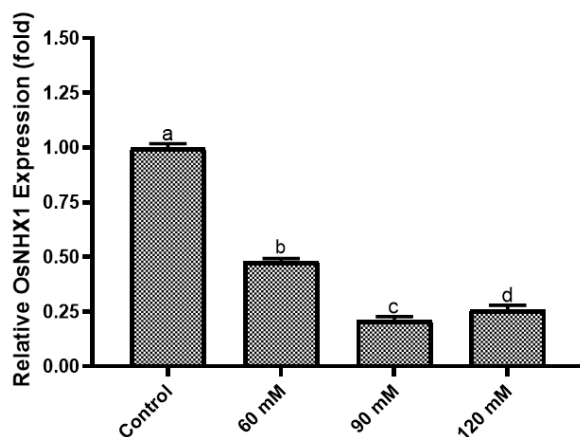


Figure 8. Effect of increasing NaCl concentrations on OsNHX1 gene expression of Osmancik-97 rice variety.

Similarly, the SOS1 gene was statistically significantly down-regulated in the salt-tolerant plant shoots under NaCl treatment compared to the control, while no significant difference was obtained in the salt-sensitive plant shoots. The SOS1 gene was statistically significantly up regulated in the roots of all tolerant or sensitive plant groups [60]. Thus, decreased expressions of SOS1 and NHX1 in shoots may be related to salinity tolerance of Osmancik-97 rice plant. Osmancik-97 rice variety was stated to be more salt tolerant than other local rice varieties in a previous study [16]. Transport of Na⁺ and K⁺ between different tissues and subcellular locations may help plants adapt to saline environment [61]. According to previous reports, the relative expression of OsNHX1 was detected maximum in the roots and greater than shoot tissues cvs. 9311 and JYGY-1 exposed to 150 mM NaCl for 24 h. After long-term NaCl exposure (72 h), OsNHX1 expression level in seedlings under salt stress decreased [62].

In our study, OsSOS1 gene expression decreased significantly with increasing stress amount in rice plants exposed to 60, 90, and 120 mM NaCl (**Figure 9**). In Osmancik-97 variety, OsSOS1 gene expression in rice exposed to 60 mM salinity decreased by 63.3% compared to the control. While OsSOS1 gene expression decreased by 85.1% in rice exposed to 90 mM salinity, a decrease of 78.3% was reported in the 120 mM salinity group. The uptake of Na⁺ ion into the cell occurs instantly. This disrupts ion homeostasis in the cell and damages the plants. SOS1 antiporters ensure the intracellular Na⁺ /H⁺ balance and provide the removal of Na⁺ out of the cell. Studies indicated that in mutant *Arabidopsis* plants lacking SOS1, there are irregularities in the excretion of Na⁺ ions, and that tolerance to salt is significantly reduced, and defects occur in ion transport from roots to shoots [63].

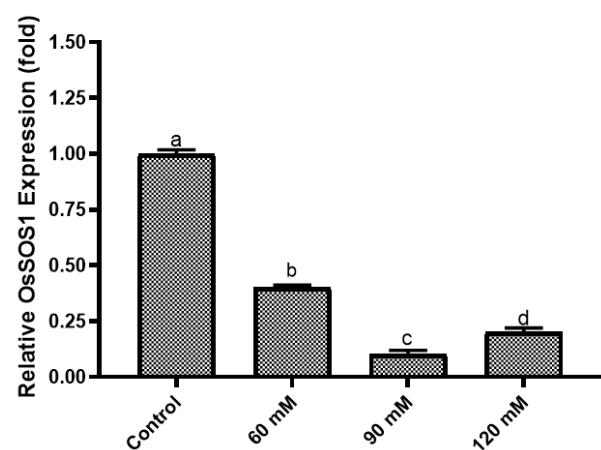


Figure 9. Effect of increasing NaCl concentrations on OsSOS1 gene expression of Osmancik-97 rice variety.

When SOS1 mutants and wild type plants were treated with 25 mM salinity, wild type plants accumulated Na⁺ more than mutants. This indicated that SOS1 is involved in controlling the sodium ion transfer to the xylem and its

transfer to the shoots [64]. However, in contrast, in control and mutant plants treated with 100 mM salinity, more sodium ion accumulation was observed in mutants compared to controls. It was thought that this could be due to the inability to export Na^+ ions from the root epidermis and the disruption of the Na^+ electrochemical gradient along the xylem-symplast boundary [64]. It was also suggested that under high salinity stress, the Na^+ ion concentration difference between the xylem parenchyma and sap could be higher than the pH gradient, and as a result, SOS1 activity could reverse, resulting in sodium ion uptake from the xylem [64]. In previous studies, it was observed that SOS1 and NHX1 exhibited a different expression pattern related to leaf age in pomegranate (*Punica granatum* L.) plants. In mature leaves, low transcript levels of these genes were detected in the early period of treatment (10 h). In young leaves, increased expression of SOS1 and NHX1 was reported (except NHX1 at 24 h) [65].

In our study, OsHKT2;1 gene expression decreased significantly with increasing salt concentration in rice plants exposed to 60, 90 and 120 mM NaCl (Figure 10). In Osmancık-97 variety, OsHKT2;1 gene expression in rice exposed to 60 mM salinity decreased by 51.4% compared to the control. While OsHKT2;1 gene expression decreased by 78.8% in plants exposed to 90 mM salinity, a decrease of 73.5% was detected in the 120 mM salinity group. OsHKT2 proteins are located in the plasma membrane and control the Na^+ entry from the medium into plant cells [66].

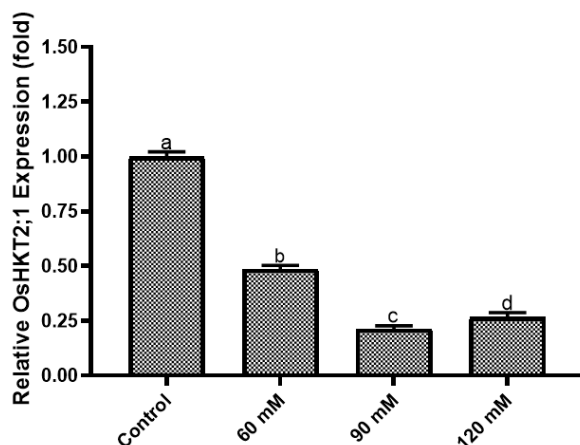


Figure 10. Effect of increasing NaCl concentrations on OsHKT2;1 gene expression of Osmancık-97 rice variety

It was reported that the expression of HKT2;1 gene decreased in the leaves of both salt-tolerant Pokkali rice variety and salt-sensitive IR29 rice variety at early hours (1-6 h) of 200 mM salt stress. In root tissues, the expression of HKT2;1 gene was decreased in the salt tolerant Pokkali variety while it decreased in the salt sensitive IR29 variety at early hours (1-6 h). Zhang et al. reported that OsHKT2;1 was down-regulated in four rice varieties (Nipponbare, 9311, JYGY-1 and JYFN-4) exposed to 125 mM NaCl for 24 and 72 h by under salt

stress [62]. Another study reported that the relative expression level of OsHKT2;1 in leaves and roots of two rice cultivars, Tampha and MSE9, exposed to 120 mM NaCl for 96 h was very low [67]. In addition, downregulation of OsHKT2;1 transporter in both root and leaf tissues limits Na^+ influx and Na^+ efflux from xylem to leaf organ. When plants are exposed to high NaCl stress, K^+ deficiency plays an important role in reducing the expression level of OsHKT2;1, which is largely regulated by the availability of K^+ ions [68].

4. Conclusion

The difference in ion homeostasis and salt tolerance among species or varieties is related to the regulation of the expression of NHX, HKT and SOS family genes [65]. However, it is worth noting that the levels of these genes do not represent a clear trend that directly explains the dynamics of Na^+ and K^+ content in different organs from different species or varieties. Soils with EC exceeding 4 dS/m (~ 40 mM) and 8 dS/m (~ 80 mM) are considered as moderate and high salt stress, respectively. Salinity levels greater than 5 dS/m (~ 50) cause a significant decrease in yield for rice. Rice, a moderately salt sensitive crop, has complex responses to salt stress and its sensitivity varies according to species, variety, growth and development stages and the duration of stress to which it is exposed. Further research is required to better understand the role of Na^+ (K^+)/ H^+ antiporters in intracellular compartmentalization under lower and higher salt stress conditions in different rice varieties.

Acknowledgement

Authors acknowledge the support of Ministry of Agriculture and Forestry, Directorate of Trakya Agricultural Research Institute (Edirne, Türkiye) in providing source of seed materials

Author's Contributions

Atilla Salman: Experimentation

Sinan Meriç: Experimentation, drafted and wrote the manuscript, result interpretation.

Tamer Gümüş: Experimentation

Çimen Atak: Supervised the experiment's progress, result interpretation and helped in manuscript preparation.

Alp Ayan: Supervised the experiment's progress, drafted and wrote the manuscript, experimentation, result interpretation.

Ethics

There are no ethical issues after the publication of this manuscript.

References

- [1]. Jena KK. The Species of the Genus *Oryza* and Transfer of Useful Genes From Wild Species Into Cultivated Rice, *O. sativa*. *Breeding Science* 2010; 60: 518–523.
- [2]. Chen T., Shabala S., Niu Y., et al. Molecular Mechanisms of Salinity Tolerance in Rice. *The Crop Journal* 2021; 9: 506–520.
- [3]. Civan P., Ali S., Batista-Navarro R., et al. Origin of the Aromatic Group of Cultivated Rice (*Oryza sativa* L.) Traced to the Indian Subcontinent. *Genome Biology and Evolution* 2019; 11: 832.
- [4]. Fukagawa NK., Ziska LH. Rice: Importance for Global Nutrition. *Journal of Nutritional Science and Vitaminology* 2019; 65: S2–S3.
- [5]. Erenstein O., Jaleta M., Sonder K., et al. Global Maize Production, Consumption and Trade: Trends and R&D Implications. *Food Security* 2022; 14: 1295–1319.
- [6]. Öztürk D., Akçay Y. Güney Marmara Bölgesinde Çeltik Üretiminin Genel Bir Değerlendirmesi. *Journal of Agricultural Faculty of Gaziosmanpaşa University* 2010; 2010: 61–71.
- [7]. Taşlıgil N., Şahin G. Türkiye’de Çeltik (*Oryza sativa* L.) Yetiştiriciliği ve Coğrafi Dağılımı. *Adıyaman Üniversitesi Sosyal Bilimler Enstitüsü Dergisi* 2011; 182–203.
- [8]. Paudel MN. Rice (*Oryza sativa* L.) Cultivation in the Highest Elevation of the World. *Agronomy Journal of Nepal* 2011; 2: 31–41.
- [9]. Bouman BAM., Hengsdijk H., Hardy B., et al. Water-wise Rice Production. *IRRI*, 2002.
- [10] Samal P., Babu SC., Mondal B., et al. The Global Rice Agriculture Towards 2050: An Inter-continental Perspective. *Outlook on Agriculture* 2022; 51: 164–172.
- [11]. Turkey Rice Area, Yield and Production, <https://ipad.fas.usda.gov/countrysummary/Default.aspx?id=TU&crop=Rice> (accessed 11 November 2024).
- [12]. Beşer N., Rice Food Security and Production in Turkey. <https://ageconsearch.umn.edu/record/164415/files/AdvancesIn.pdf#page=97> (accessed 1 August 2024).
- [13]. H.Sürek. Rice Production and Research Activities in Turkey. <https://om.ciheam.org/om/pdf/c24-2/CI011101.pdf>(accessed 1 August 2024).
- [14]. van Dijk M., Morley T., Rau ML., et al. A Meta-analysis of Projected Global Food Demand and Population at Risk of Hunger For the Period 2010–2050. *Nature Food* 2021; 2: 494–501.
- [15]. Gümüş T., Meriç S., Ayan A., et al. Plant Abiotic Stress Factors: Current Challenges of Last Decades and Future Threats. *Plant Abiotic Stress Responses and Tolerance Mechanisms* 2023; DOI: 10.5772/intechopen.110367.
- [16]. Çelik Ö., Meriç S., Ayan A., et al. Epigenetic Analysis of WRKY Transcription Factor Genes in Salt Stressed Rice (*Oryza sativa* L.) plants. *Environmental and Experimental Botany*; 2019; 159 DOI: 10.1016/j.envexpbot.2018.12.015.
- [17]. Sairam R., Physiology and Molecular Biology of Salinity Stress Tolerance in Plants. *Current Science* 2004 86:3, 407–421.
- [18]. Zhu JK. Plant Salt Tolerance. *Trends Plant Science* 2001; 6: 66–71.
- [19]. Tunç E., Tekin MS., Demir M., et al. Halophytic Species in Natural Areas Close to Agricultural Areas of Araban (Gaziantep, Turkey). *Journal of Agricultural Chemistry and Environment* 2020; 9: 48–58.
- [20]. Sadak MS. Physiological Role of Trehalose on Enhancing Salinity Tolerance of Wheat Plant. *Bulletin of the National Research Centre*. 2019 431 2019; 43: 1–10.
- [21]. Liang L., Guo L., Zhai Y., et al. Genome-wide Characterization of SOS1 Gene Family in Potato (*Solanum tuberosum*) and Expression Analyses Under Salt and Hormone Stress. *Frontiers in Plant Science*. 2023; 14: 1201730.
- [22]. Solis CA, Yong MT, Zhou M, et al. Evolutionary Significance of NHX Family and NHX1 in Salinity Stress Adaptation in the Genus *Oryza*. *Int J Mol Sci*; 23. Epub ahead of print 1 February 2022. DOI: 10.3390/IJMS23042092.
- [23]. Hamamoto S., Horie T., Hauser F., et al. HKT Transporters Mediate Salt Stress Resistance in Plants: From Structure and Function to the Field. *Current Opinion in Biotechnology* 2015; 32: 113–120.
- [24]. Stewart RRC., Bewley JD. Lipid-Peroxidation Associated with Accelerated Aging of Soybean Axes. *Plant Physiology*. 1980; 65: 245–248.
- [25]. Bates LS., Waldren RP., Teare ID. Rapid Determination of Free Proline for Water-Stress Studies. *Plant and Soil*. 1973; 39: 205–207.
- [26]. Hoagland DR., Arnon DI. The Water-Culture Method for Growing Plants Without Soil. *Circular. California Agricultural Experiment Station*; 347:39.
- [27]. Vaidyanathan H., Sivakumar P., Chakrabarty R., et al. Scavenging of Reactive Oxygen Species in NaCl-stressed Rice (*Oryza sativa* L.) - Differential Response in Salt-Tolerant and Sensitive Varieties. *Plant Science*. 2003; 165: 1411–1418.
- [28]. Demiral T., Türkan İ. Comparative Lipid Peroxidation, Antioxidant Defense Systems and Proline Content in Roots of Two Rice Cultivars Differing in Salt Tolerance. *Environmental and Experimental Botany*. 2005; 53: 247–257.
- [29]. Chen G., Zheng D., Feng N., et al. Physiological Mechanisms of ABA-induced Salinity Tolerance in Leaves and Roots of Rice. *Scientific Reports*. 2022 121; 12: 1–26.
- [30]. Atta K., Mondal S., Gorai S., et al. Impacts of Salinity Stress on Crop Plants: Improving Salt Tolerance Through Genetic and Molecular Dissection. *Frontiers in Plant Science*. 2023; 14: 1241736.
- [31]. Hariadi YC., Nurhayati AY., Soeparjono S., et al. Screening Six Varieties of Rice (*Oryza sativa*) for Salinity Tolerance. *Procedia Environmental Sciences*. 2015; 28: 78–87.
- [32]. Harizanova A., Koleva-Valkova L. Effect of Silicon on Photosynthetic Rate and the Chlorophyll Fluorescence Parameters at Hydroponically Grown Cucumber Plants Under Salinity Stress. *Journal of Central European Agriculture*. 2019; 20: 953–960.
- [33]. Jamil M., Bashir S., Anwar S., et al. Effect of Salinity on Physiological and Biochemical Characteristics of Different Varieties of Rice. *Pakistan Journal of Botany*. 2012; 44: 7–13.
- [34]. Saddiq MS., Iqbal S., Hafeez MB., et al. Effect of Salinity Stress on Physiological Changes in Winter and Spring Wheat. *Agronomy*. 2021; 11: 1193.
- [35]. Gadelha CG., Coutinho ÍAC., Pinheiro SK de P., et al. Sodium Uptake and Transport Regulation, and Photosynthetic Efficiency Maintenance as the Basis of Differential Salt Tolerance in Rice Cultivars. *Environmental and Experimental Botany*. 2021; 192: 104654.
- [36]. Chen F., Chen S., Guo W., et al. Salt Tolerance Identification of Three Species of *Chrysanthemums*. *Acta Horticulturae* 2003; 618: 299–305.

- [37]. Orcan P. Tuz Stresine Maruz Bırakılan Çeltik (*Oryza sativa* L.) Çeşitlerinde Radikal Söndürme ve Antioksidan Enzim Aktiviteleri, *Dicle Üniversitesi Fen Bilimleri Enstitüsü* <http://acikerisim.dicle.edu.tr/xmlui/handle/11468/3582> (2017, accessed 1 August 2024).
- [38]. Alharby HF., Al-Zahrani HS., Hakeem KR., et al. Identification of Physiological and Biochemical Markers for Salt (NaCl) Stress in the Seedlings of Mungbean [*Vigna radiata* (L.) Wilczek] genotypes. *Saudi Journal of Biological Science*. 2019; 26: 1053–1060.
- [39]. Munns R., Tester M. Mechanisms of Salinity Tolerance. *Annual Review of Plant Biology* 2008; 59: 651–681.
- [40]. Hu C hong, Zheng Y., Tong C ling, et al. Effects of Exogenous Melatonin on Plant Growth, Root Hormones and Photosynthetic Characteristics of Trifoliolate Orange Subjected to Salt Stress. *Plant Growth Regulation*. 2022; 97: 551–558.
- [41]. Mohamed HI., Latif HH. Improvement of Drought Tolerance of Soybean Plants by Using Methyl Jasmonate. *Physiology and Molecular Biology of Plants*. 2017; 23: 545–556.
- [42]. Meriç S., Ayan A., Atak Ç. Molecular Abiotic Stress Tolerant Strategies: From Genetic Engineering to Genome Editing Era. *Abiotic Stress Plants*. 2020. DOI: 10.5772/Intechopen.94505.
- [43]. Chunthaburee S., Dongsansuk A., Sanitchon J., et al. Physiological and Biochemical Parameters for Evaluation and Clustering of Rice Cultivars Differing in Salt Tolerance at Seedling Stage. *Saudi Journal of Biological Sciences*. 2016; 23: 467–477.
- [44]. Suzuki N., Koussevitzky S., Mittler R., et al. ROS and Redox Signalling in the Response of Plants to Abiotic Stress. *Plant Cell & Environment*. 2012; 35: 259–270.
- [45]. Rasel M., Tahjib-Ul-Arif M., Hossain MA., et al. Discerning of Rice Landraces (*Oryza sativa* L.) for Morpho-physiological, Antioxidant Enzyme Activity, and Molecular Markers' Responses to Induced Salt Stress at the Seedling Stage. *Journal of Plant Growth Regulation*. 2020; 39: 41–59.
- [46]. Khan MH., Panda SK. Alterations in Root Lipid Peroxidation and Antioxidative Responses in Two Rice Cultivars Under NaCl-salinity Stress. *Acta Physiologiae Plantarum*. 2008; 30: 81–89.
- [47]. Singh A., Sengar RS., Shahi UP., et al. Prominent Effects of Zinc Oxide Nanoparticles on Roots of Rice (*Oryza sativa* L.) Grown under Salinity Stress. *Stresses*. 2023; 3: 33–46.
- [48]. Hossen MS., Karim MF., Fujita M., et al. Comparative Physiology of Indica and Japonica Rice under Salinity and Drought Stress: An Intrinsic Study on Osmotic Adjustment, Oxidative Stress, Antioxidant Defense and Methylglyoxal Detoxification. *Stresses* 2022; 2: 156–178.
- [49]. Wu J., Yu C., Huang L., et al. A Rice Transcription Factor, OsMADS57, Positively Regulates High Salinity Tolerance in Transgenic *Arabidopsis thaliana* and *Oryza sativa* plants. *Physiologia Plantarum* 2021; 173: 1120–1135.
- [50]. Çelik Ö., Çakır BC., Atak Ç. Identification of the Antioxidant Defense Genes Which May Provide Enhanced Salt Tolerance in *Oryza sativa* L. *Physiology and Molecular Biology of Plants*. 2019; 25: 85–99.
- [51]. Ramon M., Rolland F., Thevelein JM., et al. ABI4 Mediates the Effects of Exogenous Trehalose on Arabidopsis Growth and Starch Breakdown. *Plant Molecular Biology* 2007. 63: 195–206.
- [52]. Saidi A., Hajibarat Z. Computational Analysis and Expression Study of Trehalose 6-Phosphate Synthase (TPS) in Rice (*Oryza sativa*), <http://bar.utoronto.ca/welcome.htm> (2021, accessed 5 August 2024).
- [53]. Lu X., Liu X., Xu J., et al. Strigolactone-Mediated Trehalose Enhances Salt Resistance in Tomato Seedlings. *Horticulturae*. 2023; 9: 770.
- [54]. Li HW., Zang BS., Deng XW., et al. Overexpression of the Trehalose-6-Phosphate Synthase Gene OsTPS1 Enhances Abiotic Stress Tolerance in Rice. *Planta*. 2011; 234: 1007–1018.
- [55]. Avonce N., Leyman B., Mascorro-Gallardo JO., et al. The Arabidopsis Trehalose-6-P Synthase AtTPS1 Gene is a Regulator of Glucose, Abscisic Acid, and Stress Signaling. *Plant Physiol* 2004; 136: 3649–3659.
- [56]. Fukuda A., Nakamura A., Tagiri A., et al. Function, Intracellular Localization and the Importance in Salt Tolerance of a Vacuolar Na⁺/H⁺ Antiporter from Rice. *Plant and Cell Physiology*. 2004; 45: 146–159.
- [57]. Chen M., Chen QJ., Niu XG., et al. Expression of OsNHX1 Gene in Maize Confers Salt Tolerance and Promotes Plant Growth in the Field. *Plant, Soil and Environment*. 2007; 53: 490–498.
- [58]. Yarra R. The Wheat NHX Gene Family: Potential Role in Improving Salinity Stress Tolerance of Plants. *Plant Gene* 2019; 18: 100178.
- [59]. Pabuayon ICM., Jiang J., Qian H., et al. Gain-of-function Mutations of AtNHX1 Suppress SOS1 Salt Sensitivity and Improve Salt Tolerance in Arabidopsis. *Stress Biology*. 2021; 1: 1–19.
- [60]. Liu M., Song X., Jiang Y. Growth, Ionic Response, and Gene Expression of Shoots and Roots of Perennial Ryegrass Under Salinity Stress. *Acta Physiologiae Plantarum*. 2018; 40: 1–8.
- [61]. Silva EN., Silveira JAG., Rodrigues CRF., et al. Physiological Adjustment to Salt Stress in *Jatropha curcas* is Associated With Accumulation of Salt Ions, Transport and Selectivity of K⁺, Osmotic Adjustment and K⁺/Na⁺ Homeostasis. *Plant Biology*. 2015; 17: 1023–1029.
- [62]. Zhang Y., Fang J., Wu X., et al. Na⁺/K⁺ Balance and Transport Regulatory Mechanisms in Weedy and Cultivated Rice (*Oryza sativa* L.) Under Salt Stress. *BMC Plant Biology*. 2018; 18: 1–14.
- [63]. Qiu QS., Guo Y., Dietrich MA., et al. Regulation of SOS1, A Plasma Membrane Na⁺/H⁺ Exchanger in *Arabidopsis thaliana*, by SOS2 and SOS3. *Proceedings of the National Academy of Sciences*. 2002; 99: 8436–8441.
- [64]. Shi H., Quintero FJ., Pardo JM., et al. The Putative Plasma Membrane Na⁺/H⁺ Antiporter SOS1 Controls Long-Distance Na⁺ Transport in Plants. *Plant Cell*. 2002; 14: 465–477.
- [65]. Calzone A., Cotozzi L., Pellegrini E., et al. Can the Transcriptional Regulation of NHX1, SOS1 and HKT1 Genes Handle the Response of Two Pomegranate Cultivars to Moderate Salt Stress?: Salt-tolerance of Two Pomegranate Cultivars. *Scientia Horticulturae*. 2021; 288: 110309.
- [66]. Wu H. Plant Salt Tolerance and Na⁺ Sensing and Transport. *Crop Journal*. 2018; 6: 215–225.
- [67]. Omisun T., Sahoo S., Saha B., et al. Relative Salinity Tolerance of Rice Cultivars Native to North East India: A Physiological, Biochemical and Molecular Perspective. *Protoplasma*. 2018; 255: 193–202.
- [68]. Theerawitaya C., Tisarum R., Samphumphuang T., et al. Expression Levels of the Na⁺/K⁺ Transporter OsHKT2;1 and Vacuolar Na⁺/H⁺ Exchanger OsNHX1, Na Enrichment, Maintaining the Photosynthetic Abilities and Growth Performances of Indica Rice Seedlings Under Salt Stress. *Physiology and Molecular Biology of Plants*. 2020; 26: 513–523.

DeepFake Detection Using Fine-Tuned CNN Architectures

Dilber ÇETİNTAŞ¹ , Zehra YÜCEL^{2*} 

¹ University of Malatya Turgut Özal, Faculty of Engineering and Natural Sciences, Department of Computer Engineering, Malatya, Türkiye

² Necmettin Erbakan University, Department of Computer Technologies, Konya, Türkiye

* zkarhan@erbakan.edu.tr

* Orcid No: 0000-0002-2863-9119

Received: August 9, 2024

Accepted: November 28, 2024

DOI: 10.18466/cbayarfbe.1530209

Abstract

Synthetic images have gained significant popularity, producing high-quality visuals that are challenging to distinguish from real images. Computer-generated images have become increasingly realistic and misleading as artificial intelligence models advance. The easy dissemination of synthetic images online has raised concerns about their potential misuse. An automated detection system has become essential to safeguard personal privacy. Such a system is also critical for preventing manipulation, maintaining social order, and preserving the authenticity of images. This study compares lightweight and dense models for real-fake classification tasks. In the first phase, the performance of lightweight models on the dataset is analyzed, followed by an assessment of dense models in the second phase. When the best-performing lightweight model, EfficientNetV2B0, is combined in a hybrid with the top dense model, DenseNet201, an 88% accuracy rate is observed. Moreover, a hybrid of the two most effective dense models, DenseNet121 and DenseNet201, achieved an accuracy of 89% on the test dataset. Experimental results indicate that DenseNet networks excelling in finer details achieve preferable outcomes on synthetic data.

Keywords: Artificial Intelligence, DeepFake, Fine-Tuned CNN, Real-Fake Distinction, Synthetic Images,

1. Introduction

People generally tend to trust their own eyes and ears when communicating. For this reason, audio and visual evidence have traditionally been regarded as reliable, despite a long history of forgeries such as photo tampering [1]. However, advancements in artificial intelligence (AI) have undermined this trust. The ability to generate synthetic data with great realism, often without detectable visual traces, poses a significant challenge to the authenticity of digital content. In recent years, synthetic image generation has seen rapid progress, making it increasingly difficult to distinguish between real and fake images [1, 2].

Research in this area suggests that detection methods must also advance as generative models evolve. Preventing the misuse of synthetic images depends primarily on their accurate detection. Misusing of such images can create false narratives and misinformation, leading to manipulation and deception. The manipulation of visual evidence can greatly impact individual and societal decision-making. This makes detecting synthetic images crucial in fields like cybersecurity, digital forensics, and media verification. Preparing for and

defending against the threats of synthetic data requires a detector that can classify images well [3, 4].

Studies in this area initially focused on pixel-level analysis and then explored various analytical approaches. Later studies emphasized geometric anomalies, reflections, and the uniform distribution of light. The consistency of metadata has also been taken into account [5, 6, 7].

Several studies have focused on the analysis of intrinsic patterns and artifacts present in synthetic images. Zhang et al. [8] and Frank et al. [9] investigated the detection of fake images generated by GANs by analyzing their frequency spectrum in the Fourier domain. Many detection methods remain GAN-specific, with relatively fewer studies addressing more recent generative models, such as diffusion models. However, Corvi et al. [2] analyzed the fingerprints left by diffusion models, a newer and increasingly popular class of generative models. Their work emphasizes the difficulty in distinguishing synthetic images produced by diffusion models from authentic ones and highlights the fundamental differences.

Another area of interest is the generalization of detection models across multiple datasets. Wang et al. [10]

observed that detection models performed well on a dataset generated using 11 different GAN-based image generation models. They emphasized that data augmentation improves performance but noted that there remains a need for model generalization across different generation techniques. Guarnera et al. [11] proposed a self-supervised learning-based method for distinguishing images generated by various GAN models (GDWCT, StarGAN, AttGAN, StyleGAN, StyleGAN2). Their approach involves analyzing features at different scales and employing the Expectation-Maximization (EM) algorithm to facilitate the detection process. This method allows for the effective differentiation of synthetic images by leveraging the inherent characteristics across different GAN architectures. In the context of diffusion models, Somepalli et al. [12] explored the relationship between dataset size and the similarity of diffusion models' output to training data. They demonstrated that larger training datasets enable the generation of higher-quality images.

The CNN-based transfer learning approach is widely used for detecting fake images. Malolan et al. [13] successfully distinguished between real and fake images with an accuracy of 94.33% using a CNN-based method on the FaceForensics dataset [14]. They also incorporated various explainable AI techniques, such as layer-wise relevance propagation (LRP) and local interpretable model-agnostic explanations (LIME), to enhance the interpretability of their model. Ranjan et al. [15] proposed a transfer learning-based CNN framework tested on three different datasets—DeepFakeDetection (DFD) [16], Celeb-DF [17], and the DeepFake Detection Challenge (DFDC) [18]. Additionally, they compiled a custom dataset for model evaluation, achieving 95.86% accuracy in distinguishing real and fake images.

Nida et al. [19] achieved 92.09% accuracy in detecting real and fake images using CNN-based models on the Real and Fake Face Detection dataset [20], after performing image normalization and Error Level Analysis (ELA) to enhance feature extraction prior to training.

Most studies on fake-vs.-real image detection has focused on facial images, while deepfake research involving other types of images (e.g., nature, vehicles, etc.) remains limited. Although considerable attention has been given to detecting GAN-generated images, particularly in ensuring robust detection across different types of synthetic data and applying existing deep-learning models, there is comparatively less research on images produced by diffusion models. In our study, we focus on detecting images generated by generative models, such as diffusion models, and extend the scope beyond facial images to include various other types of imagery. we aim for a generalizable detector.

Contributions of this Study:

- **Comprehensive Evaluation:** We provide a performance comparison of various fine-tuned CNN architectures for synthetic image detection.
- **Superior Model Performance:** Our experiments demonstrate that DenseNet models achieve the highest accuracy, outperforming other models.
- **Synthetic Image Detection:** Unlike many existing studies that focus solely on GAN-generated images, we provide a more generalized framework capable of detecting synthetic images from a variety of sources, including those generated by diffusion models.
- **Analysis:** We offer an analysis of each model's strengths and weaknesses in comparison to existing methods.

The rest of this paper; Section 2 presents the dataset, techniques, and models used. Section 3 presents the analyses and results of the experiments. In the last section, general conclusions and implications are presented.

2. Materials and Methods

This section contains information about the techniques, methods, and data sets used in the classification of synthetic data and real data.

2.1. Data Set

The CIFAKE [21] dataset consists of two groups: real images and fake images. The real image set consists of the CIFAR-10[22] dataset. The CIFAR-10 dataset contains 60,000 RGB images of 10 classes (deer, ship, horse, frog, aircraft, automobile, bird, cat, dog and truck) in 32x32 size. It contains 6,000 data from each of its classes.

The set of fake images of the CIFAKE dataset is obtained by applying LDM to the images in the CIFAR-10 dataset. A set of 60,000 synthetic images equivalent to 60,000 real datasets is obtained. The resolution of all images is 32x32 px. In order to achieve differentiation, the researchers used different prompt variations for each class.

In this study, evaluations were conducted using randomly generated subsets from the CIFAKE dataset. Among the created subsets, the best results were achieved with a training set containing 7,000 fake and 7,000 real images, and a test set with 1,058 fake and 1,058 real images. To ensure generalizability, datasets with varying distributions were utilized.

2.2. Pre-Trained Models

In this section, MobileNet [23], DenseNet121[24], EfficientNetV2B0[25] are discussed and briefly introduced.

MobileNet is widely used to create lightweight deep convolutional neural networks, providing an efficient architecture that does not require extensive computational resources. It is particularly prevalent in computer vision applications like object detection and classification. The architecture includes down-sampling with features derived from the previous layer and concludes with an average pooling layer. A SoftMax function is used in the final layer for classification purposes. MobileNet's architecture relies on depthwise separable convolutions, incorporating batch normalization and ReLU activation functions. The entire MobileNet model consists of 28 layers [23,26].

To further reduce computational costs, MobileNet employs width and resolution multipliers. The width multiplier thins the model by a specified factor; selecting a smaller multiplier yields a faster, smaller model but may lead to some information loss. The resolution multiplier, on the other hand, adjusts the input image resolution. Choosing a smaller resolution provides a more compact and efficient model, though potentially at the cost of detail. It is therefore critical to select these multipliers carefully to balance computational efficiency with minimal information loss [23,26]. MobileNet has been improved and extended with newer versions, such as MobileNetV2[27] and MobileNetV3[28], aiming to enhance accuracy and speed. MobileNetV2 introduced inverted residuals to achieve an expansion-filtering-squeezing mechanism [27]. In MobileNetV3, squeeze-and-excitation layers were added to the initial block structure further enhance performance [28].

Densely Connected Convolutional Networks (DenseNet), unlike other architectures, contain dense blocks of layers. Each layer is directly connected to each subsequent layer in a feed-forward manner [24]. This architecture encourages the reuse of features when addressing the gradient fading problem and therefore reduces the number of parameters. As a result, DenseNet offers a powerful approach in scenarios where small differences are important [24, 29]. There are several versions of DenseNet used in object recognition applications, for example, DenseNet121, DenseNet160, and DenseNet201. Numbers in these versions represent the number of layers in the model. The general representation of the DenseNet121 architecture is shown in Figure 1. In DenseNet121, except for the first layer that receives the input image, each subsequent convolutional layer creates an output feature map by taking the output of the previous layer [24].

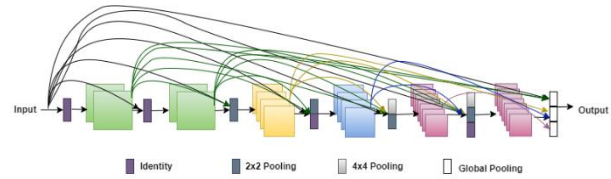


Figure 1. General Structure of DenseNet121 Architecture

EfficientNetV2B0 is an upgraded model of EfficientNet, proposed by Google Brain. It employs a mobile-dimensional convolutional network based on training-driven neural architecture search and scaling. This model outperforms previous models in terms of training speed, accuracy, and parameter efficiency. EfficientNetV2B0 demonstrates that deep convolution is slow in the early layers but becomes more efficient in later stages [25, 30]. [25, 30]. The general structure of the EfficientNetV2B0 architecture is shown in Figure 2. Architecture consists of a combination of MBConv block [31] to balance the expressive power and computational cost, and Fused-MBConv [32] to further speed up the process.

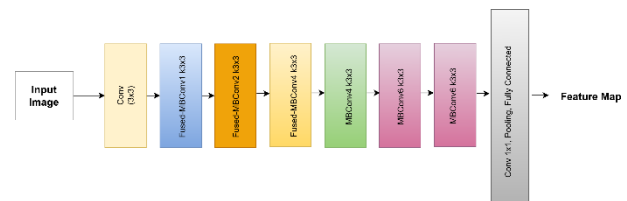


Figure 2. General Structure of EfficientNetV2B0 Network [25]

2.3. Evaluation Metrics

The confusion matrix was used to evaluate performance. In this matrix, rows indicate real classes and columns indicate predicted classifications. To measure evaluation metrics, tp (true positive), tn (true negative), fp (false positive), fn (false negative) values are used.

Precision: It is defined as the ratio of the data determined as positive among the predicted ones to the total number of positives. Calculation of the precision value is given in equation 1.

$$\text{Precision} = \frac{tp}{(tp+fn)} \quad (2.3.1)$$

Recall: It provides information about the number of data that are actually predicted as positive among the data that should be predicted as positive. Calculation of the sensitivity value is specified in equation 2.

$$\text{Recall} = \frac{tp}{(tp+fp)} \quad (2.3.2)$$

F1-Score: It is calculated by the harmonic mean of precision and sensitivity calculations. It takes values

between 0 and 1, with 1 indicating that the best result has been achieved. Calculation of the F1 score value is given in equation 3.

$$F1\text{-Score} = \frac{2 * tp}{2tp + fp + fn} \quad (2.3.3)$$

Accuracy: It is the ratio of correctly predicted data to all data. Calculation of Accuracy value is given in equation 4.

$$Accuracy = \frac{tp + tn}{tp + tn + fp + fn} \quad (2.3.4)$$

3. Results and Discussion

In the initial approach, the input layers of various lightweight models, including MobileNetV2, MobileNetV3Small, MobileNetV3Large, and EfficientNetV2B0, were adjusted to the 32x32 image size. In the second stage, this adjustment was applied to dense models, namely DenseNet121, DenseNet169, and DenseNet201. These models were then trained with frozen parameters. Subsequently, additional layers were appended to the architecture, including a GlobalAveragePooling2D layer, a Dense layer with 1024 units and ReLU activation, a Dropout layer with a rate of

0.5, and a final Sigmoid layer. The Adam optimization algorithm was used to train the models with a learning rate of 1e-5 and an epoch count of 50. Experimental evaluations were then conducted using this configuration.

In the literature, numerous studies on the classification of synthetic data have made significant contributions by evaluating different deep-learning models in this area. However, determining which models are more effective at distinguishing between real and fake data remains a challenging problem. This study compares the performance of lightweight and heavy models to analyze their impact on synthetic data classification. Lightweight models include EfficientNetV2B0, MobileNetV2, MobileNetV3Small, and MobileNetV3Large, while heavy models consist of DenseNet121, DenseNet169, and DenseNet201. The performance of these models was evaluated comparatively, with the results presented in Tables 1 and 2, model accuracy detailed through confusion matrices in Figures 3 and 4. In the matrices, the value "0" represents the "Fake" label, while "1" denotes the "Real" label.

Table 1. Performance Results Evaluation of Lightweight Models in Deepfake Detection

Models	Precision	Recall	F1-Score	Accuracy
MobileNetV2	0.30	0.73	0.42	0.59
MobileNetV3Small	0.71	0.48	0.57	0.47
MobileNetV3Large	0.72	0.82	0.77	0.78
EfficientNetV2B0	0.77	0.90	0.83	0.84

The experimental results reveal distinct performance patterns across the models tested. EfficientNetV2B0 demonstrated the highest performance among the models, achieving a precision of 0.77, recall of 0.90, F1-score of 0.83, and accuracy of 0.84. The model's high recall, coupled with robust precision and accuracy,

underscores its ability to accurately identify relevant instances while maintaining a low false-positive rate. This balanced performance makes EfficientNetV2B0 the most reliable lightweight model in this study for achieving both precise and comprehensive classification.

Table 2. Performance Results Evaluation of Compact Models for Test Data

Models	Precision	Recall	F1-Score	Accuracy
DenseNet121	0.84	0.91	0.87	0.88
DenseNet169	0.83	0.89	0.86	0.86
DenseNet201	0.85	0.90	0.88	0.88

The performance results for the DenseNet models indicate strong classification abilities across all three variations. Overall, all three DenseNet models

demonstrate excellent classification capabilities, with DenseNet201 showing a slight edge, particularly for tasks prioritizing both precision and recall.

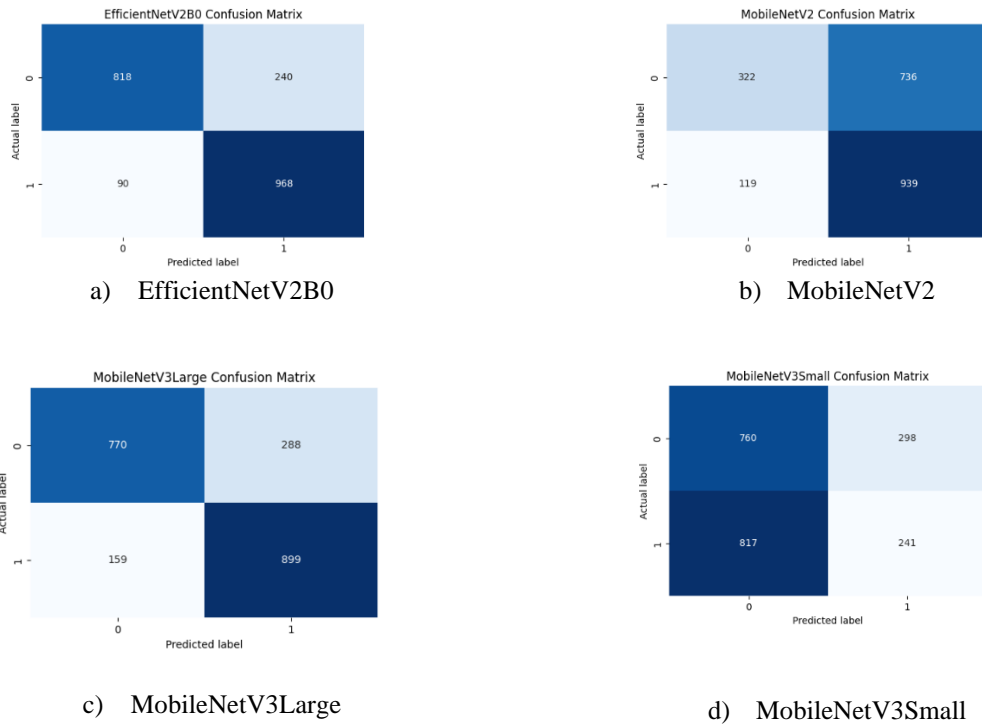


Figure 3. Confusion matrix obtained from lightweight fine-tuned CNN Architecture a) EfficientNetV2B0 b) MobileNetV2 c) MobileNetV3Large d) MobileNetV3Small

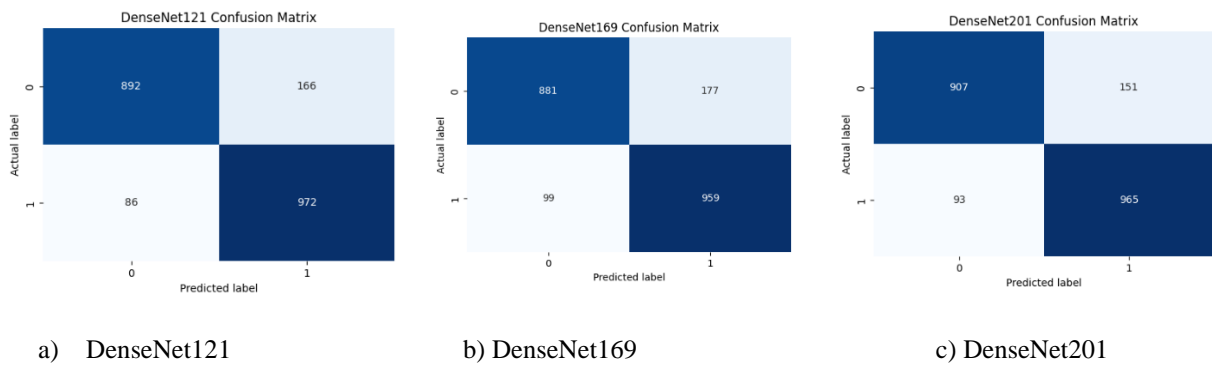


Figure 4. Confusion matrix obtained from compact fine-tuned CNN Architecture a) DenseNet121 b) DenseNet169 c) DenseNet201

The analysis of the confusion matrices for various models, including EfficientNetV2B0, MobileNetV2, MobileNetV3 (Small and Large), DenseNet121, DenseNet169, and DenseNet201, highlights differences in classification performance. DenseNet models, particularly DenseNet201 and DenseNet121, demonstrate a balanced performance with lower false negative and false positive rates, indicating strong accuracy and reliability. EfficientNetV2B0 shows high accuracy but a relatively high false positive rate, which may impact its sensitivity. MobileNet models, especially MobileNetV2 and MobileNetV3Small, display higher error rates and appear less suitable for this dataset due to

lower classification accuracy. Overall, DenseNet201 emerges as the optimal model for this task, achieving a robust balance between sensitivity and precision, making it a dependable choice for accurate classification. This study underlines the efficacy of DenseNet models, especially DenseNet201, as superior classifiers in terms of accuracy and balanced error rates. Overall, the DenseNet series models, particularly DenseNet201 and DenseNet121, stand out as models with the highest accuracy and balanced classification performance. While EfficientNetV2B0 also provides high accuracy, its relatively high false positive rate slightly limits its sensitivity. MobileNetV2 and

MobileNetV3Small demonstrate lower accuracy in comparison to other models, rendering them insufficient for the dataset. This analysis suggests that DenseNet201

could be preferred as an accurate and reliable classification model due to its strong balance between precision and sensitivity.

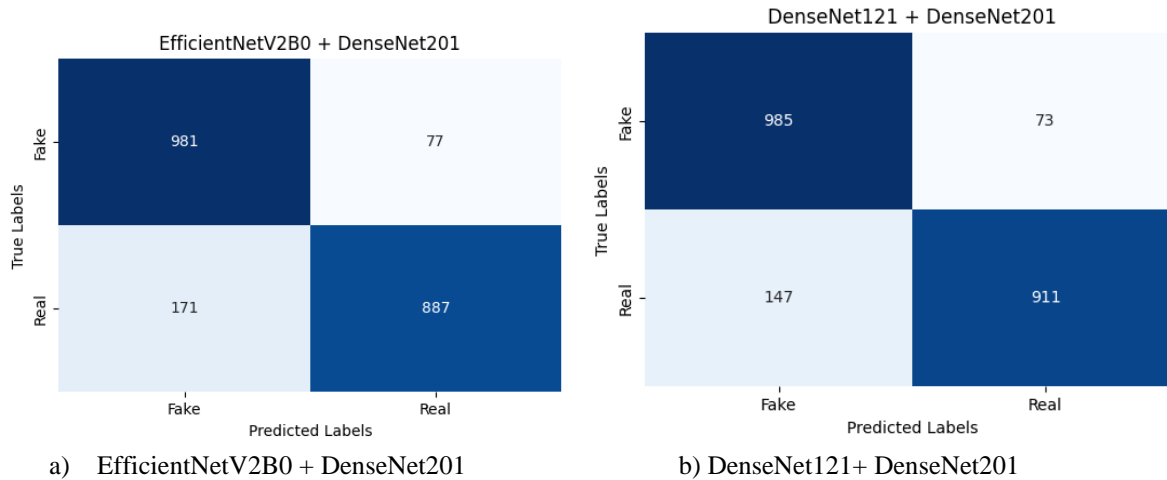


Figure 5. Deepfake detection results with DenseNet201

The hybrid model combining EfficientNetV2B0 and DenseNet201 achieved notable results in distinguishing between synthetic and real images confusion matrix, as shown in Figure 5. The model correctly identified 981 fake images (true positives) and 887 real images (true negatives), while misclassifying 77 fake images as real (false positives) and 171 real images as fake (false negatives). This performance yielded an overall accuracy of approximately 88%, indicating the model's strong capability in detecting both fake and real images.

When the two most successful dense models, DenseNet121 and DenseNet201, were combined in a hybrid approach, the classification performance demonstrated further improvements, particularly in accurately identifying real images. The confusion matrix reveals that the hybrid model correctly identified 985 synthetic (fake) images and 911 real images, resulting in 73 false positives (fake images misclassified as real) and 147 false negatives (real images misclassified as fake). This performance led to an overall accuracy of approximately 89%, highlighting the effectiveness of combining these dense networks. The results indicate that while both DenseNet121 and DenseNet201 individually excel at detecting fake images, their combined use enhances the model's ability to differentiate real images more accurately. This hybrid approach leverages the strengths of both models, providing a more robust and precise classification compared to their individual performances. The study demonstrates that integrating multiple dense architectures can effectively improve detection accuracy, particularly in challenging tasks that require high sensitivity to both synthetic and authentic visual patterns.

The method of synthetic data generation is an important limiting factor. Studies in the literature have predominantly utilized synthetic data generated with GANs. Our study addresses this gap by employing

synthetic data generated through diffusion models. Another constraint is that successful results can be achieved even with input images at a resolution as low as 32x32. This new study, contributing to the limited body of research on diffusion models, compares lightweight and dense models to evaluate which is more effective in terms of overall performance. The findings provide valuable insights into the most suitable model types for different applications. The use of hybrid models on the newly developed CIFAKE dataset has proven to yield more effective results.

4. Conclusion

The hybrid use of dense networks contributed to achieving a more balanced and successful performance across both fake and real classes, significantly enhancing classification accuracy. The ensemble method, combining these models in a hybrid fashion, produced the most successful results on the given dataset, further demonstrating the effectiveness of integrating various model features in deep learning applications. This finding suggests that optimizing dense networks for specific classes can lead to higher performance in classification tasks, highlighting the potential of hybrid approaches for improved accuracy in such applications. It gives information about the performances of our study and lightweight-compact models. The results are promising in the field of classification. This may give an idea to scientists who will work in this field.

As a future study, we aim to improve the performance of these models by utilising other distinguishing features of synthetic data. At the same time, we aim to focus on a detector that can be generalised to the dataset produced by different diffusion models. Additionally, in image detection, learning long-range dependencies through Transformer models can significantly enhance the

accuracy of synthetic data detection. As a potential direction for future research, a hybrid approach that combines CNN and Transformer models could be explored to leverage the strengths of both architectures.

Author's Contributions

All authors have contributed equally to this work. All authors have read, provided feedback on, and approved the final version of the manuscript.

Ethics

There are no ethical issues after the publication of this manuscript.

References

- [1]. Dang, L.M., Min, K., Wang, H., Piran, M.J., Lee, C.H. and Moon, H., 2020. Sensor-based and vision-based human activity recognition: A comprehensive survey. *Pattern Recognition*, 108, p.107561.
- [2]. Corvi, R., Cozzolino, D., Zingarini, G., Poggi, G., Nagano, K. and Verdoliva, L., 2023, June. On the detection of synthetic images generated by diffusion models. In *ICASSP 2023-2023 IEEE International Conference on Acoustics, Speech and Signal Processing (ICASSP)* (pp. 1-5). IEEE.
- [3]. Bonettini, N., Bestagini, P., Milani, S. and Tubaro, S., 2021, January. On the use of Benford's law to detect GAN-generated images. In *2020 25th international conference on pattern recognition (ICPR)* (pp. 5495-5502). IEEE.
- [4]. Bird, J.J., Naser, A. and Lotfi, A., 2023. Writer-independent signature verification; Evaluation of robotic and generative adversarial attacks. *Information Sciences*, 633, pp.170-181.
- [5]. Bayar, B. and Stamm, M.C., 2016, June. A deep learning approach to universal image manipulation detection using a new convolutional layer. In *Proceedings of the 4th ACM workshop on information hiding and multimedia security* (pp. 5-10).
- [6]. Verdoliva, L., 2020. Media forensics and deepfakes: an overview. *IEEE journal of selected topics in signal processing*, 14(5), pp.910-932.
- [7]. Fridrich, J. and Kodovsky, J., 2012. Rich models for steganalysis of digital images. *IEEE Transactions on information Forensics and Security*, 7(3), pp.868-882.
- [8]. Zhang, X., Karaman, S. and Chang, S.F., 2019, December. Detecting and simulating artifacts in gan fake images. In *2019 IEEE international workshop on information forensics and security (WIFS)* (pp. 1-6). IEEE.
- [9]. Frank, J., Eisenhofer, T., Schönherr, L., Fischer, A., Kolossa, D. and Holz, T., 2020, November. Leveraging frequency analysis for deep fake image recognition. In *International conference on machine learning* (pp. 3247-3258). PMLR.
- [10]. Wang, S.Y., Wang, O., Zhang, R., Owens, A. and Efros, A.A., 2020. CNN-generated images are surprisingly easy to spot... for now. In *Proceedings of the IEEE/CVF conference on computer vision and pattern recognition* (pp. 8695-8704).
- [11]. Guamera, L., Giudice, O., & Battiato, S., 2020. Deepfake detection by analyzing convolutional traces. In *Proceedings of the IEEE/CVF conference on computer vision and pattern recognition workshops* (pp. 666-667).
- [12]. Somepalli, G., Singla, V., Goldblum, M., Geiping, J. and Goldstein, T., 2023. Diffusion art or digital forgery? investigating data replication in diffusion models. In *Proceedings of the IEEE/CVF Conference on Computer Vision and Pattern Recognition* (pp. 6048-6058).
- [13]. Malolan, B., Parekh, A., & Kazi, F., 2020. Explainable deep-fake detection using visual interpretability methods. In *2020 3rd International conference on Information and Computer Technologies (ICICT)* (pp. 289-293). IEEE.
- [14]. Rössler, A., Cozzolino, D., Verdoliva, L., Riess, C., Thies, J., & Nießner, M., 2018. Faceforensics: A large-scale video dataset for forgery detection in human faces. *arXiv preprint arXiv:1803.09179*.
- [15]. Ranjan, P., Patil, S., & Kazi, F., 2020. Improved generalizability of deep-fakes detection using transfer learning based CNN framework. In *2020 3rd international conference on information and computer technologies (ICICT)* (pp. 86-90). IEEE.
- [16]. Dufour, N., & Gully, A. 2024. Contributing data to deepfake detection research. <https://research.google/blog/contributing-data-to-deepfake-detection-research/>
- [17]. Li, Y., Yang, X., Sun, P., Qi, H. and Lyu, S., 2020. Celeb-df: A large-scale challenging dataset for deepfake forensics. In *Proceedings of the IEEE/CVF conference on computer vision and pattern recognition* (pp. 3207-3216).
- [18]. Dolhansky, B., 2019. The deepfake detection challenge (DFDC) pre view dataset. *arXiv preprint arXiv:1910.08854*.
- [19]. Nida, N., Irtaza, A., & Ilyas, N. 2021. Forged face detection using ELA and deep learning techniques. In *2021 International Bhurban Conference on Applied Sciences and Technologies (IBCAST)* (pp. 271-275). IEEE.
- [20]. Real and fake face detection, <https://www.kaggle.com/ciplab/real-and-fake-face-detection> (2024).
- [21]. Bird, J.J. and Lotfi, A., 2024. Cifake: Image classification and explainable identification of ai-generated synthetic images. *IEEE Access*.
- [22]. The CIFAR-10 dataset, <https://www.cs.toronto.edu/~kriz/cifar.html> (accessed at 13.03.2024).
- [23]. Howard, A. G. (2017). Mobilenets: Efficient convolutional neural networks for mobile vision applications. *arXiv preprint arXiv:1704.04861*.
- [24]. Huang, G., Liu, Z., Van Der Maaten, L. and Weinberger, K.Q., 2017. Densely connected convolutional networks. In *Proceedings of the IEEE conference on computer vision and pattern recognition* (pp. 4700-4708).
- [25]. Tan, M. and Le, Q., 2021, July. Efficientnetv2: Smaller models and faster training. In *International conference on machine learning* (pp. 10096-10106). PMLR.
- [26]. Wang, W., Li, Y., Zou, T., Wang, X., You, J., & Luo, Y. (2020). A novel image classification approach via dense-MobileNet models. *Mobile Information Systems*, 2020(1), 7602384.
- [27]. Sandler, M., Howard, A., Zhu, M., Zhmoginov, A., & Chen, L. C. (2018). Mobilenetv2: Inverted residuals and linear bottlenecks. In *Proceedings of the IEEE conference on computer vision and pattern recognition* (pp. 4510-4520).
- [28]. Howard, A., Sandler, M., Chu, G., Chen, L. C., Chen, B., Tan, M., & Adam, H. (2019). Searching for mobilenetv3. In *Proceedings of the IEEE/CVF international conference on computer vision* (pp. 1314-1324).




[29]. Bozkurt, F. (2021). Classification of blood cells from blood cell images using dense convolutional network. *Journal of Science, Technology and Engineering Research*, 2(2), 81-88.

[30]. Zheng, T., Yang, X., Lv, J., Li, M., Wang, S. and Li, W., 2023. An efficient mobile model for insect image classification in the field pest management. *Engineering Science and Technology, an International Journal*, 39, p.101335.

[31]. Sandler, M., Howard, A., Zhu, M., Zhmoginov, A. and Chen, L.C., 2018. Mobilenetv2: Inverted residuals and linear bottlenecks. In *Proceedings of the IEEE conference on computer vision and pattern recognition* (pp. 4510-4520).

[32]. Gupta, S. and Akin, B., 2020. Accelerator-aware neural network design using automl. *arXiv preprint arXiv:2003.02838*.

Updated Distribution and Future Concerns of *Crocus balansae*

Almila Çiftçi^{1*} 

¹ İstanbul University, Biology Department, Botany Division, Vezneciler, Fatih, İstanbul, Türkiye

* almila.ciftci@istanbul.edu.tr

* 0000-0002-3406-3064

Received: October 6, 2024

Accepted: November 28, 2024

DOI: 10.18466/cbayarfbe.1562245

Abstract

Crocus balansae J.Gay ex Maw (Iridaceae) is a rare petaloid monocotyledon with fragmented habitats, under heavy anthropogenic pressure and climatic threat. Within the scope of this study, several herbariums were visited and previously collected specimens identified as *C. balansae* were examined morphologically. Field surveys were carried out to all addresses in the herbarium records, including some unidentifiable specimens, and to areas where populations are likely to be found. As a result of this study, it was determined that *Crocus balansae* populations are distributed in a narrower area than previously thought and the distribution area of *C. balansae* in Western Anatolia was updated. The challenges in accurate identification of *Crocus balansae* and the possible causes of misidentified plants were discussed. Field studies and observations revealed that some populations differ slightly morphologically from one another and that urbanization has caused the extinction of some populations. It was found that the type locality population had vanished as a result of the urbanization issue, making it impossible to compare samples from the type locality with populations that were later found using the techniques available today. The morphologically closest population to the species description is suggested in this paper.

Keywords: Anthropogenic pressure, Conservation, *Crocus*, Iridaceae, Urbanization.

1. Introduction

The Iridaceae family is poorly understood phylogenetically in terms of its systematic relationships; different authors have different ideas about genus boundaries, species relationships, and phylogenetic relationships [1]. 28 genera and over 995 species that belong to the subfamily Crocoideae make up more than half of this family [2]. With over 235 species, the genus *Crocus* L. (Iridaceae) of the subfamily Crocoideae is widely distributed, ranging from Poland to China, while the majority of its species are located in Turkey and the Balkans. Turkey is home to more than half of these species. The genus *Crocus* was divided into 2 sections and 16 series by Mathew [3]. However, Harpke et al. [4] showed that only 8 of these series are monophyletic, while the rest are polyphyletic.

A revision of the genus is needed, as several infrageneric and even intraspecific units have been shown to be para- or polyphyletic, and although more than 50 new species have been described recently [5] [6] [7], in most cases they are not assigned to existing taxonomic groups. Moreover, the relationship of the various species and infrageneric groups is still unclear.

In summary, *Crocus* is a genus with unresolved infrageneric issues, rich in neo-endemic species and currently in the middle of a speciation explosion [8]. However, while scientists continue to study the genus taxonomically, many local endemic crocus species are threatened with extinction due to anthropogenic impacts.

The study's main subject, *Crocus balansae* J.Gay ex Maw, is a corm geophyte that thrives under forests and at an elevation of 650–700 meters. Other species in the genus often grow in alpine meadows or forest clearings [9]. One of the genus' most gravely threatened species is *Crocus balansae*. The primary significant risks to this taxon are overgrazing, newly constructed highways, its limited distribution range, residing in fragmented habitats, and the low number of individuals per unit area. İzmir and Manisa are home to the species' known populations.

The purpose of this study is to assess the present condition of *C. balansae* populations and ascertain if any additional populations exist that have not yet been detected.

2. Materials and Methods

Istanbul University Faculty of Pharmacy Herbarium (ISTE), Istanbul University Faculty of Science Herbarium (ISTF), Ege University Faculty of Science Herbarium (EGE), Ankara University Faculty of Science Herbarium (ANK), Ankara University Faculty of Pharmacy Herbarium (AEF), Hacettepe University Herbarium (HUB) were visited and previously collected *C. balansae* specimens and closely related species were examined. Manisa and its surroundings, İzmir and its surroundings, Denizli and its surroundings, Aydın Dilek peninsula, Balıkesir and its surroundings were studied together with the type locality of *Crocus balansae* taxon and samples from a total of 6 populations were collected. During the field study, herbarium samples were collected for future morphological and molecular studies. Field studies were carried out in March and April in 2022-2023. The specimens are kept in Istanbul University Science Faculty Herbarium (ISTF). Identifications were made using Maw [10], Bowles [11], Mathew [3] and [12].

2. Results and Discussion

It was found that the distribution of the *Crocus balansae* species reaches up to 1200 meters in altitude. The plant can be found in alpine meadows, woodland understory, and clearings of juniper and oak (Figure 1). It turned out that the plants in Manisa-Soma and İzmir-Karaburun, two of the populations of *Crocus balansae* that have been documented, were misidentified previously.

C. olivieri J.Gay from Soma (Manisa) was identified as *C. balansae*, which is distributed together with *C. chrysanthus* Herb. and *C. flavus* Weston in Soma, Manisa. Most probably, these plants were erroneously identified as *C. balansae* due to the colorations on the outer tepals of the plants in this population, but although it is rare, such colorations can be observed in *C. olivieri*.

The plants in Karaburun, İzmir were also examined and similarly identified as *C. olivieri*. In the light of the information obtained as a result of the field studies, it was determined that *C. balansae* is distributed in a narrower area than previously thought. Address information of *C. balansae* plants collected from other locations is given in Table 1.

Table 1. The specimens collected during the field work in this study.

ISTF No.	Lokasyon	Habitat	Tarih
41782	Manisa: Soma	<i>Quercus</i> sp. clearings, 865 m	03.03.2022
41459	Manisa: Spil Dağı	<i>Juniperus</i> , <i>Pinus</i> , stony clearings, 1196 m	06.04.2022
41554	Aydın: Dilek yarımadası	<i>Pinus nigra</i> forest, 733 m	22.02.2023
41556	İzmir: Bornova, Çiçekli	<i>Pinus brutia</i> forest, 466 m	23.02.2023
41557	İzmir: Kayadibi	<i>Quercus</i> sp. clearings, stony places, 490 m	23.02.2023
41898	İzmir: Selçuk, Şirince	-	03.2023

With the collected specimens, the distribution of *C. balansae* taxon in Western Anatolia was updated (Figure 2).



Figure 1. *Crocus balansae* (a) in its habitat on Spil mountain distributing with *C. chrysanthus* and (b) habitus.

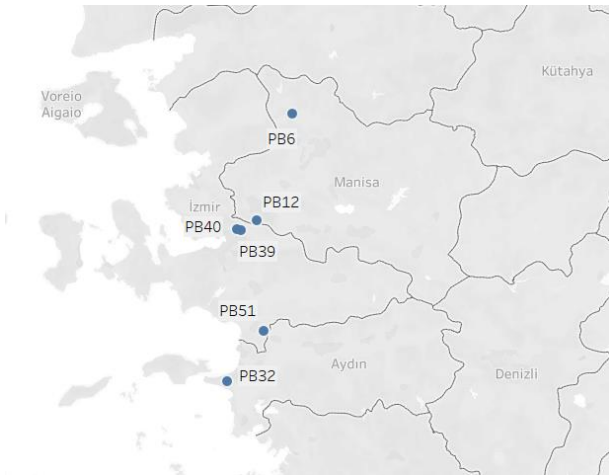


Figure 2. Current distribution map of *Crocus balansae* according to the field studies carried out within the scope of the study.

A problem often encountered during herbarium and field studies is that *C. olivieri* plants are often misidentified as *C. balansae*. Because closely related species share similar morphological traits at first look and because colors and patterns in herbarium specimens fade over time, it can be challenging to correctly identify these plants, especially for non-specialists.

Fieldwork and herbarium specimen observations demonstrated that some populations morphologically differed significantly for their classification as distinct species. Similarly, the populations reported by Mathew [12] on the islands of Kos and Samos are most likely distinct species. Urbanization appears to be the cause of the disappearance of some populations that were mentioned in the literature and herbariums. All the areas where the type specimen was located were surveyed during the field studies [Turkey, İzmir, Uncultivated hills near Smyrne, approximately 4 km SE of Koukouloudja, Bornova, 4 km SE of Altındag (Kokluca, Koukouloudja), 13 iii 1854, B. Balansa 34 (lectotype / lectotypus / lectotype: K 000802442!) [13]. Due to extensive development of cities, the location where the type specimen was discovered ended up being entirely destroyed. Under this circumstance, it is no longer possible to use contemporary methods to compare the specimens from where the type specimen was obtained with other populations. Moreover, many useful features that were once comparable in herbarium specimens have also diminished over time.

Crocus balansae has been described in various ways by Maw [10], Bowles [11], Mathew [3], Mathew [12] and Erol and Çiftçi [13]. Upon analyzing these descriptions, two things become evident:

- 1) Stigma arms having (8-)12-16 segments
- 2) Presence of distinct patterns on the back of outer tepals

Given that these two traits must coexist for the studied populations to be referred to as *C. balansae*, it is evident that Spil Mountain (Manisa) is home to the population that best fits the common description traits of *C. balansae* among the studied populations.

The plant's distribution area suggests that it is a component of the Eastern Mediterranean. The eastern Mediterranean region experiences hot, dry summers followed by warm, wet winters due to a regional climate impacted by many climatic systems that is vulnerable to atmospheric changes [14]. This region is also seeing the effects of climate change, which is a globally significant issue. Increases in average annual temperatures, drops in average annual precipitation, floods, droughts, and fires are all effects of climate change. Living things have been observed to have altered and homogenized in their community structure in response to climate change, more likely to migrate to higher elevations, and have undergone some degree of adaptation [15]. Plants are "sedentary" organisms, thus it makes sense to look into the biology of pollination and protection, as these processes are crucial to the development of adaptive individuals. As a result, *C. balansae* is the subject of an ongoing model pollination study in crocuses (I.U. BAP 37723).

Determining whether there is gene exchange between populations of plants with fragmented habitats, if not, whether this is a physical barrier due to geographical distance or a pollination barrier, identifying the population with the highest genetic diversity and determining which population should be protected as a priority is an important issue for the future of *C. balansae*, which is under both anthropogenic pressure and climatic threat. Studies on this subject are also ongoing.

3. Conclusion

Road expansion and human influences are threatening the Spil Mountain populations, which were found to be the ones that most closely matched the original description of *C. balansae*, even though they are located within the national park boundaries. Therefore, taking action for its conservation is extremely important for the transmission of this species to future generations.

Acknowledgement

I would like to thank the 4th Regional Directorate of the Ministry of Agriculture and Forestry, Manisa Provincial Branch Directorate, Spil National Park Directorate and Akhisar DKMP Directorate, Prof. Dr. Levent Şık, Rachel Mollman and Prof. Dr. Osman Erol for their support during the field studies. This study was supported by Istanbul University Scientific Research Projects Unit project number 37723.

Author's Contributions

Almila Çiftçi: Drafted and wrote the manuscript, performed the experiment and result analysis.

Ethics

There are no ethical issues after the publication of this manuscript.

References

- [1]. Rodríguez, A, Catedral, LO. 2003. Colima (Tigridieae: Iridaceae), a new genus from western Mexico and a new species: Colima tuitensis from Jalisco. *Acta Botanica Mexicana*; 65: 51–60.
- [2]. Goldblatt, P, Davies, J, Manning, J, van der Bank, M, Savolainen, V. 2006. Phylogeny of Iridaceae Subfamily Crocoideae Based on a Combined Multigene Plastid DNA Analysis. *Aliso*; 22(1): 399–411.
- [3]. Mathew, B. The Crocuses: a revision of the genus *Crocus* (1. Basim); Press: Timber Pr, B.T Batsford, Londra, 1982; pp 224.
- [4]. Harpke, D, Meng, S, Rutten, T, Kerndorff, H, Blattner, FR. 2013. Phylogeny of *Crocus* (Iridaceae) based on one chloroplast and two nuclear loci: Ancient hybridization and chromosome number evolution. *Molecular Phylogenetics and Evolution*; 66(3): 617–627.
- [5]. Şık, L, Yazıcı, C, Mollman, RR, Harpke, D, Kaleli, BS, Çiftçi, A, Erol, O. 2024. A new autumn-flowering *Crocus* (Iridaceae) from Türkiye: *C. rifatozdemiri* sp. nov. *Phytotaxa*; 665(1): 13-24.
- [6]. Yazıcı, C, Çiftçi, A, Mollman, R, Harpke, D, Erol, O. 2024. Diversity of *Crocus gargaricus* sl: resolving longstanding debates and discovering a new species. *Plant Systematics and Evolution*; 310(4): 28-.
- [7]. Çiftçi, A, Harpke, D, Mollman, R, Yıldırım, H, Erol, O. 2020. Notes on *Crocus* L. Series Flavi Mathew (Iridaceae) and a new species with unique corm structure. *Phytotaxa*; 430(2): 65-79.
- [8]. Frello, S, Ørgaard, M, Jacobsen, N, Heslop-Harrison, JS. 2004. The genomic organization and evolutionary distribution of a tandemly repeated DNA sequence family in the genus *Crocus* (Iridaceae). *Hereditas*; 141(1): 81-88.
- [9]. Ruksans, J. The world of crocuses (1st edition); Press: The Latvian Academy of Sciences, Latvia. 2017; pp. 503.
- [10]. Maw, GA. Monograph of the genus *Crocus*; Press: Dulau &Co., London, 1886; pp 530.
- [11]. Bowles EA. A Handbook of *Crocus* and *Colchicum* for Gardeners; Press: Bodley Head, London. 1952; pp. 222.
- [12]. Mathew, B. 1984. Rare and little-known crocuses in cultivation. *The Kew Magazine*; 68-74.
- [13]. Erol, O, Çiftçi, A. *Crocus* L., In: Güner, A., Kandemir, A., Menemen, Y., Yıldırım, H., Aslan, S., Ekşi, G., Güner, I. ve Çimen, A.Ö. (eds). Resimli Türkiye Florası 3a: ANG Vakfı Nezahat Gökyiğit Botanik Bahçesi Yayınları, İstanbul, 2018, pp 880-926.
- [14]. Finné, M, Holmgren, K, Sundqvist, HS, Weiberg, E, Lindblom, M. 2011. Climate in the eastern Mediterranean, and adjacent regions, during the past 6000 years—A review. *Journal of archaeological science*; 38(12): 3153-3173.
- [15]. Filipe, AF, Justin EL, Núria B. 2013. Vulnerability of stream biota to climate change in mediterranean climate regions: a synthesis of ecological responses and conservation challenges. *Hydrobiologia*; 719(1): 331-351.